ENHANCED WEATHER MODELLING
FOR DYNAMIC LINE RATING

Fulin Fan

A thesis submitted for the degree of Doctor of Philosophy to

the Department of Electronic and Electrical Engineering

University of Strathclyde

2018

Acknowledgement

Abstract

Conventional approaches to dynamic line rating (DLR) forecasting provide single point estimates with no indication of the distribution of possible errors. Furthermore, most research related to DLR forecasting deals only with continuous or steady-state ratings while less attention has been given to short-term or transient-state ratings. This thesis describes (a) weather-based models to estimate probabilistic forecasts of steady-state DLRs for up to three 10-minutes time steps ahead for a particular span and a complete overhead line (OHL) and also (b) a fast-computational weather-based approach to probabilistic forecasting of transient-state DLRs for a particular span for time horizons of 10, 20 and 30 minutes. The percentiles of DLR forecasts can be used by a system operator within a chosen risk policy informed by the probability of a rating being exceeded.

The thesis first develops time series forecasting models for different weather variables that impact on line rating (i.e. air temperature, wind speed, wind direction and solar radiation) at weather stations that are installed along the route of 132kV OHLs in North Wales. Predictive centres of weather variables are modelled as a sum of residuals predicted by a suitable auto-regressive process and temporal trends fitted by Fourier series. Conditional heteroscedasticity of the predictive distribution is modelled as a linear function of recent changes in residuals within one hour for air temperature and wind speed or concentration of wind direction observations within the most recent two hours. A technique of minimum continuous ranked probability score estimation is employed to determine predictive distributions of the measured weather variables.

Then the thesis uses Monte Carlo simulation to generate a large number of random weather samples from the modelled predictive distributions which are paired to have rank correlations similar to those among their recent observations. The probabilistic steady-state DLR forecasts for a particular span in proximity to a weather station are

estimated from the random weather samples combined with a maximum allowable conductor temperature using a thermal model of the conductors (i.e. a steady-state heat balance equation). For a complete OHL, possible weather predictions at each span are inferred from random weather samples at stations by using suitable spatial interpolation models; the steady-state DLR forecast of the OHL is then identified as the minimum DLR among all spans for each generated scenario. Using an enhanced analytical method which evolves from a non-steady-state heat balance equation to track the transient-state conductor temperature, the transient-state DLR forecast for a particular span is calculated as that which increases the conductor temperature from an initial value to the maximum allowable limit for a particular future time period (i.e. in this study, 10, 20 and 30 minutes) under each set of random weather samples. The calibration of probabilistic DLR forecasts estimated from independent or correlated random weather samples are then examined to determine which approaches are most suited to estimation of DLRs at the lower end of a predictive distribution consistent with a system operator's risk policy. The potential use of DLR forecasting is then evaluated through estimating the degree to which wind generation curtailment for various assumed installed capacities at a wind farm that is connected to the 132kV network in North Wales can be alleviated through using the lower percentiles of steady-state DLR forecasts in place of the SLRs for each 132kV OHL.

Contents

List of Figures

VIII

List of Tables

List of Abbreviations

AAAC	All Aluminium Alloy Conductor
AAC	Average Additional Capacity
ACSR	Aluminium Conductor Steel Reinforced
ANN	Artificial Neural Network
AR	Auto-Regressive
ARMA	Auto-Regressive Moving Average
AGL	Above Ground Level
ASL	Above Sea Level
BADC	British Atmospheric Data Centre
BS	Brier Score
CDF	Cumulative Distribution Function
CH	Conditionally Heteroscedastic
CIGRE	International Council on Large Electric Systems
CPI	Central Prediction Interval
CRPS	Continuous Ranked Probability Score
DG	Distributed Generation
DGPS	Differential Global Positioning System
DLR	Dynamic Line Rating
DST	Daylight Saving Time
DTO	Distance to Ocean
DTS	Distributed Temperature Sensor
EPE	Experimental Plastic Elongation
EPRI	Electric Power Research Institute
EPWS	Effective Perpendicular Wind Speed
FLIR	Forward-looking Infrared
GIS	Geographic Information System
GPS	Global Positioning System
IDW	Inverse Distance Weighting
IEEE	Institute of Electrical and Electronic Engineers
LE	Linear Elastic
LIDAR	Light Detection and Ranging
LST	Local Standard Time
LTI	Linear Time Invariant
NRS	Net Radiation Sensor

NRT	Net Radiation Temperature
OHL	Overhead Line
OPF	Optimal Power Flow
OPPC	Optical Phase Power Conductor
OTLM	Overhead Transmission Line Monitoring
PD	Power Donut
PDF	Probability Density Function
PIT	Probability Integral Transform
REE	Red Eléctrica de España
RMSE	Root Mean Square Error
RPS	Ranked Probability Score
RST	Regime-Switching Space-Time
RTTR	Real-Time Thermal Rating
RTR	Real-Time Rating
SAW	Surface Acoustic Wave
SCADA	Supervisory Control and Data Acquisition
SD	Spatial De-trending
SLR	Static Line Rating
SP	Scottish Power
SPE	Simplified Plastic Elongation
SPM	Synchronized Phasor Measurement
TB	Technical Brochure
TD	Temporal De-trending
TDD	Trigonometric Direction Diurnal
TMS	Temperature Monitoring Sensor
TSO	Transmission System Operator
USi	Underground Systems, Inc.
VAR	Vector Auto-Regressive
WS	Weather Station
WV	Wind Vector

List of Variables

A. Conductor properties

A_c	Cross-sectional area of conductor	m^2
a_c	Thermal expansion coefficient of conductor	$°C^{-1}$
C_p	Specific heat of the conductor	$J/(kg \cdot °C)$
D_c	Conductor diameter	mm
E_c	Young's modulus of conductor	Pa
g	Gravitational acceleration	$9.81\,N/kg$
m	Mass of conductor per unit length	kg/m
T_{av-H}	Average conductor temperature inferred from the measured conductor tension	$°C$
T_c	Conductor temperature	$°C$
T_{cmax}	Maximum allowable conductor temperature	$°C$
w	Weight of conductor per unit length	N/m
ε_e	Emissivity	-
ε_s	Solar absorptivity	-

B. Span properties

C_{se}	A constant in a state change equation	-
$D_L,\ D_R$	Vertical distance from the lowest point to left and right attachment point of an inclined span	m
D_m	Midpoint sag of a span	m
$D_{m,RS}$	Midpoint sag of a ruling span	m
frq_o	Fundamental frequency of a span	Hz
$H,\ H_A,\ H_B$	Horizontal conductor tension and that at left and right attachment point of a span	N
H_e	Conductor elevation above sea level	m
h_c	Vertical distance between two attachment points of an inclined span	m
L_c	Line length of a span	m

Lat, Lon	Latitude and longitude of conductor	$radians$
$P_m P_m'$	Vertical distance from the horizontal midpoint of an inclined span to the level of the higher attachment point	m
S_c	Horizontal span length	m
S_c'	Span length	m
S_{RS}	Ruling span length	m
V_A, V_B	Vertical tensions at left and right attachment points	N
x_c	Horizontal distance from a particular point to the left attachment point of a span	m
X_L, X_R	Horizontal distance from the lowest point to the left and right attachment point of an inclined span	m
$y_c(x_c)$	Vertical distance from the conductor at x_c to the left attachment point of a span	m
Z_l	Line azimuth	$radians$
$\sum M_o$	Net torque at a particular point along a line	$N \cdot m$

C. Weather data

s_r	Solar radiation	W/m^2
T_a	Air temperature	°C
v_a	Air viscosity	$Pa \cdot s$
w_s	Wind speed	m/s
w_d	Wind direction	$radians$
ε_a	Thermal conductivity of air	$W/(m \cdot °C)$
ρ_a	Air density	kg/m^3
θ_{met}	Meteorological wind direction	$radians$
θ_{polar}	Wind vector polar angle	$radains$
θ_{vect}	Wind vector azimuth	$radians$

D. Dynamic line rating calculation

A'	Projected area of conductor	m^2/m
C_s	Solar azimuth constant	$radians$

d_{num}	Day of the year	-
H_s	Altitude of sun	$radians$
I, I_{ls}	AC current	A
I_{ss}	Steady-state rating	A
I_{ss-ls}	Steady-state rating of a line section	A
K_{angle}	Wind direction factor	-
NRT	Net radiation temperature	$\degree C$
N_{MC}	Number of Monte Carlo scenarios	-
R	AC resistance per unit length	Ω/m
T_{chigh}, T_{clow}	High and low conductor temperatures for which ac resistances are specified	$\degree C$
T_{film}	Average temperature of the boundary layer	$\degree C$
Q_c	Convection heat loss rate per unit length	W/m
Q_{cf}, Q_{cf1}, Q_{cf2}	Forced convection heat loss rate per unit length	W/m
Q_{cn}	Natural convection heat loss rate per unit length	W/m
Q_r	Radiation heat loss rate per unit length	W/m
Z_s	Sun azimuth	$radians$
q_{se}	Total solar and sky radiated heat intensity at conductor elevation	W/m^2
w_h	Hour angle relative to noon	$radians$
θ_s	Effective angle of incidence of sun's ray	$radians$
ϑ_d	Wind attack angle between wind direction and conductor azimuth	$radians$
δ_s	Solar declination	$radians$
χ_s	Solar azimuth variable	-

E. Probabilistic Forecasting

$\boldsymbol{b}$, $\boldsymbol{B}$	Matrix of constant(s) and auto-regress parameters	-
c_0, c_1, c_{00}, c_{01}	Coefficients representing conditional heteroscedasticity	-
$crps, crps_l, crps_c$	Continuous ranked probability score	*

e, $\boldsymbol{E}$	Matrix of Gaussian noise terms	*
e_t, $\boldsymbol{E}_t$, $\boldsymbol{E}'_t$	Gaussian noise term(s)	*
F_c, F_l	Predictive cumulative distribution functions for a circular variable and a linear variable	-
FS_o	Offset of time series	*
FS_i, φ_i	Fourier coefficients of the ith harmonics	-
K	Number of target locations	-
L	Length of time steps ahead	-
p	Order of an AR or VAR model	-
p_{fs}	Order of Fourier series	-
$Trend$	Temporal trend	*
u, $\boldsymbol{u}$, $\boldsymbol{u}'$	Constant(s) in an AR or VAR model	*
ω_{fs}	Angular frequency of Fourier series	-
x_a, x_v, x_θ, x	Variable in probability density function	*
x_o, θ_o	Actual value of a linear or circular variable	*
X, X', Θ, Θ^*	Independent random samples from the predictive cumulative distribution function for a linear or circular variable	*
$\boldsymbol{y}$, $\boldsymbol{Y}$	Matrix of de-trended data to be forecast	*
$\boldsymbol{z}$, $\boldsymbol{Z}$	Matrix of historic de-trended data	*
$\tilde{z}_t$, $\widetilde{\boldsymbol{Z}}_t$, $\tilde{z}'_t$, $\widetilde{\boldsymbol{Z}}'_t$	De-trended data or residuals	*
β_i, β'_i, $\boldsymbol{A}_i$, $\boldsymbol{A}'_i$	Auto-regressive parameters in an AR or VAR model	-
$\boldsymbol{\beta}_p$, $\boldsymbol{\beta}_{kk}$	Matrix of auto-regressive parameters	-
β_{kk}	Partial autocorrelation function at time lag k	-
ζ_k	Auto-covariance at time lag k	-
ρ_k	Autocorrelations of time series at time lag k	-
$\boldsymbol{\rho}_p$, $\boldsymbol{P}_p$, $\boldsymbol{P}_k$	Matrix of autocorrelations	-
μ_a, σ_a	Predictive centre and spread of air temperature	* / -
μ_v, σ_v	Predictive centre and spread of wind speed	* / -
μ_θ, κ	Predictive centre and concentration parameter of wind direction	* / -
θ_1, θ_2	Random directions within an interval $[-\pi, \pi)$	$radians$

$\alpha(\cdot)$	Operator of circular distance	-
$E\{\cdot\}$	Operator of expected value	-
$f(\cdot),\ f^{N}(\cdot),$ $f^{N+}(\cdot),\ f^{VM}(\cdot)$	Predictive probability distribution and that for air temperature, wind speed and wind direction	-
$N(\cdot)$	Normal distribution	-
$N^{+}(\cdot)$	Truncated normal distribution with a cut-off at zero	-
$VM(\cdot)$	Von Mises distribution	-
$\emptyset(\cdot),\ \Phi(\cdot)$	Probability density function and cumulative distribution function of a standard normal distribution	-
$I_0(\cdot)$	Modified Bessel function of the first kind of order zero	-
$F_o(x, x_o)$	Heaviside function equalling 1 if the variable x greater than actual value x_o	-

* The unit is related to the weather variable of interest

F. Rank Correlation based Pairing

$Ca_{l,c}^2$	C-association describing the rank relationship between linear and circular variables	-
Cr_{N_r}, Cr_c, Cr_s	Coefficients for C-association calculation	-
$C_R,\ C_{MR}$	Rank correlation matrices calculated from series of recent weather data and arbitrary van der Waerden scores	-
M_R	Matrix comprising arbitrary van der Waerden scores	-
M_R^*	Matrix having a rank correlation similar to C_R	-
N_r	Number of data pairs for rank correlation calculation	-
n_R	Number of variables to be paired	-
$P_R,\ Q_R$	Lower triangular matrices obtained from C_R and C_{MR}	-
$r_{l,i}$	Linear rank of the ith linear data	-
$\Delta r_{l,i}$	Rank difference between the ith data pair for linear variables	-
$r_{c,i}$	Circular rank of the ith circular data	-
$r_{cl,i}$	Linear rank of the ith circular data when treated as linear data	-
$rc_{l,l}$	Spearman's rank correlation coefficient between linear variables	-

G. Spatial Interpolation

$a_\gamma,\ b_\gamma,\ c_\gamma$	Coefficients used in mathematical functions to fit semi-variances	-
Cov	Covariance between weather variables	*
Cov_{neg}	Covariance between weather variables at the target location and the sampled location that has a negative kriging weight	*
$ds_{i,o}$	Distance between target location and the ith sampled location	km
$error_\theta,\ error_\theta^*$	Errors of wind direction estimates	$radians$
$loc_o,\ loc_i$	Target location and the ith sampled location	-
h_s	Spatial distance lag between two weather variables	km
$\boldsymbol{K}$	Matrix of covariances between sampled locations	*
$\boldsymbol{k}$	Vector of covariances between the target and sampled locations	*
lvl_{ane}	The anemometer's height	m
lvl_{ref}	The reference level	m
me	Expected value or trend components of weather variables	*
$\xi(loc_o),\ \xi(loc_i)$	Weather data at the target location or the ith sampled location	*
$N(h_s)$	Number of pairs of weather variables, $\xi(loc_i)$ and $\xi(loc_i{\sim}h_s)$, that are a distance lag h_s apart	-
$N(loc)$	Number of sampled locations	-
q	Power parameter in an IDW method	-
rl_o	Ground roughness length	m
$w_{s,ane}$	Wind speed at an anemometer's height	m/s
$w_{s,ref}$	Wind speed at a reference level	m/s
$\gamma(h_s),\ \gamma^*(h_s)$	Empirical and fitted Semi-variances at lag h_s	*
$\lambda_i, \lambda_{IDW,i}, \lambda_{KRI,i}$ $\lambda_{KRI,i,new}$	Weight, IDW weight, kriging weight and corrected kriging weight assigned to the ith sampled location	-
$\lambda_{KRI,neg}$	Negative kriging weights	-

* The unit is related to the weather variable of interest

H. Transient-state Calculation

I_i, I_f	Initial/final line current before/after step occurs	A
$I_{i,eq}$	An equivalent steady-state line current before step changes	A
$I_{ss,1}, I_{ss,2}, I_{ss,3}$	Steady-state rating forecasts for up to three 10-minute time steps ahead	A
I_{ts}, $I_{ts,1}$, $I_{ts,2}$, $I_{ts,3}$	Transient-state rating and that for a specified time period of 10, 20 or 30 minutes	A
K_c, K_c'	The rate at which the sum of the linearized cooling terms varies with conductor temperature	$W/(m \cdot {}^\circ C)$
Q_x, ΔQ_x	A particular heating or cooling term per unit length and its step change	W/m
$Q_{c,linearized}$	Linearized convection heat loss rate per unit length	W/m
Δt	Sufficiently small time interval	sec
tp	A specified time period	min
$T_{ci,\Delta t}, T_{cf,\Delta t}, T_{cav,\Delta t}$	Initial, final and average conductor temperatures over a time interval Δt	${}^\circ C$
T_{ci}, T_{cfts}	Initial and final conductor temperatures of a specified time period	${}^\circ C$
T_{ciss}, T_{cfss}, T_{cavss}	Steady-state initial and final conductor temperatures of a specified time period and their average value	${}^\circ C$
T_{avg}	Average of T_{ci} and T_{cfss}	${}^\circ C$
$T_{c10}, T_{c20}, T_{c30}$	Transient-state final conductor temperatures at the end of 10, 20 and 30 minutes	${}^\circ C$
wc	Weather conditions after step changes	*
wf_1, wf_2, wf_3	Weather forecasts for up to three steps ahead	*
$ß_i$, $ß_f$	The rises above the air temperature for the initial conductor temperature T_{ci} and the steady-state final conductor temperature T_{cfss}	${}^\circ C$
τ, τ_x	Thermal time constant and that for the step change in a particular heating or cooling term ΔQ_x	min
$\Delta Gain$	Difference between the assumed and actual heat gain rates per unit length	W/m

$\Delta Loss_{linearized}$	Difference between the sums of linearized cooling terms that vary with conductor temperature at different rates	W/m
$F_1(\cdot),\ F_2(\cdot)$	Functions used in the secant method to determine the steady-state final conductor temperature and the transient-state rating for a specified time period	-

* The unit is related to the weather variable of interest

I. Wind Generation Calculation

a_{wp}, b_{wp}, c_{wp}	Coefficients used in a generic power curve model	-
$DLR_1,\ DLR_2,\ DLR_3$	Dynamic line rating forecasts for up to three 10-minutes time steps ahead for overhead lines	MVA
$\Delta WP^-, \Delta WP^+$	The maximum volume that a wind farm is allowed to ramp down or up in 10 minutes	W
$WP_0,\ WP_1,\ WP_2,\ WP_3$	Present wind power output and planned power outputs after 10, 20 and 30 minutes	W
$WP^{av},\ WP_1^{av},\ WP_2^{av},\ WP_3^{av}$	Expected available wind power and the forecasts for up to three 10-minutes time steps ahead	W
WP_{rated}	Rated power for a wind turbine	W
$w_{s,hub}$	Wind speed at the hub height	m/s
$w_{s,in},\ w_{s,out},\ w_{s,rated}$	Cut-in, cut-out and rated wind speeds for a wind turbine	m/s

1. INTRODUCTION

1.1. Background to Dynamic Line Rating

The real-time thermal rating (RTTR) is the maximum level of power flow at which a section of transmission or distribution network can be operated safely and reliably at the time in question [1]. In the case of overhead lines (OHLs), RTTR is typically referred to as dynamic line rating (DLR). The current passing through a line has to be limited to a certain value in order to avoid excessive conductor temperature which leads to an unwanted acceleration of aging and excessive sag of a span which may violate the minimum required clearance [2]. An OHL is conventionally operated below a static line rating (SLR) which is estimated through a thermal model of overhead conductors that has been proposed in IEEE Standard 738 [3] and CIGRE Technical Brochure 601 [4] using a maximum allowable conductor temperature and a conservative set of weather conditions such as a low wind speed and a high air temperature for a particular season [5, 6].

OHLs have received particular attention in respect of dynamic or real-time ratings due to their high dependency of safe ratings on ambient conditions. Most reported studies related to DLRs deal only with continuous or steady-state DLRs which lead to a maximum allowable conductor temperature for specified weather conditions under the assumption of the conductor being in thermal equilibrium [3]. Under transient conditions, the temperature of a conductor operated at the short-term or transient-state DLR will gradually approach the maximum allowable limit under specified weather conditions over a given short time period (typically less than half hour) considering the initial temperature and thermal inertia of the conductor [3]. The actual power transfer capacity of an OHL is usually higher than the SLR since the conservative weather conditions used to estimate the SLR rarely occur in practice. A

wind speed above the conservative level can provide a significant cooling of the conductor by convection away of the Joule heat generated by the assumed high current [7]. The Oncor Electric Delivery Company has deployed DLR technologies on eight 345kV and 138kV overhead transmission lines located in central Texas and demonstrated that the monitored steady-state ratings exceeded the SLRs for around 97% – 99% of the time for most transmission lines and provided 6% – 14% and 8% – 12% more capacities on 345kV and 138kV lines respectively than the ambient temperature-adjusted ratings which only considered changes of air temperature [8, 9]. The eight 132kV OHLs operated by Scottish Power Energy Networks in North Wales were found to have the real-time ratings calculated from weather observations above the SLRs for 84.1% – 99.9% of the time [10].

The additional headroom of an OHL's ampacity exploited by a DLR system can assist network operators to accommodate growth in power flow and alleviate transmission congestion. Talpur [11] evaluated the financial benefit related to an increase of 1GWh energy flow passing through a particular OHL in a meshed 130kV network in western Sweden that could be achieved by the DLR implementation, reconductoring and new line constructions separately considering variations in system loads and the connection of a 60MW wind farm; applying a particular DLR technique on the OHL showed a significant financial advantage in comparison with the other two traditional solutions. Furthermore, it has been widely noted that the application of DLR techniques has particular benefit for wind generation due to the positive correlation between the output of a wind farm and the ampacity of a line connecting it to the network [10, 12, 13]. That is, the high wind speeds producing high outputs from a wind farm will provide significant cooling on the nearby OHLs which can then tolerate higher levels of power transfer capacity. DLRs can therefore be exploited to alleviate curtailment of available wind power or reduce or avoid reinforcement of the connection. Heckenbergerova [12] estimated available wind powers for various assumed installed capacities at a virtual wind farm located in one

of the windiest areas in the Czech Republic which were then compared with the ratings (DLRs or SLRs) of a virtual OHL connecting it to the main grid; the use of DLRs in place of SLRs led to a significant reduction in curtailed wind generation and approximately tripled the optimal size of the wind farm in this particular case study. From the perspective of wind farm owners, Wallnerström [14] quantified the life cycle costs of implementing DLR on a particular OHL which connected a wind farm with a distribution network, compared to building an additional connection line under different wind farm capacities separately based on capital and operational expenditures of a wind power plant and a line. Though both approaches could significantly reduce wind generation curtailment compared with use of SLRs on the existing connection line, applying DLR was evaluated to provide a higher profit than building an extra line. However, the estimated profit in [14] from applying DLR did not consider the costs of investing and operating a particular DLR monitoring technique; this would provide an opportunity to estimate the maximum allowed cost of introducing DLR based on which an appropriate DLR technique could be selected. For investment planning timescales, DLRs can be considered over a range of future operating conditions and, provided the system operator has some reasonable measures available to them when power flows would exceed the real-time limits, can offer a cost-effective means to deal with power generation and demand growth or distributed generation connections that reduce the need for network reinforcement.

In recent decades, a range of DLR techniques [15-18] have been developed to estimate or predict the line's actual ampacity at a given time under prevailing or anticipated weather conditions through monitoring or inference of the state of overhead conductors. According to monitoring targets, these DLR techniques can be classified as [15]:

- the temperature-based techniques that monitor the conductor temperature;

- the sag-based techniques that measure the sag of a span;

- the tension-based techniques that measure the tension of a line section consisting of multiple suspension spans;

- the weather-based techniques that infer the conductor temperature and the line's rating from weather conditions measured at weather stations.

Alternatively, the DLR techniques can be classified as [17]:

- the single-span monitoring techniques that record the behaviour (e.g. conductor temperature or sag) of a single span or a single point along a span where the device is installed;

- the multi-span monitoring techniques that measure the average behaviour (e.g. horizontal tension) of a line section from which the behaviour of each span within the section is inferred.

The average conductor temperature, mid-point sag, and horizontal tension of a span are inter-convertible, as shown in Fig. 1-1. Assuming the conductor to be fully flexible and of a uniform weight per unit length, the mid-point sag of a span is inversely proportional to the horizontal tension (i.e. the component of the tension along the line in the horizontal direction) based on geometric characteristics of the span [19]. The mid-point sag or horizontal tension of a span can be used to roughly calculate the average conductor temperature through a state change equation [19] or a state change curve [17]. The state change equation relates the average conductor temperature to the mid-point sag of a span by modelling the conductor elongation. The state change curve uses a polynomial curve to describe the relationship between the average conductor temperature and the horizontal tension of a span. Both the state change equation and curve should be calibrated by various field measurements before using them to infer the average conductor temperature from the sag/tension measurement. The monitoring or inference of sag/tension and conductor temperature cannot be directly used by the system operator to judge the volume of additional headroom in power transfer capacity. As a result, the measured or inferred conductor

temperature should be used with weather observations in proximity to the monitored conductors and a thermal model of the conductors [3, 4] to estimate or predict DLRs which can then be provided for operators to dispatch power flows. This is generally based on inference of an 'effective' wind speed perpendicular to the conductors that provides the same cooling effect as the actual wind speeds and directions which vary along the span from measurements of the conductor temperature, line current, air temperature and solar radiation. The estimated effective perpendicular wind speed is then used with a maximum allowable conductor temperature to calculate DLRs based on the thermal model of the conductors [17]. The operating theories and features of different DLR techniques will be detailed and compared in this thesis.
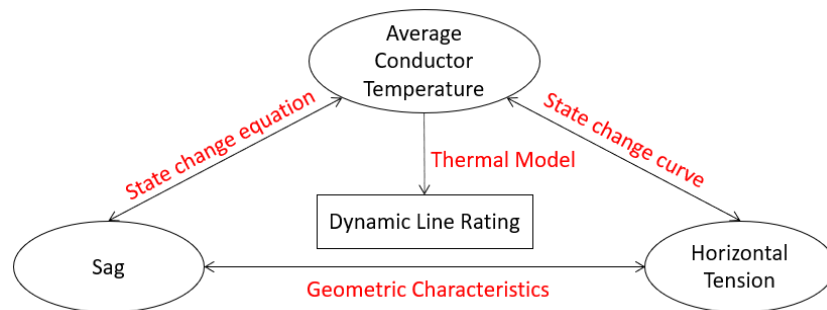
Fig. 1-1. Inter-conversion among average conductor temperature, sag and horizontal tension of a span.

1.2. Description of Dynamic Line Rating Research

1.2.1. Scottish Power Energy Networks DLR project

Previous work on dynamic line rating (DLR) undertaken by Durham University [1, 20] developed a weather-based approach to DLR estimation. Durham's approach used spatial interpolation models to infer weather conditions for each span of an overhead line (OHL) from real-time weather observations at a limited number of weather stations; the minimum of DLRs among all spans estimated from weather conditions using a thermal model of the conductors was then applied to the whole line. Based on the weather-based approach developed by Durham University, Scottish Power (SP) Energy Networks implemented a demonstration project on eight

132kV overhead circuits (C) in North Wales [10], as shown in Fig. 1-2. The 10-minute average weather data including air temperature, wind speed, wind direction and solar radiation were recorded at nine weather stations (WS) which were separately installed at six 132kV substations (B) and three double circuit steel towers along the OHL route. A geographical map of research area is shown in Fig. 1-3.
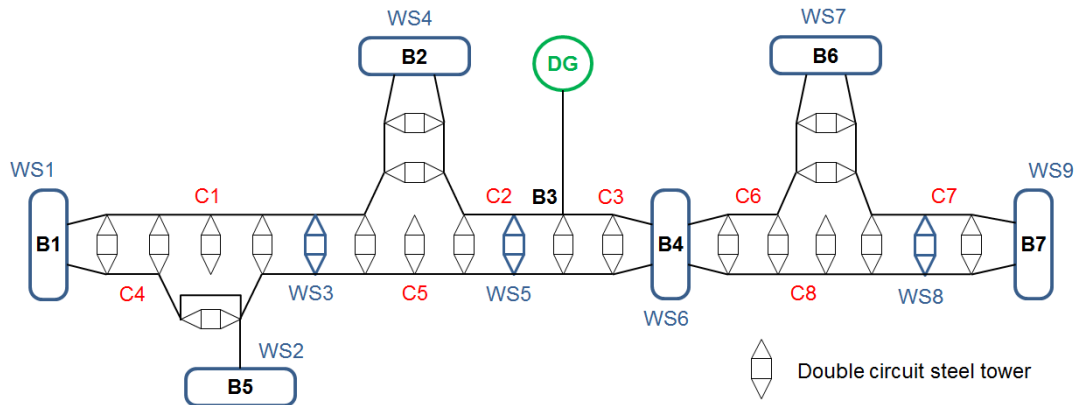
Fig. 1-2. The 132kV network in North Wales with uppercase letters B, C, WS and DG representing 132kV substation, overhead circuit, weather station and distributed generation respectively [10].
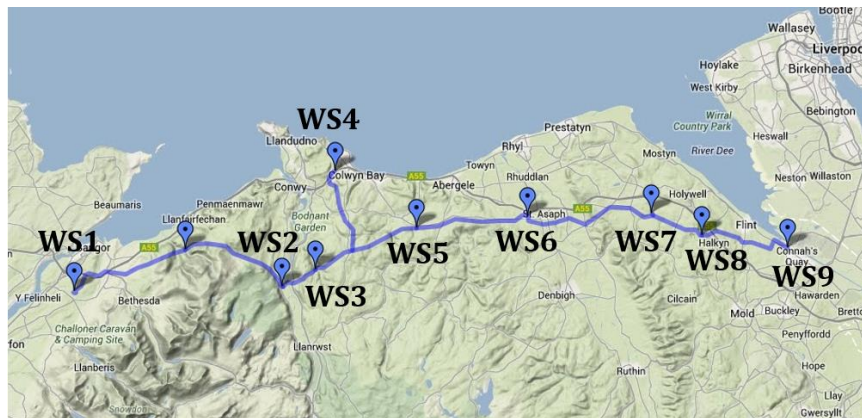
Fig. 1-3. Geographic map showing the route of studied overhead lines and locations of 9 weather stations in North Wales [10].

1.2.2. Primary objective of this research

The primary objective of this research is to enhance the weather-based approach developed by Durham University to not only provide 'real-time' ratings but also predictions of ratings so that system operators have time to take action to mitigate the

consequences of the limitations of power transfer or, alternatively and where possible, to exploit additional thermal capacity. In addition, DLR forecasts will be provided not just as a single value for a single future moment in time but in the form of percentiles describing the probability of a rating being exceeded so that the system operator can make an informed judgement about risk.

In order to achieve expected functions of the enhanced weather-based model and accomplish the primary objective of this research, the following steps are to be undertaken:

- Review DLR techniques that are described in published engineering literature;

- Develop statistical forecasting models to provide point forecasts of air temperature, wind speed, wind direction and solar radiation;

- Extend the statistical forecasting models to provide predictive distributions of weather variables;

- Develop more advanced spatial interpolation models than those used in previous work, [20], to infer weather data for each span of an OHL;

- Quantify percentiles of steady-state DLR forecasts for up to three 10-minutes time steps ahead for a particular span and a complete line;

- Quantify percentiles of transient-state DLR forecasts for time horizons of 10, 20 and 30 minutes over a particular future half-hour period for a span.

- Evaluate the potential use of DLR forecasting with respect to alleviating wind generation curtailment at a wind farm that has a connection to the 132kV network in North Wales.

The main contribution of the thesis is to propose a framework that uses time series forecasting models along with a thermal model of overhead conductors to estimate probabilistic forecasts of both steady-state and transient-state DLRs from historic weather data in Monte Carlo simulation where correlations between different weather

variables are considered. During the development of a weather-based approach to the transient-state DLR forecasting, the thesis provides insights into an enhanced version of IEEE analytical method for the transient-state conductor temperature calculation and some issues that should be paid attention to for the transient rating estimation. Furthermore, the thesis examines impacts of correlations between different weather variables on predictive distributions of DLRs and emphasises the importance of pairing random weather samples in Monte Carlo simulation.

1.2.3. Enhanced weather-based models for probabilistic DLR forecasting

In this research, enhanced weather-based DLR forecasting models have been developed to estimate probabilistic forecasts of steady-state DLRs for a particular span and a complete line. Furthermore, through an enhancement in an analytical method described in IEEE Standard 738 [3] for the transient-state conductor temperature modelling, a fast-computational approach is developed to determine predictive distributions of transient-state DLRs for a particular span.

1.2.3.1. Probabilistic steady-state DLR forecasting

A flow chart describing how an enhanced weather-based model estimates probabilistic forecasts of steady-state DLRs for an OHL is shown in Fig. 1-4. Based on historic time series of 10-minute average weather data, probabilistic forecasting models estimate (a) predictive centres of weather variables as a sum of residuals predicted by a suitable auto-regressive process and temporal trends fitted by Fourier series and (b) conditional heteroscedasticity of the distribution as a linear function of changes in residuals within the most recent one hour for air temperature and wind speed or concentration of recent wind direction observations over two hours. A technique of minimum continuous ranked probability score estimation is then used to determine models' parameters and predictive distributions for air temperature (T_a), wind speed (w_s) and wind direction (w_d) respectively. Point forecasts of solar radiation (s_r) are used here instead of probabilistic forecasts since, when wind speeds

are above a modest level [1] or when conductor temperatures are relatively high [21], conductor temperature is found to be insensitive to the change in solar radiation. This is because an increase in wind speed or the rise of conductor temperature above air temperature could lead to the convection heat loss rate significantly exceeding the solar heat gain rate. (According to [3], the latter is dependent on the solar intensity, conductor's absorptivity and diameter and not affected by the conductor temperature or wind conditions). The point forecasts of solar radiation are calculated in a similar way to estimations of predictive centres, with auto-regressive parameters being determined by least squares estimation.
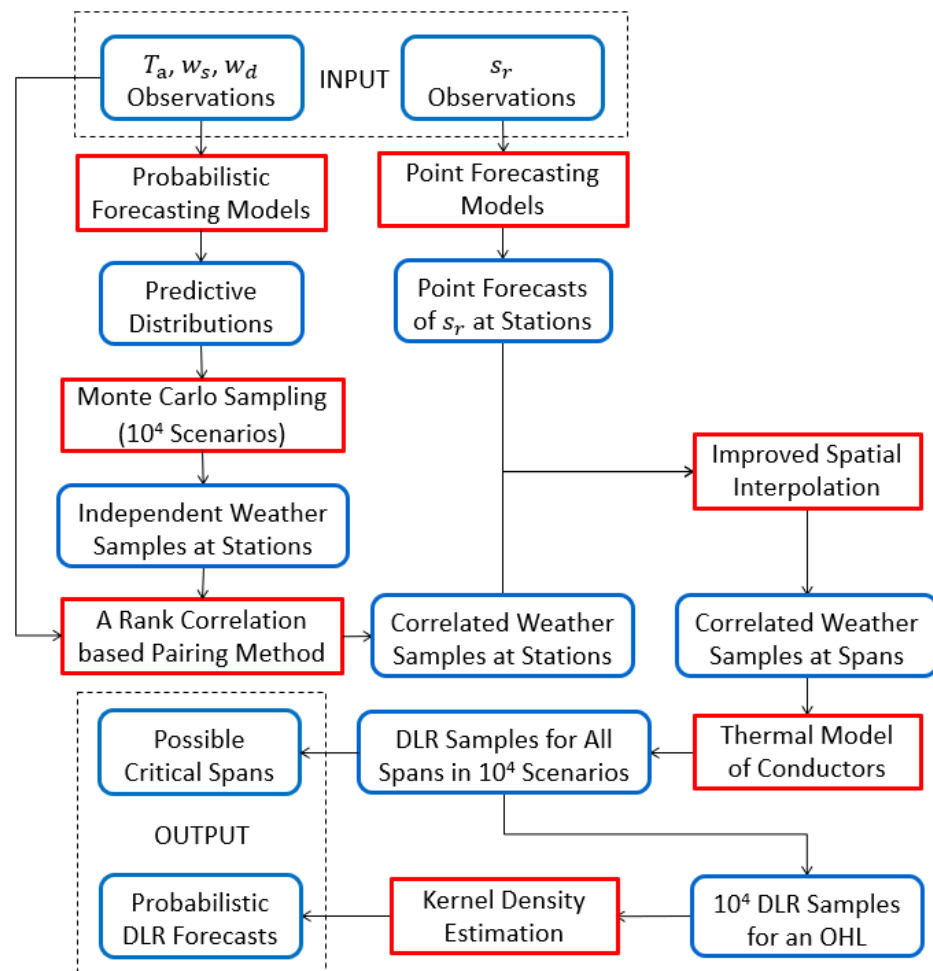
Fig. 1-4. An enhanced weather-based model for probabilistic DLR forecasting for an OHL.

A large number of random weather samples are independently generated from the modelled predictive distributions in a Monte Carlo procedure and then paired to create correlations similar to those computed from their recent observations. The sampled values of weather forecasts and point forecasts of solar radiation for all spans within an OHL are inferred from the correlated random weather samples and solar radiation predictions at weather stations using suitable spatial interpolation models. A thermal model of overhead conductors is then used to calculate steady-state DLR forecasts at a particular future time for all spans of the OHL, among which the minimum value is applied to the OHL in each generated scenario. A sample cumulative distribution function is extracted from the sampled values of DLR forecasts for the OHL and then smoothed by kernel density estimation to determine the DLR forecasts in the form of percentiles. The possible location of the critical span for the OHL is predicted from the frequency of each span having the minimum DLR forecast among all spans in all generated scenarios.

The probabilistic steady-state DLR forecasts for a particular span in close proximity to a weather station can be directly calculated from random samples of weather variables and point forecasts of solar radiation at the station without need of spatial interpolation models. The calibration of probabilistic DLR forecasts calculated from independent or correlated weather samples will be examined by the histograms of probability integral transform to determine whether the correlations should be added into the random weather samples.

1.2.3.2. *Probabilistic transient-state DLR forecasting*

The majority of published approaches to DLR deal with steady-state ratings. Less attention has been given to transient-state DLR calculations. For example, they were omitted in previous work [20] where it was speculated, though not proven, that applying transient-state DLRs would not materially elevate the power throughout in GWh per annum within the power system. This may be because the transient rating can be maintained within the given time period only, after which the power transfer

capacity would again be limited by the steady-state DLR. Furthermore, calculations of transient-state DLRs may be not necessary when sampling intervals of weather data and load data are long enough (e.g. 1 hour) for a conductor to fully respond to step changes in variables. Moreover, the computation time cost to estimate transient ratings is much greater than that for steady-state calculations since a transient rating has to be iteratively adjusted until the conductor temperature reaches the maximum permissible limit at the end of a specified time period.

Although an OHL can be operated at the level of the transient-state DLR for the specified short term only, applying transient-state DLRs will provide higher additional ampacity headroom than using steady-state ratings. This can further mitigate transmission congestions and alleviate wind generation curtailment. Most research related to transient-state DLR calculations [22-24] used a conventional approach to track transient-state conductor temperatures over a specified time period. It divides the given time period into several sufficiently small time intervals (e.g. 10 seconds or less) and then estimates the variation in conductor temperature over each time interval. IEEE Standard (Std.) 738 [3] has developed an analytical method to calculate the transient-state conductor temperature as an exponential function of time which can reduce the computation time compared with the conventional approach. However, the IEEE analytical method only considers a step change in line current and requires the conductor to be in thermal equilibrium before the step occurs. The IEEE analytical method has been enhanced in this thesis through inference of an equivalent steady-state initial line current from the initial conductor temperature and weather conditions over a given time period. In this way, the conductor's thermal equilibrium at the start of the given time period is created and the changes of weather conditions are considered.

Along with use of the enhanced analytical method, the transient-state DLR forecast of a particular span for a particular future time period (i.e. in this research, 10, 20 and 30 minutes) is calculated from random weather samples that are generated from the

11

predictive distributions for up to three 10-minutes time steps ahead in each scenario. The changes of weather forecasts at each future moment are taken into account. The probabilistic forecasts of transient-state DLRs for time horizons of 10, 20 and 30 minutes are then derived from their respective sampled values using kernel density estimation. The performance of the fast-computational approach developed here for transient-state DLR forecasting will be assessed with respect to the forecast accuracy, the calibration of probabilistic forecasts and the computation time.

1.2.3.3. *Application of DLR forecasting to reduce wind generation curtailment*

It is expected that applying DLR techniques can increase the utilisation of wind energy. North Wales has considerable renewable resources. As shown in Fig. 1-2, the electricity produced by a 90MW Rhyl Flats offshore wind farm (denoted by DG) is injected into the 132kV transmission network at a 132kV bus (B3) and dispatched to buses B2 and B4 through two 132kV OHLs C2 and C3. The potential application of probabilistic steady-state DLR forecasts will be evaluated here through an estimation of the degree to which curtailment of various assumed wind farm capacities at Rhyl Flats (90MW and a series of upscaled wind farms) can be reduced through using the lower percentiles of steady-state DLR forecasts in place of the SLRs of 132kV OHLs. The planned power output from Rhyl Flats is maximised using Optimal Power Flow subject to the maximum allowable wind generation ramp rate, the expected available power output from Rhyl Flats and DLR forecasts for up to three 10-minutes time steps ahead. The use of the maximum allowable ramp rate ensures that the power output from Rhyl Flats can decrease to the planned output estimated for the next time step in a 10-minute period.

1.3. Thesis Structure

The thesis is organised in the following way:

Chapter 2 describes some useful knowledge associated with the geometric characteristics, the state change equation and a thermal model of overhead conductors and the concept of ruling span and also reviews the operating theories and features of different DLR techniques that have been described in published engineering literature.

Chapter 3 develops different time series forecasting models to estimate predictive distributions of air temperature, wind speed and wind direction and point forecasts of solar radiation; the models using less computation time and providing the best performance with respect to the root mean square error (RMSE) for point forecasting and the continuous ranked probability score for probabilistic forecasting are adopted.

Chapter 4 describes a rank correlation based pairing method to pair the independent random samples of different weather variables to create correlations similar to those among their recent observations; then the spatial interpolation models developed in Durham's work [20] are improved by comparing different combinations of the spatial trend modelling and an inverse distance weighting or kriging interpolation model.

Chapter 5 develops different approaches to probabilistic forecasting of steady-state DLRs for a particular span and a complete OHL and assesses their performances with respect to the RMSE of point forecasts, the calibration of probabilistic forecasts and the effectiveness of using a certain percentile (e.g. the 5th percentile) from a probabilistic DLR forecast; the possible location of critical span at a particular future time is also predicted for each OHL.

Chapter 6 enhances the analytical method proposed in IEEE Std. 738 [3] to model transient-state conductor temperatures and compares its accuracy with conventional

approaches; probabilistic transient-state DLR forecasts of a particular span for a particular future half-hour period are then estimated from the initial conductor temperature combined with random sampled values of weather forecasts for up to three 10-minutes time steps ahead based on the enhanced analytical method.

Chapter 7 investigates the potential application of probabilistic DLR forecasting on wind power integration by quantifying the reduced wind generation curtailment at Rhyl Flat wind farm that is connected to the 132kV network in North Wales through replacing the SLRs by the lower percentiles of steady-state DLR forecasts for 132kV OHLs; the risk of overloading on each 132kV OHL due to use of DLR percentiles is also analysed.

Chapter 8 summarises findings from the present work, building on which future research is suggested.

1.4. Publications

The author has published the following papers during the course of Ph.D.:

F. Fan, K. Bell, D. Hill, and D. Infield, "Wind forecasting using kriging and vector auto-regressive models for dynamic line rating studies," *IEEE PowerTech Conference*, pp. 1-6, Jul. 2015.

F. Fan, K. Bell, and D. Infield, "Probabilistic weather forecasting for dynamic line rating studies," *Power Systems Computation Conference*, pp. 1-7, Jun. 2016.

F. Fan, K. Bell, and D. Infield, "Probabilistic real-time thermal rating forecasting for overhead lines by conditionally heteroscedastic autoregressive models," *IEEE Transactions on Power Delivery*, vol. 32, no. 4, pp. 1881-1890, Aug. 2017.

2. REVIEW OF DYNAMIC LINE RATING TECHNIQUES

A range of dynamic line rating (DLR) techniques have been developed in recent decades to measure or infer the thermal and mechanical behaviour of overhead conductors, most of which have been further upgraded to simultaneously monitor more than a single target. Companies owning intellectual properties of the monitoring devices have additionally developed the specific mathematical programs to calculate the real-time ratings or ratings' forecasts for different time scales based on what the devices have measured. In this chapter, some useful knowledge is introduced associated with the geometric characteristics, the state change equation and a thermal model of overhead conductors and the concept of ruling span. Then, the operating theories and features of different DLR techniques that have been described in published engineering literature are explained and summarised. These fall into four main families: based on measurement of conductor temperature; measurement of sag; measurement of conductor tension; and measurements of weather observations.

2.1. Characteristics of Overhead Conductors

2.1.1. Geometric characteristics of overhead conductors

The geometric characteristics of overhead conductors link the sag of a span and its horizontal tension. Since an overhead line (OHL) often works in rugged terrain, two attachment points of a span along the line are not always placed on the same vertical level. A span with both attachment points at the same vertical level is called a level span as shown in Fig. 2-1. Otherwise, it is called an inclined span as shown in Fig. 2-2 [25]. The symbols in Figs. 2-1 and 2-2 are explained in Table 2-1.
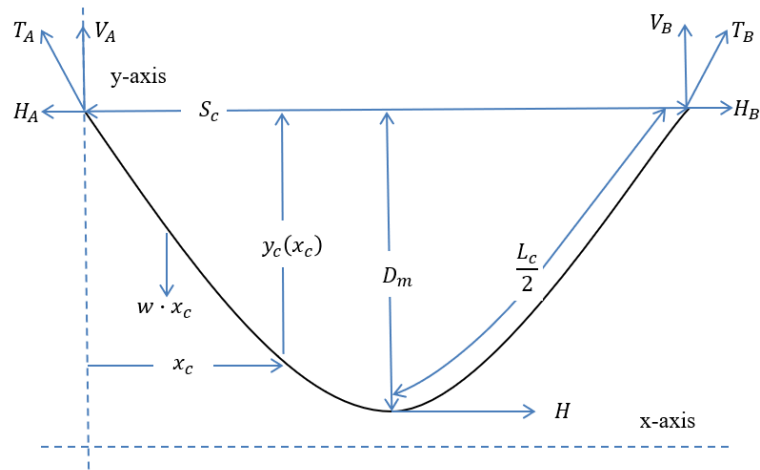
Fig. 2-1. A level span [25]
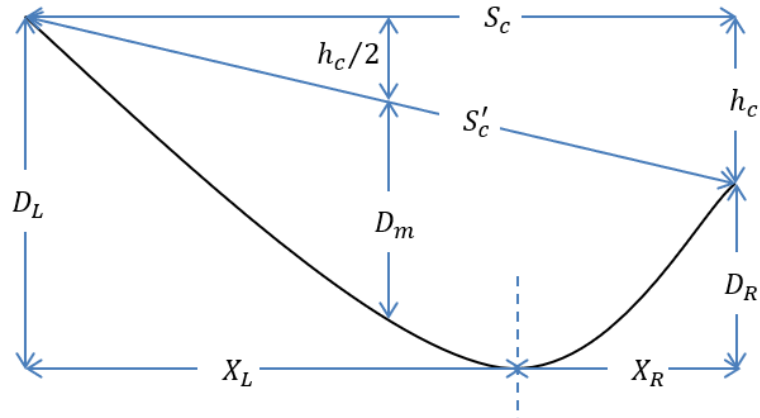
Fig. 2-2. An inclined span [25]

Table 2-1. Symbols and units of quantities for a span.

Symbol	Quantity	Unit
S_c	Horizontal span length	m
S_c'	Span length	m
D_m	Midpoint sag	m
$D_L,\ D_R$	Vertical distance from the lowest point to the left or right attachment point	m
L_c	Line length	m
H	Horizontal tension	N
w	Weight of conductor per unit length	N/m
x_c	Horizontal distance from the left attachment point	m
$y_c(x_c)$	Vertical distance from the conductor at x_c to the left attachment point	m
$X_L,\ X_R$	Horizontal distance from the lowest point to the left or right attachment point	m
h_c	Vertical distance between two attachment points	m

16

The shape of a span is generally dependent on the line's materials, supporting constructions, conductor temperatures, additional forces (e.g. ice and wind loading), etc. It can be described by an exact catenary equation in terms of horizontal tension H (i.e. the component of the tension along the line in the horizontal direction) and weight per unit length of overhead conductors w, from which the midpoint sag of a level span D_m is approximately determined as:

$$D_m = \frac{H}{w}\left[\cosh\left(\frac{wS_c}{2H}\right) - 1\right] \cong \frac{wS_c^2}{8H} \tag{2-1}$$

The expression on the right-hand side of equation (2-1) is an approximate parabolic formula based on the first term of the Maclaurin expansion of a hyperbolic cosine which is valid if $w^2S_c^2/48H^2 \ll 1$ [19]. Another means to derive the parabolic formula is listed in **Appendix A** based on the assumption of the length of a line being approximately equal to its span length, i.e. $L_c \cong S_c$. The length of the line between two attachment points of a level span is then determined as [19]:

$$L_c = \left(\frac{2H}{w}\right) \cdot \sinh\left(\frac{wS_c}{2H}\right) \cong S_c + \frac{8D_m^2}{3S_c} \tag{2-2}$$

The difference in length between span and line approximately equal to $(8D_m^2/3S_c)$ is termed the "slack" [19]. The midpoint sag D_m and the horizontal tension H can therefore be derived from the "slack" by equations (2-3) and (2-4) which indicate that a very small variation of line length will result in a large change in the midpoint sag of a span. For example, for a particular level span of span length $S_c = 200m$, the sag D_m will increase from $8.7m$ to $10.6m$ when the line length only increases from $201m$ to $201.5m$ according to equation (2-3).

$$D_m \cong \sqrt{\frac{3 \cdot S_c \cdot (L_c - S_c)}{8}} \tag{2-3}$$

$$H \cong \frac{w \cdot S_c}{2}\sqrt{\frac{S_c}{6(L_c - S_c)}} \tag{2-4}$$

An inclined span can be considered to consist of half sections of two level spans with different sags, i.e. one from the lowest point to the left with the sag D_L and the other from the lowest point to the right with the sag D_R (Fig. 2-2). The horizontal distances X_L and X_R from the lowest point to the left and right attachment points are defined respectively as:

$$X_L = \frac{S_c}{2}\left(1 + \frac{h_c}{4D_m}\right) \tag{2-5}$$

$$X_R = \frac{S_c}{2}\left(1 - \frac{h_c}{4D_m}\right) \tag{2-6}$$

where the midpoint sag for an inclined span D_m is approximately equal to the sag for a level span with an identical horizontal span length S_c [26]. Please refer to **Appendix B** where derivations of equations (2-5) and (2-6) are listed.

2.1.2. State change equation of overhead conductors

As was noted in equation (2-3), small conductor elongations may lead to a large increase in the sag of a span. The conductor temperature is a major factor that affects the conductor length. The growth in conductor temperature due to an increasing line current or a reduced wind cooling effect will elongate conductors and thus, the span will sag more.

The total length of the conductor is the sum of the original length and elastic, thermal and plastic elongations due to changes of conductor's tension, temperature and time [19]. Three models calculating the elongation of conductors have been described in [19]. The linear elastic (LE) model and the simplified plastic elongation (SPE) model theoretically estimates elastic and thermal elongations based on an assumption that the conductor elongation due to the modest changes in tension (elastic elongation) and conductor temperature (thermal elongation) is linear and reversible. The plastic elongation of conductors is completely neglected in the LE model. In the SPE model, a typical value based on engineering judgement and experience is assigned to the plastic elongation of conductors. The experimental plastic elongation (EPE) model

theoretically calculates elastic and thermal elongation as a linear function of changes in tension and temperature and estimates the plastic elongation as a function of tension and time based on laboratory tests [19].

A state change equation was used in [27] to relate the conductor temperature T_c to the mid-point sag of a span D_m through modelling the conductor elongation as a combination of the linear elastic elongation due to tension and the linear thermal elongation due to the change of T_c, as well as the plastic strain that may be included in a constant C_{se} [27]:

$$\frac{8D_m^2}{3S_c^2} - \frac{wS_c^2}{8D_m E_c A_c} - a_c \cdot T_c = C_{se} \tag{2-7}$$

where terms E_c, a_c and A_c represent Young's modulus, thermal expansion coefficient and cross-sectional area of the conductor respectively. The coefficients and constants representing physical properties of conductors should be calibrated using the field measurements in practical application [27]. The calibrated state change equation can then be used to estimate T_c from the measured or inferred D_m.

2.1.3. Ruling spans of line sections

A line section of an overhead circuit is terminated at each end by a strain structure, e.g. an angle structure or a dead-end structure as shown in Fig. 2-3 and comprised of multiple suspension spans which are supported by suspension structures as shown in Fig. 2-4 [19]. The forces caused by a relatively large change in the line's orientation are resisted by an angle structure. A dead-end structure is generally used to withstand full unbalanced tension due to the overhead conductors turning at a wide angle or into an end [28].

Fig. 2-3. Strain (angle) structure [19]   Fig. 2-4. Suspension Structure [19]

Multiple suspension spans within a line section between two strain structures generally vary in length and experience different sag and tension changes with the variations of additional forces and conductor temperatures [19]. The unbalanced tension between suspension spans is usually equalised by the very small movement of suspension insulators which are not fixed and free to move. The suspension insulator can swing longitudinally in either direction along the line to allow that the horizontal tensions along suspension spans within a line section are approximately uniform. The tension equalisation is able to reduce the tensions of suspension spans with heavy ice and wind loadings and also to reduce the sags of hotter suspension spans [17]. However, it may be hard to achieve the tension equalisation in suspension spans which are inclined sharply or of low conductor tensions [19].

The tension equalisation for reasonably level suspension spans within a line section creates the concept of a single "ruling (or equivalent)" span based on the assumption that the variation in tension in response to the changes of ice and wind loading, conductor temperature and time for the ruling span essentially applies to all suspension spans [19]. The length of ruling span S_{RS} for a line section consisting of $n(s)$ suspension spans is defined as:

$$S_{RS} = \sqrt{\frac{S_{c,1}^3 + S_{c,2}^3 + \cdots + S_{c,n(s)}^3}{S_{c,1} + S_{c,2} + \cdots + S_{c,n(s)}}} \tag{2-8}$$

where $S_{c,i}$ represents the span length of the ith span, $i = 1, \ldots, n(s)$. Equation (2-8) shows that the ruling span length is largely dependent on the span length of the longest suspension span. Based on the assumption of nearly identical tension of all suspension spans within a line section, the midpoint sag of each suspension span $D_{m,i}, i = 1, \ldots, n$ can be derived from the estimated sag $D_{m,RS}$ of the ruling span:

$$D_{m,i} = D_{m,RS} \cdot \left(\frac{S_{c,i}}{S_{RS}}\right)^2 \tag{2-9}$$

2.1.4. Thermal model of overhead conductors

Both CIGRE Technical Brochure (TB) 601 [4] and IEEE Standard (Std.) 738 [3] present steady-state and transient-state calculations for conductor temperatures and dynamic line ratings (DLRs) based on the heat exchange mechanisms of conductors. The temperatures of a conductor of LA 280 Hawk type used in a 132kV overhead line estimated by CIGRE TB 601 and IEEE Std. 738 were compared with the measured values respectively in [29] where it was found that:

1) the differences of more than 5°C between weather-based estimates and measurements were found in around 20% of cases for steady state and around 15% of cases for transient state when theoretical values of solar radiation were used;

2) the occurrence of such temperature difference was reduced to just 5% of cases for transient state when solar radiation observations were used instead of theoretical values;

3) the slight deviation between conductor temperatures estimated by CIGRE TB 601 and IEEE Std. 738 was mainly due to their different means to estimate the convection heat loss rate and solar heat gain rate;

21

4) the calculated conductor temperatures were much closer to their actual values when wind speeds were at higher levels and approximately perpendicular to the conductor [29]. In other words, it is difficult to accurately estimate the convection heat loss rate at low wind speeds based on the relevant formulae described in [3] and [4]. Although the use of the higher value of the natural and forced convection heat loss rates, as was recommended in [3] and [4], produces a conservative rating estimate at low wind speed, this will increase the errors of conductor temperature estimates.

The thermal model of overhead conductors for calculating the steady-state DLRs presented in IEEE Std. 738 [3] is introduced in this section.

2.1.4.1. Steady-state heat balance of overhead conductors [3]

The thermal balance of an overhead conductor is kept with heat generated by Joule heating $I^2 \cdot R(T_c)$ and solar heating Q_s and heat lost by convection Q_c and radiation Q_r from the conductor surface:

$$I^2 \cdot R(T_c) + Q_s = Q_c + Q_r \tag{2-10}$$

where $R(T_c)$ is the ac resistance of the conductor evaluated at a particular conductor temperature T_c, which can be approximately calculated by linear interpolation based on the known values of ac resistances, $R(T_{chigh})$ and $R(T_{clow})$, at given high and low conductor temperatures, T_{chigh} and T_{clow}:

$$R(T_c) = \left[\frac{R(T_{chigh}) - R(T_{clow})}{T_{chigh} - T_{clow}}\right](T_c - T_{clow}) + R(T_{clow}) \tag{2-11}$$

The steady-state or continuous DLR I_{ss} leading to a maximum allowable conductor temperature T_{cmax} for specified weather conditions under the assumption of the conductor being in thermal equilibrium is then defined as:

$$I_{ss} = \sqrt{\frac{Q_c + Q_r - Q_s}{R(T_{cmax})}} \tag{2-12}$$

2.1.4.2. Convection heat loss rate

Based on wind tunnel measurements reported by McAdams and his recommended cooling curves for convection from cylinders [30], three equations defining the rates of convection heat loss Q_c for different levels of wind speeds have been given in [3]. When there is no wind, the natural convection Q_{cn} occurring on the conductor surface is mainly dependent on the difference between conductor temperature T_c and air temperature T_a:

$$Q_{cn} = 0.0205\rho_a^{0.5}D_c^{0.75}(T_c - T_a)^{1.25} \tag{2-13}$$

where ρ_a is the air density (kg/m^3) and D_c is the conductor diameter (mm).

For wind speeds w_s above zero, the rates of forced convection heat loss are estimated by equations (2-14) and (2-15) for low and high wind speeds respectively:

$$Q_{cf1} = \left[1.01 + 0.0372\left(\frac{D_c\rho_a w_s}{v_a}\right)^{0.52}\right]\varepsilon_a K_{angle}(T_c - T_a) \tag{2-14}$$

$$Q_{cf2} = \left[0.0119\left(\frac{D_c\rho_a w_s}{v_a}\right)^{0.6}\right]\varepsilon_a K_{angle}(T_c - T_a) \tag{2-15}$$

where terms v_a and ε_a represent the air viscosity in $(Pa \cdot s)$ and the coefficient of thermal conductivity of air in $(W/(m \cdot °C))$ respectively. Since there is no specific boundary to classify w_s into the low or high level and equations (2-14) and (2-15) underestimate the forced convection at high and low wind speeds respectively, it is recommended that the larger value from Q_{cf1} or Q_{cf2} is used as the forced convection heat loss rate $Q_{cf} = max(Q_{cf1}, Q_{cf2})$ [3]. K_{angle} is the wind direction factor that is determined by the attack angle ϑ_d between the wind direction w_d and the conductor azimuth Z_l:

$$K_{angle} = 1.194 - \cos(\vartheta_d) + 0.194\cos(2\vartheta_d) + 0.368\sin(2\vartheta_d) \tag{2-16}$$

The larger value from Q_{cf} or Q_{cn} is recommended to be used as Q_c for low wind speeds [3]. Therefore, the convection heat loss rate Q_c is finally determined as the largest value from Q_{cf1}, Q_{cf2} or Q_{cn} for any level of wind speed.

The terms ρ_a, v_a and ε_a are all dependent on the average T_{film} of T_c and T_a:

$$\rho_a = \frac{1.293 - 1.525 \times 10^{-4}H_e + 6.379 \times 10^{-9}H_e^2}{1 + 0.00367T_{film}} \tag{2-17}$$

$$v_a = \frac{1.458 \times 10^{-6}(T_{film} + 273)^{1.5}}{T_{film} + 383.4} \tag{2-18}$$

$$\varepsilon_a = 2.424 \times 10^{-2} + 7.477 \times 10^{-5}T_{film} - 4.407 \times 10^{-9}T_{film}^2 \tag{2-19}$$

where H_e in equation (2-17) is the elevation of the conductor above sea level.

2.1.4.3. Radiation heat loss rate

The rate of radiation heat loss Q_r from the conductor surface with an emissivity ε_e is defined as:

$$Q_r = 0.0178D_c\varepsilon_e\left[\left(\frac{T_c + 273}{100}\right)^4 - \left(\frac{T_a + 273}{100}\right)^4\right] \tag{2-20}$$

2.1.4.4. Solar heat gain rate

The rate of solar heat gain Q_s of the conductor is related to the solar absorptivity ε_s, projected area of conductor per unit length A' (m^2/m), effective angle of incidence of sun's ray θ_s and the total solar and sky radiated heat intensity q_{se} (W/m^2) at the conductor's elevation H_e:

$$Q_s = \varepsilon_s q_{se} \sin(\theta_s) A' \tag{2-21}$$

where the term θ_s is derived from the altitude of the sun H_s and the deviation in azimuth between the sun Z_s and the line Z_l:

$$\theta_s = \cos^{-1}[\cos(H_s)\cos(Z_s - Z_l)] \tag{2-22}$$

The altitude of the sun H_s depends on the latitude of the conductor Lat, hour angle w_h that is the number of hours from solar noon times $\pi/12$, and the solar declination δ_s which is a function of the day of the year d_{num}:

$$H_s = \sin^{-1}[\cos(Lat)\cos(\delta_s)\cos(w_h) + \sin(Lat)\sin(\delta_s)] \tag{2-23}$$

where,

$$\delta_s = 0.4094 \sin\left(\frac{284 + d_{num}}{365} \times 2\pi\right) \tag{2-24}$$

The value of δ_s is positive for northern hemisphere and negative for southern hemisphere. It is suggested in CIGRE TB 601 [4] to correct the hour angle w_h by the longitude deviation from the standard meridian of the local time zone. If the position is on east side of standard meridian, 4 minutes per degree of longitude is added. If it is on west side of standard meridian, 4 minutes per degree of longitude is subtracted. Furthermore, it should be noted that the daylight savings time (DST) needs to be adjusted to the local standard time (LST), i.e. $LST = DST - 1h$.

The azimuth of the sun Z_s is defined as:

$$Z_s = C_s + \tan^{-1}(\chi_s) \tag{2-25}$$

where χ_s is the solar azimuth variable defined as:

$$\chi_s = \frac{\sin(w_h)}{\sin(Lat)\cos(w_h) - \cos(Lat)\tan(\delta_s)} \tag{2-26}$$

and C_s is the solar azimuth constant that is a function of w_h and χ_s:

$$C_s = \begin{cases} 0 & for \ -\pi \le w_h < 0 \ \& \ \chi_s \ge 0 \\ 2\pi & for \ \ \ 0 \le w_h < \pi \ \& \ \chi_s < 0 \\ \pi & otherwise \end{cases} \tag{2-27}$$

It is noted that all the terms representing the directions are in 'radians'.

2.2. Conductor Temperature based DLR Techniques

This section introduces the temperature based DLR techniques which typically use temperature monitoring sensors to measure conductor temperatures so as to prevent the maximum allowable conductor temperature being exceeded. In order to provide the DLR values, a weather station is usually installed in close proximity to the temperature monitoring sensor to measure the weather conditions experienced by the monitored span. The measurements of conductor temperature and weather conditions are then used to calculate the 'effective' wind speeds perpendicular to the span which

provides the same wind cooling effect as the actual wind speeds and directions which vary along the span [17]. The estimated 'effective' wind speeds are then used with a maximum allowable conductor temperature to determine real-time ratings based on a thermal model of the conductors [3]. Some of the conductor temperature-based DLR techniques have been upgraded to measure or infer other conductor characteristics such as the inclination angle, tension, and sag of a span. This may make it possible to extrapolate sags of other suspension spans within the same line section based on the concept of ruling span.

2.2.1. Overhead Transmission Line Monitoring

The overhead line monitoring devices developed by the Overhead Transmission Line Monitoring (OTLM) Company have been upgraded from measuring the conductor temperature and line current only [31] to additionally capturing the inclination angle, sag and tension of a span [32]. An OTLM system consists of several OTLM devices, as shown in Fig. 2-5, that are fixed on the predefined points (e.g. the critical spans) along a line where conductor temperatures, inclination angles and line currents are directly measured and weather stations from which ambient conditions are observed [32]. The sag and tension of the monitored span are calculated based on the real-time measurements of inclination angle and conductor temperature combined with a mathematical model which takes the geometric and mechanical characteristics of conductors into account.

Fig. 2-5. An OTLM device [32]

The actual angle of inclination measured by an inclinometer installed within an OTLM device is used to calibrate the mathematical model which calculates the angle of inclination by comparing the positions of the fixed point before and after the presence of the OTLM device for a range of conductor temperatures when there is no additional loading. If the inclination angle calculated by the calibrated mathematical model exceeds the measured value by a particular, given tolerance (normally determined by the statistical error of an angle measurement), the conductors being covered by ice or loaded with wet snow will be informed [33]. In addition, the conductor temperature measured by an OTLM device combined with weather conditions observed from the installed weather station can be used to estimate the "real-time" rating [32] based on a thermal model of the conductors proposed in [4].

The operation of an OTLM device is supplied by a built-in current transformer and no additional power source is required [32]. The weather station is powered by solar panels and batteries [34]. The OTLM device can be applied to the OHLs operating at the voltage level from 110kV to 400kV [34]. The OTLM device can only operate when the line current is greater than $65A$. Therefore, the line current measurements range from $65A$ with a resolution of $1A$. The measured conductor temperature ranges from $-40°C$ to $125°C$ with a resolution of $0.5°C$ and a deviation of $\pm 2°C$ [34]. Please refer to [34] which details technical parameters of an OTLM device.

Scheduled disconnection is recommended (but not necessary) for the installation of an OTLM device which is close to tower but after the anti-vibration device if one is present. As an OTLM device measures conductor temperature for a single span, it is valuable to place OTLM devices on critical spans which can be identified by airborne LIDAR survey technology [31]. In complex terrain areas, it is recommended that approximately 3 to 5 OTLM devices should be installed in spans where the terrains change significantly, or conductors are shielded from wind by surrounding obstacles. Two OTLM devices can be fixed at the beginning and end of a line or at the sections with considerable pivot angle in flat woodless areas [31, 32].

2.2.2. Power Donut

The 2nd generation of power donut (PD2) is introduced in this section while the 3rd generation (PD3) has been developed by the Underground Systems, Inc. (USi). A PD2 device, as shown in Fig. 2-6, can be attached onto an energized overhead conductor without a planned outage and measures the line current, voltage, active and reactive power, conductor temperature and the inclination angle from which the values of sag and tension of the monitored span can be derived [35]. The live-line installation of a PD2 device can be accomplished by a 'hot stick' [36] which is an insulated pole, usually made of fiberglass, for a lineman working on energized high voltage OHLs.
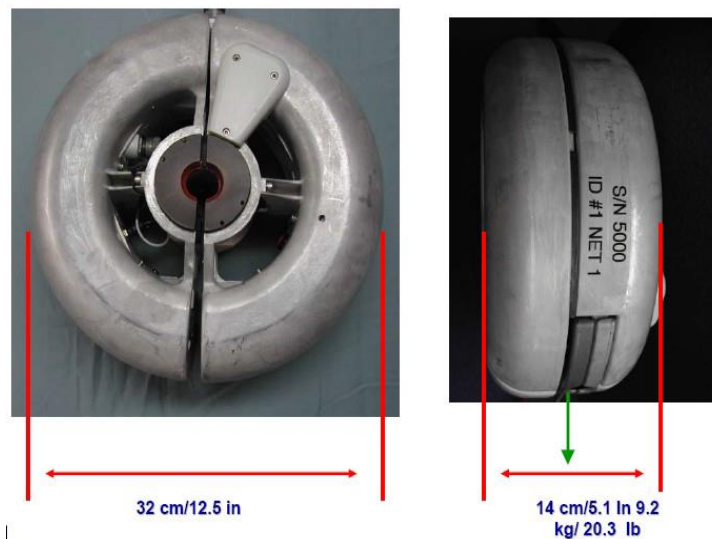
Fig. 2-6. A power donut2 (PD2) device [35]

A PD2 device can be self-powered from an energized line with a minimum current of around $60A$ $(50 - 70A)$ [35, 37]. When the current is less than the minimum value required for the device's operation, the PD2 device can be temporarily supplied for 10 hours by a battery pack which will be charged when the line current is above $120A$ and shut down at a low battery status [37] (In [35], the PD2 device is said to run on battery for one hour after which the device will automatically shut down). The PD2 device can work in systems of voltage level up to 500kV [37]. The PD3 is additionally powered by the photovoltaic cells that are attached on the upper surface

of device [35]. Please refer to [35, 37] where the device specifications and the features of measurements, i.e. ranges, resolutions and deviations are given.

A USi weather station is installed in very close proximity to the PD2 device, as shown in Fig. 2-7, to measure ambient conditions experienced at the monitored span which are used for the accurate estimations of real-time ratings [35]. The operation of a USi weather station is supplied by solar power combined with primary battery cells and external power is not required [35].
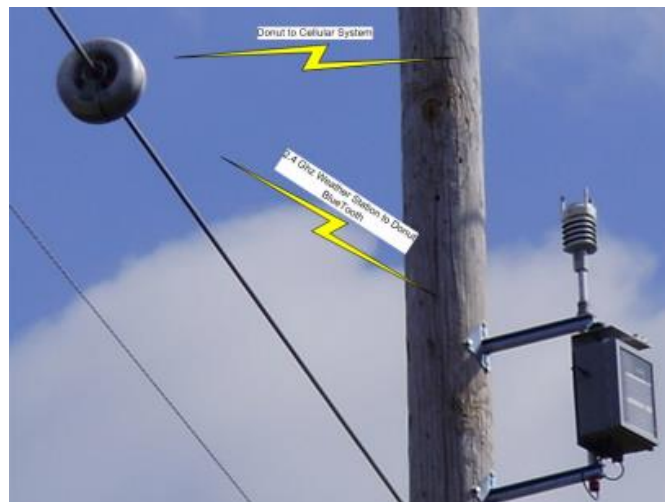
Fig. 2-7. A PD2 device and a USi weather station [35]

Two methods of estimating real-time ratings based on measurements from the PD2 device and the USi weather station are described in [35]. A traditional method is to calculate the ratings for the measured weather conditions through the thermal model of the conductors [3] directly. The other method is to first determine the 'effective' wind speed from weather measurements combined with the measured conductor temperature and line current based on the thermal model of overhead conductors [3]. The estimated 'effective' wind speed is then used to calculate the real-time rating that leads to a maximum allowable conductor temperature under the measured weather conditions [35]. The real-time ratings calculated by the traditional method ('Normal DLR IEEE 738') and the relatively complex method ('CTM DLR'), as shown in Fig. 2-8 [35], were similar for most of the time. A conservative practice may be to use the lower value of two estimates of real-time ratings.

Fig. 2-8. Real-time ratings calculated by two methods developed for a PD2 system [35].

2.2.3. Thermal-vision camera

A thermal-vision camera can record an infrared image to measure the thermal energy emitted from an object. It can therefore be applied to monitoring temperatures of overhead conductors through transferring the colour information into the corresponding value of temperature [38]. A thermo-vision camera, named FLIR ThermaCAM P65 [39], was once employed to capture conductor temperatures for each phase of a 330kV OHL in a Latvian power network [40]. Fig. 2-9 shows an example of the infrared image of two conductors, each aligned vertically in the image. The accuracy of measurements obtained from FLIR ThermaCAM P65 is $\pm 2°C$ or $\pm 2\%$ of the reading [39].
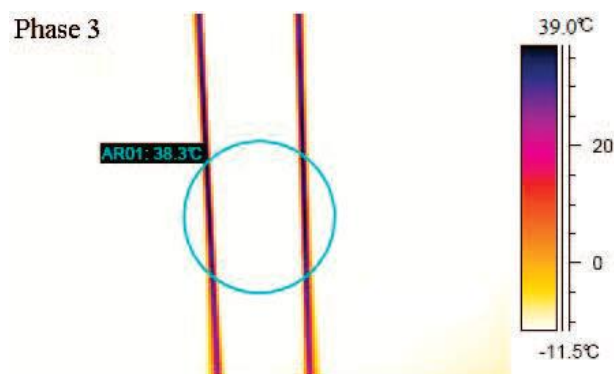
Fig. 2-9. Infrared image for one phase of a 330kV OHL recorded by FLIR ThermaCAM P65 [40].

2.2.4. Other temperature based DLR techniques

Distributed temperature sensors (DTS) can monitor the distribution of conductor temperatures along an overhead line by means of optical fibres based on detection of the back-scattering of light [41]. In a demo project, Red Eléctrica de España (REE) replaced one sub-conductor with an optical phase power conductor (OPPC) which had ten optical fibres inside a stainless steel tube close to the steel core of the OPPC [42]. According to [43], a DTS system using Brillouin analysis can cover a distance up to $100km$ at a spatial resolution of $1-20m$ and measure the conductor temperature with an accuracy of $\pm0.3℃$ and a reading resolution of $0.005℃$. DTS techniques have the advantage of detecting the variations in conductor temperature along the covered distance, compared with the OTLM and PD2 devices which can only monitor conductor temperatures at their fixing points. However, less notice has been given to the DTS technique in practical online monitoring for cost reasons [41].

Please refer to [38, 44-46] in which the techniques of conductor temperature monitoring based on surface acoustic wave (SAW) sensors and synchronized phasor measurements (SPM) are introduced.

The temperature monitoring sensor (TMS) directly attached on the conductor, e.g. equipment of OTLM, PD2 or SAW, is a heat sink so that the conductor temperatures measured by the TMS may be lower than their actual values in the free span [47], as shown in Fig. 2-10 [45]. Bernauer [44] has proposed an approach to calculating the conductor temperature in the free span based on the equivalent thermal source that is derived from the conductor temperature measured by a SAW sensor. The proposed approach was found to produce a nearly exact estimate of conductor temperature in the free span if there was a nearly constant 'ratio' between the thermal behaviours (i.e. the transient change of temperature in response to the variations in influencing factors) of the conductor and the sensor-conductor compound. Otherwise, the approach would be extended to additionally take into account the heating functions

of the conductor and the sensor at various wind speeds which largely affect the 'ratio' between thermal behaviours [45].
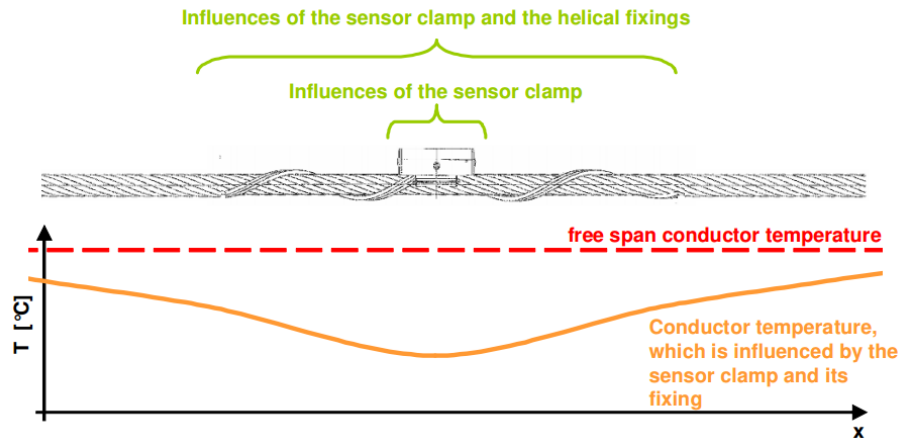
Fig. 2-10. Distribution of conductor temperatures affected by a SAW sensor (heat sink effect) [45].

The aforementioned temperature monitoring sensor (TMS), except for the DTS, can only monitor the conductor temperature at the fixing point of a single span. Though air temperatures and solar radiations may vary slightly along a line, the large variations in wind speeds and wind directions along suspension spans within a line section usually lead to conductor temperatures varying from span to span and even within a long span when the line is operated at a high current level greater than $1 \, A/mm^2$ [17]. Multiple single-span TMS are therefore required to be installed at the possible critical spans, e.g. those that may be shielded from wind. As noted in Sections 2.2.1 and 2.2.2, the OTLM and PD2 devices are both capable of inferring the sag and the horizontal tension of the monitored span from measurements of inclination angle and conductor temperature. Therefore, the sags of other suspension spans within the same line section can be estimated based on equation (2-9) if there is a satisfactory equalisation in tensions between the suspension spans [17].

2.3. Sag based DLR Techniques

This section will introduce the sag-based DLR techniques which monitor the sag/clearance of a span directly through measuring the position of the conductor in space so as to prevent the violation of the minimum clearance requirement. The measured sag of a span can be converted into the average conductor temperature of the span based on the known relationship between sag and temperature of conductor, i.e. the state change equation. In addition, the sags of other suspension spans within the same line section may be derived from the measurement of sag of the inspected span if there is an acceptable tension equalisation within the line section.

2.3.1. Laser based scanning system

A laser based scanning system has been developed by Golinelli [48] to measure not only the clearance of a span but also the rate of ice accretion on conductors. The operation of a laser based scanning system is based on detection of the intensity of backscattered signals generated by the inspected conductor when it is intercepted by a collimated scanning beam that explores an angular region of $\pm 15^{o}$ with respect to the line of sight [48]. The sag of a span can be derived from the delay in time between the scanner driving signal and the backscattered signal [49]. Fig. 2-11 shows a schematic of the laser based scanning system that is placed on the ground at a distance of around $20m$ from the monitored span [48].
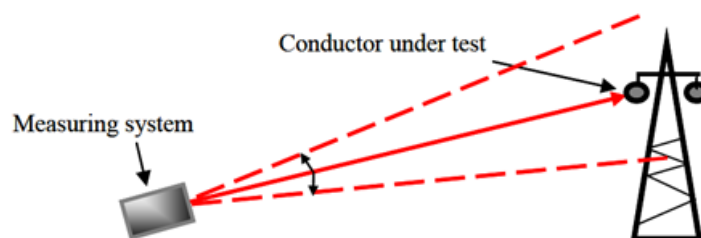
Fig. 2-11. A schematic of the laser based scanning system [48]

The sustained ice accretion on overhead conductors due to the coincidence of high winds, air temperatures between $-1℃$ and $1℃$ and snowing may stretch conductors, topple structures or even snap them [50], which leads to large economic losses and operational problems in power networks [48]. Real-time detection of the ice accretion on conductor (or the outer diameter of conductor) is therefore necessary, especially when the aforementioned weather conditions happen simultaneously. In addition to the sag of a span, the laser based scanning system can provide the value of conductor diameter which is proportional to the time duration of the backscattered signal [49]. The ice accretion on an overhead conductor can therefore be detected by comparing the measured outer diameter of conductor with the normal value.

Fig. 2-12 shows an example of the time durations of signals backscattered by a conductor with an outer diameter of $30mm$ and an iced conductor with an outer diameter of $60mm$ (i.e. widths of the highest peaks in plots) [48]. The time durations of backscattered signals for a $60mm$ iced conductor were approximately twice as long as that for a $30mm$ conductor.
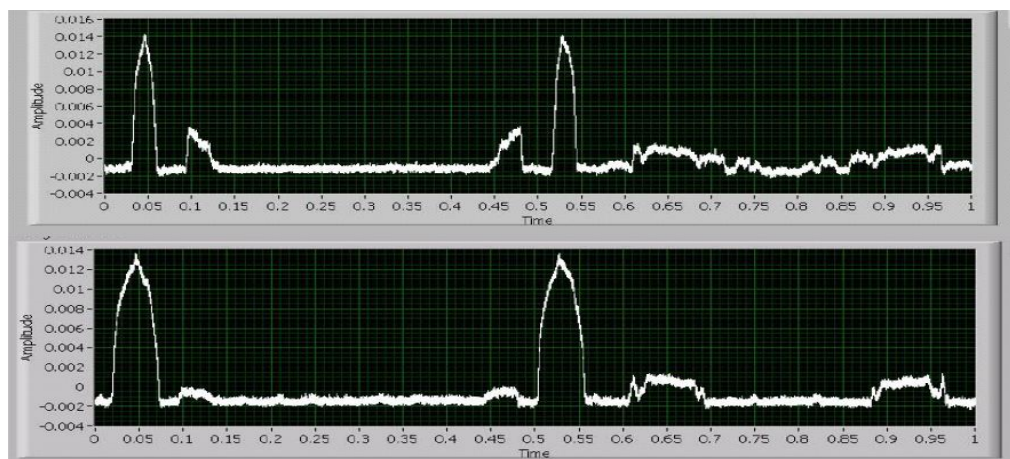
Fig. 2-12. Backscattered signals (the highest peaks) generated by a conductor of a $30mm$ outer diameter having shorter time durations of around $0.03s$ in upper plot and that for an iced conductor of a $60mm$ outer diameter having longer time durations of around $0.05s$ in lower plot [48].

Assuming a detection accuracy of ±20 samples, the laser based scanning system was shown to provide the measurement of the iced conductor diameter with an accuracy of $\pm0.5mm$ and the sag measurement with an accuracy of $\pm3.6mm$ in

the experiment carried out in [48]. The laser based scanning system has been found to perform reliably and satisfactorily during night time as well as under weather like raining and snowing [49].

2.3.2. Radar based scanning system

A radar based scanning system developed by Miceli [51] is capable of monitoring clearances of spans. Just as with the laser based scanning system, the radar based system sends a signal to a region that includes at least a portion of the monitored span and a reference object such as a ground surface or an object over the ground surface. The geometric relationship between the inspected span and the reference object can then be extracted from the reflected radar signal [51].

In common with the laser based scanning system, the radar based scanning system requires good access to the structures and overhead conductors since the monitoring devices are usually placed around the inspected spans [51]. Ground-based laser or vehicle-based radar scanning systems neither need a scheduled line outage nor affect conductors in the way that the TMS's direct attachment on conductors does. However, the line may be blown out of the laser or radar scanning range in high winds [15].

2.3.3. Video sagometer scanning system

A video sagometer scanning system, developed by the Electric Power Research Institute (EPRI), can recognize the position of a small target hung on a span based on which the catenary equation of conductors and thus the distance from any point along the span to ground (i.e. the clearance) can be determined [52]. The major components of the system are a video camera based on highly light-sensitive charge coupled device technology, a passive reflective target attached on the line (Fig. 2-13), a solid-state target illuminator which is used to illuminate the target at night or when there is insufficient ambient light, an electronics package containing a system for

data acquisition and analysis, and a communication system [52, 53]. The video camera is typically mounted on the tower supporting the monitored span or any structure in the vicinity where the camera has a good sighting of the target hung on the span [16], as shown in Fig. 2-14 [53].

Fig. 2-13. A target hung on the line [53]   Fig. 2-14. A camera mounted on a wood pole [53]

The video sagometer target can be directly installed on an accessible conductor and a planned outage is not required [52]. The operation of the video sagometer scanning system is supported by either 115V ac power or 12V dc power from a pre-packaged photovoltaic power supply [54]. The accuracy of the monitored span coordinates for the clearance calculation is within $\pm 1.27 cm$ for most cases [54]. However, a reduced clarity of the target image and a less effective operation of the unit may be caused by the extreme weather such as fog or heavy snow [55]. Please refer to [54] where detailed information about a video sagometer scanning system is given.

2.3.4. Differential global positioning system

The geographic coordinates, i.e. latitude, longitude and altitude of a location can be obtained by a global positioning system (GPS) receiver installed at the given position, but with a bad accuracy of $20m - 100m$ due to various sources [56]. Knowing the altitude of the monitored position makes it possible to measure the sag or clearance of a span. One way to improve the accuracy of the GPS measured altitude is using an additional GPS base receiver at a reference station to measure the altitude which is

36

compared with its actual value in order to get the timing error of GPS signal. The timing error is then transmitted to a GPS receiver attached on the span by a communication module to calibrate the altitude measurement at the receiver [56, 57]. This sag monitoring technique is the differential GPS (DGPS). A schematic representing a DGPS is shown in Fig. 2-15 where the base receiver is around $16km$ away from the monitored span [57].
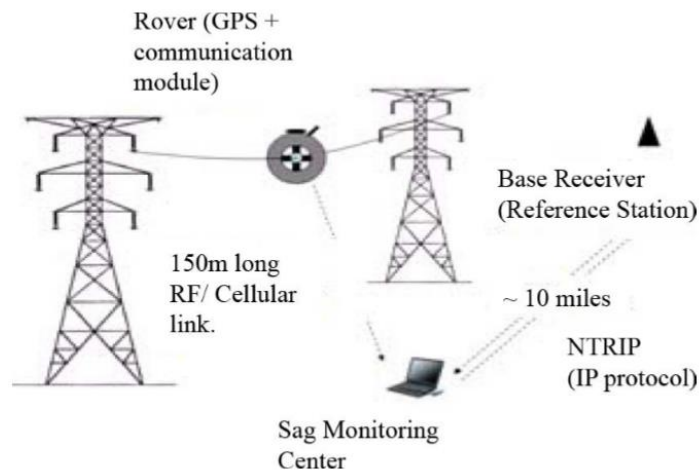
Fig. 2-15. A schematic of a DGPS [57]

In the field experiment conducted in [57], a laser based scanning system was used as a reference to calibrate DGPS measurements. The historical DGPS measurements recorded every second in a ten-second sliding training window were compared with the laser measurements in the same period, from which appropriate curve-fitting and smoothing techniques were determined so as to refine the DGPS measurements. The clearance of a span measured by the DGPS and the laser based scanning system were compared for a variety of current profiles. The error of the DGPS measurements after the calibration was around $\pm 1.27cm$ when the laser measurement was regarded as the reference [57].

2.4. Multi-span DLR Monitoring Techniques

The aforementioned conductor temperature-based and sag-based DLR techniques provide measurements only for the spans where they are installed. These techniques may be named as the single-span DLR monitoring techniques, though the measurement or inference of sag for the monitored span may be used to extrapolate the sags of other suspension spans within the same line section using the concept of ruling span if there is an acceptable tension equalisation within the line section. This section introduces two DLR technologies, i.e. a 'CAT-1' Dynamic Line Rating System and an 'Ampacimon' sensor which are both capable of monitoring the average thermal and mechanical behaviours of a line section. The 'CAT-1' Dynamic Line Rating System and the Ampacimon may be named as the multi-span DLR monitoring techniques which extrapolate a global section value to each of the suspension spans within the line section using the concept of ruling span [17].

2.4.1. CAT-1 Dynamic Line Rating System

A 'CAT-1' Dynamic Line Rating (DLR) System is designed to measure the tension and infer the sag, average temperature and real-time rating of overhead conductors between strain (dead-end or angle) structures [58] based on an assumption of horizontal tensions along a line section being nearly equalised. A CAT-1 DLR System mainly consists of load cells that measure the horizontal tensions of conductors, a net radiation sensor (NRS) representing a de-energized conductor, an air temperature sensor, a CAT-1 Main Unit responsible for the main processor and communications, and a CAT-PAC power module that supplies power for the CAT-1 DLR System's operation [58].

2.4.1.1. Load cells and sag measurements

Typically, two load cells are placed at a strain structure to monitor different line sections on each side of the structure. An example of a four-span section supported

by two strain structures and three suspension structures is shown in Fig. 2-16. The horizontal tension along suspension spans can be monitored by a load cell placed at the strain structure A or E [8]. The load cell is usually installed between the cross arm of a strain structure and the de-energized side of an insulator [58], as shown in Fig. 2-17 [59]. The measured tension of conductors generally has an accuracy of 0.25% of full scale and a resolution of 0.06% of full scale. In practice, the load cell is likely to operate at 50% of full scale and thus the accuracy and resolution are about 0.5% and 0.2% of the measured values respectively [17].
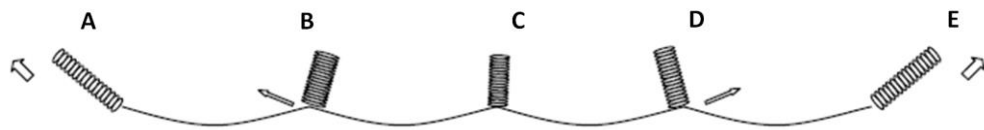
Fig. 2-16. A four-span section consisting of two strain structures and three suspension structures [8]

Fig. 2-17. Load cells mounted between the cross arm of a strain structure and insulators [59]

The sag of each suspension span within the monitored line section can be roughly determined from the measured tension by the equations relating tension to sag as described in **Appendix A and B** based on the assumption of tension equalisation between suspension spans. In practical applications, the accuracy of the sag-tension calculation is affected by several error sources such as the flexibility of structures and uncertain weights of overhead conductors [19] which must be calibrated by the field measurements [17]. The CAT-1 DLR System was stated in [59] to measure the span sag with an accuracy of $3 - 6\ cm$. The field experiment carried out in [60],

however, showed that the tension-based sag measurement of de-energized conductors had an error exceeding $8cm$ at times (but within 2% of their actual values). A scheduled line outage is required for installation of load cells.

2.4.1.2. *Net radiation sensor and average conductor temperature*

The mechanical tension measured by a load cell is also correlated with the average conductor temperature of the line section. The temperature of a de-energized conductor, i.e. net radiation temperature (NRT) was found to decrease linearly with the increase in the measured tension [60]. The NRT can be measured by a net radiation sensor (NRS) as shown in Fig. 2-18 [61] which is mainly made up of a conductor replica made of the same material, with approximately the same diameter and painted to have approximately the same absorptivity and emissivity as the actual conductor. The conductor replica is placed parallel to the line and at approximately the same height in the vicinity of the actual conductor in order to experience the same ambient conditions as the actual conductor. Therefore, the temperature of the conductor replica, i.e. the NRT is nearly the same as the actual conductor temperature when the line is not in operation.
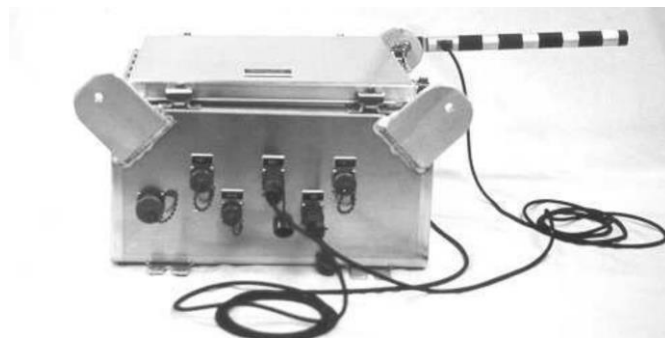
Fig. 2-18. A net radiation sensor (NRS) [61]

A state change curve [17] which indicates the relationship of average conductor temperature with tension is usually used to estimate the tension-based conductor temperature. It is recommended to use various field measurements of tensions and NRTs at low line currents to calibrate the state change curve [17, 19]. Fig. 2-19 shows the data pairs of 15-minute average tensions of the 'Hen' ACSR conductor

40

and NRTs recorded for 3 months [17]. At each NRT, the minimum tension revealing the largest sag and the highest conductor temperature was usually observed at a high current and under the worst-case ambient conditions while the maximum tension corresponded to the minimum line current approaching zero, at which the conductor temperature might by nearly equal to the measured NRT. Therefore, the data pairs of the NRTs and their corresponding maximum tensions can be used to calibrate the state change curve which is then used to estimate the average conductor temperature from the measured tension.
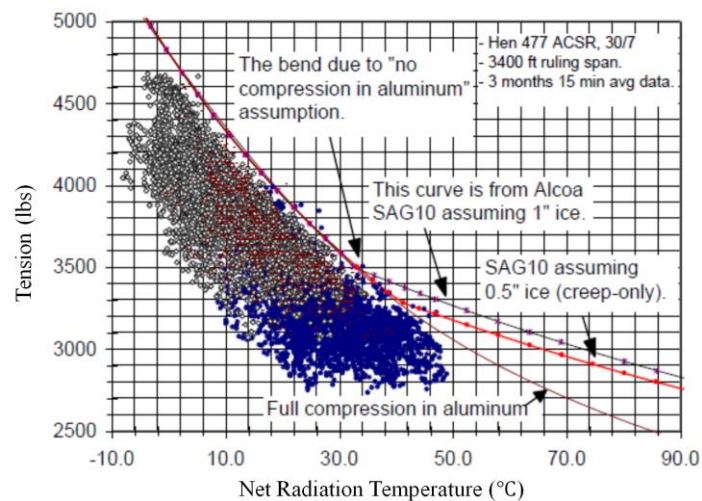
Fig. 2-19. Data pairs of tensions of the 'Hen' ACSR conductor and NRTs recorded for 3 months [17].

2.4.1.3. Dynamic line rating estimations

The concept of the 'effective' wind speed is applied to DLR calculations in the CAT-1 DLR System. The 'effective' wind speed perpendicular to a line section is determined based on the average conductor temperature derived from the measured conductor tension by the calibrated state change curve, the line current provided by the SCADA system, air temperature measured by an air temperature sensor, and the actual solar radiation input to the conductor represented by the NRT [17] combined with the thermal model of the conductors. The exact algorithm of DLR estimations used by the CAT-1 DLR System is not available in the published literature which may be due to the concerns about intellectual property rights. One possible form for the algorithm is briefly introduced as below.

The thermal balance of the conductor replica of the NRS is kept with the heat generated by solar heating Q_s only and the heat lost by convection $Q_c(NRT)$ and radiation $Q_r(NRT)$ from the surface of conductor replica evaluated at NRT:

$$Q_s = Q_c(NRT) + Q_r(NRT) \qquad (2\text{-}28)$$

For the line section operated at a line current I_{ls}, the heat is additionally generated by the Joule heating and the convection and radiation heat loss rates are estimated at the average conductor temperature T_{av-H} that is inferred from the measured conductor tension:

$$I_{ls}^2 \cdot R(T_{av-H}) + Q_s = Q_c(T_{av-H}) + Q_r(T_{av-H}) \qquad (2\text{-}29)$$

In equations (2-28) and (2-29), Q_s and the 'effective' wind speed that is used to estimate Q_c are unknown. The term Q_s can be eliminated by subtracting equation (2-28) from equation (2-29). In this manner, the 'effective' wind speed is the only unknown variable to be solved from equation (2-30):

$$I_{ls}^2 \cdot R(T_{av-H}) = Q_c(T_{av-H}) + Q_r(T_{av-H}) - Q_c(NRT) - Q_r(NRT) \qquad (2\text{-}30)$$

The estimated 'effective' wind speed is then used to calculate the corresponding steady-state rating I_{ss-ls} for the line section given a maximum allowable conductor temperature T_{cmax}:

$$I_{ss-ls} = \sqrt{\frac{Q_c(T_{cmax}) + Q_r(T_{cmax}) - Q_c(NRT) - Q_r(NRT)}{R(T_{cmax})}} \qquad (2\text{-}31)$$

2.4.2. Ampacimon

2.4.2.1. *Smart sensor Ampacimon and sag determination*

Conductors of an OHL vibrate in response to wind. The vibration frequency spectrum of a span is made up of harmonics of its fundamental frequency which is dependent on the sag of the span [62]. Ampacimon is a sensor directly attached on a conductor (Fig. 2-20) which monitors the conductor movements, analyses the conductor vibration and detects fundamental frequencies of a span from which the

span's sag is determined [63, 64]. Accelerometers built into an Ampacimon device are capable of detecting even a slight movement of $1mm$ at the lowest frequency ($0.15Hz$) for a typical span and even smaller movements at higher frequencies. The measurements of conductor vibration are processed to form a vibration frequency spectrum (Fig. 2-21) [64] from which the fundamental frequency is extracted [62].

Fig. 2-20. Ampacimon smart sensor [64]   Fig. 2-21. Vibration frequency spectrum [64]
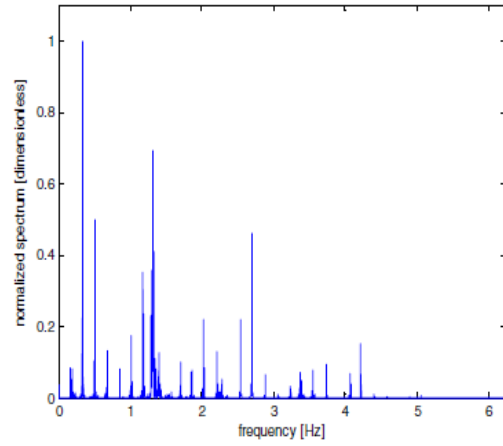
The movements of overhead conductors can be regarded as the vibration of a fixed-fixed string. A span's fundamental frequency frq_o is defined as a function of the horizontal tension H, span length S_c and the mass of the conductor per unit length m [64]:

$$frq_o = \frac{1}{2S_c}\sqrt{\frac{H}{m}} \tag{2-32}$$

According to equation (2-1) representing the sag-tension relationship, the horizontal tension H in equation (2-32) can be replaced by the mid-point sag D_m and the span length S_c:

$$frq_o = \frac{1}{2S_c}\sqrt{\frac{\frac{mgS_c^2}{8D_m}}{m}} = \frac{1}{2}\sqrt{\frac{g}{8D_m}} \tag{2-33}$$

where g is the gravitational acceleration and $m \cdot g$ equals the weight of the conductor per unit length w. It can be seen from equation (2-33) that D_m is only related to a single variable, that is, the fundamental frequency frq_o:

$$D_m = \frac{1}{32} \frac{g}{frq_o^2} \qquad (2\text{-}34)$$

Therefore, the fundamental frequency obtained from an Ampacimon device can be directly used to calculate the sag of the inspected span. The outstanding advantage of Ampacimon is that the whole process of sag estimation is only concerned with frq_o. The impacts of external conditions such as weather conditions, line currents, wind and ice loads, etc. on the sag of a span are all reflected by the frequency readings. An Ampacimon device can measure the sag over a range from $0m$ to $25m$ with an accuracy that is typically less than $10cm$ and maximum at $20cm$ [65]. In addition, an Ampacimon sensor can be easily installed anywhere along a span without the need for a line outage and self-powered from an energized line with a minimum operating line current of $80A$ [64, 66]. The specifications for an Ampacimon sensor can be found in [66].

2.4.2.2. Average conductor temperature and DLR estimation

The concept of the ruling span is used by Ampacimon to infer average conductor temperature and DLR. The sag measured for a span within a line section is converted to the sag of the ruling span by equation (2-9). The unknown constants in the state change equation (2-7) are determined based on the estimated ruling span sags and the corresponding average conductor temperatures for the ruling span that are calculated based on IEEE Std. 738 [3] combined with weather measurements during several nights when there are stable wind conditions without solar radiation [27]. The calibrated state change equation can then be used to calculate the average conductor temperature from the estimated sag of the ruling span.

The average conductor temperature of the ruling span is additionally estimated using the thermal model of the conductors [3] and ambient conditions observed from web

or weather stations. The weather-based estimate of average conductor temperature is then converted to the sag value. The deviation from the measured sag is eliminated through adapting wind speed and solar radiation to their 'effective' values in a conservative way. That is, if the measured sag is greater than the weather-based value which indicates overestimated heat losses or underestimated heat gains, the 'effective' wind speed perpendicular to the line section is first reduced and the solar radiation is then increased when the 'effective' wind speed has been reduced to zero until the difference between the measured sag and the re-calculated weather-based value is within a predefined tolerance; in the case of the sag measurement being lower than the weather-based estimate, the solar radiation is first decreased and the 'effective' wind speed is then increased when solar radiation has reduced to zero. The 'effective' wind speed estimated in this manner is conservative. The effective weather variables are then used to determine the DLR that leads to the lower value from the maximum allowable conductor temperature or the maximum conductor temperature limited by the maximum allowable span sag based on the thermal model of the conductors [27].

The static line rating (SLR) will be adopted as the line rating under conditions where the line current is too low to support operation of the Ampacimon sensor or the line current data and weather data are missing [27].

2.5. Weather-based DLR Techniques

2.5.1. ThermalRate System

A ThermalRate system estimates real-time ratings of an OHL by placing the ThermalRate sensors at a number of critical spans which model the influences of weather conditions on the inspected spans. The ThermalRate sensor (Fig. 2-22) [67] consists of two conductor replicas, each having the same material, diameter, absorptivity and emissivity as the actual overhead conductor. One replica has an internal resistive heater at a constant wattage while the other one is not heated. The

two conductor replicas are of the same length which is sufficiently long as $1ft$ $(30.48cm)$ in order to minimize the influences of thermal boundary losses [68, 69].

Fig. 2-22. A ThermalRate sensor [67]

The ThermalRate sensor is installed in the vicinity of the monitored span and may be mounted on a mast on an existing transmission tower or on a separate pole, as shown in Fig. 2-22. The sensor is placed at the average conductor height and in the same orientation of the span in order to experience the same weather conditions as the span [67]. A thermocouple embedded at the longitudinal centre of each replica can tell the difference in temperature between two replicas, from which the 'effective' wind speed perpendicular to the line conductors is determined based on IEEE Std. 738 [3] combined with air temperature from a ThermalRate ambient thermometer. The estimated 'effective' wind speed is then used to calculate the rating of the monitored span [69, 70]. The algorithms used by the ThermalRate System may be similar to equations (2-28) - (2-31), except for substituting the constant heating power for the Joule heating in equations (2-29) and (2-30). The minimum value of the calculated real-time ratings at critical spans is applied to the entire OHL.

The installation of a ThermalRate sensor does not need a scheduled line outage since it does not contact with line conductors [67]. A ThermalRate System that consumes $15W - 17W$ is supplied by a solar panel combined with a rechargeable battery [67, 69]. An outstanding advantage of a ThermalRate System is that the estimation of

'effective' wind speed and thus DLR is independent of the line current data from the SCADA system. For the Power Donut (PD), CAT-1 Dynamic Line Rating System and Ampacimon, the 'effective' wind speed may only be accurately determined in the cases of the measured average conductor temperature being several degrees Celsius higher than air temperature, which generally requires that the line current reaches a sufficiently high level, i.e. greater than $20\% - 30\%$ of its SLR or $0.5A/kcmil$ ($0.987A/mm^2$) [71]. However, the required level of line current is not often reached especially for 69kV to 230kV lines [71] and the estimates of 'effective' wind speeds may be less accurate. The ThermalRate System has the capability of settling the problem of lightly loaded lines as the temperature difference between the heated and non-heated conductor replicas is large enough to estimate the 'effective' wind speed. For lightly loaded lines that are monitored by the PD, CAT-1 or Ampacimon devices, normal SLRs can be adopted as their thermal limits which still provide considerable additional headroom for power transfer.

2.5.2. Weather-based DLR models

A weather-based DLR model determines real-time ratings of conductors by directly using ambient conditions measured at weather stations combined with conductor parameters as the inputs of the thermal model of overhead conductors [3, 4]. The conductor temperature can also be calculated if the line current is provided. To inspect ratings for an entire OHL, a sufficient number of weather stations are installed along the line, measuring the local weather conditions which are then used to estimate ambient conditions for each span through suitable spatial interpolation methods. The rating at each span is determined from the inferred weather data and the minimum value of ratings among all spans is applied to the whole OHL [20].

The weather-based DLR models usually suffer from inaccuracy of wind speed and wind direction measurements, especially at low wind speeds. In addition, weather conditions, especially wind speeds and directions, are largely affected by local effects

and may significantly vary from span to span or even along a single span. Though a weather station is installed in close proximity to the line conductors, there is a difference in wind cooling effects between the measured wind variables and the average wind conditions experienced by the span. The ratings of a 220kV OHL in France calculated by the weather-based model and the Ampacimon System were compared in [72]. The DLR estimations by using measurements of wind speed and wind direction were shown to have an error, on average, equal to around 10% of the estimations by the Ampacimon which used the deduced 'effective' wind speed [72]. However, the unsatisfactory performance of the weather-based DLR model found in [72] may be, to some extent, due to fact that weather measurements were from a weather station that was too far (a few kilometres) away from the monitored line.

Installing more weather stations along OHLs within a network requires a higher investment cost but may result in more precise interpolations of weather data which will be beneficial to provide DLR estimations of a higher reliability to operators. Therefore, there is a trade-off between the interpolation accuracy of weather conditions and the investment in weather stations. The research at Durham University recommended that the distance between two adjacent weather stations should not exceed $10km$ [10]. For the DLR project in North Wales, six weather stations have been installed at each of the 132kV substations as shown in Fig. 1-2, taking account of the benefits of secure source of electrical power that supports the operation of weather stations, reliable private-wired telecommunications networks, etc. Other weather stations were considered to be installed in the areas between two adjacent 132kV substations which are greater than $10km$ apart. Four towers along the 132kV circuits were determined as the locations of weather stations since the alternative 33kV substations were sheltered from wind due to the local geography and did not have private-wired telecommunications networks [10]. The tower-based weather station located between 132kV substations B1 and B5 (Fig. 1-2) did not work and weather measurements were only available from the other nine stations.

Due to the random character of instantaneous weather data, using average values of weather conditions generally gives more accurate estimates of ratings and conductor temperatures [73]. The duration that a conductor can be operated at the level of the calculated steady-state rating is generally determined by the frequency at which the rating is updated. For example, the conductor's ampacity would be assumed to be kept at the hourly updated steady-state rating over the present or future one hour. However, the use of weather data averaged over a relatively longer interval, e.g. one hour, may lead to a risk of the conductor's thermal overloading due to the short-term variability of weather conditions, especially wind speed [73]. It is recommended that an update interval of 10 minutes is preferred to fulfil the requirement of rating calculation for most cases [73, 74]. In this research, 10-minute average weather data are used to calculate rating forecasts.

It may be more valuable to install weather stations in close proximity to critical spans which are those likely to be sheltered from wind or exposed to direct sunlight along the monitored OHLs within a network since the rating of an OHL is limited by the minimum value of ratings of all spans which often occurs at the critical span. Furthermore, weather conditions measured for critical spans generally have conservative cooling effects or high solar radiations on conductors. The ratings for other spans deduced from interpolations of the conservative weather data and thus the rating for the entire OHL are conservative.

2.6. DLR Estimation Errors due to Measurement Accuracies

As was noted above, a DLR monitoring technique generally determines steady-state ratings of a span based on an effective wind speed perpendicular to the span that is inferred from the measured line current, air temperature and solar radiation combined with the conductor temperature obtained from what the monitoring device measures through a thermal model of the conductors. This approach can mitigate the difference between the wind conditions recorded at a meteorological station and those actually

49

experienced by the conductor [17]. However, the measuring errors of these variables, e.g. conductor temperature and solar radiation, may degrade the accuracy of effective perpendicular wind speed (EPWS) estimates, leading to an error in DLR estimation. This section will investigate the effects of measuring errors of line current, solar radiation s_r and conductor temperature T_c on the performance of the EPWS-based approach to DLR estimation.

Based on an assumption that the conductor is in thermal equilibrium, line currents passing through an ACSR 'Drake' conductor are calculated by the thermal model of the conductors [3] based on an air temperature T_a of $10°C$ and an EPWS of $1m/s$ that are combined with different values of T_c ranging from $25°C$ to $65°C$ and s_r equal to $50W/m^2$, $500W/m^2$ and $1000W/m^2$ respectively. The technical parameters describing characteristics of the 'Drake' conductor are listed in Table 2-2 [4]. The calculated line currents, as shown in Fig. 2-23, are assumed to be the 'actual' values, which are to be measured by a monitoring device, e.g. PD2, with an accuracy of around $\pm0.5\%$ of reading [37].

Table 2-2: Technical parameters of ACSR 'Drake' conductor [4]

Conductor Characteristics	ACSR 'Drake'
Conductor diameter (mm)	28.143
Emissivity (-)	0.8
Solar absorptivity (-)	0.8
Low conductor temperature for which ac resistance is specified (°C)	25
High conductor temperature for which ac resistance is specified (°C)	75
Conductor ac resistance at low conductor temperature (Ω/km)	0.0727
Conductor ac resistance at high conductor temperature (Ω/km)	0.0872
Conductor elevation above sea level (m)	0
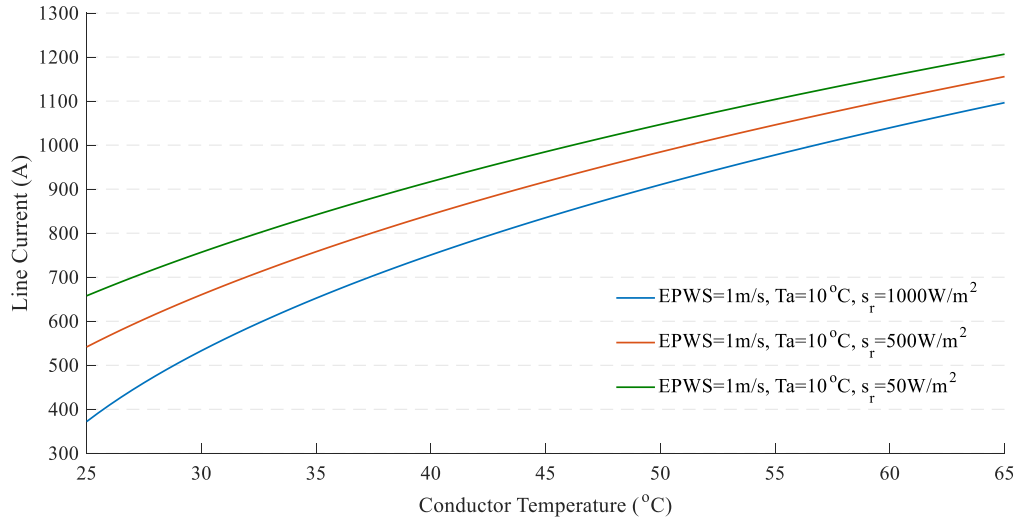
Fig. 2-23: Line currents calculated for the Drake conductor that has T_c ranging from 25℃ to 65℃ based on an EPWS of $1m/s$ and T_a of 10℃ under different values of s_r.

Based on the thermal model of the conductors [3] combined with an EPWS of $1m/s$ and T_a of 10℃, steady-state ratings of the Drake conductor at $T_{cmax} = 75℃$ are estimated to be 1199.1A, 1251.8A and 1297.4A for s_r equal to 1000 W/m^2, 500W/m^2 and 50W/m^2 respectively. When the maximum error of line current measurements, i.e. $\pm 0.5\%$ of readings, are considered only, the steady-state DLR of the Drake conductor at $T_{cmax} = 75℃$ is estimated from the EPWS which is calculated by the thermal model of the conductors [3] based on 100.5% or 99.5% of the 'actual' line current for each scenario. The percentage errors of steady-state DLRs due to the measuring errors of line currents only under different values of s_r are shown in Fig. 2-24. The $\pm 0.5\%$ measuring errors of line currents lead to similar percentage errors of DLRs at a high T_c which corresponds to a high line current. When T_c is at a low level which means a low line current, percentage errors of DLRs due to the measuring errors of line currents are reduced, especially in the scenarios of high s_r. This is because, in these scenarios, an increased proportion of s_r in the total heat gain rate constrains the impacts of the measuring errors of line currents on the EPWS estimation.
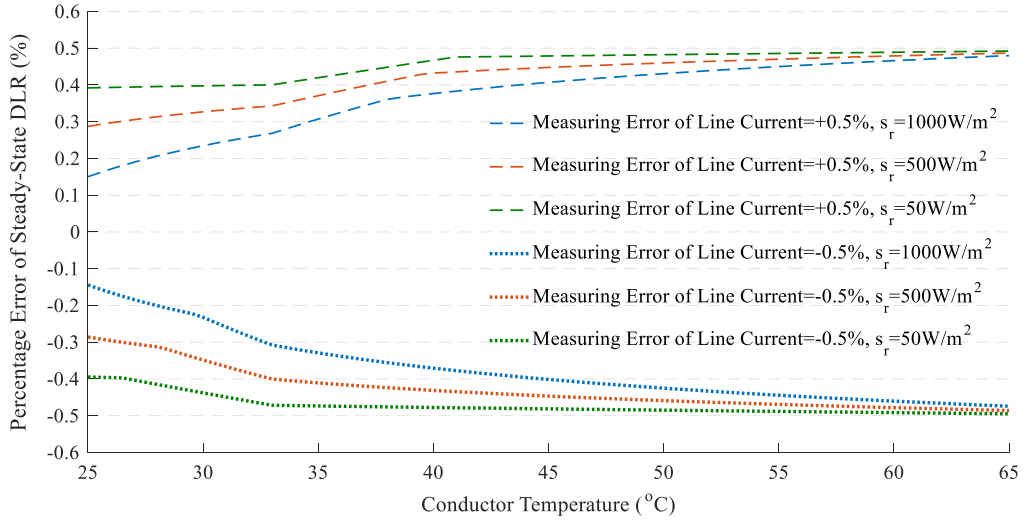
Fig. 2-24: Percentage errors of steady-state DLRs of the Drake conductor estimated by the EPWS based method due to the measuring errors of line currents only under different values of s_r.

The T_c-based monitoring devices, e.g. OTLM, usually have measuring errors of T_c (denoted by ΔT_c) equal to around $\pm 2°C$. Other DLR monitoring techniques, e.g. Ampacimon and CAT-1, generally infer T_c from measurements of sag or tension using a calibrated state change equation or curve. CIGRE Technical Brochure 498 [17] recommended that the clearance or sag of a span, i.e. the fundamental data to be checked by a system operator, should be measured or determined with a minimum accuracy of $\pm 20cm$. This may represent a variation of around $\pm 5°C$ in T_c at low conductor temperatures (e.g. below $75°C$) based on a 4th order polynomial equation relating sag to T_c which is derived for a $300m$ ruling span [17]. Since the CAT-1, Ampacimon and some sag-based monitoring techniques meet the minimum required accuracy of $\pm 20cm$, the maximum measuring errors of $\pm 5°C$ for T_c are used here to analyse the impacts of $\pm 20cm$ of errors in sag measurements on the performance of the EPWS-based approach. Figs. 2-25 and 2-26 compare percentage errors of steady-state ratings of the Drake conductor due to ΔT_c equal to $\pm 2°C$ and $\pm 5°C$ respectively under different values of s_r.

52
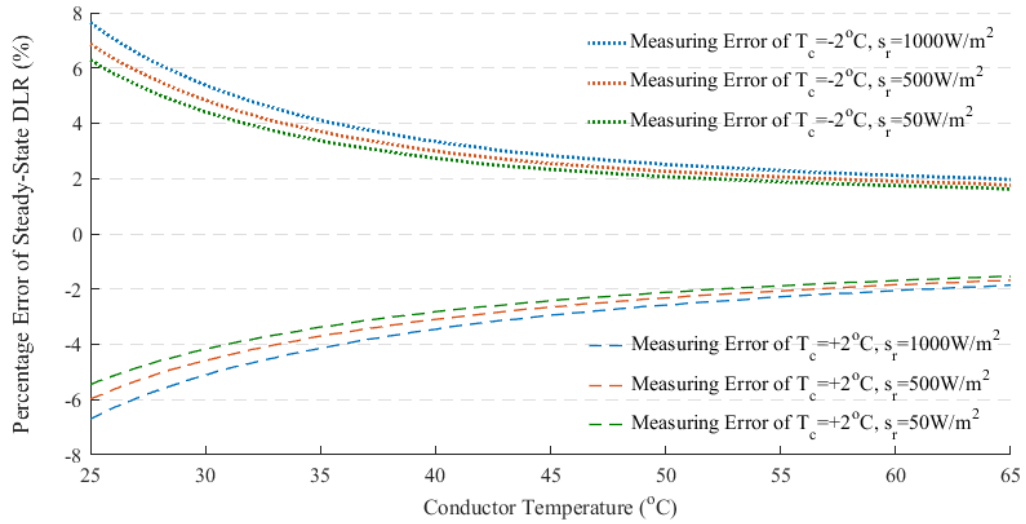
Fig. 2-25: Percentage errors of steady-state DLRs of the Drake conductor estimated by the EPWS based approach due to measuring errors of T_c equal to $\pm 2°C$ only under different values of s_r.
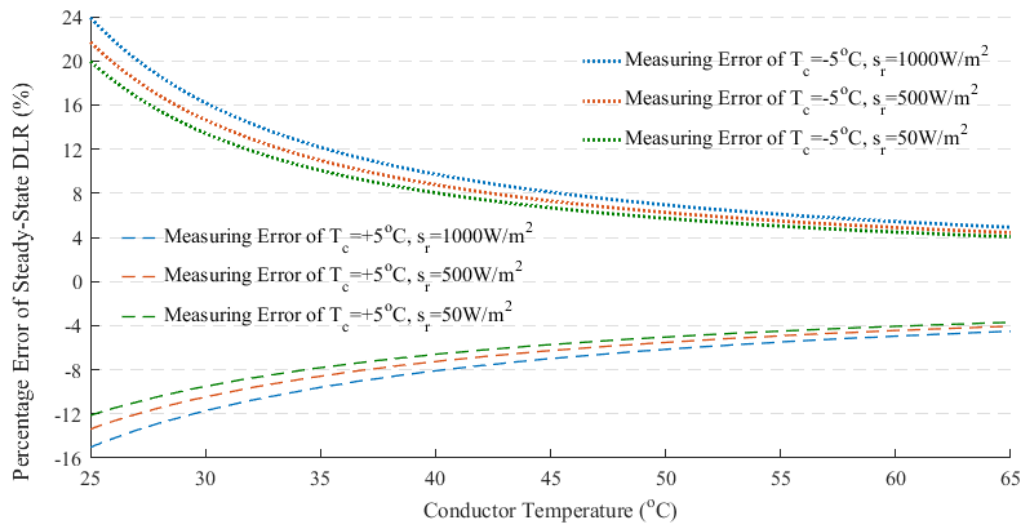
Fig. 2-26: Percentage errors of steady-state DLRs of the Drake conductor estimated by the EPWS based approach due to measuring errors of T_c equal to $\pm 5°C$ only under different values of s_r.

When calculating the EPWS from the measured T_c, ΔT_c equal to $-2°C$ or $-5°C$ will underestimate the arise of T_c above T_a, leading to an underestimation in the radiation heat loss rate Q_r. Then the underestimated temperature difference $(T_c - T_a)$ and Q_r produce an overestimated EPWS. However, the overestimation in EPWS will be mitigated by an underestimated Joule heat gain rate due to a negative ΔT_c underestimating the ac conductor resistance. Since s_r is independent of T_c, a large

proportion of s_r in total heat gain rate (e.g. when line current is low and s_r equals $1000W/m^2$) will reduce the mitigation in an overestimated EPWS by the underestimated ac resistance. Therefore, percentage errors of DLRs due to ΔT_c only evaluated at low current levels or $s_r = 1000W/m^2$ are higher than those estimated at high current levels or lower s_r, as shown in Figs. 2-25 and 2-26.

When operating the conductor at T_c close to T_{cmax} (e.g. above 60°C in this case), the EPWS-based approach is shown to produce a steady-state DLR with an accuracy of about $\pm 2\%$ or $\pm 5\%$ given that the DLR monitoring techniques have ΔT_c equal to ± 2°C (e.g. OTLM) or ± 5°C (e.g. Ampacimon) respectively. When T_c is low, e.g. 25°C in this case, the error of the EPWS-based DLR increases to around $\pm 6\%$ for $\Delta T_c = \pm 2$°C, -12% for $\Delta T_c = +5$°C and $+22\%$ for $\Delta T_c = -5$°C. It is noted that a negative ΔT_c at low T_c is shown to cause an overestimation in DLR that is higher in magnitude than an underestimation in DLR due to a positive ΔT_c.

Given that s_r is measured with an accuracy of $\pm 5\%$ [10], percentage errors of the EPWS-based steady-state DLRs of the Drake conductor evaluated at $T_{cmax} = 75$°C due to the measuring error of s_r only in different scenarios are shown in Fig. 2-27. When directly calculating DLRs from weather observations, positive errors of s_r measurements would underestimate DLRs. However, Fig. 2-27 shows that a positive measuring error of s_r cause an overestimation in the EPWS-based DLR, and vice versa. This is because the EPWS-based approach overestimates the level of EPWS given a positive error of s_r. When the difference between conductor temperature and T_a increase from $(T_c - T_a)$ to $(T_{cmax} - T_a)$, the overestimation in convection heat loss rate evaluated at T_{cmax} exceeds the overestimation in s_r, leading to a positive error of the EPWS-based DLR.
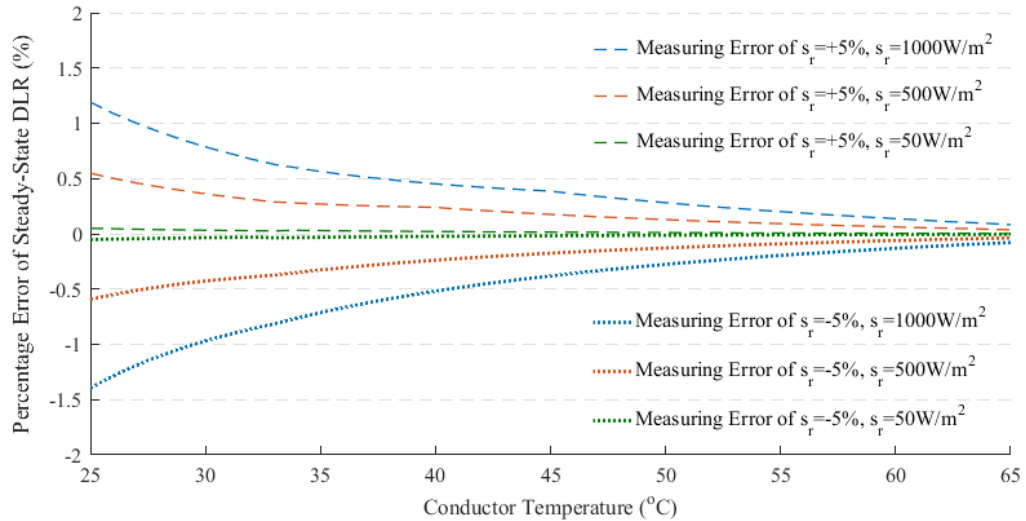
Fig. 2-27: Percentage errors of steady-state DLRs of the Drake conductor estimated by the EPWS based method due to s_r measuring errors of $\pm 5\%$ only under different values of s_r.

The above analysis shows that the accuracy of steady-state DLRs estimated by an EPWS-based approach is very sensitive to the errors of the measured or inferred T_c, especially when the conductor is operating at low T_c. Therefore, it is necessary to maintain a reasonable safety margin relative to the EPWS-based DLR.

2.7. Conclusions

This chapter has given a high level explanation and description of the theories and dynamic line rating (DLR) techniques, most of which have the capability of estimating real-time ratings of the inspected span or line section through monitoring or inference of the state of overhead conductors.

Conductor temperature-based DLR techniques such as Overhead Transmission Line Monitoring (OTLM) and Power Donut can measure the conductor temperature at the fixed point by a temperature sensor. In addition to conductor temperature, these monitoring devices have been developed to capture other characteristics of line conductors, e.g. line current and inclination angle from which the sag and tension of the monitored span can be derived. The temperature sensors being directly attached

upon conductors can effectively reduce the measurement error. However, the temperature sensors that make contact with conductors additionally suffer from heat skin effects, i.e. the measured conductor temperature being lower than the actual value in the free span [47]. The heat skin effects due to the difference in thermal behaviours between the conductor and the sensor-conductor compound can be mitigated by taking into account the heating functions of conductor and sensor for a range of wind speeds [45].

Installations of sag monitoring devices generally do not require a planned line outage since most of them such as laser and radar based scanning systems do not make contact with the conductors. In addition, a laser scanning system can additionally measure outer diameters of conductors from which the ice accretion rate on conductors can be deduced. However, the laser and radar based scanning systems do need good access to the lines and structures and may face the risk of the inspected line being blown off the scanning range in high wind speeds [15].

The CAT-1 DLR System and the Ampacimon System are both capable of capturing the average behaviour of a line section between two strain structures based on the concept of ruling span. The CAT-1 system measures the tension of line conductors from which the average conductor temperature is determined based on a calibrated state change curve. An Ampacimon sensor measures the sag of a particular span within a line section which is then converted to the ruling span sag. The average conductor temperature of the line section can be calculated from the ruling span sag based on a calibrated state change equation.

It has been argued here that CAT-1 and Ampacimon can be regarded as multi-span or line-section monitoring techniques while most of the conductor temperature-based and sag-based DLR techniques are regarded as the single-span monitoring techniques, i.e. each of their devices only monitoring a single span. The capability of monitoring multiple spans of CAT-1 and Ampacimon depends on the ruling span concept which can only be utilised when there is a reasonable tension equalisation in suspension

spans within a line section. If a satisfactory tension equalisation exists within a line section, some single-span DLR monitoring techniques that can capture the sag of a span, such as OTLM, Power Donut, laser and radar based scanning systems, may turn into multi-span monitoring techniques since the sag of the inspected span can be used to extrapolate the sags for other suspension spans through equation (2-9) based on the concept of ruling span.

DLRs cannot be determined only by measurements of conductor temperature or sag without weather data. Therefore, the monitoring devices are commonly used together with weather stations or net radiation sensors (NRS) to calculate DLRs based on the thermal model of overhead conductors. The line currents and the average conductor temperatures of the ruling span or a line section inferred from the conductor tension or sag measurements are used to estimate the 'effective' wind speeds perpendicular to line conductors. The estimated 'effective' perpendicular wind speed (EPWS) is then used to evaluate the real-time rating for the line section that increases the average conductor temperature to the maximum allowable limit.

The DLRs estimated from EPWS are generally of higher accuracy than directly using wind speeds and wind directions observed at weather stations due to less precise measurements of wind conditions at low wind speeds. Furthermore, wind variables measured at a weather station cannot accurately represent the average wind cooling effects experienced by the span. However, it should be noted that the EPWS-based DLRs may suffer from the accuracy of the variable being monitored, especially the measuring error of conductor temperature. Even so, weather-based DLR models may be the most practical technique to evaluate the thermal limits of overhead lines since installations of weather stations may be cost-effective and do not require a scheduled line outage [15]. It was recommended in [15] to use the weather-based DLR model with other DLR monitoring techniques so as to validate the outputs of the weather-based model. Moreover, additionally deploying other DLR techniques such as conductor temperature sensors can help cover microclimate regions [10].

Appropriate locations of monitoring sensors are critical since the number of sensors is normally limited by the available budget. Except for the load cells in a CAT-1 DLR System that are placed at a strain structure, it may be valuable to determine installation positions at the thermally vulnerable components, i.e. critical spans which experience low convection effects and high solar radiations. For weather based DLR models, more weather stations may be required in complex terrains.

3. POINT AND PROBABILISTIC WEATHER FORECASTING

3.1. Introduction

Dynamic Line Rating (DLR) promises to release extra power transfer capacity on a network and to reduce the need for balancing actions to modify, in the first instance, generator outputs. Depending on where dynamic line rating is deployed, this would have a clear benefit in terms of reducing curtailment of low carbon generation and reducing the total cost of balancing actions. However, many of these require some notice due to, for example, the time taken to identify and communicate the need for actions and the ramp rate limits on generation. Thus, forecasting of ratings seems necessary if system operator actions are not to be unduly conservative.

Weather-based DLR forecasting techniques which use weather predictions are being widely developed for different time horizons in operational planning and real-time system operation. Since the steady-state rating of an OHL is significantly influenced by weather conditions, reliable and accurate weather forecasting is a prerequisite for a system operator having confidence in the provided DLR forecast to dispatch power flow. For look ahead times of a few hours, time series forecasting models are well suited to DLR forecasting, producing weather forecasts from historic observations that are combined with a thermal model of overhead conductors [3, 4]. Time series approaches have been developed in [75, 76] to derive predictive distributions of weather parameters for a few hours ahead from which random weather samples were generated using Monte Carlo simulation to estimate probabilistic DLR forecasts. The accuracy of a time series forecasting model commonly decreases with the forecast time horizon. Weather forecasts from numerical weather prediction models are generally preferred for a forecast horizon greater than 4 hours ahead [77]. Numerical weather predictions and weather forecast ensembles provided by a weather service

are usually used for the estimation of point forecasts for DLR [77, 78] and the uncertainties of DLR forecasts [2] respectively for a day ahead.

The primary objective of this research is to develop an enhanced weather-based model to provide DLR forecasts in the form of percentiles which can be used by a system operator within a chosen risk policy with respect to the probability of a rating being exceeded. Predictive distributions of weather variables are estimated from their historic time series observed at weather stations by using suitable probabilistic forecasting models. The modelled distributions of weather forecasts are then used to derive the percentiles of DLR forecasts in Monte Carlo simulation. A probabilistic forecast or a predictive probability distribution can be regarded as an extension of a point forecast, indicating the size or distribution of possible errors. An accurate point forecast is therefore necessary for minimising the uncertainty of forecasts, but knowledge of the distribution is required to understand the risks.

In this chapter, time series forecasting models are first developed to estimate point forecasts for each weather variable by using an auto-regressive process that is combined with a Fourier series based de-trending method. The point or deterministic forecasting models that have an adequate forecast accuracy are then selected to model predictive centres of weather variables. Conditional heteroscedasticity of the predictive distribution is modelled as a linear function of recent changes in the de-trended data within one hour for air temperature and wind speed or the concentration of recent wind direction observations within two hours. The predictive distributions of weather variables are determined using a technique of minimum continuous ranked probability score (CRPS) estimation. The probabilistic forecasting models that have smaller CRPS values and require less computation time are used to produce predictive distributions for each weather parameter. In the case of solar radiation only point forecasts have been used here since, when wind speeds are above a modest level [1] or when conductor temperatures are relatively high [21], conductor temperature is insensitive to the change in solar radiation.

As was noted in Sections 1.2.1 and 2.5.2, 10-minute average weather data was used in this work; the examples of estimating L-step-ahead weather forecasts described here therefore use step lengths of 10 minutes. Although the first challenge is to develop reasonable forecasts for 1 step ahead, in practice, it is very difficult for system operators to make use of 10-minute steady-state DLR forecasts as updates of system state from an energy management system and implementation of any action required to secure the system would typically take at least that long. Although the notice given to operators would ideally be longer than 30 minutes, as a means of establishing the viability of the described approach and giving something of at least some value to system operators, results for 3-step-ahead are also presented. In addition to probabilistic steady-state DLR forecasts, the thesis aims to quantify lower percentiles of transient-state rating forecasts which may yield a maximum allowable conductor temperature in a specified time period (typically less than half-an-hour [3]), considering the thermal inertia of the conductor. Therefore, predictive distributions of weather variables for up to three 10-minute time steps ahead estimated in this chapter are necessary for probabilistic forecasting of transient-state DLR.

3.2. Methodology

3.2.1. Fourier series based temporal de-trending

Data applied to statistical models, like time series forecasting models, are generally required to satisfy a weak or second order stationarity. That is, neither the average nor the variance of the data should vary with time and the auto-covariance is dependent on the time lag only [79]. The inherent trends of non-stationary data may be misleading with regard to correlations among variables or the autocorrelation of a time series. Any trend implied in the non-stationary data should therefore be removed before the application of statistical models.

A temporal de-trending method using a Fourier series of a reasonable order p_{fs} is employed here to extract temporal trends from weather data [80]:

$$Trend = FS_o + \sum_{i=1}^{p_{fs}} FS_i \sin(i\omega_{fs}t + \varphi_i) \tag{3-1}$$

where terms FS_i and φ_i are the Fourier coefficients of the ith harmonics. The term FS_o is the offset of data and ω_{fs} represents the frequency. The annual trend and diurnal trend of weather data can be modelled with an annual angular frequency of $2\pi/(365 \times 24hr)$ and a diurnal angular frequency of $2\pi/24hr$ [81].

Hourly wind speed measurements over two years 2006-2007 from the British Atmospheric Data Centre (BADC) that were recorded at Rhyl weather station located in North Wales are used to illustrate the process of Fourier series based temporal de-trending. The annual trend of wind speed is first well modelled by a 3rd order Fourier series with the annual angular frequency, as shown in Fig. 3-1, and then subtracted from the original data of wind speed.
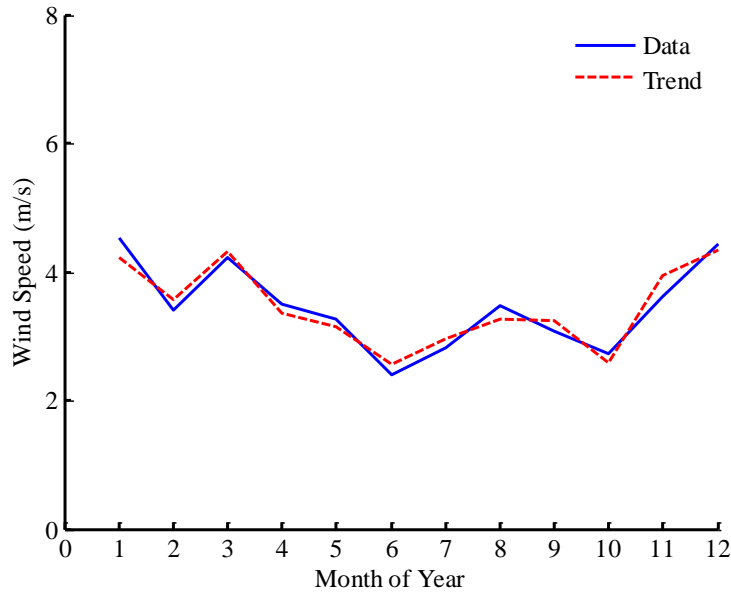
Fig. 3-1. Modelling of annual trend of wind speed over two years 2006-2007 at Rhyl

Hill [81] found that the diurnal trend of wind speed, especially at coastal locations, varies throughout the year. As a consequence, the wind speeds without the annual

trend are categorized into four groups according to four seasons, winter (December to February), spring (March to May), summer (June to August) and autumn (September to November). The diurnal trend in each season is then fitted to the average value at each hour within a day for each season by a Fourier series of order equal to two with the diurnal angular frequency, as shown in Fig. 3-2. The diurnal trends of wind speeds in spring and summer are shown to be similar and more obvious than those in autumn and winter.
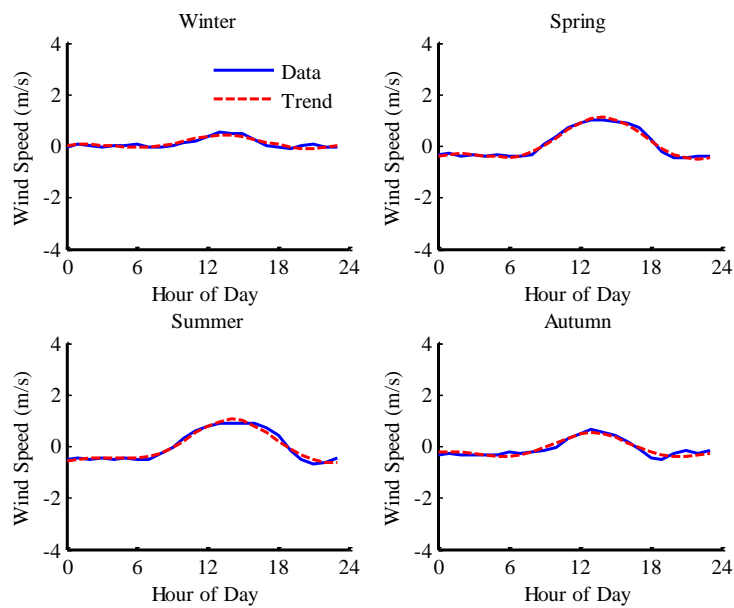
Fig. 3-2. Modelling of diurnal trends of wind speeds over two years 2006-2007 in four seasons at Rhyl

The modelled annual trend and the diurnal trends in different seasons are all removed from the original data so as to obtain the de-trended data with a reasonable degree of stationarity. To examine the effect of temporal de-trending on the stationarity of data, sample autocorrelations of the original data and the residuals are calculated for time lags up to 144 hours separately, as shown in Fig. 3-3. The autocorrelation of original data is shown to decay periodically with a period of approximately 24 hours while the autocorrelation of the residuals that are obtained via the temporal de-trending process decays to zero relatively smoothly. This confirms the necessity to remove temporal trends, especially the diurnal trends, from the original time series, which

63

would otherwise correlate the pairs of wind speed data that are at the time lags of multiples of 24 hours. The de-trended data can then be used to estimate parameters of time series forecasting models.
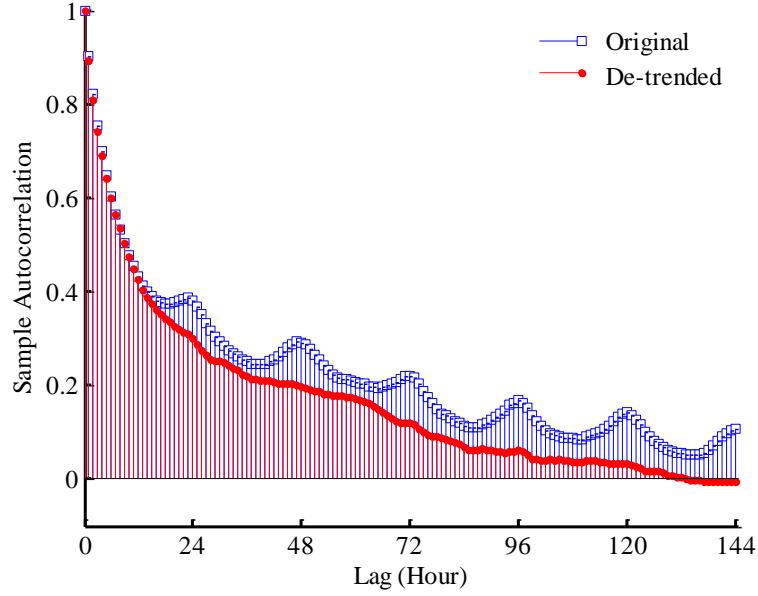
Fig. 3-3. Sample autocorrelations of the original wind speed data and the corresponding de-trended data at time lags up to 144 hours at Rhyl

3.2.2. Auto-regressive model

Time series forecasting models using an auto-regressive (AR) process calculate point forecasts of weather variables from recent observations based on their correlations extracted from historic time series. An auto-regressive (AR) model of order p is a stochastic model that estimates the forecast $\tilde{z}_t$ as a linear combination of p historic values $\tilde{z}_{t-i}$ $(i = 1, ..., p)$ at a target location and a Gaussian noise term e_t [82]:

$$\tilde{z}_t = u + \sum_{i=1}^{p} \beta_i \tilde{z}_{t-i} + e_t \tag{3-2}$$

where $\tilde{z}_t$ represents the deviation from the trend component. The term u is a constant and β_i denote the auto-regressive parameters which can be determined by using the ordinary least squares estimation [83] or Yule-Walker equations [82].

3.2.2.1. Ordinary least squares estimation [83]

For $t = 1, \dots, n$ in equation (3-2), a set of equations can be obtained:

$$
\begin{aligned}
\tilde{z}_n &= u + \beta_1 \tilde{z}_{n-1} + \beta_2 \tilde{z}_{n-2} + \cdots + \beta_p \tilde{z}_{n-p} \quad + e_n \\
\tilde{z}_{n-1} &= u + \beta_1 \tilde{z}_{n-2} + \beta_2 \tilde{z}_{n-3} + \cdots + \beta_p \tilde{z}_{n-p-1} + e_{n-1} \\
&\vdots \quad \vdots \quad \vdots \quad \vdots \quad \ddots \quad \vdots \quad \vdots \\
\tilde{z}_1 &= u + \beta_1 \tilde{z}_0 \quad + \beta_2 \tilde{z}_{-1} \quad + \cdots + \beta_p \tilde{z}_{1-p} \quad + e_1
\end{aligned}
\tag{3-3}
$$

which can be written in the matrix form as:

$$
\mathbf{y} = \mathbf{z}\mathbf{b} + \mathbf{e}
\tag{3-4}
$$

where,

$$
\mathbf{y} = \begin{bmatrix} \tilde{z}_n \\ \tilde{z}_{n-1} \\ \vdots \\ \tilde{z}_1 \end{bmatrix}
\quad
\mathbf{b} = \begin{bmatrix} u \\ \beta_1 \\ \vdots \\ \beta_p \end{bmatrix}
\quad
\mathbf{z} = \begin{bmatrix}
1 & \tilde{z}_{n-1} & \tilde{z}_{n-2} & \cdots & \tilde{z}_{n-p} \\
1 & \tilde{z}_{n-2} & \tilde{z}_{n-3} & \cdots & \tilde{z}_{n-p-1} \\
\vdots & \vdots & \vdots & \ddots & \vdots \\
1 & \tilde{z}_0 & \tilde{z}_{-1} & \cdots & \tilde{z}_{1-p}
\end{bmatrix}
\quad
\mathbf{e} = \begin{bmatrix} e_n \\ e_{n-1} \\ \vdots \\ e_1 \end{bmatrix}
$$

The auto-regressive parameters β_i and the constant u are determined to minimise the sum of squares of residuals $(\mathbf{y} - \mathbf{z}\mathbf{b})$ which is a function of variables u, $\beta_1, \dots, \beta_p$:

$$
\mathbf{b} = (\mathbf{z}'\mathbf{z})^{-1}\mathbf{z}'\mathbf{y}
\tag{3-5}
$$

3.2.2.2. Autocorrelation function [82]

Multiplying throughout in equation (3-2) by $\tilde{z}_{t-k}$ for $k > 0$, it can be obtained that:

$$
\tilde{z}_{t-k}\tilde{z}_t = \tilde{z}_{t-k}u + \sum_{i=1}^{p} \beta_i \tilde{z}_{t-k}\tilde{z}_{t-i} + \tilde{z}_{t-k}e_t
\tag{3-6}
$$

Taking the expected value $E\{\cdot\}$ of each term in equation (3-6), $E\{\tilde{z}_{t-k}e_t\}$ equals zero since $\tilde{z}_{t-k}$ are uncorrelated with e_t. $E\{\tilde{z}_{t-k}u\}$ is also equal to zero due to the de-trended data having an average equal to zero. Then it can be obtained that:

$$
\zeta_k = \sum_{i=1}^{p} \beta_i \zeta_{k-i}, \qquad k > 0
\tag{3-7}
$$

where ζ_k represents $E\{\tilde{z}_{t-k}\tilde{z}_t\}$, i.e. the auto-covariance at the time lag k. The autocorrelation function can then be obtained through dividing the terms in equation (3-7) by $E\{\tilde{z}_t^2\}$ which is the variance of the time series denoted by ζ_o:

$$\rho_k = \sum_{i=1}^{p} \beta_i \rho_{k-i}, \qquad k > 0 \tag{3-8}$$

where terms ρ_k and ρ_{k-i}, equalling ζ_k/ζ_o and ζ_{k-i}/ζ_o, are the autocorrelations of the time series at time lags k and $(k-i)$ respectively.

3.2.2.3. *Yule-Walker equations [82]*

If a time series has a weak or second-order stationarity, its auto-covariance only depends on the time lag and thus $\rho_k = \rho_{-k}$. A set of linear equations for auto-regressive parameters β_i in terms of autocorrelations ρ_k can be obtained by substituting $k = 1, \dots, p$ in equation (3-8):

$$\begin{aligned}
\rho_1 &= \beta_1 &+ \beta_2 \rho_1 &+ \cdots &+ \beta_p \rho_{p-1} \\
\rho_2 &= \beta_1 \rho_1 &+ \beta_2 &+ \cdots &+ \beta_p \rho_{p-2} \\
\vdots & \vdots & \vdots & \ddots & \vdots \\
\rho_p &= \beta_1 \rho_{p-1} &+ \beta_2 \rho_{p-2} &+ \cdots &+ \beta_p
\end{aligned} \tag{3-9}$$

The linear equations in equation (3-9) are known as the Yule-Walker equations, the matrix form of which can be written as:

$$\boldsymbol{P}_p \boldsymbol{\beta}_p = \boldsymbol{\rho}_p \tag{3-10}$$

where,

$$\boldsymbol{\rho}_p = \begin{bmatrix} \rho_1 \\ \rho_2 \\ \vdots \\ \rho_p \end{bmatrix} \qquad \boldsymbol{\beta}_p = \begin{bmatrix} \beta_1 \\ \beta_2 \\ \vdots \\ \beta_p \end{bmatrix} \qquad \boldsymbol{P}_p = \begin{bmatrix} 1 & \rho_1 & \cdots & \rho_{p-1} \\ \rho_1 & 1 & \cdots & \rho_{p-2} \\ \vdots & \vdots & \ddots & \vdots \\ \rho_{p-1} & \rho_{p-2} & \cdots & 1 \end{bmatrix}$$

Thus, the auto-regressive parameters β_i can be estimated based on the sample autocorrelations determined from the historic time series:

$$\boldsymbol{\beta}_p = \boldsymbol{P}_p^{-1} \boldsymbol{\rho}_p \tag{3-11}$$

3.2.2.4. *Partial autocorrelation function [82]*

The order of an AR model can be determined from the partial autocorrelation functions of a time series. According to equation (3-8), the ith coefficients in an AR representation of order k denoted by β_{ki} satisfy the set of equations:

$$\rho_j = \sum_{i=1}^{k} \beta_{ki}\rho_{j-i}, \qquad j = 1, \dots, k \tag{3-12}$$

which can be expressed in the form of matrix as:

$$\begin{bmatrix} 1 & \rho_1 & \cdots & \rho_{k-1} \\ \rho_1 & 1 & \cdots & \rho_{k-2} \\ \vdots & \vdots & \ddots & \vdots \\ \rho_{k-1} & \rho_{k-2} & \cdots & 1 \end{bmatrix} \begin{bmatrix} \beta_{k1} \\ \beta_{k2} \\ \vdots \\ \beta_{kk} \end{bmatrix} = \begin{bmatrix} \rho_1 \\ \rho_2 \\ \vdots \\ \rho_k \end{bmatrix} \tag{3-13}$$

or,

$$\boldsymbol{P}_k \boldsymbol{\beta}_{kk} = \boldsymbol{\rho}_k \tag{3-14}$$

Where the term β_{kk} in equation (3-13) is known as the partial autocorrelation function at time lag k. For an AR process of order p, β_{kk} is nonzero if k is less than or equal to order p and zero otherwise.

3.2.3. Vector auto-regressive model

As was noted in Section 3.2.2, an AR forecasting model considers historic time series of weather variables at the target location only. Given historic time series at other surrounding locations, a vector auto-regressive (VAR) model additionally considers spatio-temporal correlations between the target location and other locations. Provided that weather variables have strong correlations between different locations, the use of a VAR model may improve the forecast accuracy over an AR model.

3.2.3.1. Vector auto-regressive model

As an extension of a univariate AR model, a VAR model of order p offers a way of producing the forecast as a weighted sum of historic time series not only at the target location but also from $(K - 1)$ surrounding sampled locations [84, 85]:

$$\tilde{\boldsymbol{Z}}_t = \boldsymbol{u} + \sum_{i=1}^{p} \boldsymbol{A}_i \tilde{\boldsymbol{Z}}_{t-i} + \boldsymbol{E}_t \tag{3-15}$$

where $\widetilde{\boldsymbol{Z}}_t$ is a $(K \times 1)$ vector consisting of $\tilde{z}_{jt}$ $(j = 1, \dots, K)$ at K locations. $\boldsymbol{u}$ is a $(K \times 1)$ vector comprising constants. $\boldsymbol{A}_i$ represents a $(K \times K)$ matrix of model parameters at time lag i and $\boldsymbol{E}_t$ is a $(K \times 1)$ vector of noise terms [85].

$$\widetilde{\boldsymbol{Z}}_t = \begin{bmatrix} \tilde{z}_{1t} \\ \tilde{z}_{2t} \\ \vdots \\ \tilde{z}_{Kt} \end{bmatrix} \quad \boldsymbol{u} = \begin{bmatrix} u_1 \\ u_2 \\ \vdots \\ u_K \end{bmatrix} \quad \boldsymbol{A}_i = \begin{bmatrix} A_{11}^i & A_{12}^i & \cdots & A_{1K}^i \\ A_{21}^i & A_{22}^i & \cdots & A_{2K}^i \\ \vdots & \vdots & \ddots & \vdots \\ A_{K1}^i & A_{K2}^i & \cdots & A_{KK}^i \end{bmatrix} \quad \boldsymbol{e}_t = \begin{bmatrix} e_{1t} \\ e_{2t} \\ \vdots \\ e_{Kt} \end{bmatrix}$$

3.2.3.2. Multivariate least squares estimation [85]

Given that each of K locations has a time series of size T over the same period $\tilde{z}_{jT}, \dots, \tilde{z}_{j1}$ $(j = 1, \dots, K)$ and p historic values $\tilde{z}_{j0}, \dots, \tilde{z}_{j(-p+1)}$ $(j = 1, \dots, K)$, some terms are defined as:

$$Y = (\widetilde{\boldsymbol{Z}}_T, \dots, \widetilde{\boldsymbol{Z}}_1) \quad \boldsymbol{B} = (\boldsymbol{u}, \boldsymbol{A}_1, \dots, \boldsymbol{A}_p) \quad \boldsymbol{Z} = \begin{bmatrix} 1 & \cdots & 1 \\ \widetilde{\boldsymbol{Z}}_{T-1} & \cdots & \widetilde{\boldsymbol{Z}}_0 \\ \vdots & \ddots & \vdots \\ \widetilde{\boldsymbol{Z}}_{T-p} & \cdots & \widetilde{\boldsymbol{Z}}_{-p+1} \end{bmatrix} \quad E = (\boldsymbol{e}_T, \dots, \boldsymbol{e}_1)$$

Thus, a VAR process of order p can be expressed in the matrix form:

$$Y = BZ + E \tag{3-16}$$

The VAR model parameters $\boldsymbol{A}_i$ and constants $\boldsymbol{u}$ are then determined to minimise the sum of squares of residuals $(\boldsymbol{Y} - \boldsymbol{BZ})$ for each location separately:

$$B = XZ'(ZZ')^{-1} \tag{3-17}$$

3.2.4. AR and VAR models for circular data

Equation (3-2) for a univariate AR model and equation (3-15) for a VAR model can be applied to forecasting of air temperature, wind speed and solar radiation which are linear data. Some changes in both equations are made for wind direction forecasting due to the circular properties of wind direction. Care is need when dealing with wind direction since two opposite conventions are commonly used for the reference angle, i.e. the wind vector azimuth θ_{vect} and the meteorological wind direction θ_{met} [86].

Fig. 3-4 provides a clear explanation of differences between two conventions and introduces an additional reference angle, i.e. the wind vector polar angle θ_{polar}.
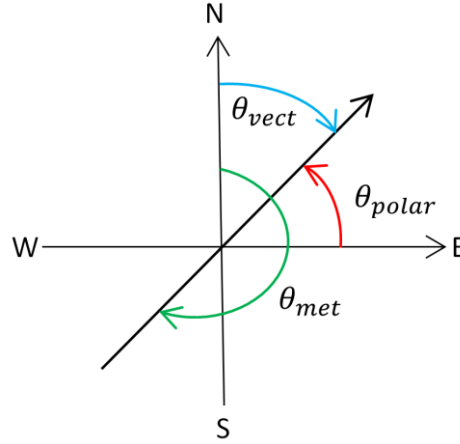
Fig. 3-4. Two conventional reference angles for wind direction record and an additional reference [86]

The wind vector azimuth θ_{vect} represents the direction towards which the wind is blowing while the meteorological wind direction θ_{met} represents the direction from which the wind is blowing. Both of them regard north as 0°, east as 90°, south as 180°, and west as 270° in clockwise order. In contrast, the wind vector polar angle θ_{polar} regards east as 0°, north as 90°, west as 180°, and south as 270° in anticlockwise order [86].

Wind direction measurements provided in this research are meteorological wind directions which have been converted to the form of the wind vector polar angle. The wind directions mentioned below are all referred to wind vector polar angles.

For wind direction (or circular data) forecasting, wind directions $w_d \in [-\pi, \pi)$ at each location are first decomposed along the easterly and northerly axes in the Cartesian coordinates as $\cos w_d$ and $\sin w_d$ respectively before the application of the AR or VAR model. Thus, the terms in equations (3-2) are redefined as:

$$\tilde{z}_t' = \begin{bmatrix} \tilde{z}_{ct} \\ \tilde{z}_{st} \end{bmatrix} \qquad u' = \begin{bmatrix} u_c \\ u_s \end{bmatrix} \qquad \beta_i' = \begin{bmatrix} \beta_{cc}^i & \beta_{cs}^i \\ \beta_{sc}^i & \beta_{ss}^i \end{bmatrix} \qquad e_t' = \begin{bmatrix} e_{ct} \\ e_{st} \end{bmatrix}$$

Each location has two time series, $\tilde{z}_{ct}$ and $\tilde{z}_{st}$, consisting of the easterly components $\cos w_d$ and the northerly components $\sin w_d$ which range between -1 and $+1$

respectively. In this way, an AR model for wind direction forecasting can be regarded as a VAR model with two variables [87, 88]. When using a VAR model to predict wind direction, the terms in equation (3-15) are redefined as:

$$\widetilde{\boldsymbol{Z}}_t' = \begin{bmatrix} \tilde{z}_{1ct} \\ \tilde{z}_{1st} \\ \vdots \\ \tilde{z}_{Kct} \\ \tilde{z}_{Kst} \end{bmatrix} \quad \boldsymbol{u}' = \begin{bmatrix} u_{1c} \\ u_{1s} \\ \vdots \\ u_{Kc} \\ u_{Ks} \end{bmatrix} \quad \boldsymbol{A}_i' = \begin{bmatrix} A_{1c1c}^i & A_{1c1s}^i & \cdots & A_{1cKc}^i & A_{1cKs}^i \\ A_{1s1c}^i & A_{1s1s}^i & \cdots & A_{1sKc}^i & A_{1sKs}^i \\ \vdots & \vdots & \ddots & \vdots & \vdots \\ A_{Kc1c}^i & A_{Kc1s}^i & \cdots & A_{KcKc}^i & A_{KcKs}^i \\ A_{Ks1c}^i & A_{Ks1s}^i & \cdots & A_{KsKc}^i & A_{KsKs}^i \end{bmatrix} \quad \boldsymbol{E}_t' = \begin{bmatrix} e_{1ct} \\ e_{1st} \\ \vdots \\ e_{Kct} \\ e_{Kst} \end{bmatrix}$$

where four redefined terms have the size of $(2K \times 1)$, $(2K \times 1)$, $(2K \times 2K)$ and $(2K \times 1)$ respectively. Then the wind direction forecast is determined based on predictions of the easterly and northerly components.

3.2.5. Probabilistic forecasting

Many users of forecasts, including power system operators, would like to know not only what the 'best' forecast is but also how wrong it might be, i.e. to have a probabilistic forecast that gives the probability of the true value of the forecasted quantity lying within a certain range [88]. When producing a probabilistic forecast, the aim is to maximize the sharpness of predictive probability distributions subject to a calibration to minimize the uncertainty [89]. The calibration represents the statistical consistency between the predictive distributions and the observations [90]. The sharpness refers to the spread or concentration of the predictive distribution [90] which can be represented by the average width of central prediction intervals. Sharper or more concentrated predictive distributions are preferred under the constraint of calibration. The histogram of probability integral transform (PIT) is an effective tool to assess the calibration of probabilistic forecasts. In this case, the PIT is the value of the predictive cumulative distribution function (CDF) evaluated at the observation [91]. An approximately uniform PIT histogram reveals probabilistic forecasts to be nearly fully calibrated.

3.2.5.1. Predictive probability distributions

When establishing a probabilistic forecasting model, it is necessary to predefine an appropriate type of probability distribution for the forecast variable with the unknown predictive centre and spread or concentrate parameter which will be determined from historic time series. The probability distribution of the forecast error or the predictand (i.e. the sum of the forecast error and its actual value) at a particular future time is usually assumed to be Gaussian [89]. The prediction distribution of air temperature is therefore taken to be normal denoted by $N(\mu_a, \sigma_a)$ as shown in Fig. 3-5. A truncated normal distribution with a cut-off at zero denoted by $N^+(\mu_v, \sigma_v)$ is employed as the predictive distribution of wind speed due to its non-negativity [89], as shown in Fig. 3-5. Since probabilistic forecasting aims to quantify the possible size of the forecast error, the Weibull distribution that is usually used to model the distribution of wind speed time series over a year [92] may be not an appropriate representation for the distribution of the wind speed forecast error at a particular future moment. In order to address the circular properties of wind direction, the predictive distribution of wind direction is assumed to be von Mises denoted by $VM(\mu_\theta, \kappa)$ as shown in Fig. 3-6, which is regarded as the circular analogue of the Gaussian distribution [93]. Their probability density functions (PDFs) for L steps ahead are defined as [94, 95, 93]:

$$f^N_{\mu_{a,t+L}, \sigma_{a,t+L}}(x_a) = \frac{1}{\sigma_{a,t+L}} \emptyset\left(\frac{x_a - \mu_{a,t+L}}{\sigma_{a,t+L}}\right), \quad x_a \in (-\infty, \infty) \tag{3-18}$$

$$f^{N^+}_{\mu_{v,t+L}, \sigma_{v,t+L}}(x_v) = \frac{\frac{1}{\sigma_{v,t+L}} \emptyset\left(\frac{x_v - \mu_{v,t+L}}{\sigma_{v,t+L}}\right)}{1 - \Phi\left(-\frac{\mu_{v,t+L}}{\sigma_{v,t+L}}\right)}, \quad x_v \in [0, \infty) \tag{3-19}$$

$$f^{VM}_{\mu_{\theta,t+L}, \kappa_{t+L}}(x_\theta) = \frac{e^{\kappa_{t+L} \cos(x_\theta - \mu_{\theta,t+L})}}{2\pi I_0(\kappa_{t+L})}, \quad x_\theta \in [-\pi, \pi) \tag{3-20}$$

where terms $\mu_{a,t+L}$ and $\mu_{v,t+L}$ are the predictive centres and terms $\sigma_{a,t+L}$ and $\sigma_{v,t+L}$ are the predictive spreads of probability distributions for the L-step-ahead air

temperature and wind speed forecasts respectively. The L-step-ahead predictive centre and concentration parameter of a von Mises distribution for wind direction are denoted by $\mu_{\theta,t+L} \in [-\pi, \pi)$ and $\kappa_{t+L} \in [0, \infty)$. $\emptyset(\cdot)$ and $\Phi(\cdot)$ represent the PDF and CDF of a standard normal distribution respectively. $I_0(\cdot)$ refers to the modified Bessel function of the first kind of order zero.
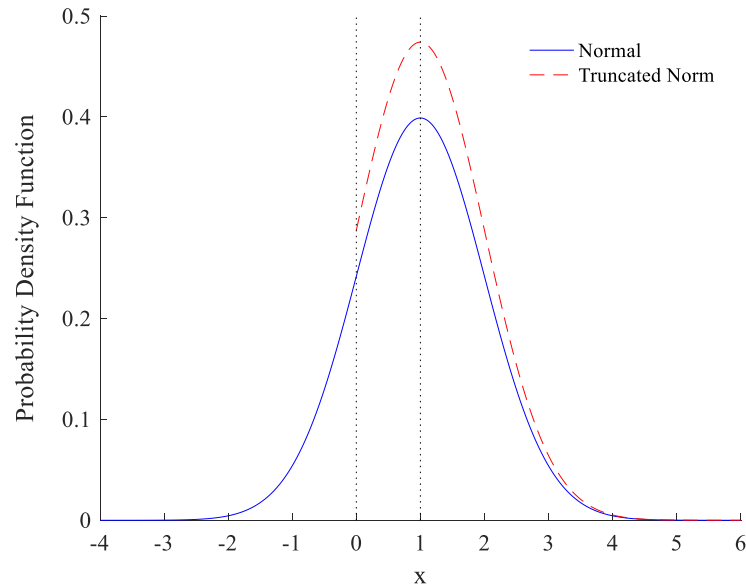
Fig. 3-5. Probability density functions of a normal (or Gaussian) distribution and a truncated normal distribution with a cut-off at zero, both having a mean of one and a standard deviation of one
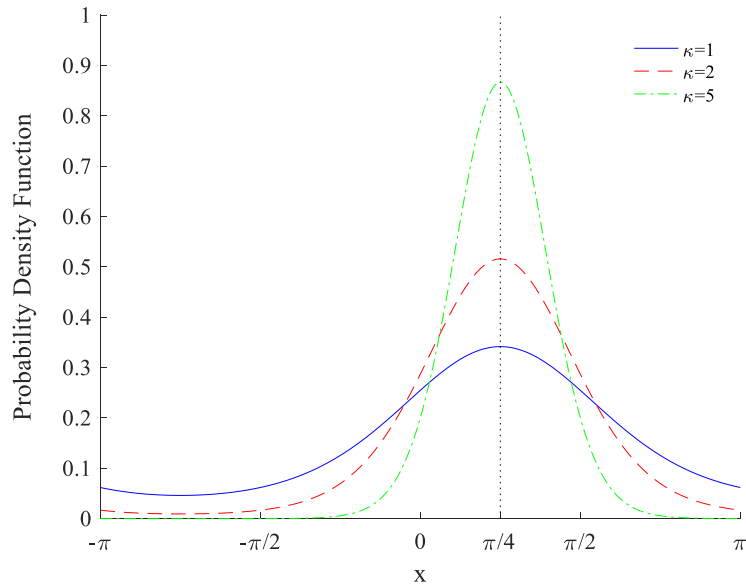
Fig. 3-6. Probability density functions of von Mises distributions with the same mean of $\pi/4$ and different concentration parameters equal to 1, 2 and 5

The centres of predictive distributions can be modelled as a sum of residuals predicted by the AR or VAR forecasting models and the corresponding diurnal trends fitted by Fourier series. Conditional heteroscedasticity considers the spread or concentration parameter of predictive distribution to be time variable. The predictive spread σ_{t+L} or concentration parameter κ_{t+L} for L steps ahead is modelled as a linear function of the root mean square of recent changes in residuals Res at the target location for air temperature and wind speed, assessed over 1 hour, as in equation (3-21). For wind direction, due to its circular nature, the concentration of recent observations at the target location is used, in this research over a period of 2 hours, as in equation (3-22). The concentration of recent wind direction observations, κ_o, is calculated based on the code provided by Berens [96]. In this research, steps of 10 minutes are used to reflect the input data.

$$\sigma_{t+L} = c_0 + c_1 \left[\frac{1}{5} \sum_{j=0}^{4} \left(Res_{t-j} - Res_{t-j-1} \right)^2 \right]^{\frac{1}{2}} \tag{3-21}$$

$$\kappa_{t+L} = cc_0 + cc_1 \kappa_o \tag{3-22}$$

where c_0, c_1, cc_0 and cc_1 are non-negative coefficients. The experimental results obtained suggest that the selected lengths of one and two hours used to model the conditional heteroscedasticity result in an effective probabilistic forecasting model. The homoscedastic model, which assumes a constant spread or concentration parameter, is also constructed as a comparison to analyse the advantages of the conditionally heteroscedastic model.

3.2.5.2. Continuous ranked probability score

A technique of minimum continuous ranked probability score (CRPS) estimation proposed by Gneiting [97] is used to estimate the predictive probability distributions of weather variables. The CRPS is one of the scoring rules and can be used as a summary indicator to assess performance of probabilistic forecasting models with respect to the calibration and sharpness [95].

For a point forecasting assessment, the scoring rule refers to mean absolute error or root mean square error that describes the differences between point forecasts and actual values on average. For a probabilistic forecasting assessment, a numerical score is assigned to each probabilistic forecast according to the predictive distribution and the observation. The Brier score (BS) is a traditional scoring rule to verify the prediction of the occurrence of a specific event by considering two options that the event occurs or does not occur [98]. The ranked probability score (RPS) generalises the BS by dividing the range of the parameter of interest into more classes. Then the CRPS is generated when the number of classes is infinite. Compared with the RPS, the CRPS takes account of the whole permissible range of parameter of interest and does not require the predefined classes [98].

In the case of predictive distribution, events are characterised in terms of percentiles. The CRPS gives a numerical score to the event based on the difference between the predictive PDF f and the observation x_o [98]:

$$crps(f, x_o) = \int_{-\infty}^{\infty} \left[\int_{-\infty}^{x} f(y)\, dy - F_o(x, x_o) \right]^2 dx \tag{3-23}$$

where $\int_{-\infty}^{x} f(y)\, dy$ represents the predictive probability for $x \geq x_o$. $F_o(x, x_o)$ is the Heaviside function and equal to 1 if the event that the percentile $x \geq x_o$ happens and 0 otherwise. The $crps$ value at a future moment may be regarded as the sum of the squares of the difference between $\int_{-\infty}^{x} f(y)\, dy$ and $F_o(x, x_o)$ at each percentile with zero width [87]. The average value of $crps$, used to assess probability forecasts, should be minimised for probabilistic forecasting. For linear variables, wind speed and air temperature, equation (3-23) can be written equivalently as [99]:

$$crps_l(F_l, x_o) = E\{|X - x_o|\} - \frac{1}{2} E\{|X - X'|\} \tag{3-24}$$

where X and X' represent independent random samples from the linear predictive CDF F_l and $E\{\cdot\}$ denotes the expectation operator. The expressions derived by

Gneiting can be directly used to calculate the $crps_l$ value for the normal distribution $N(\mu, \sigma)$ [97] and the truncated normal distribution with a cut-off at zero $N^+(\mu, \sigma)$ [95]:

$$crps(N(\mu, \sigma^2), x_o) = \sigma\left\{\frac{x_o - \mu}{\sigma}\left[2\Phi\left(\frac{x_o - \mu}{\sigma}\right) - 1\right] + 2\emptyset\left(\frac{x_o - \mu}{\sigma}\right) - \frac{1}{\sqrt{\pi}}\right\} \quad (3\text{-}25)$$

$$\begin{aligned}
crps&(N^+(\mu, \sigma^2), x_o) \\
&= \sigma\Phi\left(\frac{\mu}{\sigma}\right)^{-2} \times \left\{\frac{x_o - \mu}{\sigma}\Phi\left(\frac{\mu}{\sigma}\right)\left[2\Phi\left(\frac{x_o - \mu}{\sigma}\right) + \Phi\left(\frac{\mu}{\sigma}\right) - 2\right]\right. \\
&\quad \left. + 2\emptyset\left(\frac{x_o - \mu}{\sigma}\right)\Phi\left(\frac{\mu}{\sigma}\right) - \frac{1}{\sqrt{\pi}}\Phi\left(\sqrt{2}\frac{\mu}{\sigma}\right)\right\}
\end{aligned} \quad (3\text{-}26)$$

The circular $crps_c$ for wind direction forecasting is estimated by using the angular distance $\alpha(\cdot)$ instead of the Euclidean distance in equation (3-24) [93]:

$$crps_c(F_c, \theta_o) = E\{\alpha(\Theta, \theta_o)\} - \frac{1}{2}E\{\alpha(\Theta, \Theta^*)\} \quad (3\text{-}27)$$

where Θ and Θ^* represent the independent randomly sampled wind directions from the circular predictive CDF F_c. The term θ_o represents the observed wind direction. The angular distance $\alpha(\cdot)$ is defined as:

$$\alpha(\theta_1, \theta_2) = \begin{cases} |\theta_1 - \theta_2| & for \;\; 0 \leq |\theta_1 - \theta_2| < \pi \\ 2\pi - |\theta_1 - \theta_2| & for \;\; \pi \leq |\theta_1 - \theta_2| < 2\pi \end{cases} \quad (3\text{-}28)$$

where θ_1 and θ_2 are two random directions within the interval $[-\pi, \pi)$. The first term on the right-hand side of equation (3-27) can be expressed as [93]:

$$E\{\alpha(\Theta, \theta_o)\} = \frac{1}{2\pi I_0(\kappa)}\int_{-\pi}^{\pi} \alpha(x_\theta, \theta_o)e^{\kappa\cos(x_\theta - \mu_\theta)}\,dx_\theta \quad (3\text{-}29)$$

where μ_θ is the predictive centre of von Mises distribution. It is found that $E\{\alpha(\Theta, \theta_o)\}$ is only dependent on the concentration parameter κ and the angular distance between θ_o and μ_θ. Therefore, a look-up table for $E\{\alpha(\Theta, \theta_o)\}$ in terms of both κ with accuracy of 0.1 and $\alpha(\theta_o, \mu_\theta)$ with accuracy of 0.0017 (0.1^o) is built up in order to reduce computation time due to iterative calculation for the determination of model parameters. How the value of $E\{\alpha(\Theta, \theta_o)\}$ varies with κ for typical values of $\alpha(\theta_o, \mu_\theta)$ is shown in Fig. 3-7 [87].
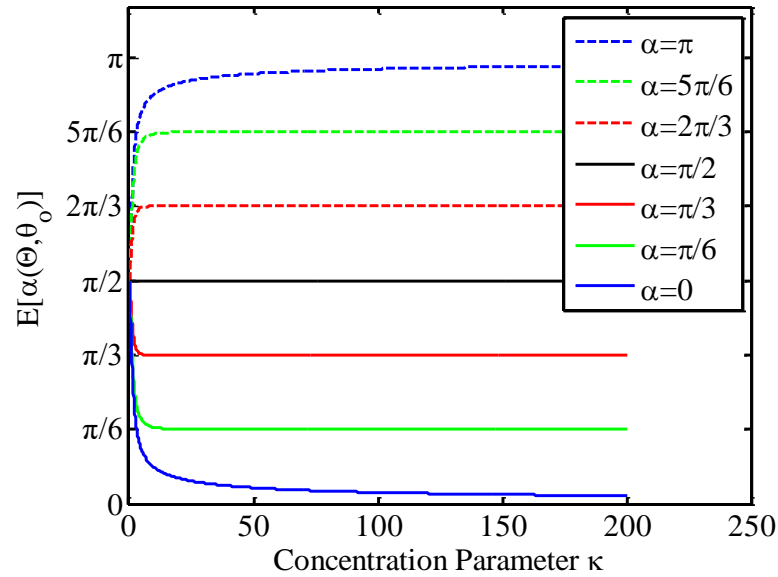
Fig. 3-7. $E\{\alpha(\theta,\theta_o)\}$ varying with κ under typical $\alpha(\theta_o,\mu_\theta)$ values [87]

The second term on the right-hand side of equation (3-27) is only dependent on κ. It equals $\pi/4$ for $\kappa = 0$ and is approximated to $1/(2\pi\kappa)^{1/2}$ when κ approaches infinity (≥ 200) [93]. The second term for $0 < \kappa < 200$ is calculated by standard Monte Carlo integration [100]. A look-up table is also built for the second term $\frac{1}{2}E\{\alpha(\theta,\theta^*)\}$ in terms of κ with accuracy of 0.1 and is smoothed by the lowess technique [101] according to the procedure in [93]. How the value of $\frac{1}{2}E\{\alpha(\theta,\theta^*)\}$ varies with the concentration parameter $0 \leq \kappa \leq 200$ is plotted in Fig. 3-8 [87].
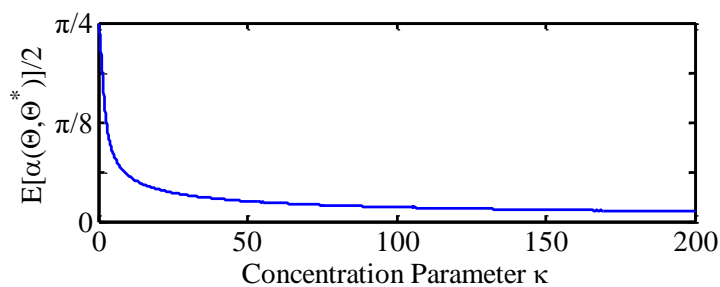
Fig. 3-8. $\frac{1}{2}E\{\alpha(\theta,\theta^*)\}$ varying with κ [87]

The parameters in the AR and VAR forecasting models and the coefficients representing the predictive spread or concentration parameter are determined with the objective of minimising the average value of $crps_l$ or $crps_c$. Initial values of

76

the AR and VAR parameters are determined from the de-trended data at each location using least squares estimation [83, 85]. Initial values of the non-negative coefficients modelling the spread or concentration parameter are set to be 0.1 and 1.0 respectively. The dependencies of the probability distribution of wind direction, $E\{\alpha(\Theta, \theta_o)\}$ and $\frac{1}{2}E\{\alpha(\Theta, \Theta^*)\}$ on concentration parameter κ have been explored as shown in Figs. 3-7 and 3-8 and there is little change for κ over 200. Therefore, κ is limited to a maximum value of 200 [88].

3.3. Results and Model Validation of Point Forecasting

This section will develop different time series forecasting models to estimate point forecasts for each weather variable using an auto-regressive process that is combined with the Fourier series based de-trending method. Through a comparison between their performances in terms of the root mean square errors of predictions for a number of time steps ahead, the point forecasting models that provide a reasonable forecast accuracy are selected to model predictive centres of predictive distributions.

3.3.1. Air temperature forecasting

A persistence forecasting method that supposes the predictions in the future being equal to the present values [102] may work well for the very-short-term prediction of air temperature due to the slow fluctuation of air temperature [103]. In addition to the linear regression-based forecasting methods, an average changes method and a precedent-based forecasting method were developed in [103] to predict air temperature according to the similarities of air temperature variations over the same periods in different days [103]: an average changes method estimated air temperature at one future moment as an average of historic values that were recorded at the same time point within recent days; the precedent-based forecasting method first determined the historic time series segments of air temperature that had high

77

similarities with the current segment, and their subsequent observations were then averaged as the air temperature forecast following the current segment [103].

The de-trended data was used in [104] to train an artificial neural network (ANN) model for short-term air temperature forecasting. A better performance was achieved by using two ANN models which were trained based on the de-trended data of air temperatures in warm months (April to September) and those in cold months (October to March) separately. However, Yang [80] mentioned some disadvantages of an ANN model, such as computation time and the risk of under-fitting or over-fitting which might increase the out-of-sample forecasting errors.

Yang [80] modelled air temperature's annual movement by month and the diurnal movement by hour based on Fourier series. The Fourier coefficients were estimated from historic time series of air temperature using least squares estimation and were then used to predict the future movements of air temperature. This is the so-called 'Fourier series forecasting model'. The forecast accuracy achieved in Yang's work may be improved if the deviations from temporal movements or trends (i.e. the de-trended data) are additionally forecast by an AR or VAR model. In this section, the point forecast of air temperature will be estimated as a sum of the de-trended data predicted by the AR or VAR forecasting models and the corresponding diurnal trend fitted by Fourier series.

3.3.1.1. AR and VAR model validation procedure

Air temperature forecasts are determined based on historic observations within a sliding training window, from which the diurnal trends are first extracted by the 2nd order Fourier series for each weather station as shown in Fig. 3-9. The parameters in the AR and VAR forecasting models are then estimated from the de-trended data within the training window for each station using least squares estimation [83, 85]. The forecasts of residuals and the corresponding fitted diurnal trends are added up as point forecasts of air temperature.
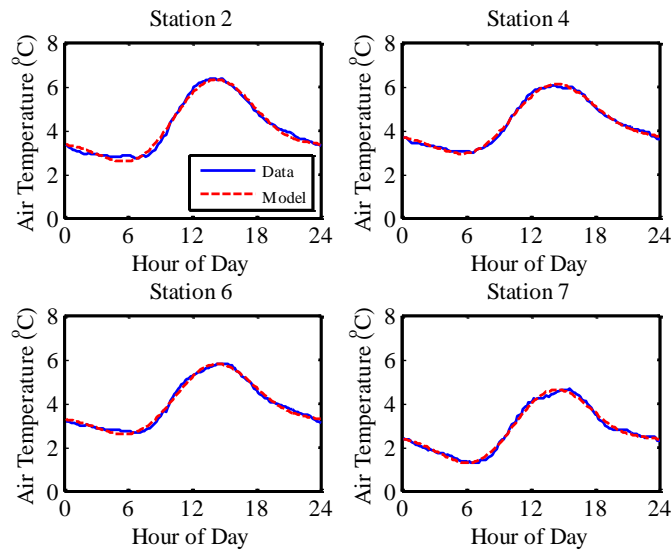
Fig. 3-9. Diurnal trends modelled from air temperature observations from 00:00 on 01/02/2013 to 23:50 on 17/03/2013 at stations 2, 4, 6 and 7

As noted in Section 3.2.5.2, a point forecasting model's performance can be assessed in terms of the root mean square error (RMSE) of predictions [105]. The length of sliding training window will be determined as that which gives the best improvement in RMSE over persistence forecasting. In addition to the inspection of partial autocorrelation functions [82] as introduced in Section 3.2.2.4, the orders of the AR and VAR models can be determined by the comparison of forecast errors for different model orders [81, 106].

In order to determine the window lengths, an order of 2 is initially used for both AR and VAR models based on Hill's work [81] in which varying the order from 2 to 4 produced less than 1% improvement in RMSE of 1-step-ahead forecasts of hourly wind speed. As an illustration, the improvements over persistence in RMSE of air temperature forecasts for up to 3 steps (half hour) ahead for AR(2) and VAR(2) models with varying training window length are tested for all stations and the results at weather station 2 are shown in Fig. 3-10 where the RMSE of persistence forecasts for each time step ahead is $0.2062°C$, $0.3454°C$ and $0.4644°C$ respectively.
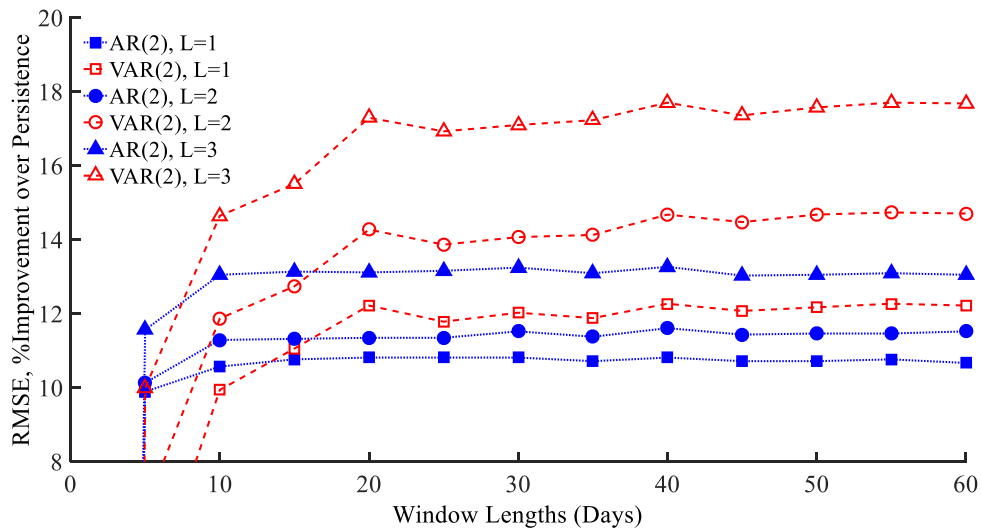
Fig. 3-10. Improvement over persistence in RMSE of air temperature forecasts for $L = 1, 2, 3$ steps ahead for AR(2) and VAR(2) models with varying training window length at station 2

The experimental results demonstrate that (a) the performance of AR(2) and VAR(2) models with a window length of smaller than 5 days are worse than the persistence forecasting; (b) given a sufficiently long training window, VAR(2) models perform better than AR(2) models; (c) the improvement over persistence for AR(2) and VAR(2) models are usually more significant with the forecast horizon going further; and (d) although there will be a range of effective training window lengths, 40 days are reasonable choices for both AR and VAR models here since the selected length have been found to work well for all weather stations. (It is noted that an increased training window length does not need extra computation time). The VAR forecasting models with a 20-day sliding training window are shown to have similar accuracies to those that use a training window of 40 days at weather station 2. This may be because the auto-regressive parameters derived from a longer training window would accurately represent the correlations between the de-trended data as the statistical variability is reduced in the estimation, whereas the seasonal variations in air temperature reflected by the fitted diurnal trends would be smoothed to some extent, and vice versa [95].

In order to confirm the models' orders the air temperature forecasts for up to 3 steps ahead at weather station 2 produced by the AR and VAR models of different orders p are compared with persistence forecasts, as shown in Fig. 3-11. It is found that less than 1% improvements are achieved for air temperature forecasts for up to 3 steps (half hour) ahead when orders are greater than 2. Furthermore, the VAR model is generally shown to give a lower RMSE than the AR model of a same order due to the additional capture of the spatial correlations among the field data [81]. Therefore, a VAR(2) model with a sliding training window of 40 days is adopted here to model the centres of predictive distributions for air temperature for up to 3 steps ahead.
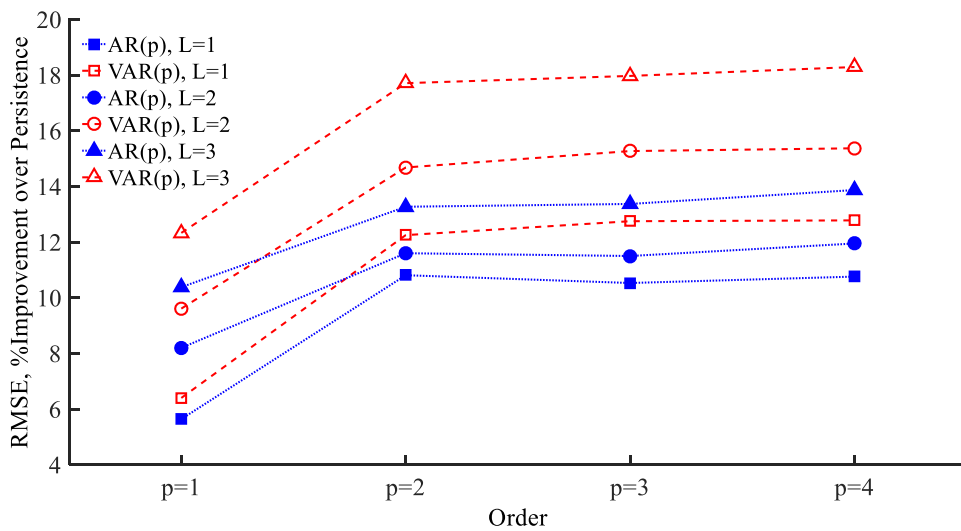
Fig. 3-11. Improvement over persistence in RMSE of air temperature forecasts for $L = 1, 2, 3$ steps ahead for AR and VAR models of different orders at station 2

It is noted that auto-regressive parameters and Fourier coefficients are updated once a day which has been proved to be sufficient to give accurate forecasts in this research. For example, updating the VAR(2) model from daily to hourly achieves less than 0.5% improvement for 1-step-ahead air temperature forecasts at station 2.

3.3.2. Wind speed and wind direction forecasting

For wind speed forecasting, the VAR forecasting model was shown to give greater improvement over persistence than a simple AR forecasting model in [81] which suggested that the spatial correlations among wind speeds at different locations

captured by the VAR model made the main contribution to the improvement. For wind direction forecasting, an inverse of link function was used in [107] to convert circular variables (wind directions) to linear variables; predictions of linear data estimated by an auto-regressive moving average (ARMA) method were then converted back to the circular data by a link function. In El-Fouly's work [108], the forecasts of hourly wind speed and wind direction for up to 24 hours ahead were estimated as a weighted sum of historic values recorded at the same time points within recent years separately. Although the forecasting model presented in [108] performed better than persistence forecasting a large storage of historic data was required.

Wind directions have been incorporated as additional variables in several approaches to wind speed forecasting. A regime-switching space-time (RST) approach which relied on the pre-analysis of local geographic features and wind direction observations was developed to model the centres of predictive distributions for wind speed [95]. However, it may be complicated to determine the number and boundaries of the regimes in the RST approach. Hering and Genton [109] proposed a trigonometric direction diurnal (TDD) model in which sine and cosine values of wind directions (i.e. the northerly and easterly components) were included as the covariates affecting wind speed forecasts in their later work. In Erdem's work [110], historic wind directions were classified into three clusters based on the levels of their corresponding wind speeds (e.g. low, medium and high speeds) using k-means algorithm. The clusters that wind directions were forecast to be located at were represented by dummy variables, which were subsequently used as additional variables in a linear regression forecasting model to estimate wind speed predictions.

The time series models that forecast wind speeds in connection with wind directions have also been developed. In Erdem's another work [107] wind speeds were decomposed into the easterly and northerly components according to their accompanying wind directions and the predictions of components were combined to

obtain the forecasts of wind speed and direction. In addition, wind speed and wind direction could be regarded as the magnitude and phase of a complex value respectively which was used to establish the forecasting models [111].

The AR and VAR forecasting models will be developed for wind speed and direction separately in this section. It is noted that wind directions are processed in the Cartesian coordinates before the application of AR and VAR models according to the procedure as introduced in Section 3.2.4. The performance of the selected forecasting models will be additionally compared with the approach presented in [107] which decomposes wind speeds into the easterly and northerly components with respect to their associated wind directions and then determines the forecasts of wind speed and wind direction from the components predicted by an AR model.

3.3.2.1. Validation procedure of AR and VAR models for wind speed

The sliding window technique is also applied to wind speed forecasting in this study. The diurnal trends of wind speed are modelled by the 2nd order Fourier series (as shown in Fig. 3-12) and then removed from historic time series within the training window to obtain the de-trended data for all weather stations, based on which the auto-regressive parameters are calculated using the least squares estimation.
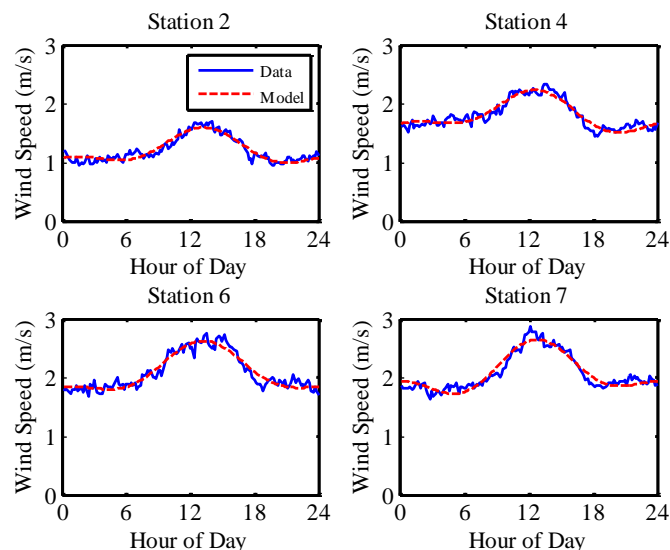
Fig. 3-12. Diurnal trends modelled from wind speed observations from 00:00 on 01/02/2013 to 23:50 on 17/03/2013 at stations 2, 4, 6 and 7

The improvements over persistence in RMSE of wind speed forecasts for up to 3 steps (half hour) ahead for AR(2) and VAR(2) models that use different training window lengths are examined at all stations so as to select the reasonable window lengths and the results at station 2 are shown in Fig. 3-13 as an illustration where the RMSE of persistence forecasts for each time step ahead is $0.3771m/s$, $0.4395m/s$ and $0.482m/s$ respectively.
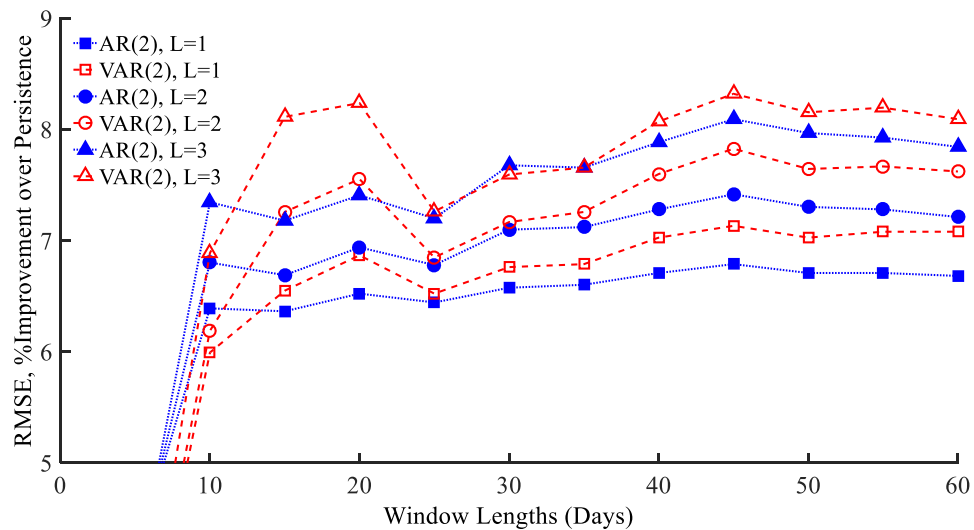
Fig. 3-13. Improvement over persistence in RMSE of wind speed forecasts for $L = 1, 2, 3$ steps ahead for AR(2) and VAR(2) models with varying training window length at station 2

The experimental results indicate that (a) VAR(2) models perform better than AR(2) models when the training window is sufficiently long; (b) AR(2) and VAR(2) models give greater improvement over persistence with a longer forecast horizon; (c) the VAR(2) models with a training window of 20 and 45 days have similarly high forecast accuracies, meaning a trade-off in the determination of window length between the respective advantages of a shorter training window and a longer window as discussed in Section 3.3.1.1; and (d) 45 days are selected among a range of effective window lengths for AR and VAR models since the use of a 45-day training window is found to result in reasonable forecasting performance at all stations.

The accuracies of wind speed forecasts for up to 3 steps ahead produced by AR and VAR models of different orders are compared with persistence forecasts (as shown in Fig. 3-14) to select an appropriate order for each model. Although a higher-order

84

forecasting model is usually shown to generate more accurate wind speed forecasts, less than 1% improvement can be achieved by the VAR models when the model order increases from 2 to 4. However, the AR(4) models could give approximately 1% more improvement over persistence than the AR(2) models. Furthermore, the AR(4) models have a similar or even better forecasting capability than the VAR(2) models for wind speed forecasting. Moreover, the probabilistic forecasting model established based on the AR(4) model has fewer auto-regressive parameters and requires less computation time in the process of minimising the average value of continuous ranked probability score (CRPS). For example, it costs around 3.7 and 22.5 seconds to determine parameters of the AR(4) and VAR(2) based probabilistic forecasting models respectively that minimise the average value of CRPS. (The computer being used for weather forecasting has a 64-bit operating system, 8GB of RAM, and an Intel Core i7-4500U, 2.4GHz processor). Therefore, the AR(4) model with a 45-day training window is used here to predict wind speeds for up to 3 steps ahead.
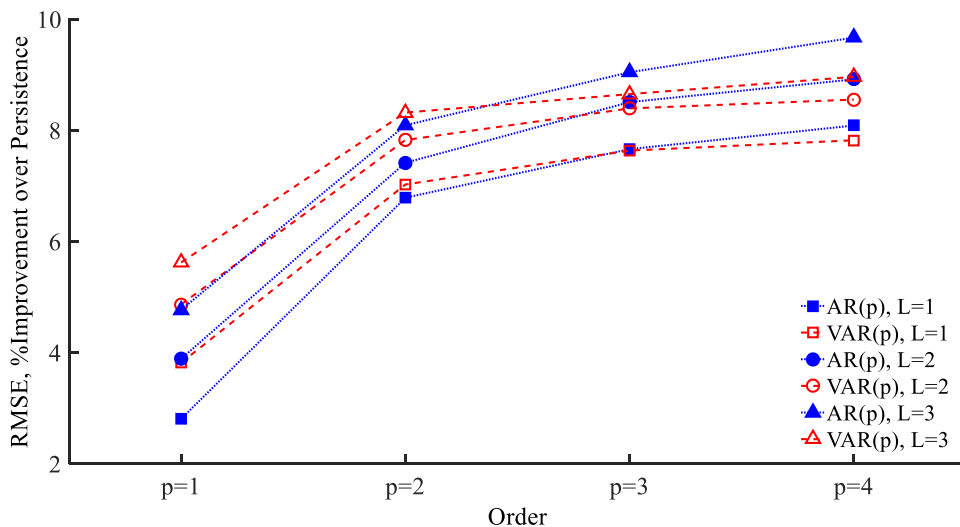
Fig. 3-14. Improvement over persistence in RMSE of wind speed forecasts for $L = 1, 2, 3$ steps ahead for AR and VAR models of different orders at station 2

3.3.2.2. Validation procedure of AR and VAR models for wind direction

The diurnal trends of the northerly and easterly components of wind directions were separately modelled from historic time series within a training window based on the 2nd order Fourier series, as shown in Figs. 3-15 and 3-16. The residuals of the

85

northerly and easterly components are then used to determine the parameters of AR and VAR models. The wind direction forecast is derived from the predictions of two components estimated by the AR or VAR forecasting model that are combined with the fitted diurnal trends. As was noted in Section 3.2.4, an AR model developed here for wind direction (circular data) forecasting can be regarded as a VAR model that consists of two variables.
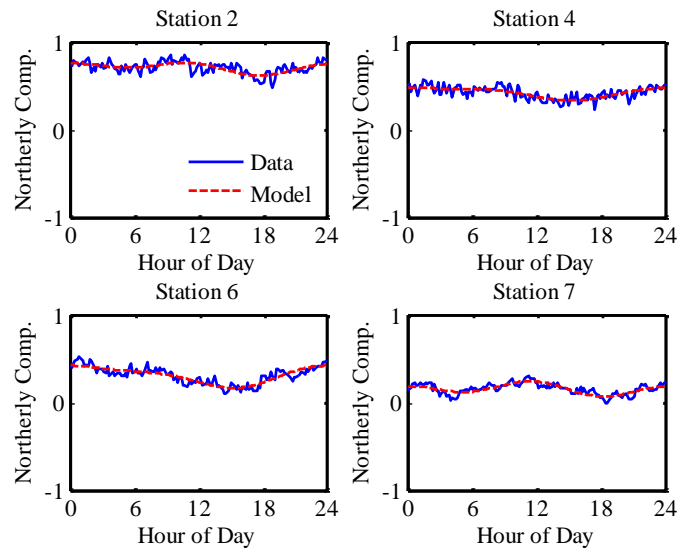
Fig. 3-15. Diurnal trends modelled from the northerly components of wind direction observations from 00:00 on 01/02/2013 to 23:50 on 17/03/2013 at stations 2, 4, 6 and 7
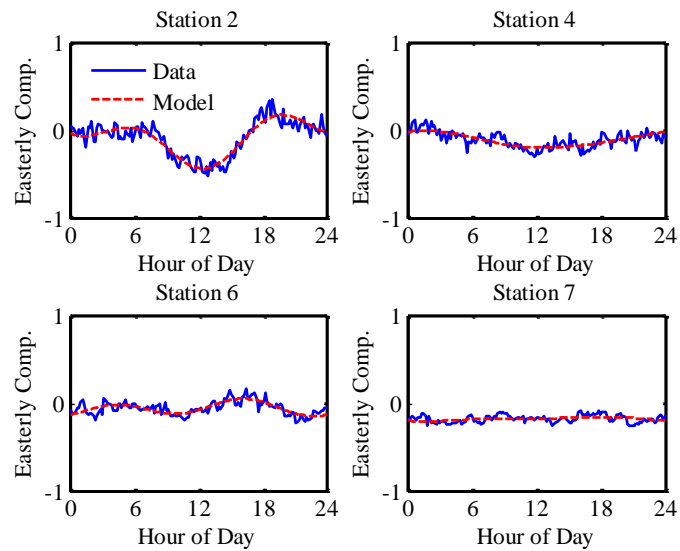
Fig. 3-16. Diurnal trends modelled from the easterly components of wind direction observations from 00:00 on 01/02/2013 to 23:50 on 17/03/2013 at stations 2, 4, 6 and 7

Like the procedure of validating the forecasting models for air temperature and wind speed, the improvements over persistence in RMSE of wind direction forecasts for up to 3 steps (half hour) ahead for AR(2) and VAR(2) models with varying training window length are assessed in order to confirm the length of sliding training window. As an illustration, the results at station 2 are shown in Fig. 3-17 where the RMSEs of persistence forecasts for different time steps ahead are 0.8, 0.843, and 0.872 radians respectively. It is noted that the error of wind direction forecast is calculated as the angular distance between the prediction and the actual value via equation (3-28).
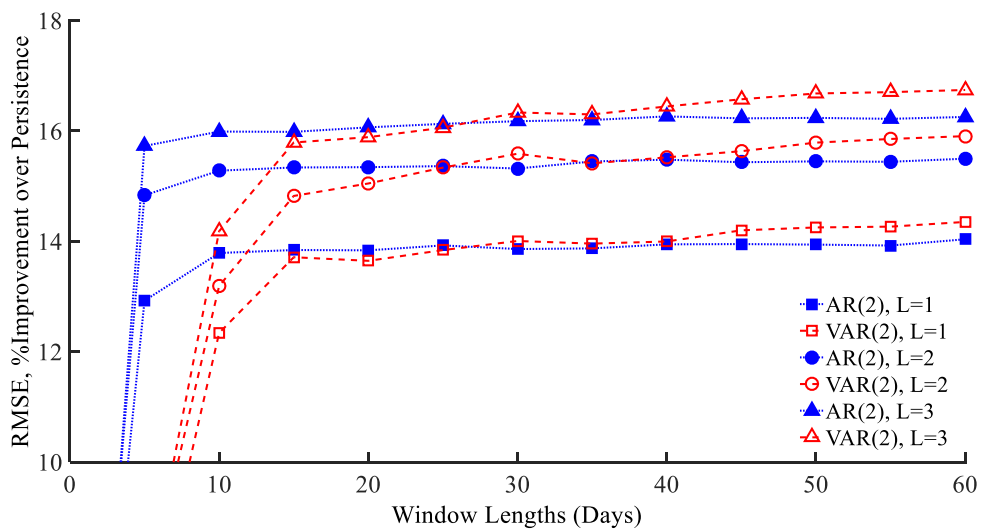
Fig. 3-17. Improvement over persistence in RMSE of wind direction forecasts for $L = 1, 2, 3$ steps ahead for AR(2) and VAR(2) models with varying training window length at station 2

The experimental results indicate that (a) the AR(2) and VAR(2) models have similar performances when their parameters are determined from the de-trended data within a training window of 15 – 40 days; (b) the improvement over persistence increases with the forecast look ahead time; (c) a training window of 45 days is selected for AR and VAR models which can produce wind direction predictions with a reasonable accuracy at all stations.

The accuracies of wind direction forecasts determined by AR and VAR models of different orders are compared with persistence forecasts and the results at station 2 are shown in Fig. 3-18. For 1-step-ahead wind direction forecasting, the AR(4) models having fewer auto-regressive parameters are shown to perform similarly to or

even better than the VAR(2) models. As noted in section 3.3.2.1, having fewer auto-regressive parameters reduces computation time required to minimise the average value of continuous ranked probability score. Therefore, the AR(4) model with a 45-day training window is used to model predictive centres of wind direction for 1 step (10 minutes) ahead. For 2-step-ahead and 3-step-ahead forecasting, the AR(6) models having reasonable forecast accuracies and fewer auto-regressive parameters are preferred here rather than the VAR models.
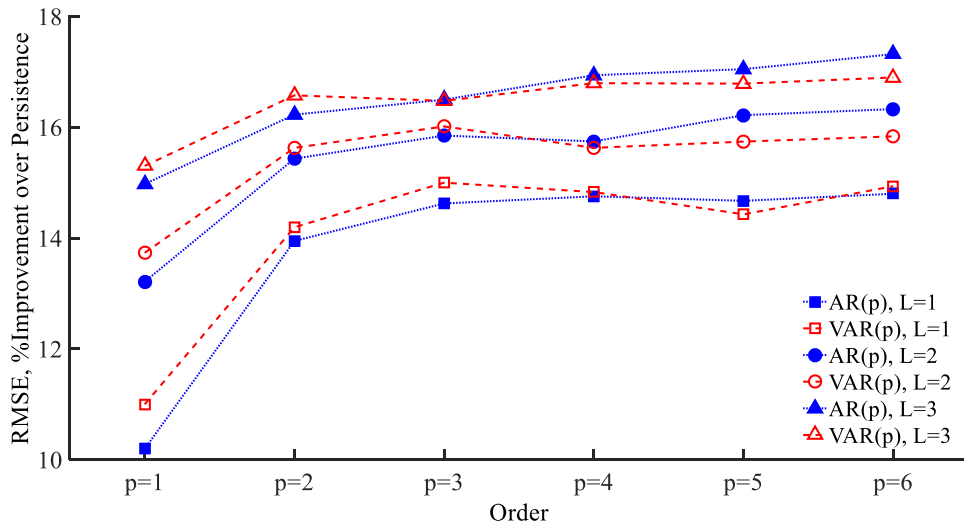
Fig. 3-18. Improvement over persistence in RMSE of wind direction forecasts for $L = 1, 2, 3$ steps ahead for AR and VAR models of different orders at station 2

3.3.2.3. Wind vector forecasting model

A time series forecasting model which decomposes wind speeds into the northerly and easterly components based on their associated wind directions and determines the predictions of wind speed and direction from the forecasts of components is referred to here as a wind vector forecasting model. The diurnal trends of the northerly and easterly components are extracted from their respective historic time series within a training window by Fourier series and then removed to obtain the de-trended data from which auto-regressive parameters are determined. Like the AR model developed for wind direction forecasting in this work, an AR process utilised in the wind vector forecasting model can be regarded as a VAR process that consists of two variables, i.e. the northerly and easterly components. The forecast of each

component is calculated as a sum of the residual predicted by an AR or VAR model and the corresponding fitted diurnal trend.

The forecasts of wind speed and wind direction for up to 3 steps (half hour) ahead estimated by the wind vector (WV) forecasting model using an AR(6) process with a training window of 45 days are compared with those that are produced by the forecasting models selected in Sections 3.3.2.1 and 3.3.2.2. As an illustration, their forecasting performances for wind speed and wind direction at weather stations 2, 4 and 6 are shown in Fig. 3-19 where WV-AR(6) represents an AR(6) process based WV forecasting model.
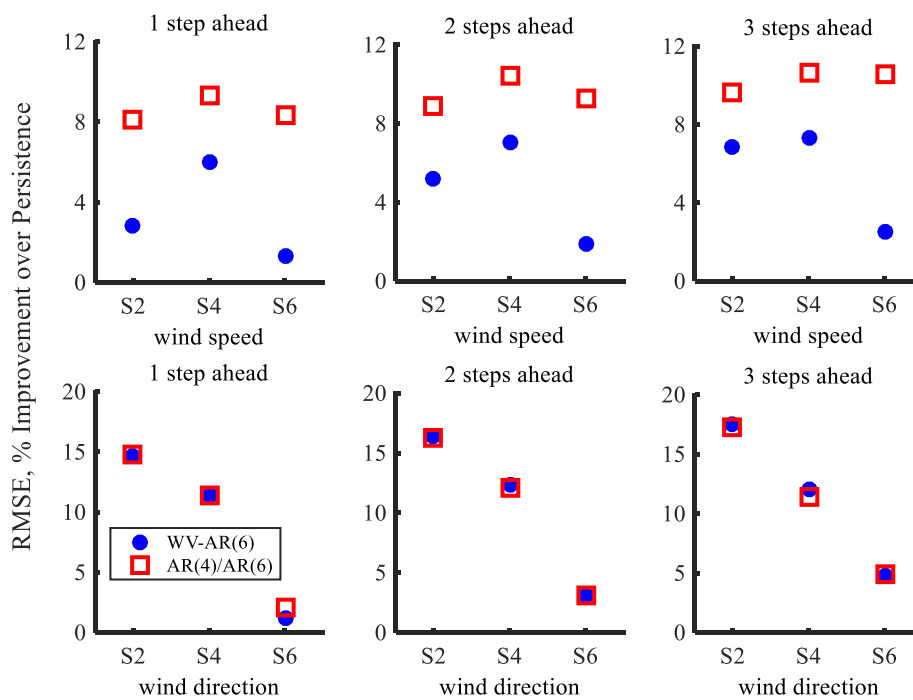
Fig. 3-19. Improvement over persistence in RMSE of wind speed and wind direction forecasts for up to 3 steps ahead for WV-AR(6) models, AR(4) and AR(6) models at stations 2, 4 and 6

For wind speed forecasting, the AR(4) models that take account of wind speeds only are shown to give greater improvement over persistence than the WV-AR(6) models which decompose wind speeds with respect to their accompanying wind directions in the Cartesian coordinates. This may be because the auto-regressive parameters in the WV-AR(6) models are determined to minimise the sum of squares of errors for each component separately while the AR(4) models focus on the total wind speed directly.

89

Furthermore, the wind speed time series has high autocorrelation coefficients at time lags up to 30 minutes. After decomposing wind speeds into the easterly and northerly components, autocorrelation coefficients for the time series of each component and correlation coefficients between them are reduced. For example, the autocorrelation coefficient of the original 10-minute average wind speed time series within 45 days from 01/02/2013 to 17/03/2013 at weather station 2 was equal to 0.9 at the time lag of 10 minutes while the corresponding autocorrelation coefficients for the time series of two components were 0.64 and 0.8 respectively and the correlation coefficient between two components was only -0.26.

For wind direction forecasting, the WV-AR(6) models are shown to perform similarly to the AR(4) and AR(6) models, with a slight improvement less than 1% in certain cases. The experimental results suggest that, in the work conducted here, the wind vector forecasting model that estimates wind speed and direction forecasts from the predictions of wind components does not have a significant enhancement over the use of two individual AR forecasting models to predict wind speed and wind direction separately.

3.3.3. Solar radiation forecasting

A number of methods for solar radiation forecasting have been detailed in [112, 113]. According to different forecast horizons, solar radiation forecasting approaches can be basically categorized as:

- time series forecasting models for 5 minutes to 6 hours ahead;
- satellite images (e.g. cloudiness and cloud motion vectors) based forecasting model for 30 minutes to 6 hours ahead;
- numerical weather predictions for 6 hours onwards;
- hybrid models for adjustable time scales.

Although the short-term forecast accuracy of solar radiation may be largely influenced by cloud transients [114], a time series forecasting model is preferred here

considering the available data in this research. In Huang's work [113], a persistence forecasting model and an auto-regressive moving average (ARMA) model were both applied to short-term solar radiation forecasting. It was found that the persistence forecasting model performed well for 1 step (1 hour) ahead only, whereas the ARMA model exceled for a longer forecast horizon, e.g. 5 steps (5 hours) ahead.

In order to reduce the influence of diurnal trends of solar radiation on the determination of a forecasting model's parameters, a local polynomial regression fitting method was used in [114] to model the diurnal cycles of solar radiation. Fourier series has also been employed in [115, 116] to extract temporal trends from historic solar radiation time series, which were then removed to generate the de-trended data with a reasonable order of stationarity. Liu [117] used Fourier series to capture the annual trend of solar radiation and the remaining diurnal trend was modelled by the second-order Chebyshev polynomials. In this section, the AR and VAR processes combined with a Fourier series based de-trending method and a sliding window technique will be developed for point forecasting of solar radiation.

3.3.3.1. AR and VAR model validation procedure

The 2nd order Fourier series is first used to model diurnal trends of solar radiation from historic time series within a 45-day training window, as shown in Fig. 3-20. The diurnal trends fitted by the 2nd order Fourier series are generally higher than the actual values around sunrise and sunset due to zero solar radiation before the sunrise and after the sunset. A feasible solution is to model the diurnal trends between sunrise and sunset only, exclusive of the other time periods at which zero solar radiations are observed. An alternative solution is to extract diurnal trends of solar radiation by using a higher-order Fourier series [118]. Fig. 3-21 shows that the diurnal trends fitted by the 3rd order Fourier series are much closer to the actual values than those that are modelled by the 2nd order Fourier series, especially around sunrise and sunset.
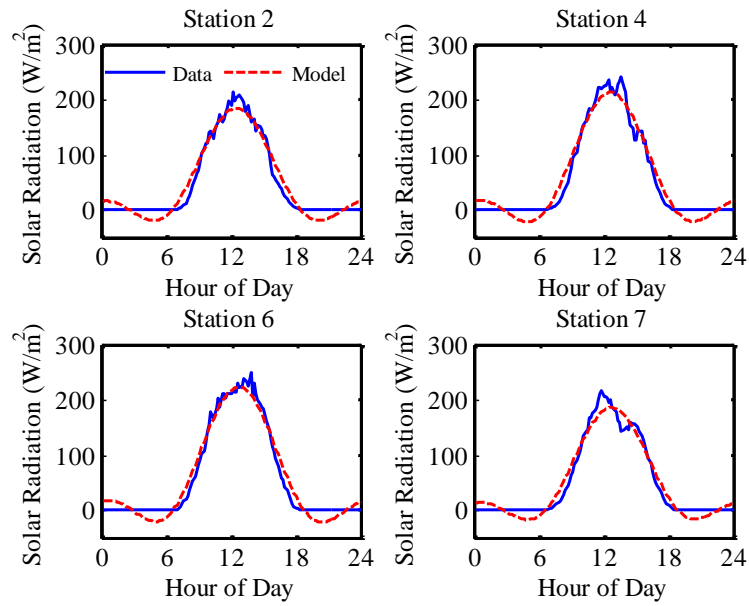
Fig. 3-20. Diurnal trends modelled from solar radiation observations from 00:00 on 01/02/2013 to 23:50 on 17/03/2013 based on the 2nd order Fourier series at stations 2, 4, 6 and 7
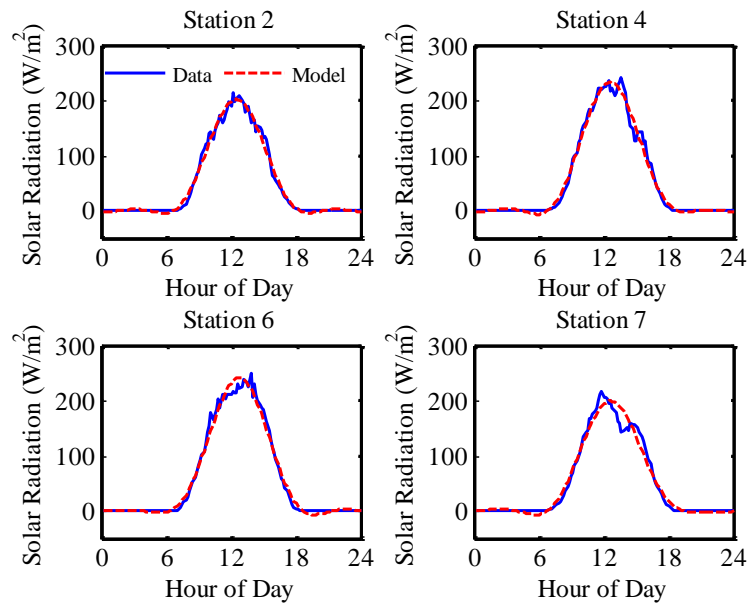
Fig. 3-21. Diurnal trends modelled from solar radiation observations from 00:00 on 01/02/2013 to 23:50 on 17/03/2013 based on the 3rd order Fourier series at stations 2, 4, 6 and 7

Due to solar radiations being zero during the night, the correlations between the de-trended data during the daytime are only considered for solar radiation forecasting. The parameters of AR and VAR models are determined to minimise the sum of squares of differences between the residuals and their expected values during the

daytime over a training window. The solar radiation forecast is then calculated as a sum of the fitted diurnal trend and the de-trended data predicted by an AR or VAR model.

In order to determine the training window lengths, forecast accuracies of solar radiation for up to 3 steps (half hour) ahead during the daytime produced by AR(2) and VAR(2) models with varying window length are assessed with persistence forecasting being adopted as a benchmark, as shown in Fig. 3-22 where the RMSE of persistence forecasts for each time step ahead is $72.235W/m^2$, $88.193W/m^2$ and $93.808W/m^2$ respectively.
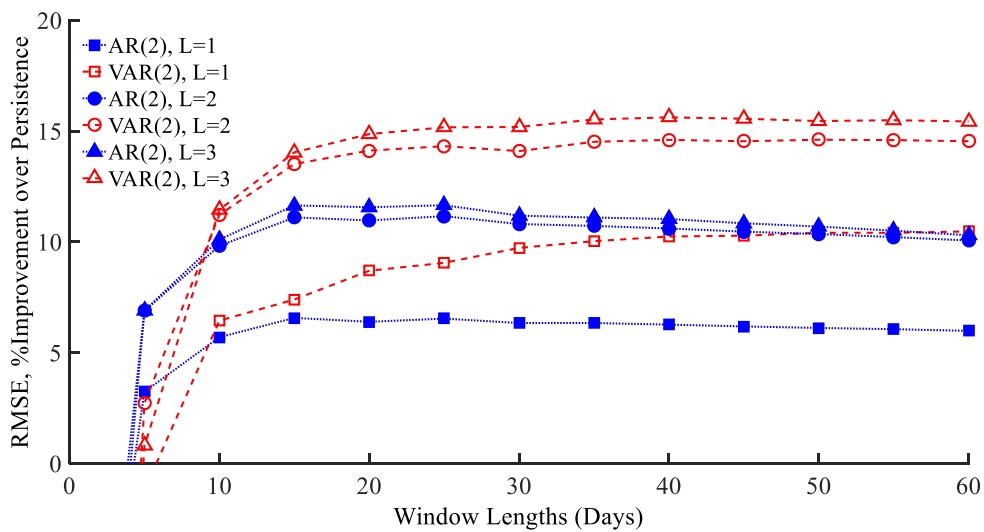
Fig. 3-22. Improvement over persistence in RMSE of solar radiation forecasts for $L = 1, 2, 3$ steps ahead for AR(2) and VAR(2) models with varying training window length at station 2

The experimental results suggest that 25 and 45 days should be selected for AR and VAR models respectively among a range of effective training window lengths since these selected lengths are found to work well for all stations. In order to determine the models' orders, the solar radiation forecasts produced by AR and VAR models of different orders are compared with persistence forecasts, as shown in Fig. 3-23. Performing better than the AR models, the VAR(1) models are employed here to forecast solar radiations for up to 3 steps (half hour) ahead due to insignificant improvement using higher orders.
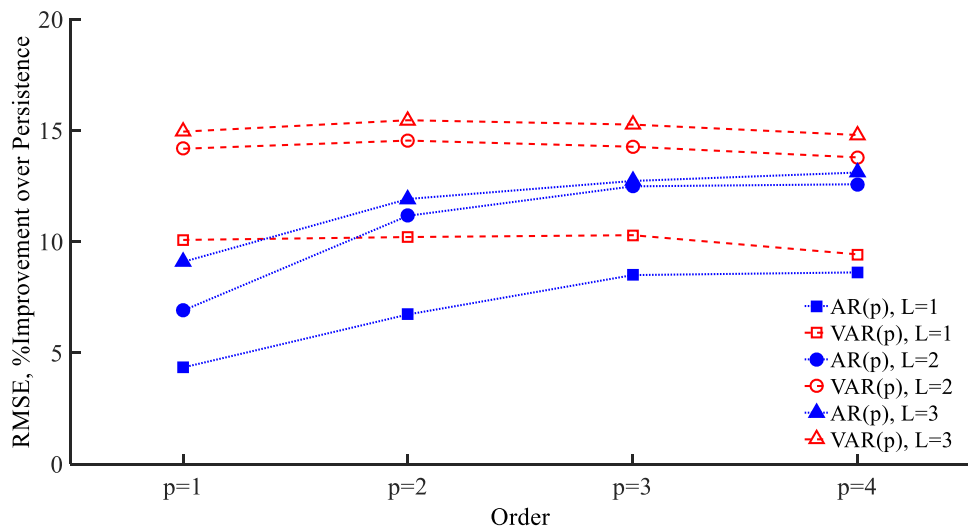
Fig. 3-23. Improvement over persistence in RMSE of solar radiation forecasts for $L = 1, 2, 3$ steps ahead for AR and VAR models of different orders at station 2

3.3.4. Summary of auto-regressive models applied to point forecasting

Based on the experimental results and associated analysis described in previous sections, the AR and VAR forecasting models employed here for different weather variables and forecast horizons are summarised in Table 3-1. The Fourier coefficients and auto-regressive parameters in the forecasting models are daily updated.

Table 3-1. Types of the forecasting models used for different weather parameters and forecast horizons

	Air temperature	Wind speed	Wind direction	Solar radiation
1 step ahead	VAR(2) – 40 days	AR(4) – 45 days	AR(4) – 45 days	VAR(1) – 45 days
2 steps ahead	VAR(2) – 40 days	AR(4) – 45 days	AR(6) – 45 days	VAR(1) – 45 days
3 steps ahead	VAR(2) – 40 days	AR(4) – 45 days	AR(6) – 45 days	VAR(1) – 45 days

The RMSEs of point forecasts for up to 3 steps (half hour) ahead for the selected models and persistence forecasting model are evaluated for each weather variable at all stations, as listed in Tables 3-2, 3-3, 3-4 and 3-5. Their improvements over persistence are shown in Fig. 3-24. The AR and VAR forecasting models are mostly shown to provide distinct improvement over persistence with the forecast horizon going further, especially for air temperature and solar radiation forecasting. The

insignificant improvement over persistence in some particular cases, e.g. wind direction forecasting at station 8, may be due to its RMSEs of persistence forecasts being sufficiently small, meaning that the use of an advanced forecasting model can lead to a slight improvement in forecast accuracy only in such cases. The selected point forecasting models will be used to model the centres of predictive distributions for each weather variable in next section.

Table 3-2. RMSEs (℃) of air temperature forecasts for up to 3 steps ahead estimated by the selected VAR(2) forecasting models and the persistence forecasting models for all weather stations.

Station	Persistence Forecasting			Selected Forecasting Model		
Index	1-step-ahead	2-step-ahead	3-step-ahead	1-step-ahead	2-step-ahead	3-step-ahead
WS1	0.2159	0.3373	0.4359	0.2057	0.3144	0.3977
WS2	0.2118	0.3489	0.4616	0.1892	0.3035	0.3884
WS3	0.2815	0.4386	0.5617	0.2659	0.4048	0.5036
WS4	0.1865	0.3057	0.4068	0.1687	0.2690	0.3480
WS5	0.1873	0.2866	0.3601	0.1797	0.2688	0.3299
WS6	0.1887	0.3094	0.4138	0.1699	0.2686	0.3482
WS7	0.2616	0.3971	0.5105	0.2487	0.3608	0.4478
WS8	0.1669	0.2523	0.3157	0.1621	0.2391	0.2931
WS9	0.1848	0.3012	0.3994	0.1679	0.2652	0.3394

Table 3-3. RMSEs (m/s) of wind speed forecasts for up to 3 steps ahead estimated by the selected AR(4) forecasting models and the persistence forecasting models for all weather stations.

Station	Persistence Forecasting			Selected Forecasting Model		
Index	1-step-ahead	2-step-ahead	3-step-ahead	1-step-ahead	2-step-ahead	3-step-ahead
WS1	0.6095	0.7080	0.7829	0.5630	0.6514	0.7142
WS2	0.4125	0.4806	0.5295	0.3808	0.4397	0.4802
WS3	0.5786	0.6471	0.6859	0.5162	0.5707	0.6062
WS4	0.4766	0.5575	0.6000	0.4394	0.5091	0.5509
WS5	0.6380	0.7621	0.8318	0.5981	0.7054	0.7696
WS6	0.5032	0.5865	0.6442	0.4636	0.5345	0.5805
WS7	0.3578	0.4316	0.5001	0.3365	0.4094	0.4765
WS8	0.6191	0.7418	0.8335	0.6062	0.7250	0.8106
WS9	0.4852	0.5670	0.6139	0.4492	0.5188	0.5618

Table 3-4. RMSEs (radians) of wind direction forecasts for up to 3 steps ahead estimated by the selected AR forecasting models and the persistence forecasting models for all weather stations.

Station	Persistence Forecasting			Selected Forecasting Model		
Index	1-step-ahead	2-step-ahead	3-step-ahead	1-step-ahead	2-step-ahead	3-step-ahead
WS1	0.6613	0.7439	0.7753	0.6221	0.6846	0.7150
WS2	0.7950	0.8411	0.8749	0.6794	0.7051	0.7211
WS3	0.7776	0.8135	0.8398	0.6888	0.7129	0.7337
WS4	0.6480	0.6869	0.7126	0.5803	0.6115	0.6378
WS5	0.6097	0.6705	0.7046	0.5807	0.6170	0.6462
WS6	0.4692	0.5649	0.6180	0.4583	0.5456	0.5869
WS7	0.2978	0.3774	0.4485	0.2992	0.3849	0.4581
WS8	0.3651	0.4257	0.4597	0.3630	0.4224	0.4571
WS9	0.4374	0.5112	0.5517	0.4214	0.4902	0.5337

Table 3-5. RMSEs (W/m^2) of solar radiation forecasts for up to 3 steps ahead estimated by the selected VAR(1) forecasting models and the persistence forecasting models for all weather stations.

Station	Persistence Forecasting			Selected Forecasting Model		
Index	1-step-ahead	2-step-ahead	3-step-ahead	1-step-ahead	2-step-ahead	3-step-ahead
WS1	66.6860	80.2963	88.4812	62.1556	71.6979	77.4574
WS2	65.8288	79.8972	85.6799	59.2281	69.4389	73.1703
WS3	68.5600	82.1641	86.1539	60.7509	68.5204	71.3597
WS4	65.4434	79.3437	90.0054	58.7159	67.7287	73.2744
WS5	71.7106	89.0890	95.6463	62.8960	73.3579	77.3509
WS6	69.9859	85.2411	94.0595	62.4857	72.2760	76.8391
WS7	28.9470	43.2171	56.7475	27.9074	39.6308	49.4930
WS8	54.2907	67.6353	75.3186	48.8133	56.9653	61.6906
WS9	73.1843	84.5242	91.6000	64.3684	71.2387	75.6061
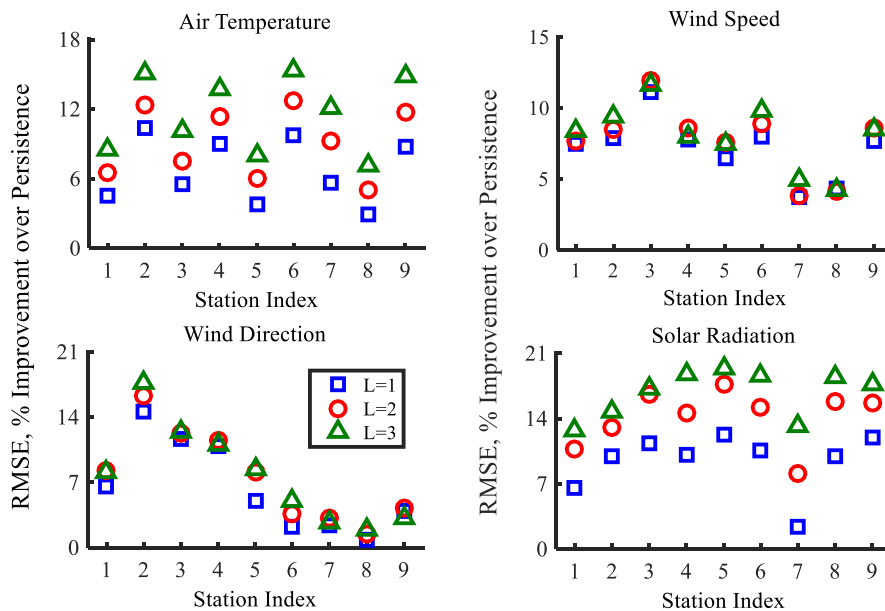
Fig. 3-24. Improvement over persistence in RMSE of weather forecasts for $L = 1, 2, 3$ steps ahead for the selected AR and VAR forecasting models at all weather stations

3.3.5. Effects of forecast errors of individual weather variables on DLR

In order to assess the effect of the performance of the AR or VAR forecasting model for each individual weather variable on the forecast accuracy of weather-based DLRs, 3-step-ahead steady-state DLR forecasts at two particular spans, i.e. CQ34-CQ35 and AC102-AC101B in close proximity to weather stations 4 and 6, are calculated from forecasts of an individual weather variable and observations of other variables based on a thermal model of the conductors [3]. The two spans comprise 'Lynx' ACSR $175mm^2$ and 'Poplar' AAAC $200mm^2$ conductors with maximum allowable conductor temperatures of 50℃ and 75℃ which are reduced to 45℃ and 70℃ respectively for reasons of conservatism [10]. This is because the weather-based model that directly estimates DLRs from weather data may suffer from the difference between the wind conditions recorded at a weather station and those actually experienced by the conductor. Furthermore, values of the conductor's emissivity and absorptivity coefficients that determine rates of radiation heat loss and solar heat gain respectively are usually not very accurate. The technical parameters describing the characteristics of 'Lynx' and 'Poplar' conductors are listed in Table 3-6.

Table 3-6. Characteristics of 'Lynx' ACSR 175mm² and 'Poplar' AAAC 200mm² conductors.

Conductor Characteristics	ACSR 'Lynx'	AAAC 'Poplar'
Conductor diameter (mm)	19.53	20.09
Emissivity (-) / Solar absorptivity (-)	0.6 / 0.5	0.9 / 0.9
Low/high conductor temperature for which ac resistance is specified (℃)	20 / 45	20 / 70
Conductor ac resistance at low/high conductor temperature (Ω/km)	0.1583 / 0.1740	0.1404 / 0.1600
Conductor elevation above sea level (m)	16.7	36.6
Conductor orientation (degree counter-clockwise rotation from East)	35.4525	167.0054
Reduced maximum allowable conductor temperature (℃)	45	70
Static line rating for Winter/Spring or Autumn/Summer (A)	485 / 450 / 389	607 / 581 / 533

Tables 3-7 and 3-8 compare RMSEs of steady-state DLR forecasts for 3 steps ahead at CQ34-CQ35 and AC102-AC101B that are affected by the forecast errors of each individual weather variable at stations 4 and 6 respectively. The effects of forecast errors of each individual weather variable estimated by the AR or VAR models listed in Table 3-1 and persistence forecasting models are both examined.

Table 3-7: RMSEs of weather forecasts of each individual variable at station 4 and their corresponding steady-state DLR forecasts at span CQ34-CQ35 for 3 steps ahead along with the AR/VAR forecasting models' improvements over persistence.

Weather Variable of Interest	RMSE of Weather Forecasts		Imp. over Persistence	RMSE of DLR Forecast (A)		Imp. over Persistence
	AR/VAR	Persistence		AR/VAR	Persistence	
T_a (℃)	0.3480	0.4068	14.45%	2.7027	3.0805	12.26%
w_s (m/s)	0.5509	0.6000	8.18%	46.7385	52.1028	10.30%
w_d ($radians$)	0.6378	0.7126	10.48%	45.7737	48.3927	5.41%
s_r (W/m^2)	73.2744	90.0054	18.59%	3.3683	4.1498	18.83%

Table 3-8: RMSEs of weather forecasts of each individual variable at weather station 6 and their corresponding steady-state DLR forecasts at span AC102-AC101B for 3 steps ahead along with the AR/VAR forecasting models' improvements over persistence.

Weather Variable of Interest	RMSE of Weather Forecasts		Imp. over Persistence	RMSE of DLR Forecast (A)		Imp. over Persistence
	AR/VAR	Persistence		AR/VAR	Persistence	
T_a (℃)	0.3482	0.4138	15.85%	2.3955	2.7686	13.48%
w_s (m/s)	0.5805	0.6442	9.89%	60.1287	65.7099	8.49%
w_d ($radians$)	0.5869	0.6180	5.03%	66.1046	67.3369	1.83%
s_r (W/m^2)	76.8391	94.0595	18.31%	4.7942	5.8826	18.50%

Since it is the wind attack angle (or the angle of incidence) between wind direction and line orientation that determines the convection heat loss rate, wind direction forecasts for 3 steps ahead estimated by the AR(6) model and the persistence method are converted to attack angles which have RMSEs (radians) of 0.3740 and 0.3852 respectively for span CQ34-CQ35. For span AC102-AC101B, RMSEs (radians) of the attack angle forecasts for the two methods are 0.3218 and 0.3355 respectively. The improvements over persistence in RMSEs of attack angle forecasts for the AR(6) models at two spans are 2.93% and 4.08% respectively, which are smaller than that for wind direction forecasting. This may be one of the reasons causing the AR(6) models' improvements over persistence in RMSEs of wind direction forecasts to be higher than those for their corresponding steady-state rating forecasts, as shown in Tables 3-7 and 3-8.

Tables 3-7 and 3-8 indicate that the VAR model gives an improvement greater than 10% over persistence in RMSEs of steady-state DLR forecasts that include forecast errors of T_a or s_r. However, T_a or s_r forecasts based DLRs at the two spans have smaller RMSEs than w_s or w_d forecasts based DLRs. Fig. 3-25 shows percentage errors of DLR forecasts for 3 steps ahead at the two spans that are caused by forecast errors of each individual weather variable. It is shown that forecast errors of T_a or s_r generally lead to percentage errors of DLR forecasts that are much smaller than those for w_s or w_d in this research. As was noted in Section 1.2.3.1, a large rise of the convection heat loss rate above the solar heat gain rate due to an increment in w_s or conductor temperature would reduce the impact of the change of s_r on conductor temperature. Therefore, forecast errors of s_r are shown to have a slight effect on the forecast accuracy of steady-state DLRs evaluated at a maximum allowable conductor temperature T_{cmax}.
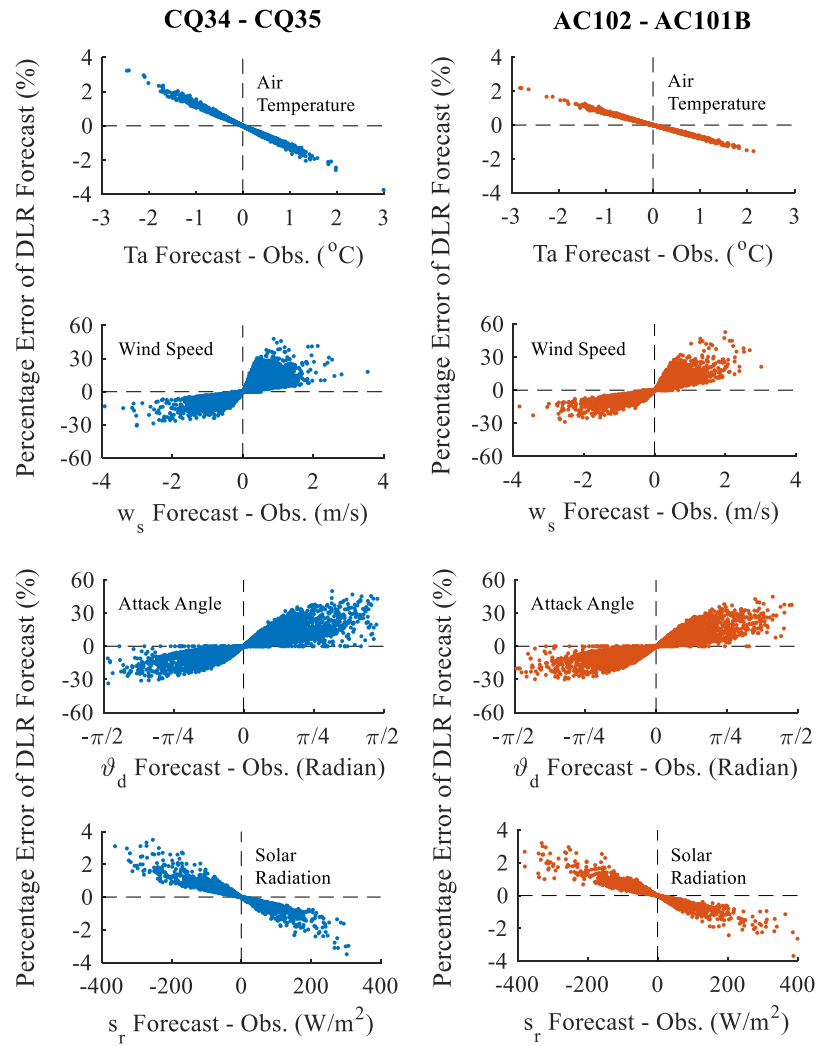
Fig. 3-25: Percentage errors (%) of steady-state DLR forecasts for 3 steps ahead at different spans estimated from forecasts of each individual weather variable.

As was noted in Sections 2.1.4.2 and 2.1.4.3, the convection Q_c and radiation Q_r heat loss rates for steady-state DLR calculation are both dependent on the difference between T_{cmax} and T_a. The DLR demonstration project by Scottish Power Energy Networks [10] reported that T_a measured at nine weather stations over a full year from 24th September 2012 to 23rd September 2013 ranged from $-6.1°C$ to $30.3°C$. Assuming T_a to be forecast with errors of $\pm 3°C$ (i.e. the maximum magnitude of T_a forecast error as shown in Fig. 3-25), the ratio of the forecast Q_r to the actual Q_r is calculated by equation (2-20) based on T_a that ranges from $-10°C$ to $30°C$ combined with T_{cmax} for each span, as shown in Fig. 3-26. The forecast error of T_a

shows a larger impact on Q_r at a higher T_a for span CQ34-CQ35 that has a smaller T_{cmax}, i.e. a smaller difference between T_a and T_{cmax}.
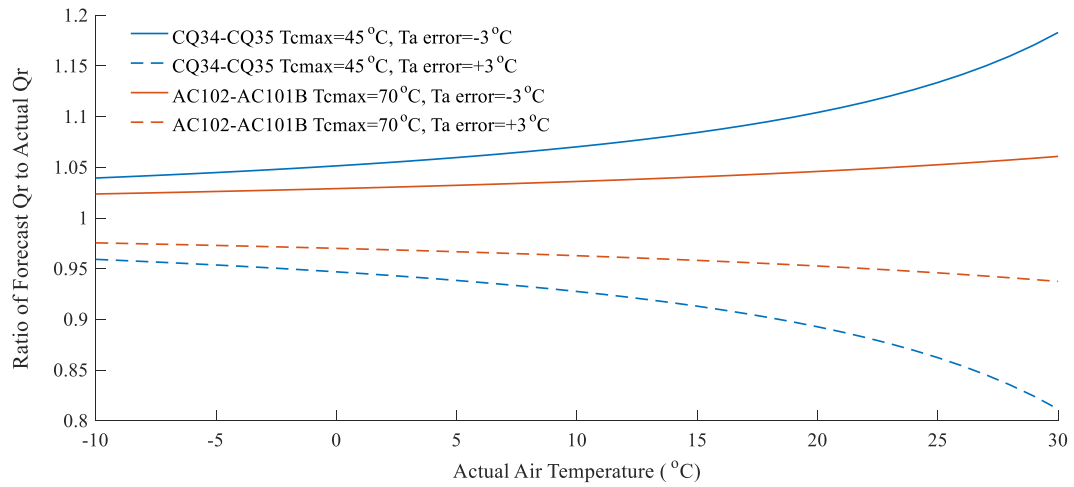
Fig. 3-26: Ratios of the forecast Q_r to the actual Q_r evaluated at T_a ranging from $-10°C$ to $30°C$ combined with T_{cmax} for different spans based on T_a forecast error equal to $\pm3°C$.

Since Q_c evaluated at T_{cmax} is found to be determined by the forced convection heat loss rate Q_{cf} in greater than 96.33% and 98.03% of cases for CQ34-CQ35 and AC102-AC101B respectively in this research, the ratio of the forecast Q_{cf} to the actual Q_{cf} is estimated for the two spans based on their T_{cmax} and T_a that ranges from $-10°C$ to $30°C$ with a forecast error of $\pm3°C$. It may be noted that the ratios for Q_{cf1} and Q_{cf2} calculated by equations (2-14) and (2-15) are similar since an error of $\pm3°C$ in T_a forecasts has a slight impact on air properties (i.e. the density, viscosity and thermal conductivity coefficient of air) which are determined by equations (2-17), (2-18) and (2-19). Therefore, the ratios of the forecasts to the actual values for Q_{cf2} that have slightly higher magnitudes are presented here as shown in Fig. 3-27. The forecast error of T_a is shown to have a larger influence on Q_{cf2} at a higher T_a for the span CQ34-CQ35 which has a lower T_{cmax}, i.e. a smaller arise of T_{cmax} above T_a.
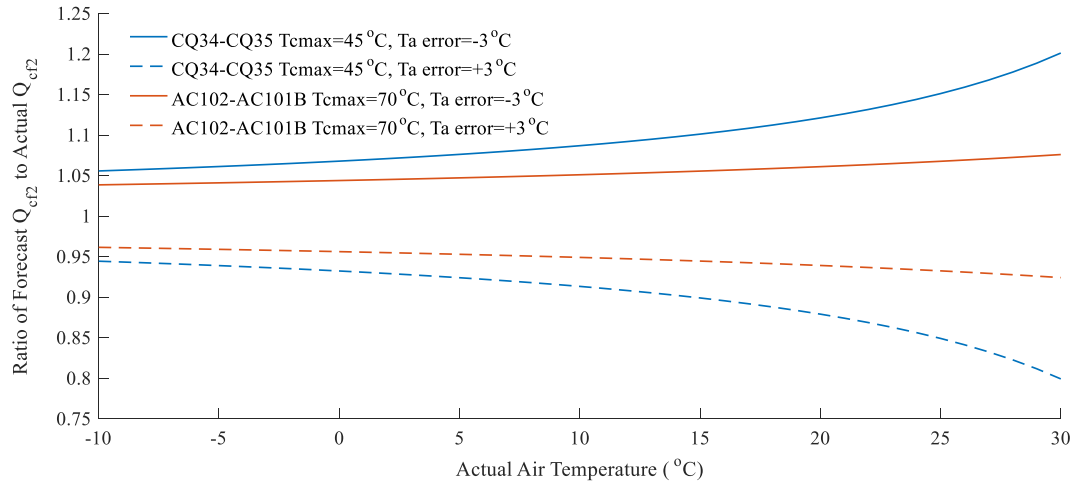
Fig. 3-27: Ratios of the forecast Q_{cf2} to the actual Q_{cf2} evaluated at T_a ranging from $-10°C$ to $30°C$ combined with T_{cmax} for different spans based on T_a forecast error equal to $\pm3°C$.

Figs. 3-26 and 3-27 show that a forecast error of $\pm3°C$ for $T_a = 30°C$ would lead to a significant underestimation or overestimation in Q_r and Q_{cf} by around 20% for span CQ34-CQ35. This will cause the steady-state DLR to be underestimated or overestimated by about 10% when there is no solar radiation. Given a non-zero solar radiation, the forecast error of the steady-state DLR would then be less than 10%. Since T_a recorded for span CQ34-CQ35 over the period evaluated in this research (January, February and March in 2012) was under 13.5°C, a forecast error of $\pm3°C$ for T_a would cause Q_r and Q_{cf} to be underestimated or overestimated by around 10%. This means that the steady-state DLR forecast error could reach less than 5% of the actual rating, which is mostly less significant than the forecast error induced by wind conditions, as shown in Fig. 3-25. Therefore, wind conditions are generally the dominant factors affecting the forecast accuracy of steady-state DLRs.

3.4. Results and Model Validation of Probabilistic Forecasting

As was noted in Section 3.2.5, the 'accuracy' of probabilistic forecasts can be evaluated through checking their calibration which is the consistency between the predictive distribution and the actual value. The calibration of probabilistic forecasts can be examined by the histogram of probability integral transform (PIT). For fully

calibrated probabilistic forecasts, the percentage of the actual value being lower than the nth percentile just equals $n\%$ for each percentile, i.e. a uniform PIT histogram.

A sharper predictive probability distribution (i.e. a smaller predictive spread or a higher concentration parameter) is desired under the constraint of calibration. The sharpness of a predictive probability distribution can be indicated by the average width of central prediction intervals (CPIs), e.g. the average width of 50% CPIs between the 25th and 75th percentiles. In addition to the calibration and sharpness, the performance of a probabilistic forecasting model can be assessed by the continuous ranked probability score (CRPS) which is a summary metric representing the average difference between the predictive distribution and the actual value. Small values are sought for the average width of CPIs and the CRPS value.

Based on the point forecasting models validated in Section 3.3 which are employed to model the predictive centres of weather variables, the probabilistic forecasting models are developed here by modelling the conditional heteroscedasticity of the predictive distribution as a linear function of recent changes in the de-trended data within one hour for air temperature and wind speed or concentration of recent wind direction observations within two hours. To analyse the advantage of modelling the predictive spread as time dependent (i.e. the conditional heteroscedasticity), the homoscedastic model is additionally constructed which assumes a constant predictive spread or concentration parameter that is updated once a day.

In this section, the CRPS values, calibration and sharpness are assessed for different probabilistic forecasting models. The models having the best performance are selected to generate predictive distributions for each weather parameter.

3.4.1. Assessments of probabilistic weather forecasting

The parameters in the auto-regressive (AR) and vector auto-regressive (VAR) models and the non-negative coefficients representing the predictive spread or concentration parameter are determined to minimise the average value of CRPS based on historic

time series within a training window. Probabilistic 1-step-ahead weather forecasts produced by the four models, homoscedastic AR(4)-H and VAR(2)-H models and conditionally heteroscedastic AR(4)-CH and VAR(2)-CH models, are assessed. The average CRPS values and average widths of 50% CPIs of probabilistic forecasts for each weather parameter at stations 2, 4 and 6 are listed in Table 3-9 where the smallest values among the four models are highlighted in red.

Table 3-9. CRPS and average widths of 50% CPIs of probabilistic 1-step-ahead forecasts produced by four probabilistic forecasting models for air temperature T_a, wind speed w_s and wind direction w_d at stations 2, 4 and 6.

		Station No.	AR(4)-H	VAR(2)-H	AR(4)-CH	VAR(2)-CH
T_a (℃)	CRPS	2	0.0947	0.0928	0.0922	**0.0904**
		4	0.0839	0.0829	0.0811	**0.0803**
		6	0.0833	0.0820	0.0800	**0.0790**
	50%CPIs	2	0.1895	**0.1855**	0.1979	0.1940
		4	0.1592	**0.1557**	0.1692	0.1660
		6	0.1533	**0.1505**	0.1655	0.1628
w_s (m/s)	CRPS	2	0.2025	0.2042	**0.1972**	0.1988
		4	0.2341	0.2373	**0.2290**	0.2318
		6	0.2465	0.2475	**0.2392**	0.2402
	50%CPIs	2	0.4617	0.4594	**0.4584**	0.4586
		4	**0.5251**	0.5299	0.5290	0.5353
		6	0.4999	**0.4998**	0.5336	0.5436
w_d (radians)	CRPS	2	0.3563	0.3598	**0.3395**	0.3450
		4	0.2812	0.2829	**0.2514**	0.2546
		6	0.1986	0.1977	**0.1882**	0.1886
	50%CPIs	2	**0.7433**	0.7553	0.7600	0.7672
		4	**0.4665**	0.4672	0.5448	0.5451
		6	**0.2965**	0.2966	0.3820	0.3779

The experimental results show that over half of the time the predictive distributions modelled by conditionally heteroscedastic models are more concentrated than the distributions modelled by homoscedastic models. For example, predictive spreads of air temperature for 1 step (10 minutes) ahead determined by the VAR(2)-CH model at station 2 are smaller than those that are estimated by the VAR(2)-H model for about 61.3% of the time. However, due to some extremely dispersive distributions for conditionally heteroscedastic models, most of the average widths of 50% CPIs modelled by the homoscedastic models are smaller on average, at the cost of losing a certain calibration. This can be inspected from their PIT histograms, as shown in Figs. 3-28 – 3-30 where the relative frequency of 0.1 per 10 percentiles for a uniform PIT histogram which reveals probabilistic forecasts to be fully calibrated is denoted by a black dashed line. In addition, the probabilistic forecasts estimated by conditionally heteroscedastic models are generally shown to have a smaller CRPS value than those for homoscedastic models.
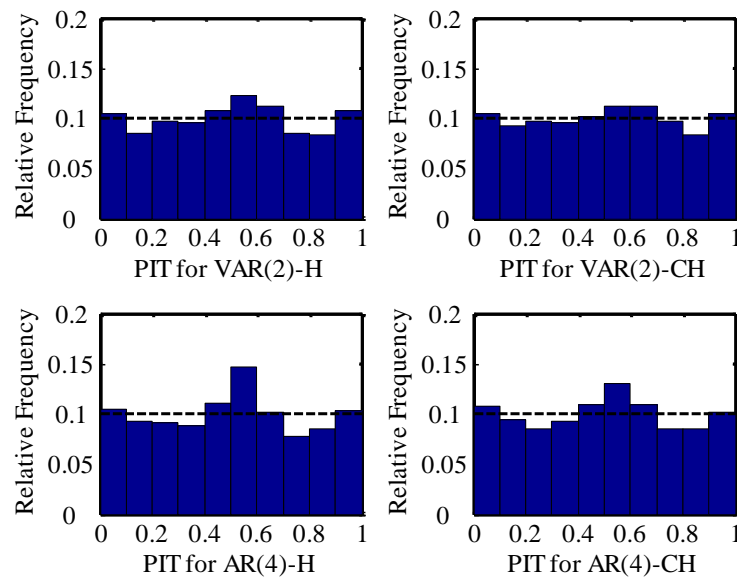
Fig. 3-28. PIT histograms for probabilistic 1-step-ahead air temperature forecasts produced by four probabilistic models at station 2
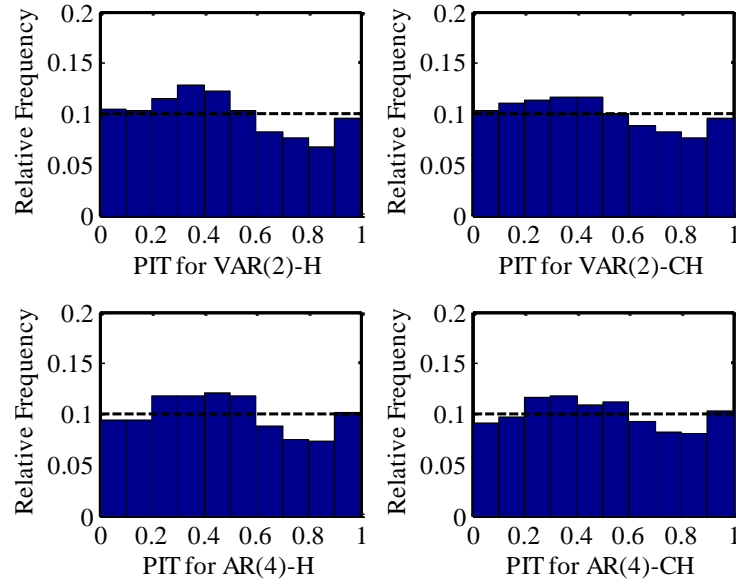
Fig. 3-29. PIT histograms for probabilistic 1-step-ahead wind speed forecasts produced by four probabilistic models at station 2
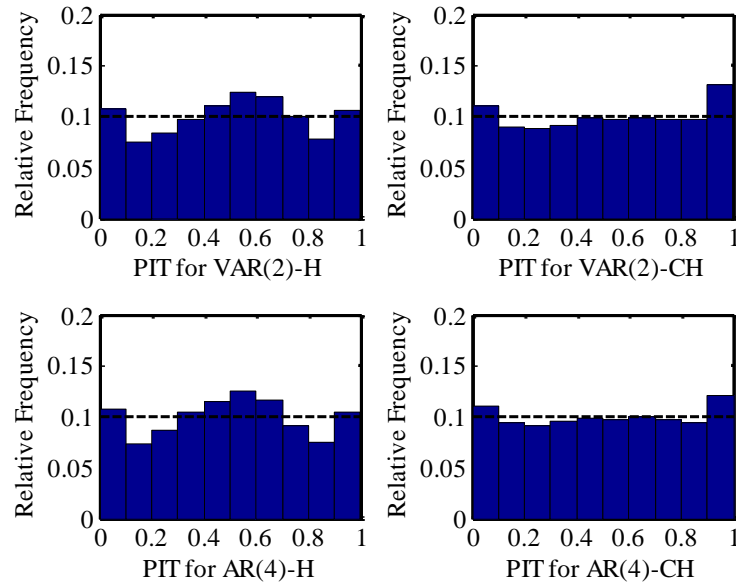
Fig. 3-30. PIT histograms for probabilistic 1-step-ahead wind direction forecasts produced by four probabilistic models at station 2

The PIT histograms in Figs. 3-28 – 3-30 demonstrate that the conditionally heteroscedastic models generally show a better calibration than their respective homoscedastic models. The variance of relative frequency at each percentile can be used as an indicator to assess the distribution of a PIT histogram and thus the

calibration of probabilistic forecasts. A smaller variance indicates that the PIT histogram is closer to a uniform distribution, i.e. the probabilistic forecasts having a better calibration. Fig. 3-31 shows that the variance of relative frequency at each predictive percentile for 3 steps ahead for the conditionally heteroscedastic (CH) models is smaller than that for their respective homoscedastic (H) models for each weather parameter at all stations.
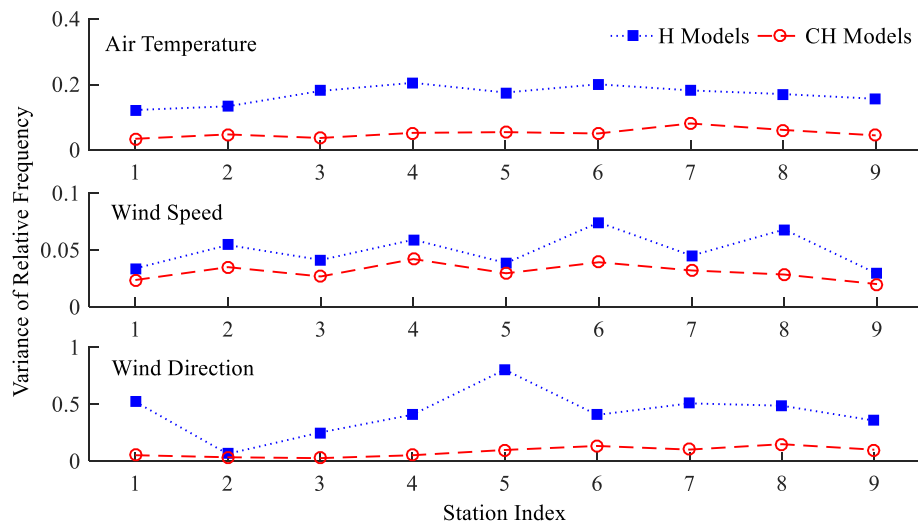
Fig. 3-31. Variances of relative frequency at each predictive percentiles for 3 steps (half hour) ahead estimated by the homoscedastic (H) models and the conditionally heteroscedastic (CH) models for each weather variable

As a summary indicator reflecting both calibration and sharpness of probabilistic forecasts, the average CRPS values of conditionally heteroscedastic models and their respective homoscedastic models are compared for each weather parameter at all weather stations, as shown in Figs. 3-32 – 3-34. The experimental results suggest that the VAR(2)-CH, AR(4)-CH and AR(4)-CH models having smaller CRPS values are used to estimate probabilistic 1-step-ahead forecasts for air temperature, wind speed and wind direction respectively. For 2 and 3 steps ahead, the VAR(2)-CH, AR(4)-CH and AR(6)-CH models are selected for each weather parameter.
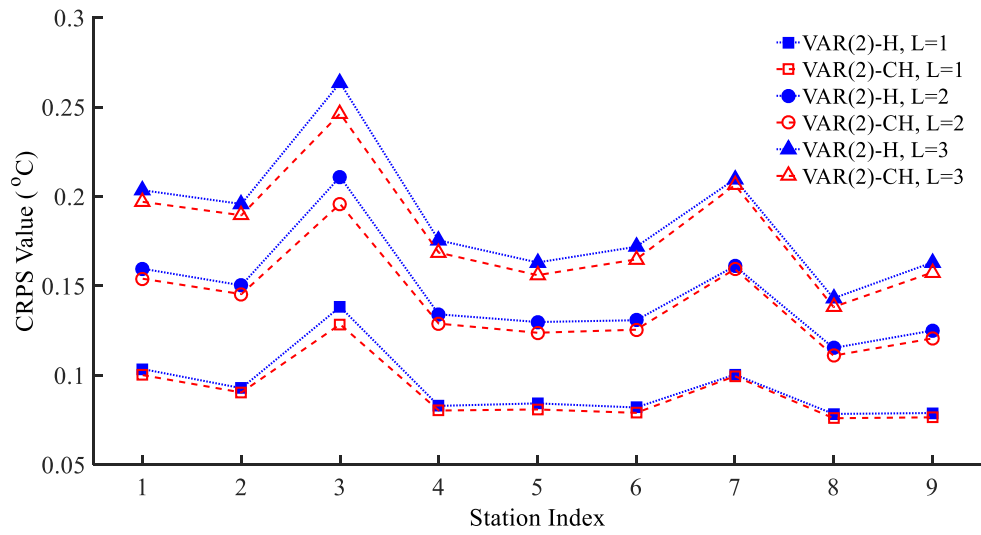
Fig. 3-32. CRPS values (℃) of probabilistic air temperature forecasts for $L = 1, 2, 3$ steps ahead produced by the VAR(2)-CH and VAR(2)-H models
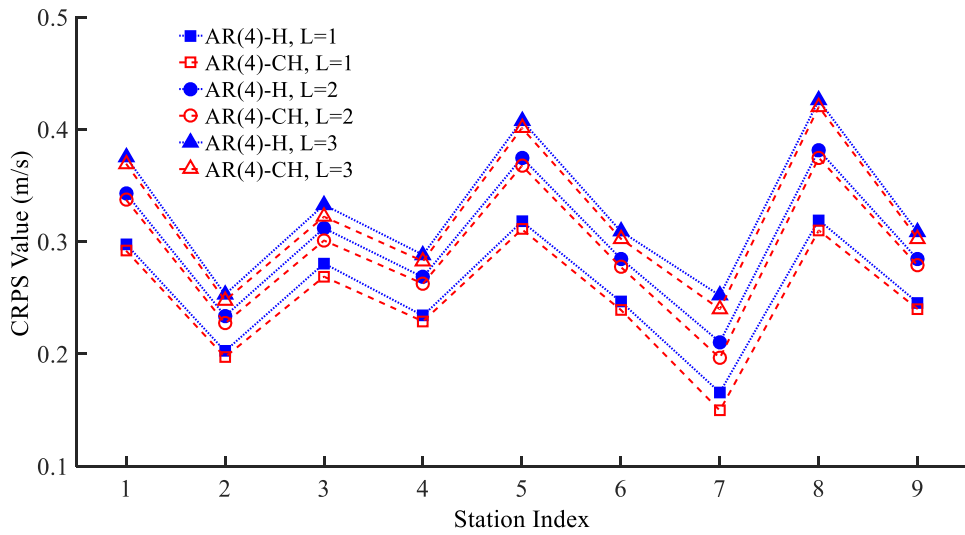
Fig. 3-33. CRPS values (m/s) of probabilistic wind speed forecasts for $L = 1, 2, 3$ steps ahead produced by the AR(4)-CH and AR(4)-H models

109
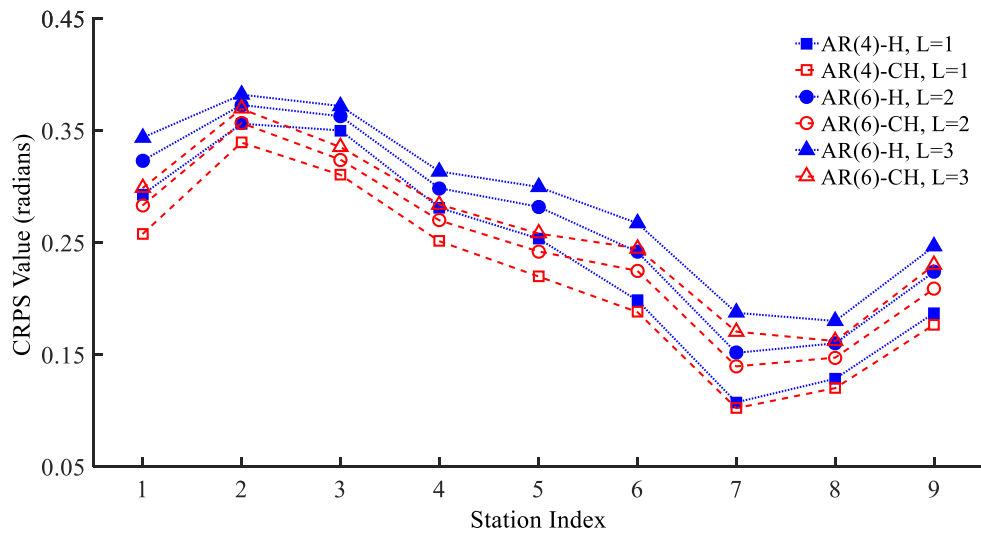
Fig. 3-34. CRPS values (radians) of probabilistic wind direction forecasts for $L = 1, 2, 3$ steps ahead produced by the AR-CH and AR-H models

The 50% and 90% CPIs associated with their 1- and 3-step-ahead predictive centres for wind speed and direction on 27/03/2013 at station 2 are shown in Figs. 3-35 and 3-36 respectively. For probabilistic forecasting of wind speed, the observations locate within the 1-step-ahead and 3-step-ahead 50% CPIs for around 52.9% and 54.8% of the time respectively and within the 90% CPIs for approximately 88.8% and 88.7% of the time respectively. In addition, the expected values of probabilistic wind speed forecasts (equivalent to the point forecasts) for 1 and 3 steps ahead estimated by the AR(4)-CH models having RMSEs of $0.38\,m/s$ and $0.48\,m/s$ respectively give 7.7% and 9.4% improvement over persistence forecasts.

For probabilistic forecasting of wind direction, the observations locate within the 1-step-ahead and 3-step-ahead 50% CPIs for about 48.8% and 46.1% of the time respectively and within the 90% CPIs for around 86.9% and 85.8% of the time respectively. Furthermore, the expected values of probabilistic wind direction forecasts for 1 and 3 steps ahead generated by the AR(4)-CH and AR(6)-CH models have RMSEs of 0.68 radians and 0.72 radians respectively, which give 14.5% and 17.6% improvement over persistence forecasts.

110
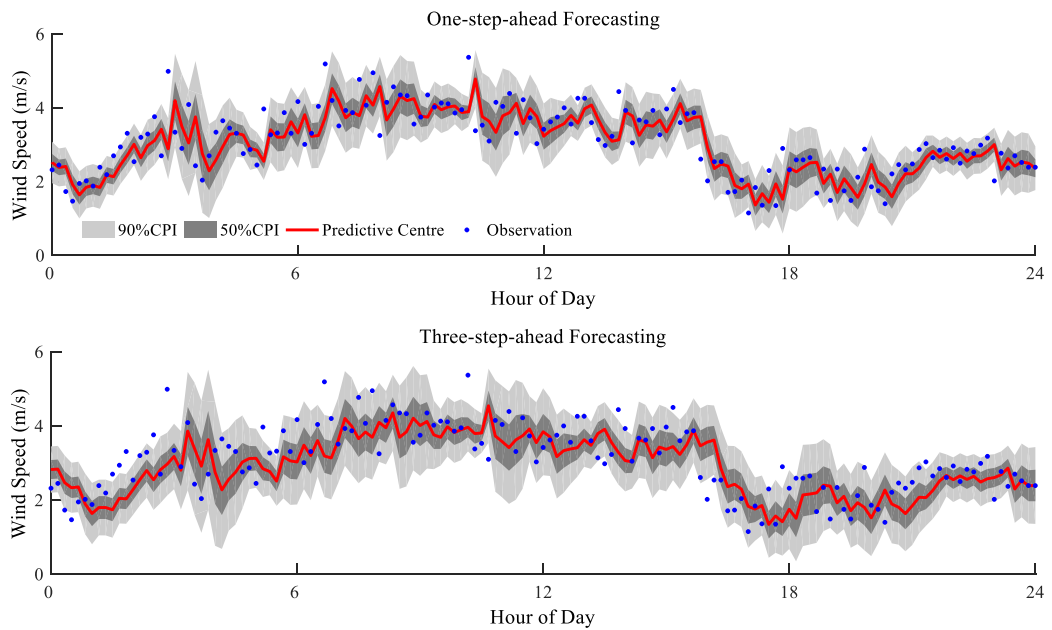
Fig. 3-35. The 50% and 90% CPIs associated with 1-step-ahead and 3-step-ahead predictive centres of wind speed modelled by the AR(4)-CH models on 27/03/2013 at station 2
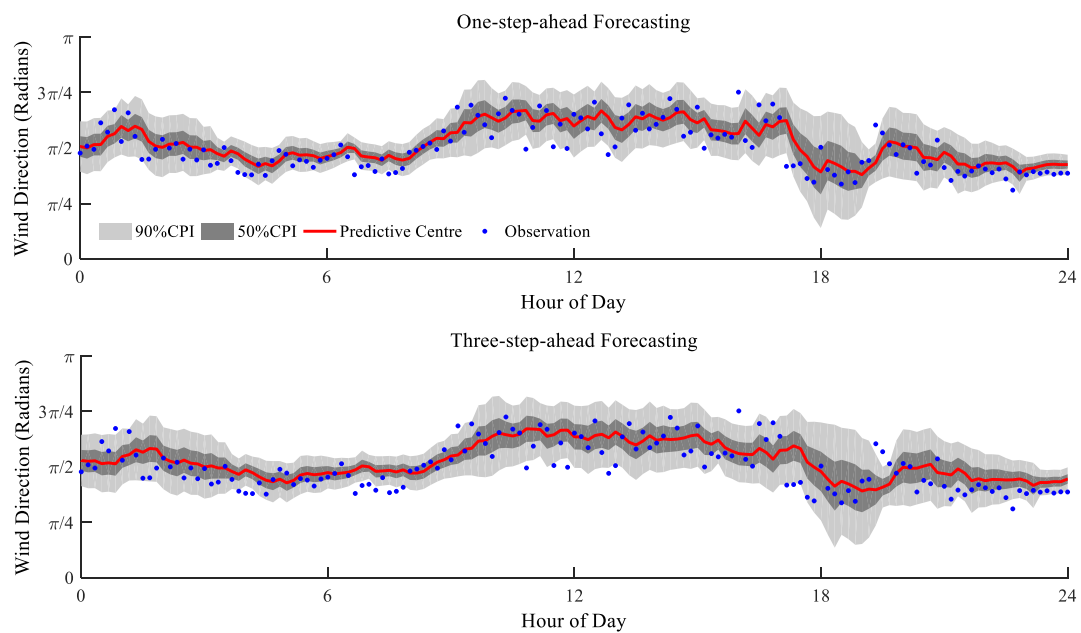
Fig. 3-36. The 50% and 90% CPIs associated with 1-step-ahead and 3-step-ahaed predictive centres of wind direction modelled by the AR(4)-CH and AR(6)-CH models on 27/03/2013 at station 2

It can be found that the predictive distributions for 3 steps (half hour) ahead are less concentrated than the distributions for 1 step (10 minutes) ahead. This is because a satisfactory calibration is to be preserved while the forecast error increases for 3

111

steps ahead. As the time horizon increases, the reduction in the sharpness or concentration of predictive distribution results in an increase in the CRPS value as shown in Figs. 3-32 – 3-34.

3.5. Conclusions

A number of point (or deterministic) and probabilistic forecasting models have been developed for different weather parameters in this chapter by the use of an auto-regressive process that is combined with a technique of minimum continuous ranked probability score (CRPS) estimation. The time series forecasting models have been selected for each weather parameter based on their performances reflected by the root mean square error (RMSE) for point forecasts and the CRPS value for probabilistic forecasts.

The point forecasting models are first determined for each weather parameter for different time horizons since they are the basis on which the probabilistic forecasting models are established. In the main, the point forecast of a weather variable is modelled as a sum of the fitted diurnal trend component and the corresponding de-trended data forecast by an auto-regressive (AR) or vector auto-regressive (VAR) model. The 2nd order Fourier series is used to extract diurnal trends from historic time series within a sliding training window for air temperature, wind speed and the easterly and northerly components of wind direction separately; diurnal trends of solar radiation are fitted by the 3rd order Fourier series which accurately models the variation in solar radiation, especially around sunrise and sunset. The AR and VAR models are then applied to the de-trended data within the training window.

The point forecasts of weather variables for up to 3 steps (half hour) ahead estimated by the AR and VAR models are assessed for different training window lengths and different model orders. Given a sufficiently long training window, the VAR forecasting models are generally shown to perform better than the AR models in a

preliminary test where the model order of 2 is used. There is a trade-off in the selection of training window length between using a longer window to reduce the statistical variability in the estimation of model parameters and using a shorter window to avoid the seasonal variations being excessively smoothed. Amongst a range of effective training window lengths, for AR and VAR models here 40, 45 and 45 days are reasonable choices for air temperature, wind speed and wind direction respectively since they have been found to work well at all weather stations. For solar radiation, 25 and 45 days are selected for AR and VAR models respectively.

Using the selected training window lengths, the VAR models are mostly shown to perform better than the AR models of a same order due to additionally capturing the spatial correlations among the field data. The VAR(2) and VAR(1) models are selected for air temperature and solar radiation respectively since they give better performances than the AR models and insignificant improvements are obtained when using higher orders. For wind speed and wind direction, the AR models of a higher order have fewer auto-regressive parameters and perform similarly to or even better than the VAR models of a lower order. Since having fewer parameters can reduce computation time in the process of minimising CRPS value, the AR(4) models are used to predict wind speeds for up to 3 steps ahead. For wind direction, the AR(4) model is employed for 1-step-ahead forecasting and the AR(6) forecasting models are preferred for 2 and 3 steps ahead in this research. Through an assessment of forecast errors of steady-state ratings at two particular spans in close proximity to weather stations due to the forecast uncertainty of each individual weather variable, wind conditions are found to be the dominant factors that affect the forecast accuracy of steady-state DLRs.

Two approaches to modelling the spreads or concentration parameters of predictive distributions have been compared: a homoscedastic (H) model that assumes a constant predictive spread and a conditionally heteroscedastic (CH) model that estimates the predictive spread as time variable based on recent changes in weather

data. Due to the constantly adjusted predictive spreads, the predictive distributions generated by the CH models are found to be of better calibration and more concentrated in most cases than those that are produced by the H models. However, most of the average widths of central prediction intervals modelled by CH models are larger on average due to some extremely dispersive distributions. The calculated CRPS values demonstrate that the VAR(2)-CH, AR(4)-CH and AR(4)-CH models give the best performance considering the trade-off between calibration and sharpness and should be used to generate probabilistic 1-step-ahead forecasts for air temperature, wind speed and wind direction respectively. For two and three 10-minutes time steps ahead, the VAR(2)-CH, AR(4)-CH and AR(6)-CH models should be employed for each weather parameter respectively in this research. The predictive distributions estimated by the CH forecasting models for air temperature, wind speed and wind direction and point forecasts of solar radiation will be used to generate probabilistic forecasts of DLRs for spans and overhead lines.

4. RANK CORRELATION BASED PAIRING AND SPATIAL INTERPOLATION

4.1. Introduction

The thermal rating of an overhead conductor is influenced by different weather variables in a complex way. It is difficult to directly calculate the probabilistic forecasts of dynamic line rating (DLR) from predictive distributions of weather variables through a thermal model of overhead conductors [3]. For example, the convection heat loss rate of the conductor per unit length is estimated as the largest value of three components that are determined by air temperature, wind speed and wind direction in different ways as defined by equations (2-13) - (2-15). Alternatively, Monte Carlo simulation [119] allows us to model different combinations of weather input variables, as well as their interdependent relationships. It is used to produce a large number of sampled values of steady-state DLR forecasts by evaluating the outputs (ratings) of the thermal model of overhead conductors [3] for inputs of values randomly sampled from the predictive probability distributions of air temperature, wind speed and wind direction modelled by the conditionally heteroscedastic auto-regressive models and point forecasts of solar radiation.

In order to cover a range of possible weather conditions, a sufficiently large number, say $N_{MC} = 10^4$ of weather input variables are randomly sampled from the modelled normal, truncated normal and von Mises distributions, as appropriate to the different variables, through the codes provided in [120, 121, 96]. The numerous random weather input variables can be regarded as being independent of each other since they are randomly and independently sampled from their own predictive distributions. For example, two series consisting of 10^4 random samples that are independently generated from a standard normal distribution typically have a correlation less than 0.01.

Different pairs of weather variables are correlated. A rank correlation based pairing method [122], independent of the type of distribution, is used to pair independently sampled random weather variables so as to create a correlation similar to that calculated from weather observations over recent days. For a single span in proximity to an installed weather station, the uncertainty of DLR forecasts is mainly determined by the distribution of weather prediction errors. The independent or correlated (paired) weather samples at the station are directly applied to the thermal model of the conductors to estimate probabilistic DLR forecasts for the span. For an entire overhead line (OHL), the possible weather predictions for each span are extrapolated from the correlated or independent random samples of the measured weather variables by using suitable spatial interpolation models. The minimum value of the steady-state ratings for all spans within an OHL derived from inferences of weather samples is then applied to the entire OHL in each of 10^4 scenarios.

This chapter describes the application of the rank correlation based pairing method to random weather samples of both different parameters and the same parameters at all stations. In addition, the spatial interpolation methods that were used in previous research [20] are improved here through an investigation into a number of available spatial interpolation methods and a comparison between their performances for each weather variable.

4.2. Methodology

4.2.1. Rank correlation based pairing method [122]

The Spearman's rank correlation coefficient represents the statistical dependence between the rankings of two variables. For linear variables, the Spearman's rank correlation coefficient $rc_{l,l}$ is defined as [75]:

$$rc_{l,l} = 1 - \frac{6 \sum \Delta r_{l,i}{}^2}{N_r(N_r^2 - 1)} \tag{4-1}$$

where N_r is the number of data pairs which have rank differences $\Delta r_{l,i}, i = 1, \ldots, N_r$. The term $rc_{l,l}$ ranges from -1 to $+1$ with $rc_{l,l} = 0$ indicating two independent linear variables, i.e. no correlation, and $rc_{l,l} = \pm 1$ meaning a significant positive/negative correlation between their ranks. The uniform score or circular rank $r_{c,i}$ associated with wind direction $w_{d,i}$ is defined as [123]:

$$r_{c,i} = \frac{2\pi r_{cl,i}}{N_r}, i = 1, \ldots, N_r \tag{4-2}$$

where $r_{cl,i}$ represents the linear rank of $w_{d,i}$ when $w_{d,1}, \ldots, w_{d,N_r}$ are treated as linear data and it is multiplied by $2\pi/N_r$ to obtain the corresponding circular rank $r_{c,i}$. The C-association $Ca^2_{l,c}$ describing the rank relationship between a linear variable of rank $r_{l,i}, i = 1, \ldots, N_r$ and a circular variable of rank $r_{c,i}, i = 1, \ldots, N_r$ is evaluated by [124]:

$$Ca^2_{l,c} = Cr_{N_r} \left(Cr^2_c + Cr^2_s \right) \tag{4-3}$$

where,

$$Cr_c = \qquad Cr_s = \qquad Cr_{N_r} =$$
$$\sum r_{l,i} \cos r_{c,i} \quad \sum r_{l,i} \sin r_{c,i} \quad \begin{cases} 1/[1 + 5\cot^2(\pi/N_r) + 4\cot^4(\pi/N_r)] & N_r \text{ even} \\ 2\sin^4(\pi/N_r)/[1 + \cos(\pi/N_r)]^3 & N_r \text{ odd} \end{cases}$$

It is noted that the C-association between a linear variable and a circular variable is non-negative. They are independent of each other if $Ca^2_{l,c} = 0$ and are highly correlated if $Ca^2_{l,c}$ approaches 1. Please refer to [124] which details the T-monotone association that represents the rank relationship between circular variables.

Based on equations (4-1) – (4-3), the elements in a $(n_R \times n_R)$ rank correlation matrix C_R that is made up of the rank correlations among n_R weather variables can be computed from each pair of weather observations taken over recent days. A new matrix M_R of size $(N_{MC} \times n_R)$ is generated in which each column comprises arbitrary van der Waerden scores $\Phi^{-1}(i/(N_{MC} + 1)), i = 1, \ldots, N_{MC}$ [122]. The lower triangular matrices P_R and Q_R are obtained through Cholesky factorization such that $P_R P'_R = C_R$ and $Q_R Q'_R = C_{MR}$ where C_{MR} is the sample rank correlation

matrix associated with M_R. The matrix $M_R^* = M_R(P_R Q_R^{-1})'$ would have a rank correlation matrix quite similar to C_R. Then the random weather input variables sampled from each independent marginal distribution are sorted according to the order of corresponding column in M_R^* [122]. In this manner, the dependence among historic time series of weather variables within the most recent days is incorporated into the paired multivariate random weather input variables.

4.2.2. Spatial interpolation

Spatial interpolation models that estimate ambient conditions for each span from the measured weather data enable the weather-based DLR model to assess the spare ampacity of an entire OHL. The inverse distance weighting (IDW) method was previously used in [10, 20] to calculate the sampling weight as a decreasing function of distance from the target location. However, the influences of geographical variables of interest on local weather conditions were not considered except for the use of a wind profile power law with a reference level of 200m above ground level for wind speed interpolation. In addition to the IDW method, a geostatistical interpolation method, kriging, is developed in this section to estimate weather data for each span. The kriging model additionally takes account of spatial correlations not only between the target and sampled locations but also between the sampled locations themselves and does not assign an unduly high weighting to what are effectively duplicate measurements in similar locations. Furthermore, the effects of the associated geographical variables on local weather conditions are investigated and considered in the process of spatial interpolation.

4.2.2.1. Inverse distance weighting and kriging

Inverse distance weighting (IDW) and kriging both infer the value at a target location as a weighted sum of observations at surrounding sampled locations [125]:

$$\xi(loc_o) - me(loc_o) = \sum_{i=1}^{N(loc)} \lambda_i [\xi(loc_i) - me(loc_i)] \qquad (4\text{-}4)$$

where $\xi(loc_o)$ and $\xi(loc_i)$ are values at the target location loc_o and the sampled location loc_i respectively. The terms $me(loc_o)$ and $me(loc_i)$ represent the expected values or trend components of $\xi(loc_o)$ and $\xi(loc_i)$. $N(loc)$ is the number of sampled locations and λ_i is the weight assigned to the sampled location $loc_i, i = 1, ..., N(loc)$.

IDW is a relatively simple spatial interpolation method. The IDW weights $\lambda_{IDW,i}$ are inversely proportional to the distances $ds_{i,o}$ between loc_o and loc_i:

$$\lambda_{IDW,i} = \frac{1/ds_{i,o}^q}{\sum_{j=1}^{N(loc)}(1/ds_{j,o}^q)} \tag{4-5}$$

where q is a power parameter. A higher power parameter q will increase the influences of the nearest sampled locations while the use of a lower q results in a smoother interpolation surface [126]. A default value of q equal to 2 was used in [20].

The kriging weights are determined to minimise the variance of estimation errors. In addition to the distance $ds_{i,o}$, kriging weights $\lambda_{KRI,i}$ largely depend on spatial relationships among weather variables at all locations [125]:

$$\lambda_{KRI,i} = \boldsymbol{K}^{-1}\boldsymbol{k} \tag{4-6}$$

where $\boldsymbol{K}$ represents the matrix of covariances between the sampled locations and $\boldsymbol{k}$ is the vector of covariances between the target and sampled locations. The elements in both $\boldsymbol{K}$ and $\boldsymbol{k}$ are estimated using a semi-variogram model which describes how the spatial variability between weather variables represented by the semi-variance increases with distance. The semi-variogram model is fitted to the empirical semi-variance $\gamma(h_s)$ calculated from historic time series at sampled locations [127]:

$$\gamma(h_s) = \frac{1}{2N(h_s)}\sum_{i=1}^{N(h_s)}[\xi(loc_i) - \xi(loc_i \sim h_s)]^2 \tag{4-7}$$

where $N(h_s)$ is the number of pairs of observations $\xi(loc_i)$ and $\xi(loc_i \sim h_s)$ which are a distance lag h_s apart. The semi-variogram that models the spatial

variability among weather variables can be fitted by several mathematical functions, e.g. a spherical model, an exponential model and a Gaussian model [127] which are listed in equations (4-8) – (4-10) respectively:

$$\gamma^*(h_s) = \begin{cases} 0, & h_s = 0 \\ b_\gamma + c_\gamma \left\{ \dfrac{3h_s}{2a_\gamma} - \dfrac{1}{2}\left(\dfrac{h_s}{a_\gamma}\right)^3 \right\}, & 0 < h_s < a_\gamma \\ b_\gamma + c_\gamma, & h_s \geq a_\gamma \end{cases} \tag{4-8}$$

$$\gamma^*(h_s) = \begin{cases} 0, & h_s = 0 \\ b_\gamma + c_\gamma \left\{ 1 - exp\left(-\dfrac{3h_s}{a_\gamma}\right) \right\}, & h_s > 0 \end{cases} \tag{4-9}$$

$$\gamma^*(h_s) = \begin{cases} 0, & h_s = 0 \\ b_\gamma + c_\gamma \left\{ 1 - exp\left(-\dfrac{3h_s^2}{a_\gamma^2}\right) \right\}, & h_s > 0 \end{cases} \tag{4-10}$$

where the coefficients in three functions a_γ, b_γ and c_γ represent the 'range', 'nugget' and 'partial sill' respectively which are the major characteristics of a semi-variogram. The semi-variograms modelled by different mathematical functions with $a_\gamma = 0.8$, $b_\gamma = 0.1$ and $c_\gamma = 0.9$ are shown in Fig. 4-1. The 'nugget' is an estimate of the uncorrelated noise in space, representing the spatial variability between two locations that are very close. This is mainly caused by the measurement error or/and the spatial variability at distances smaller than the sampling distance [127]. For a spherical model, the semi-variance increases with distance and just reaches the maximum value $(b_\gamma + c_\gamma)$ at the 'range'. The maximum value of semi-variance is known as the 'sill'. The calculated semi-variance between variables separated by a distance in excess of the 'range' is equal to 'sill', implying that they have no impact on each other. For the exponential and Gaussian models, the semi-variance gradually approaches the 'sill' with the increase in distance and reaches $0.95(b_\gamma + c_\gamma)$ at the 'range' [128].
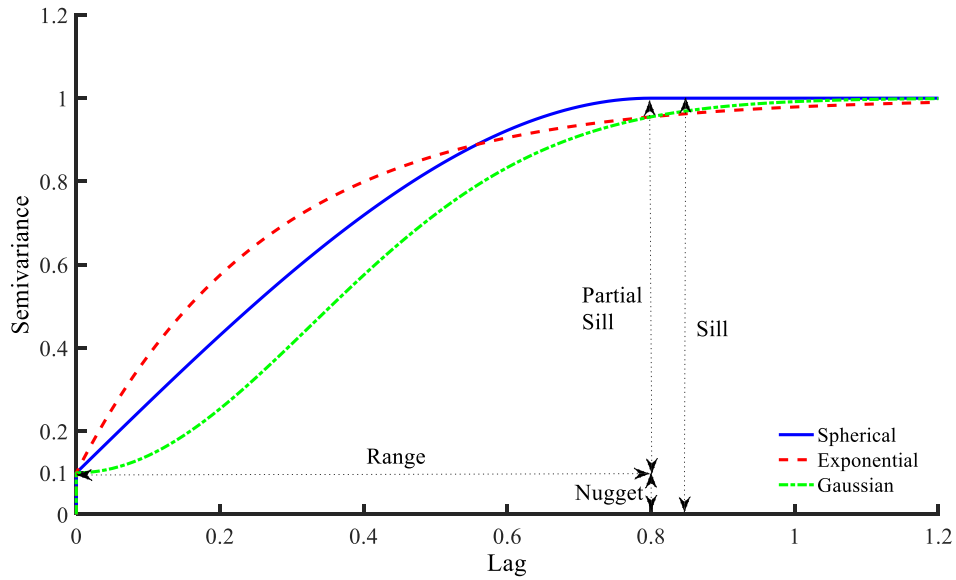
Fig. 4-1. The semi-variogram determined by the spherical, exponential and Gaussian models with range $a_\gamma = 0.8$, nugget $b_\gamma = 0.1$ and partial sill $c_\gamma = 0.9$

The type of function for the semi-variogram fitting can be determined based on the empirical semi-variances computed from historic weather data. A spherical model is usually selected if empirical semi-variances have clear range and sill. An exponential model is preferred when empirical semi-variances clearly show the nugget and sill and asymptotically approaches the sill. If empirical semi-variances vary smoothly and have a parabolic behaviour at the origin a Gaussian model is usually adopted [127, 129]. The $N(loc) \cdot (N(loc) - 1)/2$ empirical semi-variance points calculated from $N(loc)$ sampled locations are likely to show an unclear increasing pattern which makes it difficult to select an appropriate mathematical model to fit the semi-variogram and will also increase computation time [130]. A feasible solution is to categorise the calculated empirical semi-variances into a number of isotonic distance lag bins [131]. The averages of empirical semi-variances and their accompanying distance lags at each bin are then used to determine the type of the mathematical model with coefficients being estimated from the averages by the least squares fitting [132]. Then, the elements of covariance $Cov(h_s)$ in $\mathbf{K}$ and $\mathbf{k}$ can be estimated via the equation:

$$Cov(h_s) = Sill - \gamma^*(h_s) \tag{4-11}$$

It should be noted that the semi-variance $\gamma^*(0)$ at distance lag $h_s = 0$ is equal to zero rather than the nugget b_γ when calculating the covariance $Cov(0)$ in $\boldsymbol{K}$ and $\boldsymbol{k}$. When a spherical model is used, the non-diagonal elements in matrix $\boldsymbol{K}$ and elements in vector $\boldsymbol{k}$ can be represented as:

$$Cov(h_s) = (b_\gamma + c_\gamma) - \left\{ b_\gamma + c_\gamma \left\{ \frac{3h_s}{2a_\gamma} - \frac{1}{2}\left(\frac{h_s}{a_\gamma}\right)^3 \right\} \right\}$$

$$= c_\gamma \left\{ 1 - \frac{3h_s}{2a_\gamma} + \frac{1}{2}\left(\frac{h_s}{a_\gamma}\right)^3 \right\}, \qquad 0 < h_s < a_\gamma$$

(4-12)

If $\gamma^*(0) = b_\gamma$, all the diagonal elements of matrix $\boldsymbol{K}$ are equal to $(b_\gamma + c_\gamma) - b_\gamma = c_\gamma$. Then all the elements in $\boldsymbol{K}$ and $\boldsymbol{k}$ have a common coefficient equal to the partial sill c_γ. Thus, the values of b_γ and c_γ will not affect the determination of kriging weights. If $\gamma^*(0) = 0$, the diagonal elements of matrix $\boldsymbol{K}$ are all equal to $(b_\gamma + c_\gamma)$. The kriging weights are then dependent on the ratio between b_γ and c_γ in addition to the type of the mathematical function selected to model the semi-variogram [133]. The kriging model with a large b_γ will assign similar kriging weights to sampled locations, largely smoothing the interpolation surface [134]. When the nugget is equal to the sill, i.e. a nugget model with $c_\gamma = 0$ [127], sampled locations will have the same weights.

It can be found that besides the distances from the target location, kriging weights are dependent on the spatial correlations not only between the sampled and target locations but also between sampled locations themselves. In an isotropic region, i.e. one that has the same characteristics in all directions, the sum of kriging weights assigned to the sampled locations within a cluster is generally similar to the weight assigned to an isolated sampled location if they have similar distances from the target location. Fig. 4-2 provides an example where an isolated sampled location loc_3 and a cluster consisting of two sampled locations loc_1 and loc_2 are located on one side of a target location loc_o in a line with similar distances from the target location. The

IDW weights and the kriging weights calculated based on an exponential model of $a_\gamma = 20, b_\gamma = 0.1, c_\gamma = 1.9$ are listed in Table 4-1.

loc_1 loc_2 loc_o loc_3

0.2 0.9 1.0
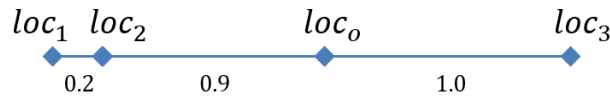
Fig. 4-2. An example showing kriging's compensation for cluster effects

Table 4-1. IDW weights and kriging weights assigned to an isolated loc_3 and a cluster consisting of loc_1 and loc_2.

	loc_1	loc_2	loc_3
IDW	0.2700	0.4033	0.3267
Kriging	0.1651	0.3583	0.4472

The sum of IDW weights assigned to loc_1 and loc_2 within the cluster equals 0.6733 that is twice as high as the IDW weight assigned to loc_3. The estimate at loc_o is therefore largely dependent on the cluster though the isolated sampled location and the centre of the cluster are both 1.0 from the target location. In the kriging process which takes into account the significant correlation between loc_1 and loc_2 within the cluster, the weights assigned to loc_1 and loc_2 are reduced along with a growth in the weight at loc_3. The total kriging weight of the cluster (i.e. the sum of 0.1651 for loc_1 and 0.3583 for loc_2) equals 0.5234 which is similar to the kriging weight assigned to the isolated sampled location loc_3 (i.e. 0.4472). Therefore, compared to the IDW method giving a significant weight to clusters, the effect of clusters can be mitigated by the kriging process.

4.2.2.2. Correction for negative weights [135]

Negative weights may be produced in a kriging process. The estimate at a target location may be negative and nonphysical when negative weights are assigned to the sampled locations that have high sampled values, like extreme wind speeds. Therefore, negative kriging weights have to be corrected. An algorithm developed by Deutsch [135] is used here to correct negative weights through setting the negative weights and relevant positive weights to zero and normalising the remaining positive weights as described below.

Given average magnitude of negative weights equal to $\left|\bar{\lambda}_{KRI,neg}\right|$ and the average of the covariances between the target location and the sampled locations with negative weights equal to $\overline{Cov}_{neg}$, the initial kriging weights $\lambda_{KRI,i}, i = 1, ..., N(loc)$ are corrected based on the following steps:

1) $\lambda'_{KRI,i} = \lambda_{KRI,i}$;

2) If $\lambda_{KRI,i} < 0$, then $\lambda'_{KRI,i} = 0$;

3) If $\lambda_{KRI,i} > 0$ and $\lambda_{KRI,i} < \left|\bar{\lambda}_{KRI,neg}\right|$ and $Cov_i < \overline{Cov}_{neg}$ where Cov_i is the covariance between the target location loc_o and the sampled location loc_i, then $\lambda'_{KRI,i} = 0$;

4) $\lambda'_{KRI,i}$ are normalised to sum to one:

$$\lambda_{KRI,i,new} = \frac{\lambda'_{KRI,i}}{\sum_{i=1}^{N(loc)} \lambda'_{KRI,i}} \tag{4-13}$$

In this manner, the corrected weights $\lambda_{KRI,i,new}$ are non-negative and unbiased.

4.2.2.3. Spatial de-trending

Weather conditions are influenced by local geographic parameters. For example, air temperature generally decreases with the elevation above sea level. Spatial de-trending is used to remove the trend surfaces or spatial trends that are fitted to weather data in terms of the associated geographic variables. The modelled trend surfaces are added back in the interpolations at the end of the IDW or kriging process. In this manner, the effects of these geographic variables on both spatial correlations and interpolations of weather parameters can be mitigated [136]. The elevation above sea level is a major factor influencing air temperature and wind speed. Typically, measurements of air temperature and wind speed at weather stations are first converted to a common reference level at which the IDW and kriging interpolations, as well as the subtraction and addition of trend surfaces are carried out. The interpolation results at the reference level are then converted back to the elevation of the target location [20, 106, 128, 137].

The air temperature generally decreases with the elevation above sea level at a rate named as the lapse rate. A typical value of $-6.0\text{°C}/km$ [128, 137] is used here to convert air temperatures at the elevations of weather stations to that at sea level. An alternative approach could be to extract the decreasing rate of air temperature with elevation from historic time series of air temperature recorded at weather stations by the linear fitting. For wind speed, the anemometers' heights lvl_{ane} above ground level and the ground roughness lengths rl_o are additionally required to convert wind speeds $w_{s,ave}$ from the anemometers' heights lvl_{ane} to a common reference level lvl_{ref} (e.g. 300m above sea level) based on a log-law wind profile [138]:

$$w_{s,ref} = w_{s,ane} \frac{\ln(lvl_{ref}/rl_o)}{\ln(lvl_{ane}/rl_o)} \tag{4-14}$$

In order to minimise the spatial variation further, the trend surface of wind speeds $w_{s,ref}$ at the reference level of 300m above sea level is modelled in terms of distance to ocean (DTO) as shown in Fig. 4-3. The weather stations closer to the coast are generally known to have higher wind speed averages in this case, which is also discovered by Nawri [139] and Xue [140].
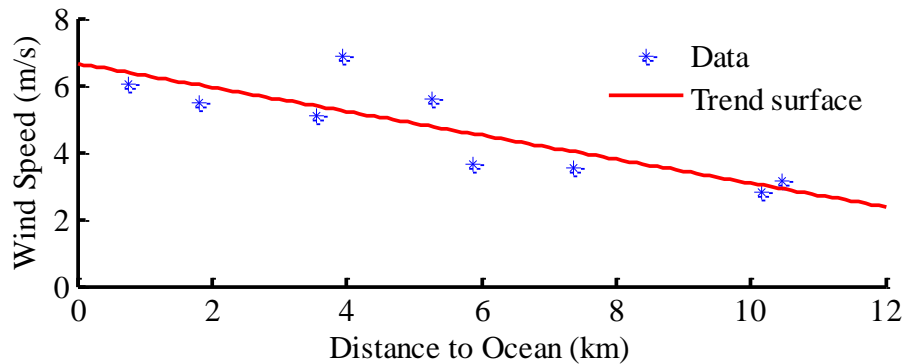
Fig. 4-3. Modelling of trend surfaces of wind speeds at the reference level of 300m above sea level in terms of distance to ocean (DTO) based on wind speed observations over 45 days from 00:00 on 14/12/2012 to 23:50 on 27/01/2013

4.2.2.4. Temporal de-trending

As was noted in Section 3.2.1, data applied to statistical models are generally required to satisfy a weak or second order stationarity. Spatial correlations between weather variables may be misled by the inherent trends of non-stationary data. The spatial de-trending method has been used to remove the trend surfaces of weather variables in terms of the associated geographic variables. The temporal trends of weather variables at the reference level should be additionally removed using the Fourier series based temporal de-trending method as described in Section 3.2.1.

Fig. 4-4 compares the empirical semi-variances (m^2/s^2) which are calculated from (a) the wind speed residuals after temporal de-trending (TD) and spatial de-trending (SD); (b) the wind speed residuals after SD only; and (c) original wind speeds at the reference level of 300m above sea level. The empirical semi-variances calculated from original wind speeds at the reference level are shown to be higher than those that are estimated from the residuals without spatial trends in terms of DTO. In addition, the indistinct pattern of growth in semi-variance with distance lag makes it difficult to select an appropriate mathematical function to model the semi-variogram. Moreover, the semi-variogram modelled from original wind speeds may not accurately indicate spatial correlations among wind speeds at the reference level due to the interference of trend surfaces in terms of DTO. When TD and SD are both applied to the original data at the reference level, the empirical semi-variances calculated from the de-trended data are smaller than that for original data and are clearly shown to asymptotically approach the maximum value, i.e. the sill, illustrating the importance of detrending.
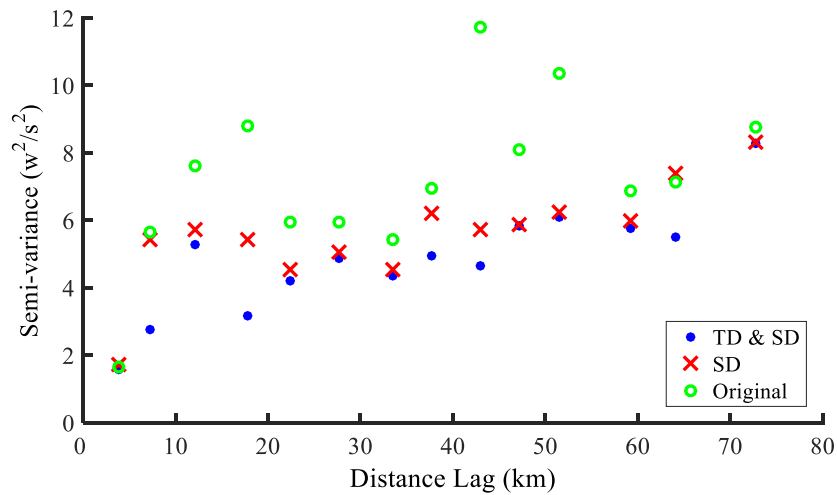
Fig. 4-4. Empirical semi-variances calculated from (a) residuals of wind speed after temporal de-trending (TD) and spatial de-trending (SD); (b) wind speed residuals after SD only; and (c) original wind speeds at the reference level of 300m above sea level over 45 days from 00:00 on 14/12/2012 to 23:50 on 27/01/2013

4.3. Results of Rank Correlation based Pairing

Pairs of weather variables including different parameters at a particular location and the same parameters at different locations are correlated. In the Monte Carlo process, 10^4 weather samples are randomly and independently generated from the modelled predictive distributions of the measured weather variables including air temperature (T_a), wind speed (w_s) and wind direction (w_d). These random weather samples at a particular future time are paired based on the rank correlations calculated from recent weather observations taken to be within 15 days. Fig. 4-5 shows that the paired random weather samples at a single station have similar rank correlations to those between their recent observations, especially the paired samples of air temperature and wind speed. The magnitudes of correlations between the unpaired weather samples are smaller than 0.01 which confirms that they are independent of each other.

127
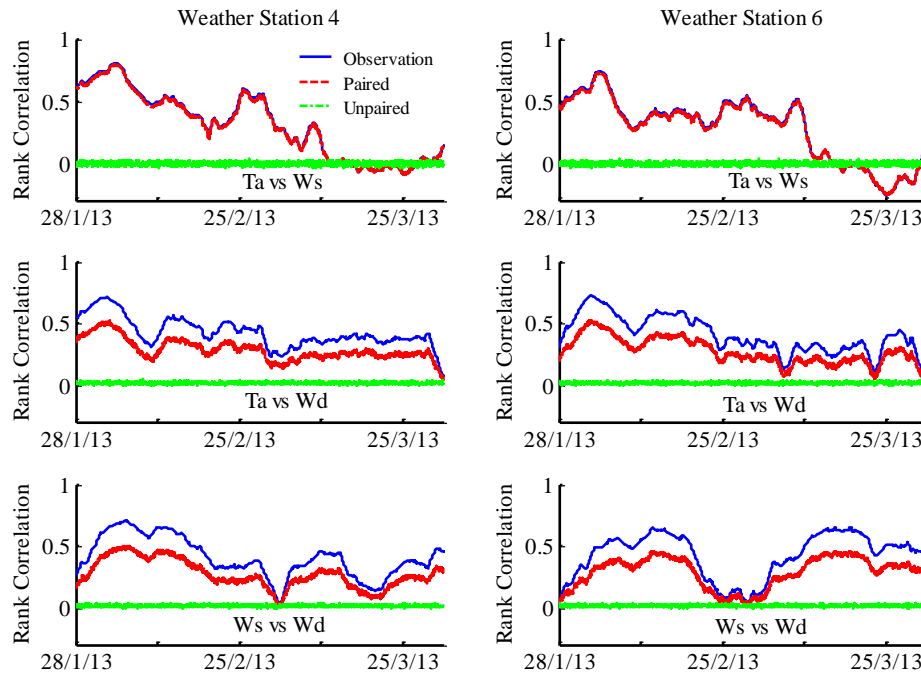
Fig. 4-5. Rank correlations between paired, unpaired random samples of weather variables and their recent observations within 15 days at the same weather stations 4 and 6

The paired random samples of air temperature and wind speed at different stations having rank correlations quite close to those between their recent observations are shown in Fig. 4-6. The same weather parameters between different weather stations generally have positive rank correlations which are relatively higher than those between different weather parameters. Due to the paired samples of air temperature between different weather stations having significant positive rank correlations, the paired wind speed samples at a particular station are shown to have similar rank correlations with air temperature samples at different stations. When calculating the rating for an entire OHL, random samples of air temperature and wind speed at different stations are only paired. This is because the rank correlation matrix C_R computed from recent observations may not be positive definite when additionally considering wind direction samples, which means that the Cholesky factorization could not be implemented.
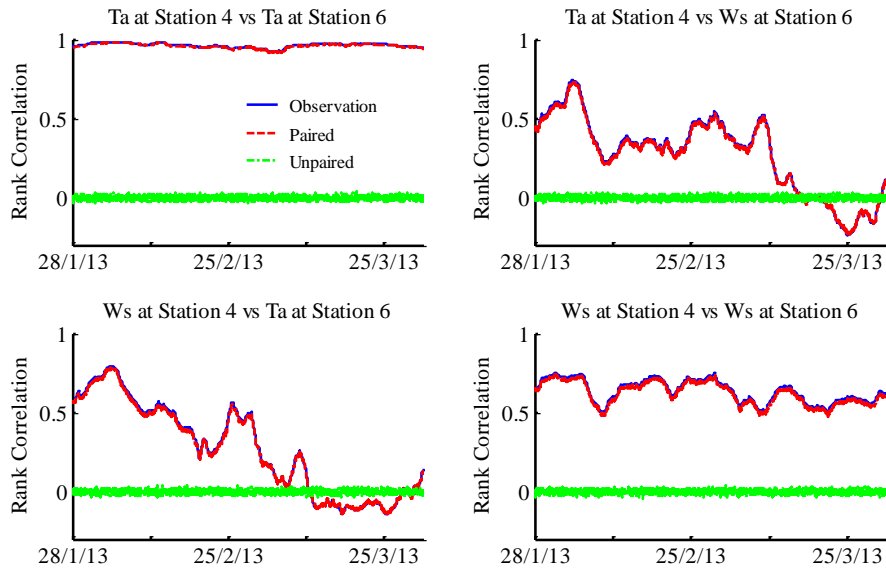
Fig. 4-6. Rank correlations of paired, unpaired random samples of air temperature and wind speed and their recent observations between stations 4 and 6 within 15 days.

The paired (correlated) weather samples at a particular station can be directly used to calculate probabilistic forecasts of steady-state DLRs for the span in close proximity to the station. To estimate probabilistic DLR forecasts for an entire OHL, the paired samples of air temperature and wind speed, unpaired (independent) wind direction samples and point forecasts of solar radiation at different weather stations are first used to infer possible weather predictions for all spans within the OHL by suitable spatial interpolation methods which will be determined in Section 4.4.

4.4. Results of Spatial Interpolation

As was noted in Section 4.2.2, the inverse distance weighting (IDW) method assigns weights to sampled locations considering their distances from the target location only. In addition to the distances, the kriging weights are largely influenced by spatial relationships between different locations which are modelled from historic time series of the measured weather variables within a sliding training window. The training window length used for spatial interpolation is the same as that selected for probabilistic forecasting for each weather variable. In the kriging process, the

semi-variogram model used to determine covariances between locations is fitted to the empirical semi-variances that are computed from the de-trended data after removing temporal trends and trend surfaces (or spatial trends) of weather data in terms of the associated geographical variables at a predefined reference level.

The performances of different spatial interpolation methods are assessed by calculating their root mean square errors (RMSEs) [105] when taking each weather station as the target location in a cross-validation procedure. Since the captured spatial correlations between locations additionally affect the kriging weights, the semi-variogram model for each weather variable is first examined, as shown in Fig. 4-7 where weather station 2 is regarded as the target location. Due to the circular properties of wind direction, measurements of wind directions are decomposed into the easterly and northerly components and the semi-variogram is then fitted for each component separately.
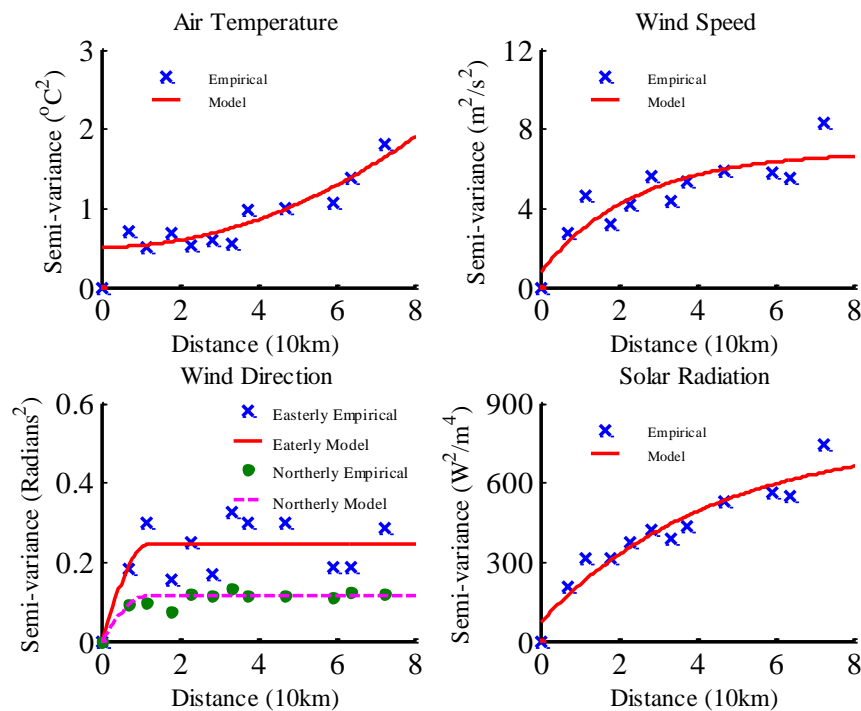
Fig. 4-7. The semi-variogram fitted to empirical semi-variances calculated from the de-trended data within the training window from 00:00 on 14/12/2012 to 23:50 on 27/01/2013 for air temperature at sea level, wind speed at 300m above sea level, easterly and northerly components of wind direction, and solar radiation when weather station 2 is regarded as the target location

The spatial relationships of air temperature referenced to sea level and solar radiation in the research area are successfully represented by Gaussian and exponential models respectively. A relatively large deviation between the semi-variance fitted by an exponential model and the empirical value is observed at around $10km$ distance lag for wind speed at 300m above sea level (ASL), meaning that the actual spatial correlations between wind speeds that are approximately $10km$ apart at 300m ASL may be lower than the modelled correlations. The semi-variances fitted for the northerly and easterly components of wind directions reach their respective maximum values or sills at a very short distance lag (around $10km$). The IDW interpolation method is therefore applied to each component of wind direction.

Previous work [20] undertaken by Durham University used the IDW method for each weather variable. A wind profile power law with a reference level of 200m above ground level (AGL) was additionally used for wind speed interpolation [20]. In this section, a number of spatial interpolation models are developed through different combinations of the interpolation methods, i.e. IDW or kriging (KRI) and spatial de-trending, as listed in Table 4-2. It is noted that the sliding training windows for the modelling of spatiotemporal trends and the determination of kriging weights are of the same lengths as those that are selected for weather forecasting models and are updated at each 10-minutes time step. The improvements in RMSEs for spatial interpolation of each weather variable over the Durham's methods for the models that are developed in this research are shown in Figs. 4-8, 4-9, 4-12 and 4-14 respectively in the following subsections.

Table 4-2. Spatial interpolation models developed in previous work [20] and in this section

	Air Temperature	Wind Speed	Wind Direction	Solar Radiation
Durham	IDW	IDW + 200m AGL	IDW	IDW
New 1	IDW + Lapse Rate	IDW + 300m ASL	IDW + Cartesian Coordinates	KRI
New 2	KRI + Lapse Rate	IDW + 300m ASL + DTO		
New 3		KRI + 300m ASL + DTO		

4.4.1. Spatial interpolation of air temperature
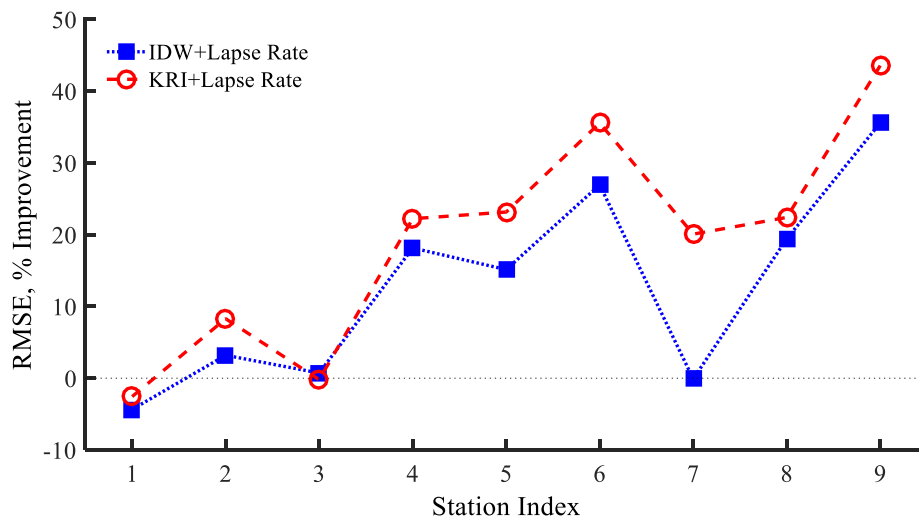
Fig. 4-8. Improvement in RMSEs for air temperature interpolation over the Durham's method for the models developed in this section when taking each weather station as the target location

The spatial interpolation models taking account of the lapse rate are shown to perform better than the IDW method used in [20] for air temperature interpolation at most weather stations. The improvements over the IDW method without use of the lapse rate are significant at the weather stations on east side of the research area (i.e. stations 5 – 9) which have large variations in altitude. This means that the conversion of air temperature between original heights and the sea level (i.e. the reference level at which the spatial interpolation is carried out) can effectively mitigate impacts of the elevation above sea level on spatial interpolation of air temperature.

However, the accuracies of air temperature estimates for stations 1 and 7 are not improved with the additional consideration of the lapse rate. It is found that the differences in air temperature between station 1 and its adjacent stations 2 and 3 at their original heights are slightly smaller on average than that at the sea level. Table 4-3 describes a particular case where the use of the lapse rate in the IDW method does not significantly reduce the error of air temperature estimate for station 7. The elevations (m) ASL, average air temperatures (℃) at original levels and the sea level of station 7 and its surrounding stations 5, 6, 8 and 9 on which it largely depends on 16/02/2013 are listed in Table 4-3. The IDW weights assigned to the stations in proximity to station 7 and their kriging weights are also given in Table 4-3 together with the corresponding estimates for station 7. Since there are slight changes in kriging weights at each 10-minutes time step, the kriging weights evaluated at 00:00 on 16/02/13 are applied to average air temperatures to estimate the interpolation.

Table 4-3. Elevation (m) ASL, average air temperature (℃) at original heights and the sea level of stations 5 – 9, IDW weights and kriging weights assigned to stations 5, 6, 8 and 9 and the corresponding estimates (℃) for station 7

Station Index	5	6	7	8	9	Estimates (℃)	
						IDW	Kriging
Elevation (m)	136.2	32.5	175.7	256.6	9.0	N/A	
Original (℃)	3.2403	3.8514	2.6528	1.6637	3.5804	2.3626	N/A
Sea Level (℃)	4.0575	4.0464	3.7070	3.2033	3.6344	3.4715	3.7192
IDW	0.0362	0.1311	N/A	0.6737	0.1018	N/A	
Kriging	0.1224	0.2450	N/A	0.3091	0.2620	N/A	

The average air temperature of station 7 at the original height is shown to be higher than that at the nearest station 8 but lower than those at other surrounding stations. When the average air temperatures are converted from original levels to the sea level, these relatively large deviations from surrounding stations are significantly reduced. Though it is more reasonable to take account of the effect of lapse rate on air

temperature, the direct use of the IDW method happens to result in an error similar to that for the additional consideration of lapse rate.

The kriging model is shown to give further improvements at most stations due to it additionally taking into account spatial correlations between different locations. It is found that the empirical semi-variances between air temperatures that are short distances apart (e.g. within $35km$ as shown in Fig. 4-7) are very similar meaning that the actual value at the target location may be closer to the observation at a sampled location relatively further away from it than the nearest sampled location. For example, the difference (0.07℃) in average air temperature at the sea level between stations 7 and 9 is smaller than that (0.5℃) between stations 7 and 8 and that (0.43℃) between stations 8 and 9 as listed in Table 4-3 though station 8 is the nearest location to both stations 7 and 9. The large weight assigned to the nearest sampled location in the IDW process may therefore lead to a relatively large error of air temperature estimate.

Fig. 4-7 shows that the semi-variances of residuals of air temperature at the sea level fitted by a Gaussian model increase slowly at the origin due to the similar empirical semi-variances at short distance lags. This weakens the impact of the nearest sampled location and increases the weights assigned to sampled locations that are relatively further away from the target location. In addition, the smoothing effect of the nugget reduces the influence of the nearest location on the target location. For example, when station 7 is regarded as the target location, the IDW weight assigned to the nearest station 8 is 0.67 which reduces to 0.31 in the kriging process along with the increasing impacts of other stations as listed in Table 4-3. In this calculation example, the kriging estimate has an error of 0.01℃ which is much smaller than the error of IDW estimate equal to 0.24℃. Therefore, in this study where the air temperatures that are short distances apart have similar spatial correlations, the kriging model shows a better performance than the IDW method through weakening

the weight given to the nearest sampled location. The kriging model with an addition of lapse rate is therefore used here for air temperature interpolation.

4.4.2. Spatial interpolation of wind speed
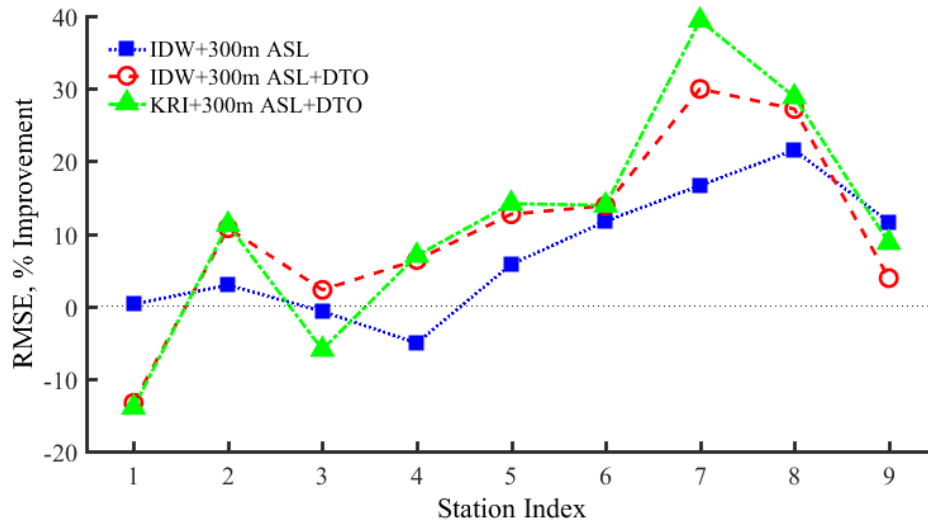
Fig. 4-9. Improvement in RMSEs for wind speed interpolation over the Durham's method for the models developed in this section when taking each weather station as the target location

The experimental results show that 300m ASL is a better choice as the reference level in this case where weather stations are located in the mountainous terrain. Using the reference level of 300m ASL and the IDW method, the additional modelling of the surface trend in terms of distance to ocean (DTO) improves the accuracy of wind speed interpolation further at most stations, except for stations 1 and 9. As can be seen from Fig. 1-3, stations 1 and 9 are located on the edge of the research area and their estimates largely depend on the nearest stations 2 and 8 respectively. It is found in some cases that removing the trend surfaces increases the differences in residuals between the target locations and their adjacent sampled locations. As shown in Fig. 4-10, for example, wind speeds of station 9 (i.e. the target location) and station 8 at the reference level of 300m ASL have a slight difference of $0.14\,m/s$ at 00:10 on 28/01/2013. However, the difference between their residuals increases to $1.35\,m/s$ when the trend surface in terms of DTO modelled from sampled locations (i.e. stations 1 to 8) is removed.

135
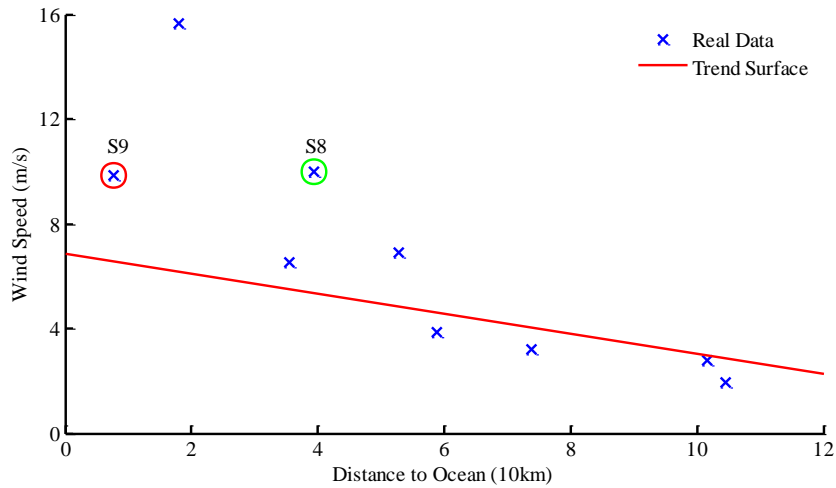
Fig. 4-10. Wind speeds at 300m ASL at 00:10 on 28/01/2013 and the trend surfaces in terms of DTO modelled from the data within recent 45 days at stations 1 – 8

The kriging model performs just slightly better than the IDW method at most stations when both make use of spatial de-trending. The limited improvement might be due to the insufficient number and distribution of weather stations. Since the wind speed is largely affected by local effects and varies significantly across the study region, the limited number of weather stations results in an inadequate number of empirical semi-variance points to fit an accurate semi-variogram to represent spatial correlations of wind speed, especially at short distance lags. As was noted in Section 4.2.2.1, the kriging model can mitigate the effects of clusters. However, the weather stations are fairly well distributed and there are no severe clusters so that kriging's advantage of being able to compensate for cluster effects is limited.

An unsatisfactory performance of kriging is observed at station 3 compared to the IDW, which may be due to the smoothing effect of the nugget. Regarding station 3 as the target location, the IDW method gives a high weight of 0.75 to the nearest station 2 while the kriging weight is around 0.58. It is found that the empirical semi-variance of wind speed residuals at 300m ASL between stations 2 and 3 that are 3.8km apart (i.e. the minimum sampling distance in the research area) equals approximately 1.6 m^2/s^2, which is much smaller than the semi-variances at other

distance lags as shown in Fig. 4-11. This indicates a strong correlation between wind speeds that are quite close in space. Therefore, the weakened influence of the nearest station 2 in the kriging process leads to less accurate estimates for station 3.
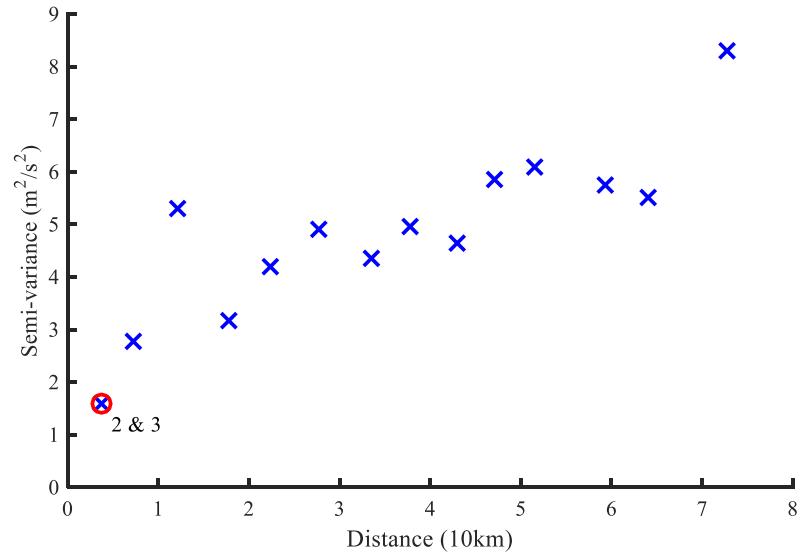
Fig. 4-11. Empirical semi-variances calculated from residuals of wind speeds at all weather stations at 300m ASL over the period from 00:00 on 14/12/2012 to 23:50 on 17/01/2013

Considering the strong correlations between wind speeds that are very close in space, the IDW method combined with the modelling of trend surfaces of wind speed at 300m ASL in terms of DTO is employed here to estimate wind speeds for overhead spans that are located below 300m ASL. For a limited number of spans that are above 300m and 400m ASL, the reference levels of 400m and 500m ASL are adopted respectively. Although the use of 400m and 500m ASL is found to slightly reduce the accuracy of wind speed interpolation in the cross-validation procedure, the spans above 300m and 400m ASL may rarely limit the rating for an OHL since they usually experience relatively higher wind speeds and lower air temperatures, i.e. a higher convection cooling than those that are located at lower elevations.

4.4.3. Spatial interpolation of wind direction
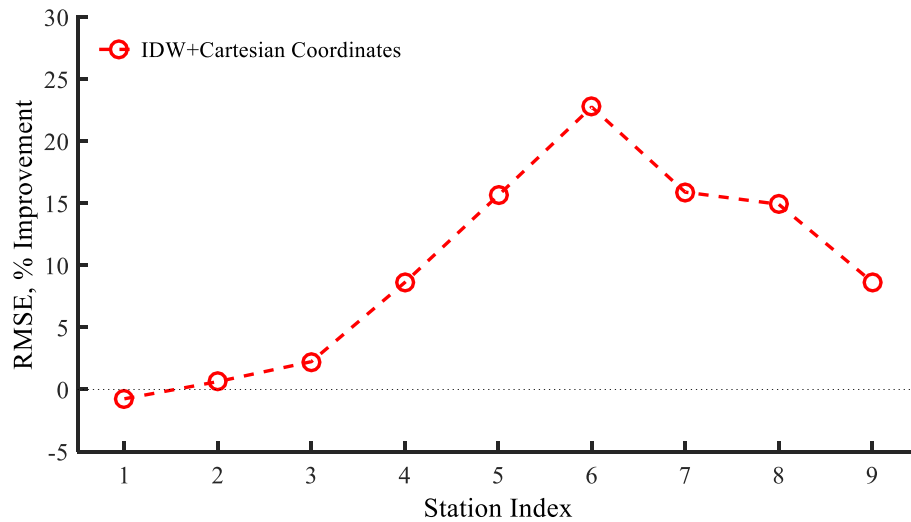
Fig. 4-12. Improvement in RMSEs for wind direction interpolation over a simple IDW method for a combination of the IDW method and the Cartesian coordinates when taking each weather station as the target location

Decomposing wind directions along the easterly and northerly axes in Cartesian coordinates successfully addresses the circular properties of wind direction $w_d \in (-\pi, \pi]$ and results in more accurate interpolations than directly applying IDW to original wind directions. It was mentioned in [20] that the direct application of IDW may result in erroneous wind direction estimates, in particular when concurrent observations at weather stations are around $-\pi$ and π. In this case, the inference of wind direction for the target location may be around 0, leading to an error of π between the actual value and the estimate. However, an error of π in wind direction provides the same cooling as the actual wind direction due to the fact that the forced convection heat loss rate is determined by the angle between the conductor axis and wind direction [3]. Therefore, the maximum error of $\pm\pi$ in wind direction interpolation would not affect the cooling effect estimation [20], while an error of $\pi/2$ may be a real problem for certain wind directions, e.g. those that are approximately parallel or perpendicular to the conductor.

To assess the accuracy of wind direction interpolations with respect to their impacts on the wind cooling effect, errors of wind direction estimates $error_\theta$ are converted into the interval of $(-\pi/2, \pi/2]$:

$$error_\theta^* = \begin{cases} error_\theta + \pi & for & error_\theta \leq -\pi/2 \\ error_\theta & for & -\pi/2 < error_\theta \leq \pi/2 \\ error_\theta - \pi & for & error_\theta > \pi/2 \end{cases} \qquad (3\text{-}15)$$

The RMSEs of $error_\theta^*$ are calculated for both spatial interpolation models, as shown in Fig. 4-13 where the additional use of the Cartesian coordinates gives significant improvement in RMSEs of $error_\theta^*$ over the Durham's method at most stations. Therefore, the IDW method is combined with the Cartesian coordinates to estimate wind directions for spans in this study.
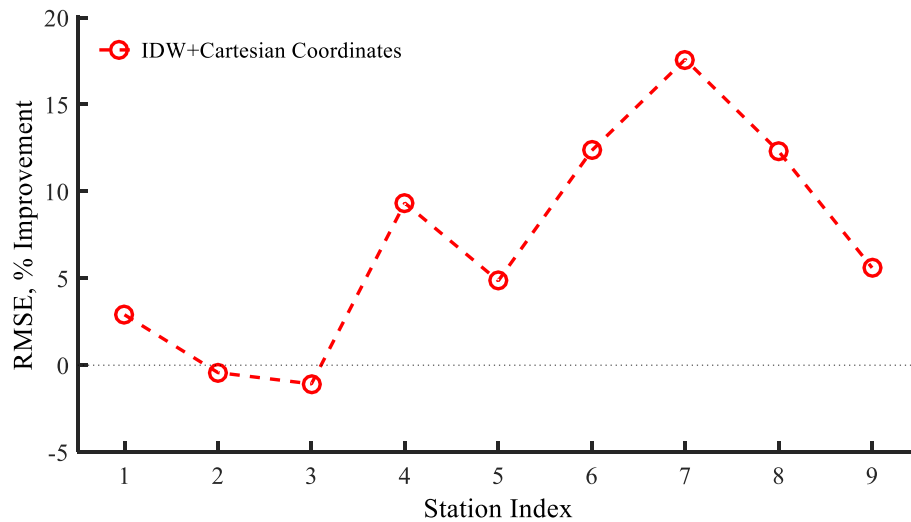
Fig. 4-13. Improvements in RMSE of $error_\theta^* \in (-\pi/2, \pi/2]$ over a simple IDW method for a combination of the IDW method and the Cartesian coordinates when taking each weather station as the target location

4.4.4. Spatial interpolation of solar radiation
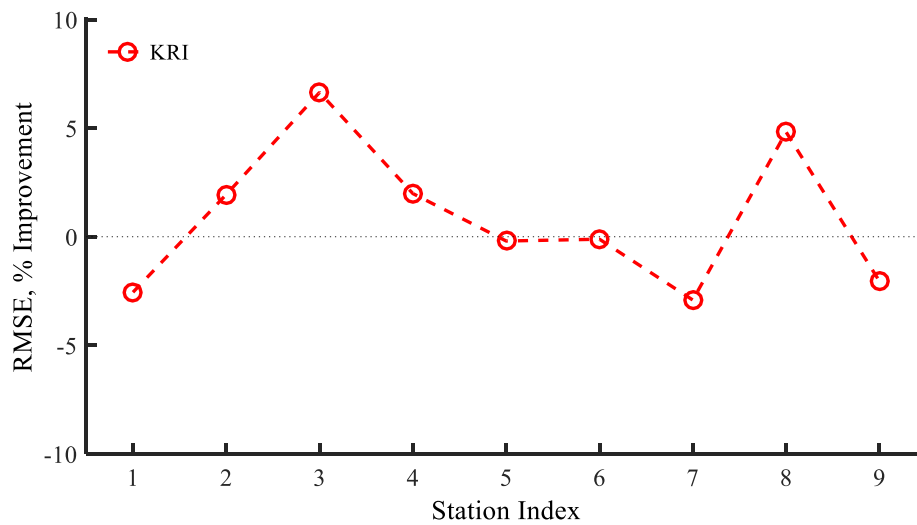
Fig. 4-14. Improvement in RMSEs for solar radiation interpolation over IDW for kriging when taking each weather station as the target location

Although the semi-variogram model was successfully fitted for solar radiation, the kriging is shown to perform similarly to IDW. This may be because weather stations are in fairly even distribution where kriging may give a similar interpolation accuracy to other interpolation methods [141]. In addition to the spatial interpolation algorithm used to calculate weights, the accuracy of solar radiation estimate is influenced by associated meteorological parameters such as precipitation, relative humidity, vapor pressure deficit, cloudiness, etc. [142]. Local topographic features (i.e. elevation, slope and aspect) provided by a digital elevation model could also be used for solar radiation interpolation. Solar radiation mapping techniques have been developed in a geographic information system (GIS) to estimate the potential solar radiation from topographic information that is combined with different physical parameterization [143]. The GIS based solar radiation map was additionally refined by comparing the physical estimates with their corresponding actual observations [144]. However, the GIS based solar radiation mapping generally requires the associated meteorological parameters which may be difficult to obtain [145]. Bezzi and Vitti [146] defined a morphological index for each location by combining the

classes of the local slope and aspect, and developed a linear function to model the variation in direct solar radiation with the order of the morphological index that was sorted based on the average of the measured direct solar radiation. It may be feasible to use the combined re-classification of the slope and aspect classes to model the trend surfaces of solar radiation if the associated meteorological parameters are fairly uniform in the research area.

Since the associated meteorological parameters and topographic features are not available in this study, the IDW method that shows similar performance and requires less computation time than the kriging model is used to infer solar radiations for overhead spans.

4.5. Conclusions

A rank correlation based paring method and spatial interpolation models have been developed in this chapter to generate appropriate correlated weather samples for each overhead span. To determine probabilistic forecasts of steady-state ratings, a large number of random weather samples are independently generated from the predictive distributions modelled for the measured weather variables. These independent random weather samples are paired to have rank correlations similar to those that are computed from recent weather observations within the most recent 15 days. The correlations of the paired weather samples are close to those from historic weather data, especially for linear variables, i.e. air temperature and wind speed. The random samples of air temperature and wind speed at different stations are only paired for the rating estimation for an entire overhead line (OHL). This is because the rank correlation matrix calculated from recent weather observations may not be positive definite when including variables for wind direction, which would disable the rank correlation based pairing method.

The correlated random samples of air temperature and wind speed, independent wind direction samples and point forecasts of solar radiation at different stations are used to infer possible weather conditions experienced at all spans within an OHL through suitable spatial interpolation methods. An appropriate spatial interpolation method is determined for each weather parameter by comparing performances of an inverse distance weighting (IDW) model that was employed in previous work [20] and a kriging interpolation model that assigns weights based on a data-driven weighting function. In addition, spatial de-trending has been used to fit spatial trends or trend surfaces to weather data in terms of the associated geographic variables, e.g. air temperature decreasing with elevation above sea level (ASL) and wind speed at a reference level of 300m ASL decreasing with distance to ocean. Then the modelled trend surfaces are removed from weather data at the reference level so as to mitigate the impacts of geographic variables on spatial correlations among the field data as well as the interpolation process. The semi-variogram fitted to the empirical semi-variances that are computed from residuals after Fourier series based temporal de-trending and spatial de-trending does not suffer from the interference of the trends implied in weather data. Compared to the semi-variogram derived from the original data, the residuals based semi-variogram clearly shows the pattern of semi-variances between weather variables increasing with distance lag. The additional use of spatial de-trending makes the main contribution to the accuracy of spatial interpolation for air temperature and wind speed. Furthermore, more accurate wind direction estimates are obtained by using the IDW method that is combined with the decomposition of wind direction in the Cartesian coordinates.

Due to the similar spatial correlations between air temperatures that are short distances apart, a Gaussian model with a non-zero nugget is selected to fit empirical semi-variances in the kriging process. This weakens the kriging weight assigned to the nearest sampled location and smooths the interpolation surface, which results in a higher accuracy of air temperature interpolation in this study. For wind speed and

solar radiation, the kriging model performs just slightly better than the IDW method at most stations, which might be due to the insufficient number of weather stations and their fairly even distribution in the research area. Compared to the IDW that uses an arbitrary function to give a decreasing weight with increasing distance from the target location, the main advantage of kriging is that it does not assign an unduly high weighting to what are effectively duplicate measurements in similar locations, an advantage that is not significant in this case. An insufficient number of sampled locations could result in that the fitted semi-variogram not accurately representing the spatial correlations among weather variables, especially at a short distance lag. Furthermore, the smoothing effect of the nugget in the kriging process could degrade the performance of wind speed interpolation for the target location that is very close to its nearest sampled location. This is because wind speeds show significant spatial correlations at short distance lags while the nugget effect reduces the influence of the nearest sampled location on the target location.

Through a detailed comparison and assessment of the accuracy of different spatial interpolation methods for each weather parameter, the following spatial interpolation methods are employed in this research:

- Kriging combined with the lapse rate for air temperature;

- IDW combined with the modelling of the trend surface of wind speed at the reference level of 300m ASL in terms of distance to ocean (DTO) for wind speed; (The reference levels of 400m and 500m ALS are adopted for the overhead spans that are located above 300m and 400m ASL respectively);

- IDW combined with the decomposition of wind direction in the Cartesian coordinates for wind direction;

- IDW for solar radiation.

It should be noted that it cannot be guaranteed that any particular spatial interpolation method will be suitable for all cases [147]. The modelling of spatial trends in terms

of geographic parameters is location specific. For example, the effect of DTO on wind speed has been tested and considered for spatial interpolation in this research which focuses on a coastal area. However, this may be not applicable for an inland region or a particular area where there is no clear relationship between wind speed and DTO. Furthermore, spatial correlations among weather variables generally vary in different research areas, which may affect the selection of spatial interpolation models. As was discussed above, kriging works better than IDW for air temperature interpolation in this study since kriging takes account of similar spatial correlations between air temperatures at short distance lags and weakens the weight assigned to the nearest sampled location. For other study regions where air temperature shows a strong spatial correlation at short distance lags, kriging may have a performance similar to or worse than IDW. Moreover, as noted above, a fairly even distribution and a limited number of weather stations in a research area may degrade the performance of kriging which has an advantage of compensation for cluster effects and relies on the accurate modelling of spatial correlations between weather variables. Therefore, for different weather parameters or study regions of interest, an appropriate spatial interpolation method in each case has to be determined through assessment of the possible approaches [106].

5. PROBABILISTIC FORECASTING OF STEADY-STATE DYNAMIC LINE RATING

5.1. Introduction

The probabilistic forecasts of steady-state dynamic line rating (DLR) for up to a half hour (3 steps) ahead at two particular spans, CQ34-CQ35 and AC102-AC101B in proximity to weather stations 4 and 6 and eight 132kV overhead lines (OHLs) in the research area, are studied. The 132kV OHLs are composed of 'Lynx' ACSR $175mm^2$ and 'Poplar' AAAC $200mm^2$ conductors with maximum allowable conductor temperatures of 50℃ and 75℃ which are reduced to 45℃ and 70℃ respectively for reasons of conservatism [10], as was discussed in Section 3.3.5. The static line ratings (SLRs) for the two spans are $485A$ and $607A$ in winter (January and February) and $450A$ and $581A$ in spring (March) respectively [10].

Using the rank correlation based pairing method and the spatial interpolation model adopted for each weather parameter, 10^4 sets of correlated and independent random weather samples are generated for each span from the predictive distributions of the measured weather variables at a particular future moment. These correlated and independent weather inputs are then separately used to determine the possible forecasts of steady-state DLRs for each span based on a thermal model of overhead conductors [3]. The minimum value of DLR forecasts for all spans within an OHL is identified as the rating for the whole line in each of 10^4 scenarios. A sample cumulative distribution function (CDF) can be extracted from 10^4 sampled values of DLR forecasts for a particular span or an entire OHL. The percentiles of DLR forecasts are then smoothed and estimated by kernel density estimation [148].

The calibration of probabilistic steady-state DLR forecasts estimated by different approaches, i.e. the conditionally heteroscedastic (CH) models based on correlated weather samples, the CH models based on independent weather samples, and the

homoscedastic models based on independent weather samples, will be examined by their histograms of probability integral transform (PIT) so as to determine which approaches are most suited to estimation of DLRs, especially at lower percentiles for a particular span and an OHL. The forecast accuracies of the selected approaches will be assessed for different rating levels using persistence forecasting as a benchmark. It is noted that, in this chapter, steady-state DLRs estimated from weather observations through the thermal model of the conductors are regarded as the 'actual' ratings and that the uncertainty of DLR forecasts is modelled based on weather forecast errors only under an assumption of perfect spatial interpolation between weather variables.

5.2. Probabilistic DLR Forecasting for a Single Span

Random weather inputs for a particular span are separately estimated through a spatial interpolation between correlated and independent weather samples which are generated from the predictive distributions of the measured weather variables. For a single span in close proximity to a weather station, weather measurements at the station can be directly used to calculate probabilistic DLR forecasts for the span. The probabilistic 1-step-ahead and 3-step-ahead DLR forecasts at two spans CQ34-CQ35 and AC102-AC101B in proximity to weather stations 4 and 6 are studied here.

5.2.1. Calibration of probabilistic forecasts for a single span

When calculating probabilistic DLR forecasts for a single span in close proximity to an installed weather station, only correlations between random samples of different weather parameters at the station are considered. The predictive distribution of steady-state DLR is derived from the 10^4 sets of random weather samples using Monte Carlo simulation. Fig. 5-1 shows the predictive distributions of the measured weather variables for 3 steps ahead at station 4 and the corresponding distribution of DLR forecasts at span CQ34-CQ35 estimated from the correlated random weather

samples. The percentiles of DLR forecasts are then smoothed and estimated by kernel density estimation [148].
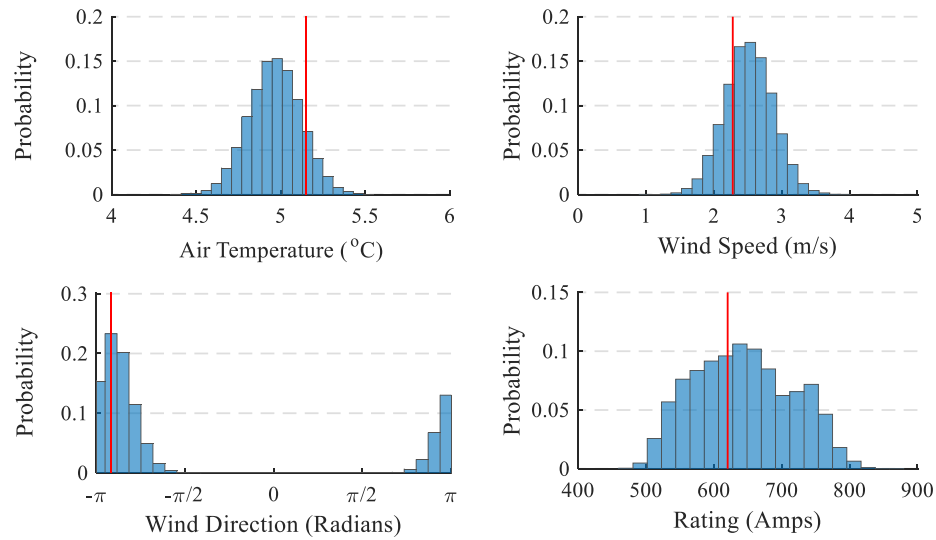
Fig. 5-1. Predictive distributions of weather conditions at weather station 4 and the corresponding steady-state DLR at span CQ34-CQ35 derived from the paired weather samples for 3 steps ahead at 12:00 on 25/02/2013 (observed values are represented by red lines).

Figs. 5-2 and 5-3 show the ratios of $5^{th} - 95^{th}$ percentiles, $25^{th} - 75^{th}$ percentiles, point forecasts of continuous DLRs modelled by the conditionally heteroscedastic (CH) models based on correlated (CH-C) weather samples for 1 step ahead and 3 steps ahead and weather observation based DLRs to the static line ratings (SLRs) on 27/03/2013 for CQ34-CQ35 and AC102-AC101B respectively. The distributions of 3-step-ahead DLR forecasts are less concentrated than that of 1-step-ahead forecasts on average due to the fact that a satisfactory calibration is to be preserved while the forecast errors increase for DLRs for 3 steps ahead.
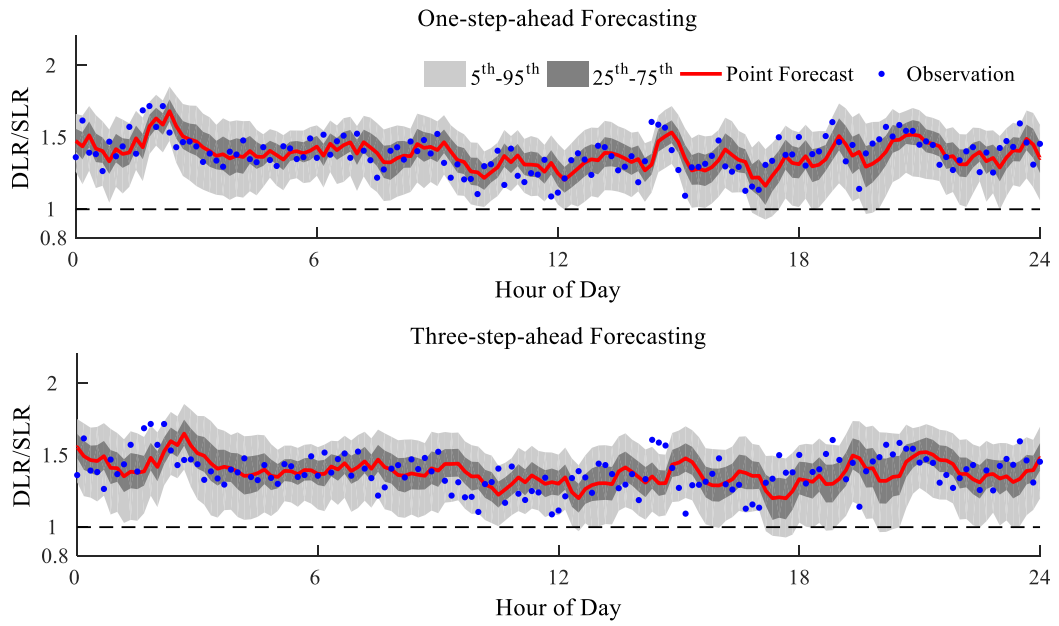
Fig. 5-2. Probabilistic 1-step-ahead and 3-step-ahead steady-state DLR forecasts on 27/03/2013 for span CQ34-CQ35
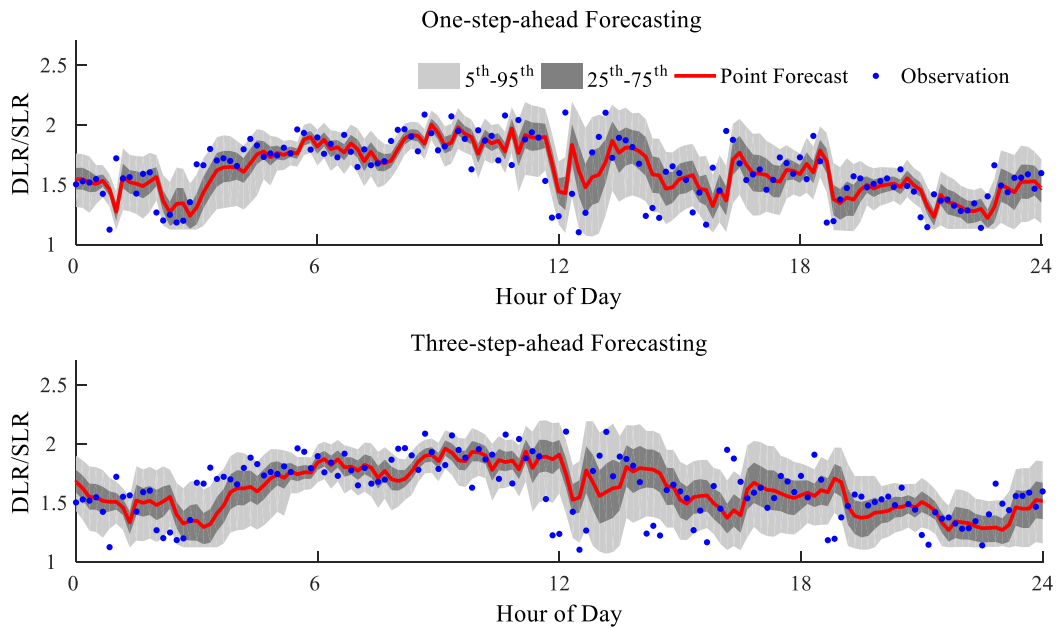
Fig. 5-3. Probabilistic 1-step-ahead and 3-step-ahead steady-state DLR forecasts on 27/03/2013 for span AC102-AC101B

As was noted in Section 3.2.5, the calibration of probabilistic forecasts can be assessed by the histogram of the probability integral transform (PIT). An approximately uniform PIT histogram reveals probabilistic forecasts to be fully calibrated. The PIT histograms for probabilistic steady-state DLR forecasts for half

hour ahead generated by the CH-C weather inputs, the CH models based on independent (CH-I) weather inputs, and the homoscedastic (H) models based on independent (H-I) weather inputs for two spans are plotted in Fig. 5-4. The relative frequency of 0.01 per percentile for a uniformly distributed PIT histogram is represented by a black solid line.
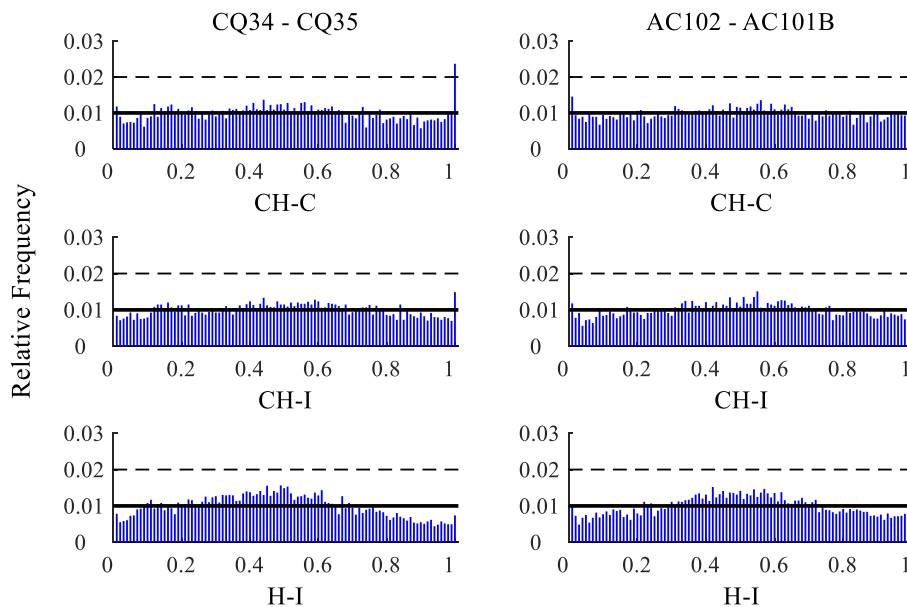
Fig. 5-4. PIT histograms of probabilistic 3-step-ahead steady-state DLR forecasts for the two spans

The PIT histograms of probabilistic steady-state DLR forecasts derived from the CH models are shown to have a better calibration than those derived from the H models. The hump shaped PIT histograms of DLR forecasts estimated by the H-I weather inputs indicate that the H-I probabilistic DLR forecasts are too dispersive on average. Furthermore, the relative frequencies at both ends of the CH-C PIT histograms are high which reveals that the predictive distributions of DLRs are less dispersive for most of the time. This might be due to the long-term positive correlations between the paired random samples of air temperature and wind speed as shown in Fig. 4-5. The increased cooling effect induced by high wind speeds is usually reduced by accompanied high air temperatures, and vice versa. This hypothesis is tested by comparing the PIT histograms of DLR forecasts for half hour ahead at the span

CQ34-CQ35 that are derived from (a) the independent random weather inputs, (b) the independent wind direction samples and the correlated samples of wind speed and air temperature that are paired based on historic weather observations and (c) the independent wind direction samples and the correlated samples of air temperature and wind speed that are paired based on a specified rank correlation of 0.9. These are shown in Fig. 5-5.
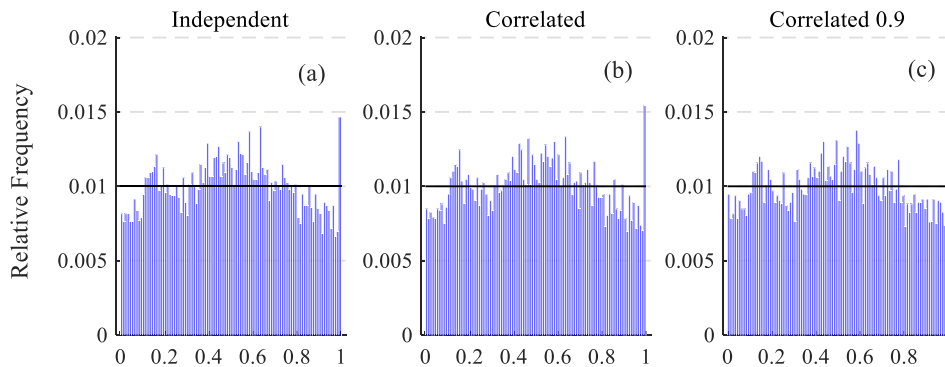
Fig. 5-5. PIT histograms of 30-minutes-ahead steady-state DLR forecasts at the span CQ34-CQ35 estimated from (a) the independent weather samples, (b) the independent wind direction samples and the correlated air temperature and wind speed samples that are paired based on historic weather observations and (c) the independent wind direction samples and the correlated air temperature and wind speed samples that are paired based on a specified rank correlation of 0.9.

When pairing the samples of air temperature and wind speed only, the PIT histogram (b) is very similar to the PIT histogram (a) derived from the independent random weather inputs. When a specified rank correlation of 0.9 is imposed on the random samples between air temperature and wind speed, the relative frequencies at both ends of the PIT histogram (c) are slightly higher than those that are derived from the independent random weather samples. This means that it is the correlation between wind speed and wind direction samples that makes the main contribution to the overconcentration of the CH-C model based predictive distributions of DLRs on average. This may be because air temperature predictions are so accurate that the range of air temperature samples at a particular future time is very small, leading to a slight impact of the correlation between wind speed and air temperature samples on the distribution of DLR forecasts. In addition, it is the rise of the maximum allowable

conductor temperature T_{cmax} above air temperature that determines the convection and radiation heat loss rates which affect steady-state DLRs. As was noted in Section 3.3.5, given a large difference between T_{cmax} and air temperature, the small range of air temperature samples at a particular future moment would have similar impacts on the prediction of steady-state DLRs.

The significant deviations from the ideal relative frequency of 0.01 at both ends of the CH-C PIT histograms are mitigated in the CH-I PIT histograms as shown in Fig. 5-4. In theory, the independent random weather samples should be treated as correlated. However, the additional correlations aggravate the concentration of under-dispersive CH-I probabilistic DLR forecasts in this research. Through checking the correlation between PIT values of the probabilistic DLR forecasts for each of the weather predictions, wind speed is found to be the dominant factor affecting the distributions of the PIT histograms of DLR forecasts. (The correlations in PIT values between DLR forecasts for the two spans and wind speed forecasts at the local weather stations are 0.75 and 0.67 respectively.) The PIT histograms of probabilistic steady-state DLR forecasts for 1 step (10 minutes) ahead are similar to the PIT histograms for 3 steps (half hour) ahead derived from the same models. The conclusions obtained from the histograms for 3 steps ahead can also be summarised from the histograms for 1 step ahead.

5.2.2. Accuracy of DLR forecasts for a single span

In spite of the extra current-carrying capacity released by DLRs being several times higher than the SLRs for most of the time, as shown in Figs. 5-2 and 5-3, in practical application, the upgrading of ratings will usually be limited to levels around 25% above the SLRs to prevent the protection scheme tripping and to reflect the constraints of other circuit equipment [71, 149]. Although the estimated lower DLR percentiles were found to exceed the uprating limit in some cases, the weather-based model developed here is necessary for the cases where the percentiles adopted from

probabilistic DLR forecasts are below 125% of SLRs. The accuracies (root mean square error, RMSE) of DLR forecasts estimated by the CH-I models for the three levels of less than 100% SLR, 100-125% SLR and above 125% SLR, are estimated respectively as tabulated in Table 5-1. It may be noted that the accuracies of point forecasts of steady-state DLRs calculated from the correlated and independent random weather samples are quite similar.

Table 5-1. RMSE (A) of steady-state DLR forecasts estimated by the CH-I models for the three levels of improvement of SLR and their improvement (%) over persistence

Span		CQ34-CQ35		AC102-AC101B	
Step(s) ahead		1	3	1	3
Total	RMSE	53.3	61.7	65.1	77.6
	Improve.	11.34%	12.07%	9.25%	11.46%
≤100% SLR	RMSE	80.7	95.1	N/A[†]	N/A
	Improve.	−7.51%	−5.03%	N/A	N/A
100-125% SLR	RMSE	52.9	59.1	89.9	113.6
	Improve.	17.45%	18.59%	−4.25%	−2.56%
>125% SLR	RMSE	48.6	57.0	61.0	71.6
	Improve.	12.95%	13.42%	12.21%	14.95%

[†]Only one rating observation was found below SLR for AC102-AC101B.

The CH-I model based DLR predictions are shown to be significantly better than persistence. For the key level of 100-125% SLR, the CH-I models perform much better for CQ34-CQ35, but worse for AC102-AC101B, than persistence. That is, the CH-I forecasting models perform worse for both spans at the levels of their respective lower ratings (the levels below SLR for CQ34-CQ35 and of 100-125% SLR for AC102-AC101B). It is found that wind speed observations corresponding to lower rating levels are mainly within the ranges of smaller values where the improvement in RMSE over persistence for the AR(4)-CH forecasting models is quite small, i.e. 0.66% at CQ34-CQ35 and 0.27% at AC102-AC101B. The

distributions of errors of DLR forecasts for 3 steps ahead at the level below the SLR and the distributions of corresponding wind speed and wind direction observations and their 3-step-ahead forecasts for CQ34-CQ35 are compared in Fig. 5-6.
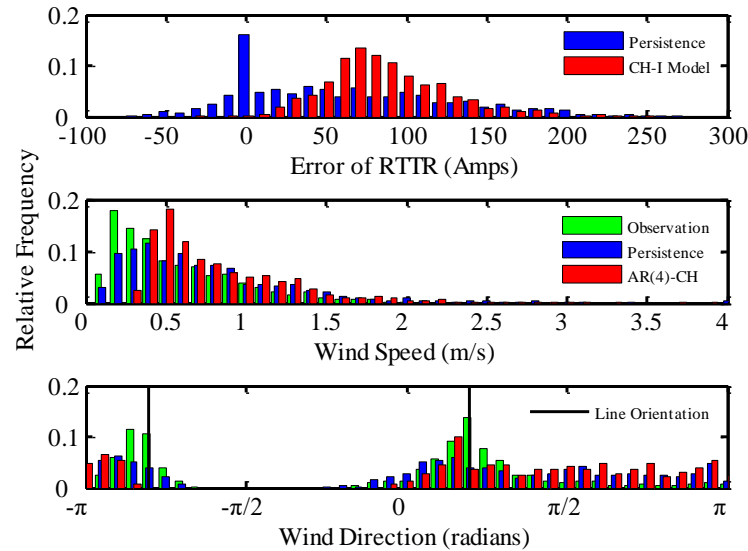
Fig. 5-6. Distributions of errors of 3-step-ahead steady-state DLR forecasts, the wind speed and wind direction observations and their 3-step-ahead forecasts corresponding to the rating level below the SLR for CQ34-CQ35

Fig. 5-6 reveals that the DLRs predicted by the CH-I models are usually overestimated at the low rating levels (<SLR) due to the wind speed forecasts being significantly overestimated by the AR(4)-CH models. It is interesting that a significant proportion of the DLR persistence forecast errors are concentrated around zero which might be due to the predicted and observed wind speeds having very low values ($\leq 0.4 m/s$). This will lead to small differences between the predicted and observed DLRs, especially when wind directions are nearly parallel to the overhead span which mitigates wind cooling. The experimental results indicate that, at this low rating level, the persistence forecasts and observations of wind speed are both under $0.4 m/s$ for 23.6% of the time and both under $0.3 m/s$ for 10.3% of the time, while for the AR(4)-CH model, the corresponding percentages of time are only 6.5% and 0.3% respectively. The AR(4)-CH model's overestimation at lower values of wind speed can also explain the unsatisfactory performance of the CH-I model at the level

of 100-125% SLR for AC102-AC101B. Therefore, the lower percentiles of DLR forecasts derived from the CH-I model should be applied so as to avoid the risk of using the overestimated point predictions of steady-state DLRs for a particular span.

The average additional capacities (AAC) above SLR (in %) released by the CH-I 1st, 3rd and 5th percentiles for 3 steps (30 minutes) ahead and the percentage of time that these percentiles are above SLR are listed in Table 5-2. The extra thermal headroom which can be exploited by lower percentiles for AC102-AC101B is much higher than that for CQ34-CQ35. Furthermore, the lower rating percentiles for AC102-AC101B are usually greater than its SLRs. It is found that the SLRs used for AC102-AC101B (i.e., $607A$ for winter and $581A$ for spring [10]) are smaller than those (i.e., $654.4A$ and $609.1A$) that are calculated by the thermal model of the conductors [3] based on the 'worst-case' weather assumptions for the SLR estimation (wind speed of $0.5\,m/s$, wind attack angle of 12.5^o, zero solar radiation and air temperatures of 2℃ and 9℃ for winter and spring respectively) [150]. This may be because the emissivity (ranging from 0 to 1) of the 'Poplar' conductor studied here was estimated to be 0.9 for AC102-AC101B after a few years' service, which increased the radiation heat loss rate and the SLRs. If the SLRs of AC102-AC101B were replaced by $654.4A$ and $609.1A$ for winter and spring respectively, the CH-I 1st, 3rd and 5th percentiles of DLR forecasts for half hour ahead would be higher than the updated SLRs in 83.26%, 88.25% and 91.06% of cases.

Table 5-2. The average additional capacities (AAC) above SLR (%) for CH-I 1st, 3rd and 5th percentiles for 3 steps ahead and the percentages of time for the percentiles above SLR

	1st Percentiles		3rd Percentiles		5th Percentiles	
% above SLRs	AAC	Time	AAC	Time	AAC	Time
CQ34-CQ35	3.5%	44.5%	8.0%	54.1%	10.7%	59.3%
AC102-AC101B	24.9%	99.2%	29.1%	99.6%	31.6%	99.8%

5.2.3. Effectiveness of using lower percentiles for a single span

In order to have clear limits to system operation that, in turn, drive decisive action, a system operator is likely to set a policy in which a particular percentile is adopted from a probabilistic forecast and regarded as The Limit. This is consistent with current practice in Britain in which static line ratings (SLRs) are calculated based on a certain small probability of the actual rating being greater than the quoted SLR [5]. One reasonable policy that might be adopted would be to ensure that the loading on a line never exceeds the 5th percentile (P5 value) from the probabilistic forecast. The effectiveness of any policy should be checked. Fig. 5-7 shows the differences between the 3-step-ahead P5 forecast and the actual rating when the time comes. If the probabilistic forecasting works well then, on average, the actual rating should be less than the P5 forecast in no more than 5% of cases.
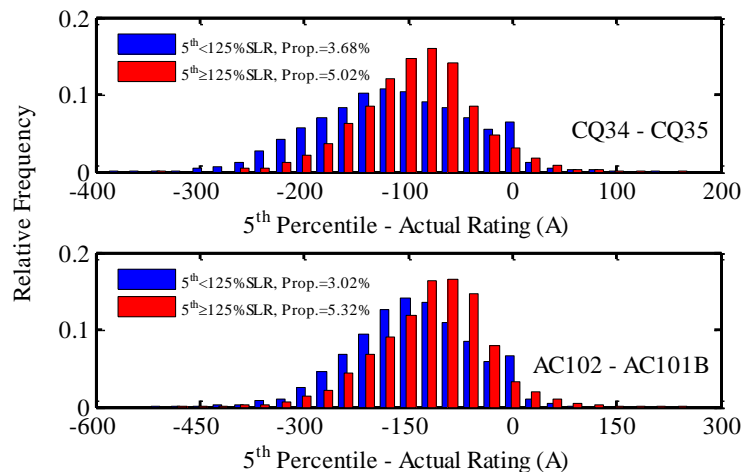
Fig. 5-7. The distributions of differences between the 5th percentile (P5) forecasts for 3 steps ahead and their corresponding actual ratings and the proportion of positive differences for cases (a) when P5 forecast is less than 125% of SLR and (b) when it is greater than or equal to 125% of SLR

As noted above, various practical issues will prevent more than a certain uprating relative to the SLR, e.g. 25%. As a consequence, Fig. 5-7 shows two sets of two results for two different overhead spans: for 6662 and 4207 cases in which the P5 forecast was less than 125% of SLR; and 2410 and 4865 cases in which it was greater than or equal to 125%. For CQ34-CQ35, the test set showed 3.68% of the

former cases in which the actual rating was less than the P5 value and 5.02% of the latter. For AC102-AC101B, the actual rating was less than the P5 forecast in 3.02% of cases when the P5 forecast rating was less than 125% of SLR and 5.32% otherwise. Although these seem reasonable results, the test set contains an example of a quite large positive difference between the P5 forecast ($1091.9A$) and the actual value ($829.3A$) on AC102-AC101B: $262.6A$ compared with the relevant seasonal SLR of $607A$. This occurred after a period of 6 hours in which the wind speed had been greater than $3m/s$ which led to a forecast wind speed of $3.29m/s$ but where it turned out actually to be $1.31m/s$. In addition, at that moment, the wind blew at 43.14^o to the span whereas it had previously been perpendicular to it, leading to a forecast angle of incidence equal to 89.33^o. The convection heat loss rate per unit length estimated from the actual weather data was around $88.94\,W/m$ while it was forecast to be about $188.11\,W/m$. However, regardless of how much above 125% the P5 forecast was, if the system operator limited loading on the line to no more than 125%, such a limit would have proved to be too high relative to the actual rating in only 3% and 2.1% of cases for the different spans and the extreme case noted would have presented no problem. Moreover, it can be seen from Fig. 5-7 that the standard deviation of differences is higher for cases forecasting a small uprating than for those that forecast a higher uprating. This can be explained by the precise uprating being more sensitive to the exact wind speed at low speeds than at high wind speeds.

5.3. Probabilistic DLR Forecasting for a Complete OHL

The weather-based DLR model developed for a single span is extended to estimate probabilistic forecasts of steady-state DLRs for an entire overhead line (OHL) by using the spatial interpolation models refined in Chapter 4 to infer the possible weather conditions for each span within the line from the independent and correlated weather forecasts randomly sampled from the conditionally heteroscedastic (CH)

distributions of the measured weather variables. The minimum value of DLR forecasts for all spans calculated from the inferred weather samples is applied to the whole OHL in each of the generated 10^4 scenarios. The cumulative distribution function extracted from the 10^4 sampled values of steady-state DLR forecasts at a particular future time is then smoothed by kernel density estimation [148] to determine predictive DLR percentiles for the entire OHL. The probability of each span within an OHL being the critical span at a particular future time is defined as the frequency of the span having the minimum value of DLR forecasts at all spans in the 10^4 scenarios. As was noted in Section 4.3, random samples of air temperature and wind speed are only paired for the estimation of probabilistic DLR forecasts for an entire OHL since the rank correlation matrix calculated from recent weather observations at different weather stations may not be positive definite when additionally including wind direction samples.

In this section, the calibration of probabilistic steady-state DLR forecasts for an OHL estimated by different approaches is assessed so as to determine a conservative approach to producing lower percentiles of DLR forecasts. The forecast accuracies of steady-state DLRs and critical spans for an OHL estimated by the adopted approach are then examined for each of the eight 132kV OHLs in the research area.

5.3.1. Calibration of probabilistic DLR forecasts for an overhead line

Details of eight 132kV overhead circuits in North Wales between Pentir and Connah's Quay covering the number of spans, circuit length (km), conductor types and average elevations (m) above sea level are provided in Table 5-3 [10]. Since the ampacity of a line is limited by the span that has the lowest rating, static line ratings (SLRs) of an OHL comprising two conductor types are determined as those for the 'Lynx' ACSR conductor. Therefore, the circuit from Kinmel Bay Tee (B3) to St Asaph (B4) has the SLRs of $607A$ in winter and $581A$ in spring while all the other circuits have the SLRs of $485A$ in winter and $450A$ in spring.

Table 5-3. Details of eight 132kV overhead circuits in North Wales [10]

Circuit No.	Circuit	No. of Spans	Total Length (km)	Conductor Types	Max./Min. Elevation (m)	Average Elevation (m)
C1	Pentir (B1) to Colwyn Bay (B2)	153	42.0	6.0km Poplar 36.0km Lynx	420/3	194
C2	Colwyn Bay (B2) to Kinmel Bay Tee (B3)	74	21.2	19.9km Lynx 1.3km Poplar	310/3	110
C3	Kinmel Bay Tee (B3) to St Asaph (B4)	22	6.7	Poplar	201/24	110
C4	Pentir (B1) to Dolgarrog (B5)	87	24.0	18.0km Lynx 6.0km Poplar	219/21	79
C5	Dolgarrog (B5) to St Asaph (B4)	94	26.9	7.5km Poplar 19.4km Lynx	308/3	164
C6	St Asaph (B4) to Holywell (B6)	50	13.4	Lynx	252/11	114
C7	Holywell (B6) to Connah's Quay (B7)	50	15.7	Lynx	285/14	145
C8	St Asaph (B4) to Connah's Quay (B7)	98	29.8	Lynx	285/11	129

Fig. 5-8 shows the ratios of 5th – 95th percentiles, 25th – 75th percentiles, point forecasts of steady-state DLRs modelled by the CH models based on correlated weather samples for 3 steps (half hour) ahead and weather observation based DLRs to the SLRs on 27/03/2013 for the overhead circuit C2 from Colwyn Bay (B2) to Kinmel Bay Tee (B3) and the circuit C3 from Kinmel Bay Tee (B3) to St Asaph (B4). The PIT histograms of probabilistic 3-step-ahead DLR forecasts generated by the CH models based on correlated (CH-C) and independent (CH-I) weather samples for the different 132kV OHLs are plotted in Figs. 5-9 and 5-10.
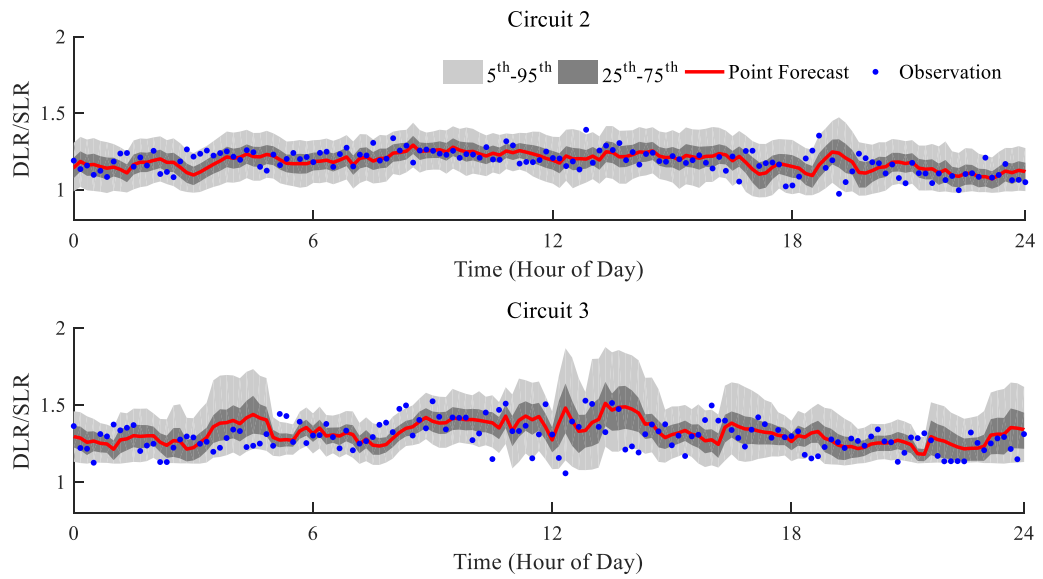
Fig. 5-8. Probabilistic steady-state DLR forecasts for 3 steps ahead on 20/03/2013 for the circuit C2 from Colwyn Bay (B2) to Kinmel Bay Tee (B3) and C3 from Kinmel Bay Tee (B3) to St Asaph (B4)
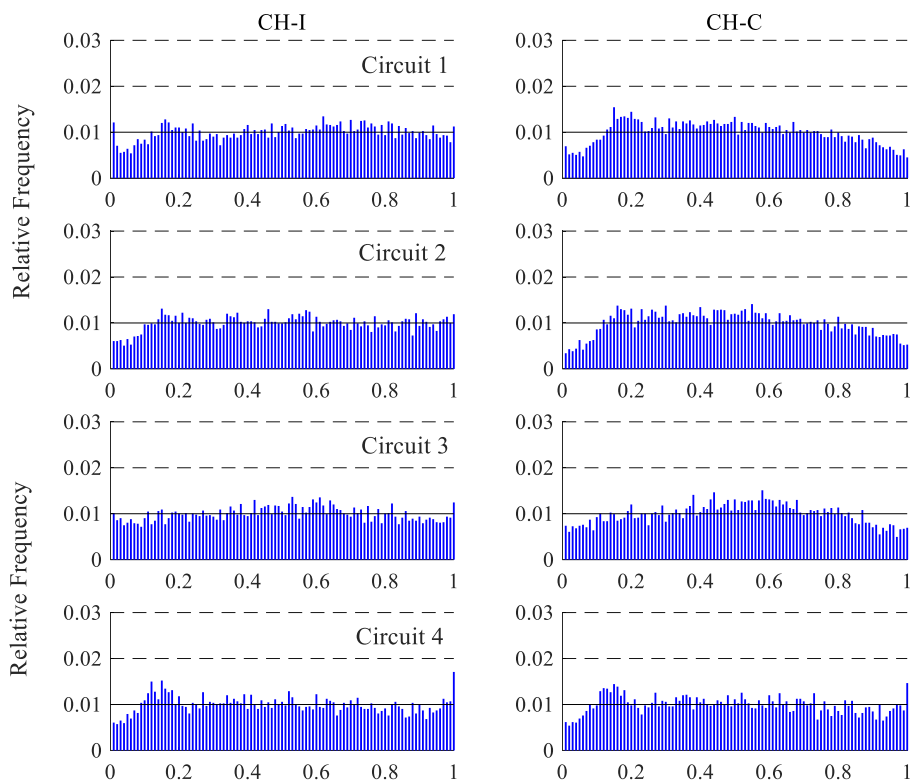
Fig. 5-9. PIT histograms of probabilistic 3-step-ahead steady-state DLR forecasts for OHLs C1 – C4
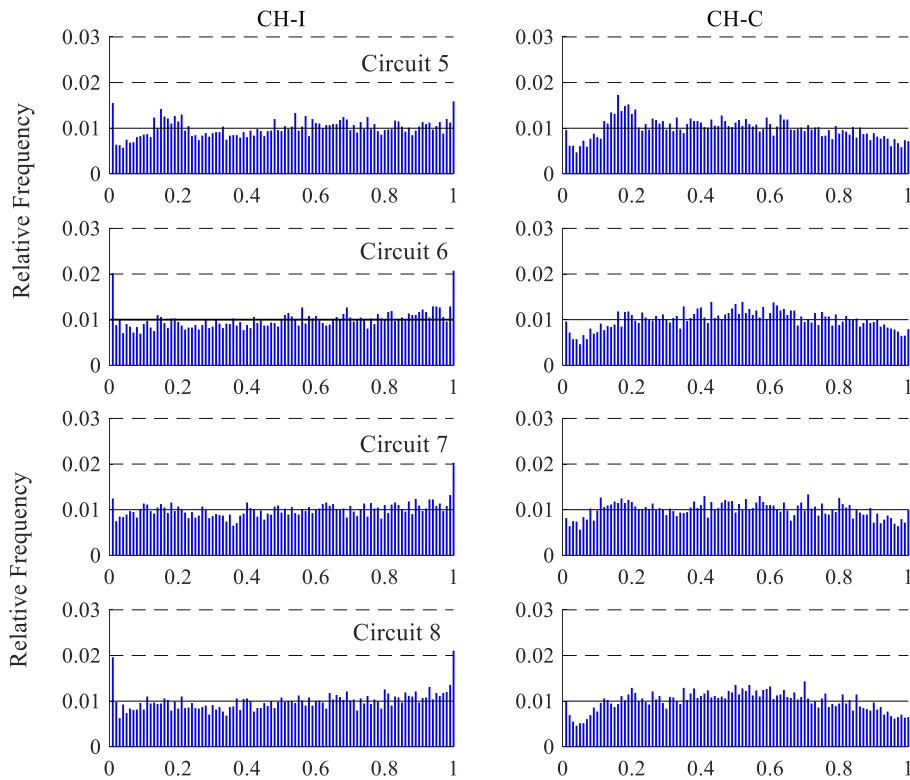
Fig. 5-10. PIT histograms of probabilistic 3-step-ahead steady-state DLR forecasts for OHLs C5 – C8

The relative frequencies at both ends of the CH-I PIT histograms are higher than those of the CH-C PIT histograms, especially for overhead circuits C5 – C8, meaning that the distributions of DLR forecasts derived from the independent random weather samples are on average less dispersive. In other words, the CH-I lower percentiles of DLR forecasts are overestimated while the higher percentile forecasts are underestimated for most of the time. The significant deviations from the ideal relative frequency of 0.01 at both ends of the CH-I PIT histograms are mitigated in the CH-C PIT histograms. This might be due to the positive correlations between the paired random samples of the same weather parameters at different weather stations as shown in Fig. 4-6.

As noted in Section 5.2.1, wind speed is the dominant factor affecting the rating of an overhead conductor. The values of the paired (correlated) wind speed samples at different weather stations in each of the 10^4 scenarios will be at the similar levels

with respect to their respective ranges of 10^4 sampled values due to the significant positive correlations among them. That is, the wind speed sample from a 'low' value at a station is usually accompanied by 'low' wind speed samples at the other stations in a particular scenario. Therefore, the possible wind speeds at all spans within an OHL inferred from the paired samples of 'low' wind speeds at stations are at their respective 'low' levels as well, which leads to a 'low' rating sample applied to each OHL. When using the independent weather inputs, all the stations having 'low' wind speed samples in a particular scenario would rarely happen. A span having a low wind speed sample may not be the critical span due to the fact that the conductor rating is also determined by other weather parameters. For example, a particular span that has a relatively high wind speed sample blowing parallel to the span or accompanied by a high air temperature sample may be the critical span. Therefore, the lower percentiles of DLR forecasts derived from the correlated wind speed samples for an entire OHL are generally smaller than those that are estimated from the independent samples. Similarly, the higher DLR percentiles generated by the CH-C models are generally greater than those for the CH-I models.

The influence of positive correlations between the paired air temperature samples at different stations on the concentration of predictive distributions of DLRs for an OHL can be explained in a similar way. Due to their significant positive correlations, the paired samples of air temperature that are at 'high' levels with respect to their respective distributions in a particular scenario would lead to each span within an OHL having a 'high' air temperature sample. This ensures that the minimum of DLR forecasts among all spans is at a 'low' level in that particular scenario. Therefore, the lower percentiles of DLR forecasts calculated from the correlated air temperature samples are smaller than those for the independent samples. However, the positive correlations among air temperature samples at different stations may have a less significant impact on the dispersion of predictive distributions of DLRs than that among wind speed samples due to the relatively high accuracy of air temperature

prediction. It can be concluded that the positive correlations between the paired random weather samples of the same parameters (i.e. air temperature and wind speed) at different stations help mitigate the overestimation of lower DLR percentiles that are derived from independent weather samples for an OHL.

5.3.2. Accuracy of DLR forecasts for an overhead line

The point forecasts of steady-state DLRs for up to 3 steps (half hour) ahead produced by the CH-C forecasting models are compared with persistence forecasts in root mean square errors (RMSEs) for each overhead circuit, as shown in Fig. 5-11 which demonstrates that the CH-C forecasting models give a significant improvement in RMSE over persistence for all OHLs.
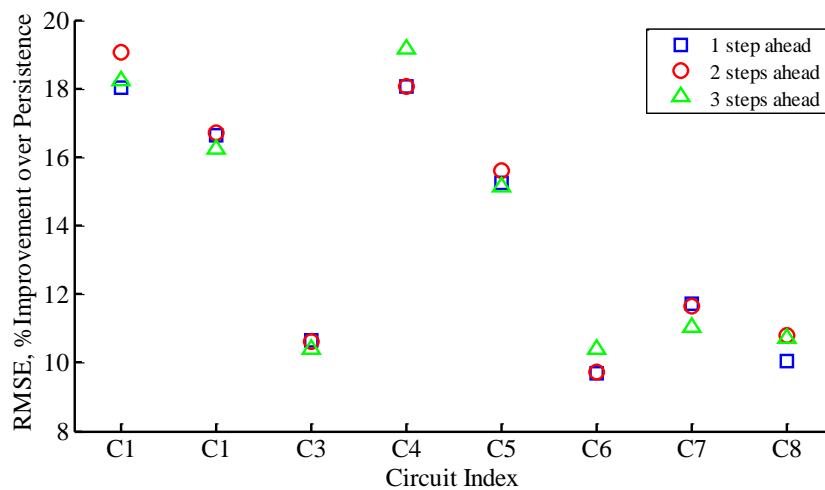
Fig. 5-11. Improvements over persistence in RMSE of point forecasts of steady-state DLRs for up to 3 steps ahead for the CH-C forecasting models for each OHL.

The accuracies (RMSE) of DLR forecasts estimated by the CH-C models for the five levels of less than 90% SLR, 90-100% SLR, 100-110% SLR, 110-120% SLR and above 120% SLR, are calculated respectively for each circuit as tabulated in Tables 5-4 and 5-5. The experimental results show that the CH-C forecasting models perform similarly to or even worse than persistence forecasting for most circuits at the levels of their respective low ratings (the levels of 100-110% SLR for circuit C3

and below 90% SLR for the other circuits). It is found that the DLR point predictions are usually overestimated by the CH-C forecasting models at the low rating levels due to the overestimation of corresponding wind speed forecasts by the AR(4)-CH forecasting models. Figs. 5-12 and 5-13 show the distributions of errors of 3-step-ahead DLR forecasts at the low rating levels for circuits C3 and C6 and the distributions of corresponding wind speed observations and their 3-step-ahead forecasts at the most influential weather stations (stations 5 and 6 for C3 and stations 6 and 7 for C6) respectively. Therefore, the lower percentiles of DLR forecasts should be applied for an entire OHL so as to avoid the risk of using the overestimated point forecasts of steady-state DLRs.

Table 5-4. RMSEs (*A*) of 3-step-ahead DLR forecasts for CH-C models for the five levels of improvement of SLR and their improvement (%) over persistence for circuits C1 – C4

Circuit		C1	C2	C3	C4
Total	RMSE	37.8	37.6	58.0	63.0
	Improve.	18.22%	16.25%	10.41%	19.18%
≤90% SLR	RMSE	41.2	48.8	N/A	89.7
	Improve.	5.19%	−1.65%	N/A	−2.84%
90-100% SLR	RMSE	31.9	38.8	N/A	69.0
	Improve.	17.05%	4.01%	N/A	11.63%
100-110% SLR	RMSE	31.4	32.6	85.1	49.4
	Improve.	33.00%	25.74%	−8.28%	26.54%
110-120% SLR	RMSE	38.7	32.1	68.4	39.7
	Improve.	23.75%	27.54%	3.39%	40.02%
>120% SLR	RMSE	50.8	40.8	53.9	75.8
	Improve.	9.29%	13.69%	14.12%	15.04%

Table 5-5. RMSEs (*A*) of 3-step-ahead DLR forecasts for CH-C models for the five levels of improvement of SLR and their improvement (%) over persistence for circuits C5 – C8

Circuit		C5	C6	C7	C8
Total	RMSE	46.9	35.7	45.4	33.1
	Improve.	15.14%	10.39%	11.03%	10.72%
≤90% SLR	RMSE	49.8	33.1	60.5	31.2
	Improve.	1.46%	−12.55%	−20.35%	−12.78%
90-100% SLR	RMSE	41.8	30.3	47.5	29.0
	Improve.	11.05%	7.93%	−5.45%	9.05%
100-110% SLR	RMSE	41.6	33.2	41.4	30.8
	Improve.	28.75%	20.44%	12.92%	18.99%
110-120% SLR	RMSE	40.0	36.6%	40.8	34.7
	Improve.	30.63%	15.18%	21.85%	15.96%
>120% SLR	RMSE	55.2	39.3	45.5	36.2
	Improve.	9.10%	9.35%	13.68%	9.71%
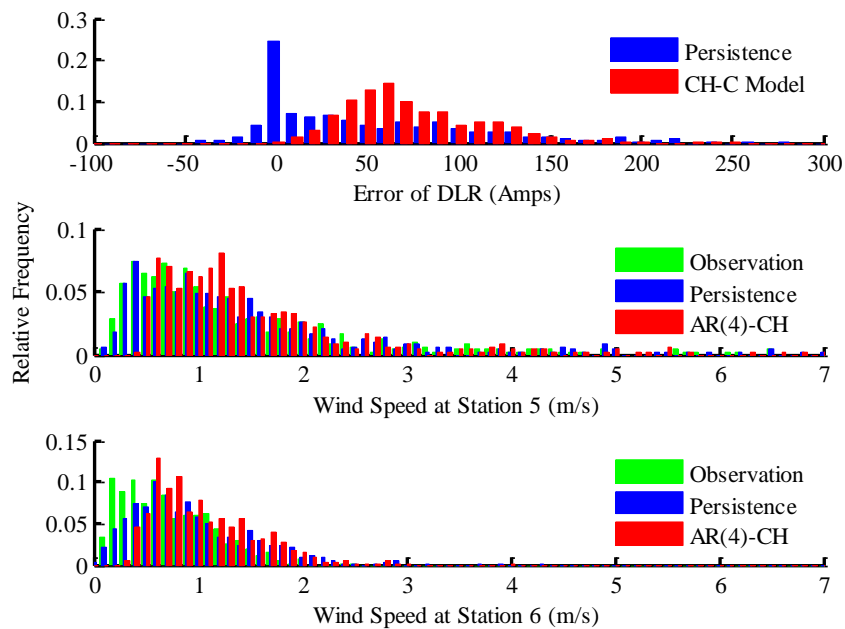
Fig. 5-12. Distributions of errors of 3-step-ahead DLR forecasts, the wind speed observations and their 3-step-ahead forecasts at weather stations 5 and 6 corresponding to the rating level below 110% SLR for circuit C3.

164
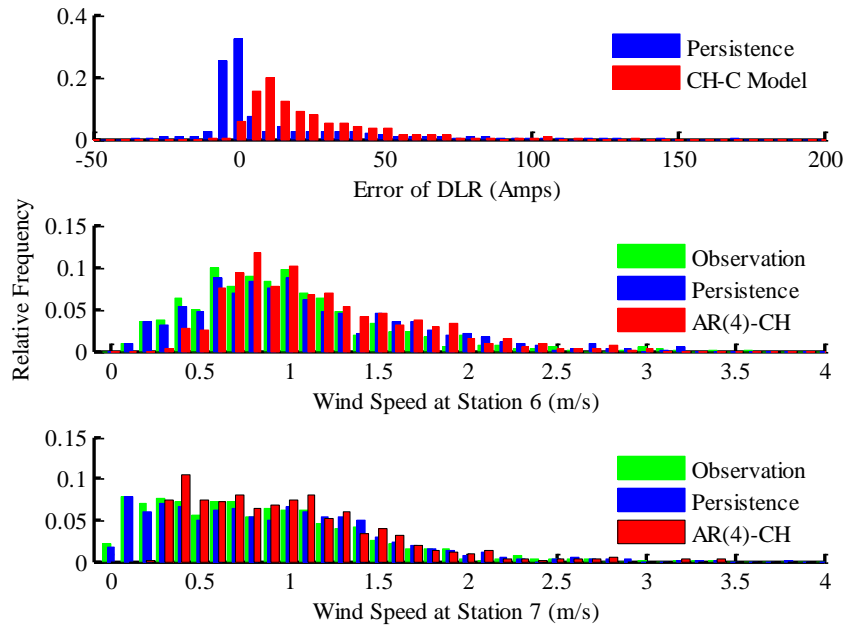
Fig. 5-13. Distributions of errors of 3-step-ahead DLR forecasts, the wind speed observations and their 3-step-ahead forecasts at weather stations 6 and 7 corresponding to the rating level below 90% SLR for circuit C6.

5.3.3. Forecast precision of critical span for an overhead line

The critical span that limits the rating of an entire OHL at a particular future time is identified in each of the 10^4 scenarios. The probability of each span within a circuit being the critical span is then defined as the frequency of the span having the minimum DLR forecast among all spans in the 10^4 scenarios. Fig. 5-14 shows the probabilities of each span within the circuit C3 being the critical span for 3 steps (half hour) ahead during 00:00–00:20 on 27/03/2013. For a particular future moment, the five most frequent critical spans could be predicted. The forecast precision of each most frequent critical span is defined here as the ratio of the number of the case where the frequent critical span accurately predicts the actual critical span when the time comes to the total amount of cases. The forecast precision of each most frequent critical span and their total precision that is the percentage of cases that the actual critical span is accurately forecast by any of the five most frequent critical spans for 3 steps ahead along each circuit are plotted in Fig. 5-15.

165
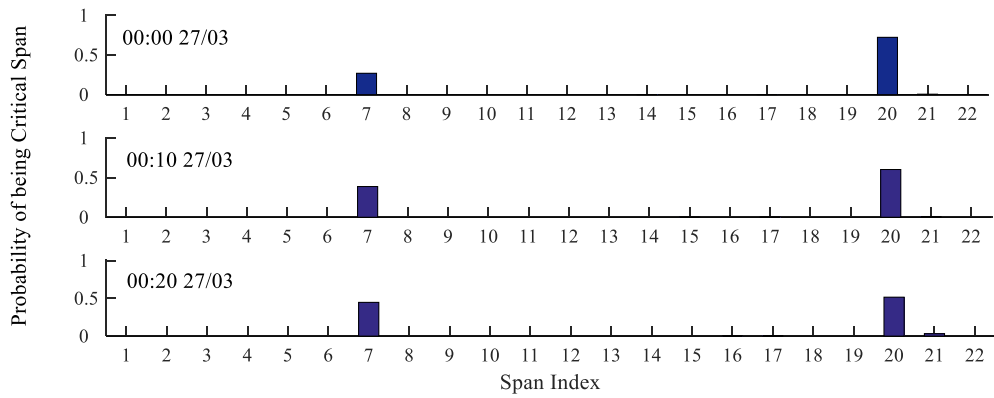
Fig. 5-14. Probabilities of each span within circuit C3 being the critical span for 3 steps ahead during 00:00–00:20 on 27/03/2013
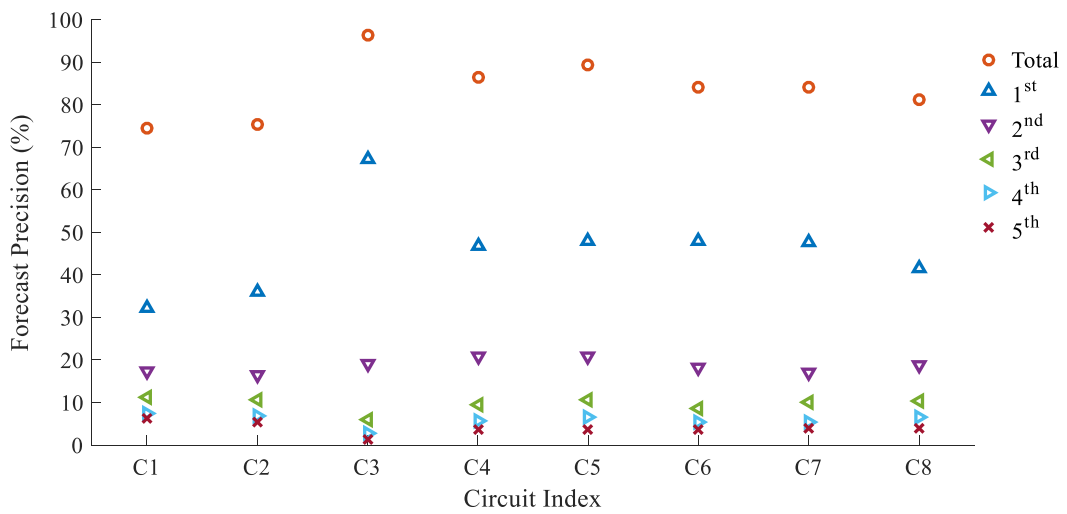
Fig. 5-15. Forecast precisions of the five most frequent critical spans for 3 steps (half hour) ahead along each circuit

The experimental results indicate that the location of critical span is accurately predicted by the 5 most frequent critical spans in greater than 70% of cases for most overhead circuits. The forecast precision of critical span is influenced by a number of factors in a complex way, e.g. forecast accuracies of the measured weather variables, numbers and orientations of spans within a circuit, etc. The number of spans within an OHL and the variation in line's orientation are important factors that are discussed here. An OHL having a large number of spans usually covers a long distance and crosses different terrains, which may increase the difficulty of predicting the location of critical span. As shown in Fig. 5-15, the forecast precision of critical span for C1 that consists of 153 spans and covers a long distance of $42km$ is relatively lower

than other circuits, while circuit C3 that consists of 22 spans and covers $6.7km$ has the most accurate predictions of critical spans.

The large variation in orientation of circuit C1 from 132kV bus B1 (in proximity to weather station WS1) to B2 (in proximity to WS4), as shown in Fig. 1-3, may be an additional reason for the less precise prediction of the critical span. Since it is the angle between line orientation and wind direction that affects the convection cooling on conductors, an error in wind direction forecast can result in very different effects on two spans which are perpendicular to each other, i.e. maximum convection cooling on one span and minimum cooling on the other. Therefore, the differences in wind direction between forecasts and actual values may easily lead to an incorrect prediction of the critical span for a circuit which has significant variations in orientation. If the spans within a circuit are of similar orientations, the influence of forecast errors of wind direction on the critical span prediction may be reduced to some extent. There are only minor changes in orientation of circuit C5 from bus B5 (in proximity to WS2) to B4 (in proximity to WS6) as shown in Fig. 5-16. Though C5 consisting of 94 spans covers a large area, the forecast precision of critical span is similar to that for C6 (from B4 to B6 in proximity to WS7) and C7 (from B6 to B7 in proximity to WS9) which are both made up of only 50 spans but have relatively large variations in orientations as shown in Fig. 5-16. Furthermore, the differences in orientation between particular spans within each of circuits C6 and C7 almost reach 90°, increasing the influence of wind direction forecast error on the precision with which the critical span is identified.
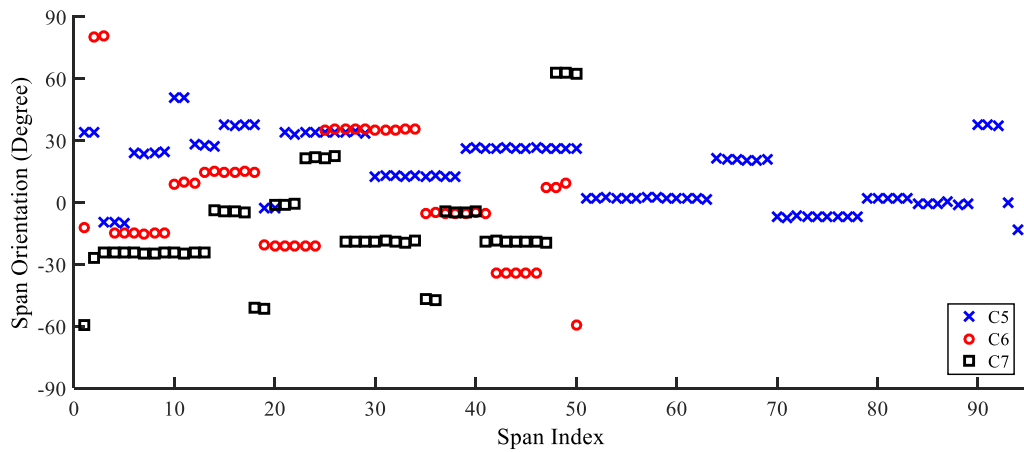
Fig. 5-16. Orientations (in degree) of spans within circuits C5, C6 and C7

5.3.4. Effectiveness of using lower percentiles for an overhead line

As noted above, a particular lower DLR percentile, e.g. the 5th percentile (P5 value) is likely to be adopted from a probabilistic DLR forecast and regarded as the thermal limit for an OHL so as to avoid the risk of using overestimated point forecasts of DLRs. Since the upgrading of ratings is usually limited to around 25% above the SLRs in practical applications, the effectiveness of using P5 values as thermal limits for OHLs are verified for two different situations, i.e. $P5 < 125\% \, SLR$ and $P5 \geq 125\% \, SLR$. Fig. 5-17 shows the differences between the P5 forecasts for 3 steps (half hour) ahead and the actual ratings when the time comes for circuits C2 and C3. For circuit C2, the actual rating exceeds the P5 value in 2.01% of the former cases and in 4.72% of the latter. For circuit C3, the actual rating is less than the P5 forecast in 3.17% of cases that forecast a small uprating and in 4.3% otherwise.
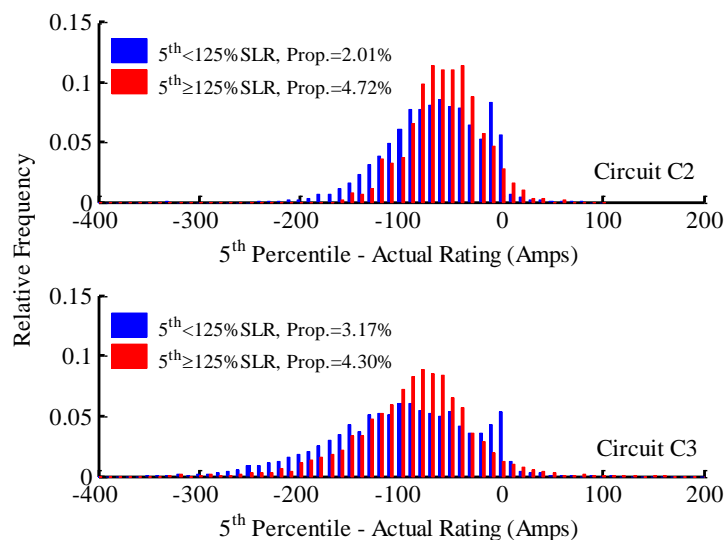
Fig. 5-17. The distributions of differences between the 5th percentile forecasts for half hour ahead and their corresponding actual ratings and the proportion of positive differences for cases (a) when the 5th percentile forecast is less than 125% of SLR and (b) when it is greater than or equal to 125% for circuits C2 and C3

It is interesting that a significant proportion of differences between the actual ratings and the P5 forecasts that provide a small uprating are concentrated around zero. This might be because, in some particular cases, probability densities at the lower end of predictive distributions of DLRs are so high that values of the lower DLR percentiles are quite similar. For example, the differences between P25 (the 25th percentile) and P5 forecasts are less than $10A$ and $5A$ in 951 cases and 439 cases respectively (i.e. 11.25% and 5.19% of the cases where $P5 < 125\% \, SLR$) for C2, and in 397 cases and 152 cases respectively (i.e. 6.8% and 2.6% of the cases where $P5 < 125\% \, SLR$) for C3. Therefore, the actual ratings may be very close to the P5 forecasts though their corresponding PIT values are greater than 0.05.

The percentages of time that the actual ratings are less than the P1 (the 1st percentile), P3 (the 3rd percentile) and P5 forecasts for 3 steps (half hour) ahead are evaluated to be mostly smaller than their corresponding theoretical values, meaning that the predictive lower DLR percentiles are conservative on average. When the upgrading of ratings is limited to 125% of the SLRs, the percentages of time for which the actual ratings exceed the corrected lower DLR percentiles are smaller than those for

the original percentiles, as listed in Table 5-6. Therefore, the corrected lower DLR percentile for a reasonable calibration has the potential to be employed in system operation decision making.

Table 5-6. The percentages of time for which the actual ratings exceed the 3-step-ahead P1, P3 and P5 forecasts and those that are limited to 125% of SLRs for each circuit

% Time below Percentiles	P1 Forecasts		P3 Forecasts		P5 Forecasts	
	Original	Corrected	Original	Corrected	Original	Corrected
C1	0.75%	0.75%	1.78%	1.74%	2.92%	2.89%
C2	0.36%	0.34%	1.17%	1.04%	2.19%	1.95%
C3	0.82%	0.62%	2.14%	1.47%	3.57%	2.46%
C4	0.63%	0.62%	1.78%	1.73%	3.07%	2.97%
C5	1.00%	1.00%	2.21%	2.19%	3.30%	3.27%
C6	0.99%	0.99%	2.27%	2.21%	3.44%	3.27%
C7	0.83%	0.69%	2.22%	1.70%	3.50%	2.58%
C8	1.03%	1.01%	2.24%	2.17%	3.23%	3.11%

The average additional capacities (AAC) above SLRs (in %) released by the original (ORIG) and corrected (CORR) P1, P3 and P5 forecasts for 3 steps ahead and the percentages of time for which these percentiles are above SLRs are estimated for each circuit as tabulated in Table 5-7. Except for circuit C3 comprising 'Poplar' AAAC conductors only, the predictive lower DLR percentiles at the other circuits are usually below the SLRs. The extra thermal headroom that can be exploited by lower percentiles for C3 is much higher than those for the other circuits. Furthermore, the slight reductions in AAC at some circuits (e.g. C1) due to the limitations on uprating mean that the original forecasts of lower DLR percentiles do not often exceed 125% of SLRs.

Table 5-7. The average additional capacities (AAC) above SLRs (%) for the original (ORIG) and corrected (CORR) P1, P3 and P5 forecasts for 3 steps ahead and the percentage of time for the percentiles above SLRs

% above SLR	P1 Forecasts			P3 Forecasts			P5 Forecasts		
	AAC ORIG	AAC CORR	Time	AAC ORIG	AAC CORR	Time	AAC ORIG	AAC CORR	Time
C1	-9.80%	-9.81%	5.25%	-8.34%	-8.37%	9.87%	-7.30%	-7.35%	13.56%
C2	-2.65%	-2.76%	32.12%	0.07%	-0.17%	41.10%	1.69%	1.33%	46.10%
C3	17.38%	14.09%	99.08%	20.31%	15.80%	99.49%	22.06%	16.77%	99.67%
C4	-7.29%	-7.37%	13.27%	-4.97%	-5.11%	22.04%	-3.35%	-3.54%	28.38%
C5	-8.64%	-8.78%	8.35%	-6.73%	-6.96%	15.02%	-5.39%	-5.67%	19.78%
C6	-3.24%	-3.57%	28.72%	-0.86%	-1.36%	35.90%	0.53%	-0.08%	40.65%
C7	5.20%	3.50%	50.62%	8.49%	6.02%	58.54%	10.34%	7.37%	62.52%
C8	-3.61%	-3.79%	27.79%	-1.31%	-1.63%	34.18%	0.03%	-0.39%	38.35%

5.3.5. Effects of interpolation errors of weather variables on DLRs

As was detailed above, probabilistic forecasts of steady-state DLRs estimated for a particular future time for a complete line have considered the uncertainty of weather forecasts only. However, the uncertainty of spatial interpolation of weather variables cannot be modelled by the inverse distance weighting or kriging methods developed in Chapter 4 and was not reflected on the distributions of steady-state DLRs for a line. Therefore, it should be noted that the above analysis of steady-state DLR forecasting for a complete line, e.g. calibration and accuracy of probabilistic DLR forecasts and possible critical spans, is based on an assumption of perfect spatial interpolation of weather variables. In order to examine influences of spatial interpolation errors of weather variables on the accuracy of DLR estimates, the interpolation value of a particular weather variable at a particular station inferred from observations at other stations by the spatial interpolation method selected in Chapter 4 and measurements of other weather variables at the station are used to calculate the steady-state DLR

for a span in the vicinity of the station. Fig. 5-18 shows percentage errors of DLR estimates for spans CQ34-CQ35 and AC102-AC101B that are affected by the spatial interpolation errors of each weather variable respectively.
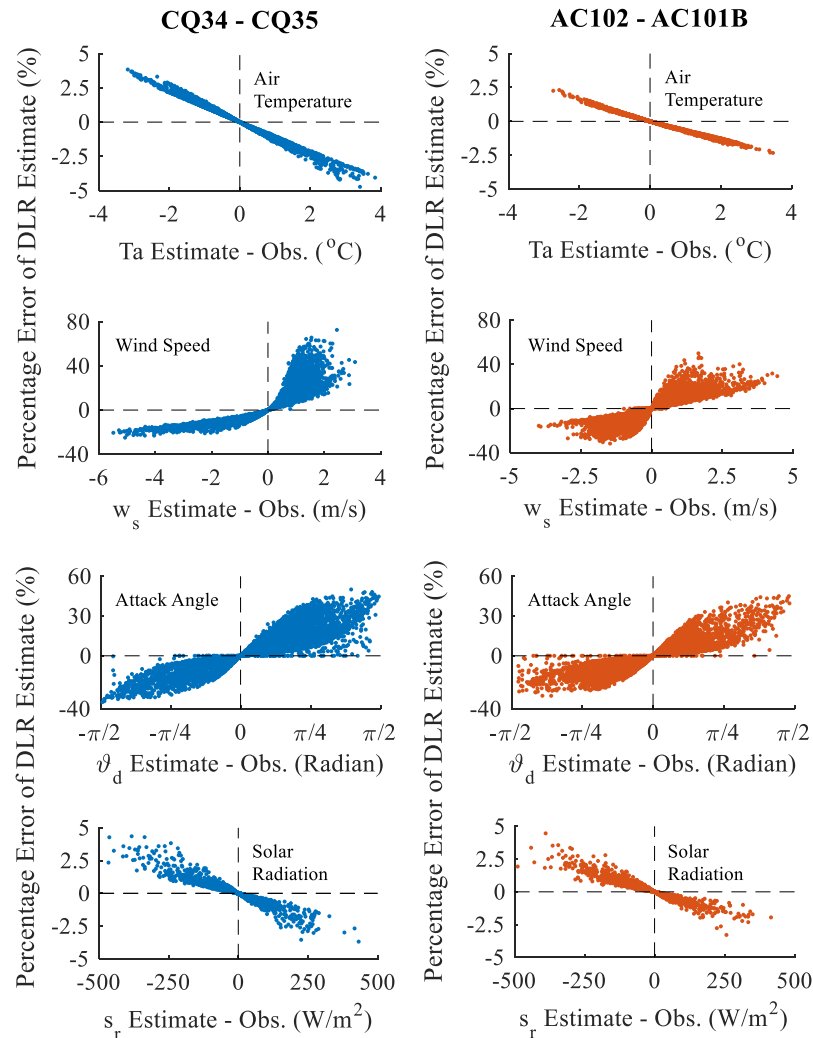
Fig. 5-18: Percentage errors of steady-state DLR estimates at different spans that are calculated from interpolation values of each weather variable and observations of other variables.

As noted in Section 3.3.5, the accuracy of steady-state DLR estimates is generally more sensitive to the errors of wind speed and attack angle between wind direction and line orientation. This can also be summarised from Fig. 5-18. Furthermore, the maximum magnitudes of spatial interpolation errors of weather variables are shown to be higher than those for weather forecast errors, leading to more significant errors of DLR estimates. Table 5-8 tabulates RMSEs of steady-state DLRs calculated for

nine spans that are in close proximity to nine weather stations respectively based on interpolation values of weather variables inferred from observations at the other eight stations by the spatial interpolation models chosen in Chapter 4 when taking each station as the target location. Comparing RMSEs of DLRs for spans CQ34-CQ35 and AC102-AC101B due to spatial interpolation errors (as shown in Table 5-8) to those due to forecast errors (as listed in Table 5-1), the uncertainty of spatial interpolation between weather variables is likely to cause more significant errors of DLR estimates on average. Therefore, quantifying the possible sizes of spatial interpolation errors of weather variables and reflecting this uncertainty on the distribution of DLR estimates should be addressed in future research.

Table 5-8: RMSEs (A) of steady-state DLRs estimated for nine spans in the vicinity of nine weather stations respectively based on interpolation values of weather variables.

Span (Closest Weather Station)	Conductor Type	RMSE (A) of DLR Estimates
AD90-AD89 (WS1)	Poplar	226.25
AD2-AC193 (WS2)	Lynx	115.30
AC177-AC178 (WS3)	Lynx	103.19
CQ34-CQ35 (WS4)	Lynx	122.50
AC137-AC138 (WS5)	Lynx	118.41
AC102-AC101B (WS6)	Poplar	114.37
AC301-AC302 (WS7)	Lynx	96.95
AC33-AC34 (WS8)	Lynx	124.78
AC6-AC7 (WS9)	Lynx	110.70

5.4. Conclusions

This chapter has described weather based approaches to probabilistic forecasts of steady-state dynamic line rating (DLR) for both a single span and an entire overhead line (OHL) based on a combination of a thermal model of overhead conductors and a Monte Carlo method where random weather inputs are sampled from the modelled

predictive distributions of the measured weather variables and then paired to have a correlation close to that computed from recent observations. The spatial interpolation models refined in Chapter 4 are additionally used to infer possible ambient conditions at each span within an OHL from random weather samples at weather stations for the DLR prediction for the entire OHL.

The proposed approaches have been tested on two spans comprising different types of overhead conductors and eight 132kV OHLs in the research area. The point forecasts of steady-state DLRs estimated by the conditionally heteroscedastic (CH) forecasting models have shown a significant improvement over persistence for up to half hour (3 steps) ahead. However, the overestimation of wind speed forecasts at lower values by auto-regressive (AR) models leads to unsatisfactory performance of DLR forecasting at low rating levels for both a single span and an entire OHL. In practice, a risk averse system operator is likely to adopt a policy in which there is a small probability of an actual rating being lower than the limit applied to power flows. Such a policy could use a certain lower percentile from a probabilistic DLR forecast and, for the case study discussed, this overcomes the low wind speed problem to some extent.

The predictive DLR percentiles for a particular span derived from independent random weather samples generated from AR-CH forecasting models and the DLR percentiles for an OHL derived from the paired (correlated) samples of air temperature and wind speed and independent wind direction samples are preferred in this study due to their good calibration at lower percentiles. The correlations added into random weather samples (especially between wind speed and wind direction) narrow the predictive distributions of DLRs for a particular span, which become more concentrated. When determining predictive DLR percentiles for an entire OHL, significant positive correlations added into random weather samples of the same parameters at different stations expand the range of sampled values of DLR forecasts at a particular future time, which mitigates the overconcentration of the distribution

of DLR forecasts derived from the independent weather samples. In addition, the correlations added into random samples between air temperature and wind speed and those among air temperature samples at different weather stations seem to have slight impact on the concentration of predictive distributions of DLRs due to the relatively high accuracy of air temperature prediction.

In practice, although heat transfer around each span of an OHL might suggest possible uprating of 100% or more relative to the seasonal static line rating (SLR) at a particular future time, the upgrading of ratings will usually be limited to 125% of SLRs due to the settings of protection on the circuit and other considerations. The corrected lower DLR percentiles have been shown to be conservative since the percentage of time for the actual ratings exceeding the lower DLR percentiles is mostly smaller than the theoretical value.

The critical span within an OHL at a particular future time is also predicted in Monte Carlo simulation. The location of the critical span is accurately predicted for the five most frequent critical spans in greater than 70% of cases for most circuits. A high forecast precision of critical span is generally achieved for the OHL that covers a short distance and comprises a small number of spans of similar orientation.

Perfect spatial interpolation of weather variables are assumed during the analysis of probabilistic forecasts of steady-state DLR for a complete line and possible critical spans. However, spatial interpolation errors of weather variables are found to cause more significant errors of steady-state DLR estimates than weather forecast errors on average. Although the weather-based model developed here for DLR forecasting for an OHL has successfully considered the uncertainty of weather forecasts, the sizes of possible errors of spatial interpolation between weather variables should be modelled and reflected on the distribution of DLR estimates in future research.

6. PROBABILISTIC FORECASTING OF TRANSIENT-STATE DYNAMIC LINE RATING

6.1. Introduction

Most reported studies on the application of weather-based dynamic line ratings (DLRs) consider continuous or steady-state DLRs only. Less attention has been given to short-term or transient-state DLRs, partly due to the increased computation time required. The conventional approach to tracking the transient-state conductor temperature within a specified time period is to divide the time period (typically 10 minutes) into several sufficiently small time intervals (e.g. 10 seconds) and then calculate the change in conductor temperature over each time interval [3, 4]. Clearly, if a time period of 10 minutes is divided into a series of 10-second time intervals, the estimation of conductor temperature change has to be carried out 60 times. IEEE Standard (Std.) 738 [3] and CIGRE Technical Brochure (TB) 601 [4] have both developed analytical methods to calculate the transient-state conductor temperature as an exponential function of time which can reduce computation time compared with the conventional approach. However, the analytical method developed in IEEE Std. 738 [3] only considers a step change in line current and requires the conductor to be in thermal equilibrium before the step occurs. In an example of transient-state conductor temperature calculation given in [4] where the conventional approach was adopted as a benchmark, the CIGRE analytical method was shown to underestimate the final conductor temperature by around 0.76℃ when an initial steady-state condition was not achieved.

This chapter first describes conventional approaches and analytical methods that are developed in [3] and [4] to track transient-state conductor temperatures. Then the IEEE analytical method is enhanced to consider changes in weather variables and fulfil the requirement of the conductor's thermal equilibrium at the start of a given

176

time period. Based on the experimental data used in the calculation example given in [4], the influence of the time interval length used in the conventional approach on the transient-state conductor temperature modelling is investigated. The accuracies of the enhanced analytical method and the CIGRE analytical method are then assessed using the conventional approach as a benchmark. Furthermore, a fast-computational approach is developed to estimate probabilistic forecasts of transient-state DLRs for time horizons of 10, 20 and 30 minutes for two particular spans CQ34-CQ35 and AC102-AC101B based on the predictive distributions modelled for the weather variables measured at stations 4 and 6 for up to three 10-minutes time steps ahead respectively along with use of the enhanced analytical method. The histograms of probability integral transform (PIT) for probabilistic transient-state DLR forecasts calculated based on the independent or correlated weather samples are compared to determine whether the correlations among different weather variables at different future moments should be added into random weather samples.

6.2. Methodology

6.2.1. Conventional approaches to conductor temperature modelling

A specified time period after step changes in line current and weather variables is to be divided into several sufficiently small time intervals, Δt, in the conventional approach to the transient-state conductor temperature modelling. The variation in conductor temperature over each Δt is then calculated by the non-steady-state heat balance equation [3]:

$$T_{cf,\Delta t} - T_{ci,\Delta t} = \frac{\Delta t}{m \cdot C_p(T_{ci,\Delta t})} \left\{ I^2 \cdot R(T_{ci,\Delta t}) + Q_s - Q_c(T_{ci,\Delta t}) - Q_r(T_{ci,\Delta t}) \right\} \quad (6\text{-}1)$$

where terms $I^2 \cdot R$, Q_s, Q_c and Q_r represent the rates of Joule heat gain, solar heat gain, convection heat loss and radiation heat loss per unit length respectively. Terms $T_{cf,\Delta t}$ and $T_{ci,\Delta t}$ are the final and initial conductor temperatures of Δt. The term

$m \cdot C_p$ in $J/(m \cdot °C)$ represents the total heat capacity of the conductor per unit length and is estimated as the sum of heat capacities of different materials [3]:

$$m \cdot C_p = \sum m_j \cdot C_{p,j} \qquad (6\text{-}2)$$

where terms m_j and $C_{p,j}$ are the mass per unit length (in kg/m) and the specific heat (in $J/(kg \cdot °C)$) for the jth conductor material respectively. The ac conductor resistance R, Q_c, Q_r and $C_{p,j}$ are all dependent on conductor temperature T_c and were evaluated at $T_{ci,\Delta t}$ of each 1-minute Δt in the calculation examples given in [3] and [4]. IEEE Std. 738 [3] suggests that it is usually sufficient to select Δt equal to 1% of the conductor thermal time constant (according to [3], the latter is typically 5 – 20 minutes) and that Δt of 10 seconds or less is mostly a reasonable choice.

An alternative approach is to evaluate the T_c dependent variables at the average $T_{cav,\Delta t}$ of $T_{ci,\Delta t}$ and $T_{cf,\Delta t}$ over each Δt. Because of the dependency of some variables on T_c, the latter is iteratively adjusted over each Δt until both sides of the non-steady-state heat balance equation (6-1) are equal. This approach is expected to give more accurate estimates of T_c, at a cost of extra computation time.

6.2.2. Analytical methods for conductor temperature modelling

6.2.2.1. IEEE analytical method [3]

The forced convection heat loss rate per unit length Q_{cf}, $I^2 \cdot R$ and Q_s are linear with T_c, whereas the natural convection heat loss rate Q_{cn} and Q_r are nonlinear with T_c [3]. As noted in Section 2.1.4, Q_c is determined as the larger value between Q_{cn} and Q_{cf} in [3]. Therefore, Q_c will be non-linear with T_c if it is (a) determined by Q_{cn} throughout a specified time period, or (b) determined by Q_{cf} at the start of the time period and then determined by Q_{cn} at the conductor temperature which occurs long after the step change (i.e. the steady-state final conductor temperature). Assuming these nonlinear terms to be linear with T_c, an analytical method is developed in IEEE Std. 738 [3] to estimate the transient-state conductor temperature

as an exponential function of time after the step change in line current based on the assumption that the conductor is in thermal equilibrium prior to the step occurs:

$$T_c(t) = T_{ciss} + \left(T_{cfss} - T_{ciss}\right) \cdot \left(1 - e^{-t/\tau}\right) \tag{6-3}$$

where $T_c(t)$ is the transient-state conductor temperature at time t. T_{ciss} and T_{cfss} represent the steady-state conductor temperatures corresponding to the initial current I_i prior to the step occurs and the final current I_f after the step change respectively. The term τ is a thermal time constant at which the change in conductor temperature $\left(T_c(\tau) - T_{ciss}\right)$ reaches 63.2% of $\left(T_{cfss} - T_{ciss}\right)$ and is approximately equal to [3]:

$$\tau = \frac{\left(T_{cfss} - T_{ciss}\right) \cdot m \cdot C_p(T_{cavss})}{R(T_{cavss}) \cdot \left(I_f^2 - I_i^2\right)} \tag{6-4}$$

where R and $m \cdot C_p$ are evaluated at the average T_{cavss} of T_{ciss} and T_{cfss}. The IEEE analytical method only considers the step change in line current and requires the conductor to be in thermal equilibrium at the start of the given time period [3].

6.2.2.2. CIGRE analytical method [4]

The CIGRE analytical method estimates $T_c(t)$ as an exponential function of time, like the IEEE analytical method does, but calculates the thermal time constant for the change in each of the heating and cooling terms separately:

$$\tau_x = \left| \frac{\left(\text{ß}_f - \text{ß}_i\right) \cdot m \cdot C_p(T_{ci})}{\Delta Q_x} \right| \tag{6-5}$$

where,

ß_i is the rise of the initial conductor temperature T_{ci} above air temperature T_a;

ß_f is the rise above T_a for T_{cfss} that is estimated from I_f;

ΔQ_x represents the step change in a particular heating or cooling term Q_x;

$m \cdot C_p(T_{ci})$ is the total heat capacity of the conductor evaluated at T_{ci}.

The rise $ß(t)$ of $T_c(t)$ above T_a is then modelled as an exponential function of time:

$$ß(t) = ß_f - \left(ß_f - ß_i\right) \cdot e^{-t/\tau_J} \cdot e^{-t/\tau_s} \cdot e^{-t/\tau_c} \cdot e^{-t/\tau_r} \tag{6-6}$$

where terms τ_J, τ_s, τ_c and τ_r represent the thermal time constants for the changes in Joule heat gain rate ΔQ_J, solar heat gain rate ΔQ_s, convection heat loss rate ΔQ_c and radiation heat loss rate ΔQ_r respectively. Equation (6-6) can be equivalently written as:

$$ß(t) = ß_i + \left(ß_f - ß_i\right) \cdot \left(1 - e^{-t/\tau_J} \cdot e^{-t/\tau_s} \cdot e^{-t/\tau_c} \cdot e^{-t/\tau_r}\right) \tag{6-7}$$

or,

$$T_c(t) = T_{ci} + \left(T_{cfss} - T_{ci}\right) \cdot \left(1 - e^{-t/\tau_J} \cdot e^{-t/\tau_s} \cdot e^{-t/\tau_c} \cdot e^{-t/\tau_r}\right) \tag{6-8}$$

which is similar to the form of equation (6-3).

6.2.2.3. Enhanced analytical method

The IEEE analytical method is enhanced here to additionally consider variations in weather conditions and fulfil the requirement of the conductor's thermal equilibrium at the start of a specified time period. Given T_{ci} and weather conditions wc over a specified time period tp, the conductor's thermal equilibrium at the beginning of tp is created by inference of an equivalent steady-state initial line current $I_{i,eq}$ based on the steady-state heat balance equation [3]:

$$I_{i,eq}^2 = \{Q_c(T_{ci}, wc) + Q_r(T_{ci}, wc) - Q_s(wc)\}/R(T_{ci}) \tag{6-9}$$

In this manner, the transient-state impact of the actual line current and weather conditions prior to tp on the conductor is converted into the steady-state influence of $I_{i,eq}$ and wc. As a result, the enhanced analytical method successfully takes changes of weather conditions into account.

It is noted that a negative $I_{i,eq}^2$ may be obtained in some particular cases where, for example, there is a significant increase in solar radiation or a reducing cooling effect

due to an increment in air temperature or a decrease in the 'effective' wind speed perpendicular to the conductor. A negative value of $I_{i,eq}^2$ means that wc over tp are less conducive to cooling the conductor and T_c will increase rapidly at an earlier stage of tp. Due to that an imaginary value of $I_{i,eq}$ is obtained from a negative $I_{i,eq}^2$, the inferred $I_{i,eq}^2$ is directly used to determine the thermal time constant:

$$\tau = \frac{\left(T_{cfss} - T_{ci}\right) \cdot m \cdot C_p \left(\dfrac{T_{cfss} + T_{ci}}{2}\right)}{R\left(\dfrac{T_{cfss} + T_{ci}}{2}\right) \cdot \left(I_f^2 - I_{i,eq}^2\right)} \tag{6-10}$$

where terms $m \cdot C_p$ and R are approximately evaluated at the average conductor temperature $\left(T_{cfss} + T_{ci}\right)/2$. Please refer to **Appendix C** which gives formula derivations of the thermal time constant τ in the enhanced analytical method. It is found that the final conductor temperature at the end of tp would be overestimated by the enhanced analytical method under the assumption that Q_c and Q_r linearly changed with T_c. As detailed in **Appendix C**, this is because the enhanced analytical method evaluating the ac resistance R at $\left(T_{cfss} + T_{ci}\right)/2$ leads to a non-negative difference between the overestimations in the heat gain rate $\Delta Gain$ and the linearized heat loss rate $\Delta Loss_{linearized}$ (n.b. a negative $\Delta Gain$ or $\Delta Loss_{linearized}$ means an underestimation) at T_c which varies between T_{ci} and T_{cfss}:

$$\Delta Gain(T_c) - \Delta Loss_{linearized}(T_c)$$
$$= \left(I_f^2 - I_{i,eq}^2\right) \cdot \left[\frac{R\left(T_{cfss}\right) - R(T_{ci})}{2}\right] \cdot \left(1 - \frac{T_c - T_{ci}}{T_{cfss} - T_{ci}}\right) \tag{6-11}$$

However, in actuality, the change rate of Q_r is not constant but increases with T_c. Furthermore, as noted in Section 6.2.2.1, Q_c may also be non-linear with T_c. Therefore, the enhanced analytical method may underestimate the final conductor temperature at the end of the time period given a considerable overestimation in the cooling terms after the linearization.

6.2.3. The secant method

Since T_{cfss} cannot be directly solved from the final line current I_f and weather conditions wc via the steady-state heat balance equation [3], the value of T_{cfss} has to be iteratively adjusted until the calculated line current equals the given I_f, which will increase computation time of the analytical method. The use of a root-finding algorithm can quickly determine T_{cfss} and effectively reduces computation time.

The bisection method [151] is a simple, but relatively slow root-finding algorithm which halves the search space at each iteration. Newton's method [152] has a faster convergence process but requires the derivative of the function to be known. Newton's method may be not applicable in this case since it is difficult to evaluate the derivative of the steady-state heat balance equation with respect to conductor temperature. Just as the derivative of the function is represented by tangent lines in Newton's method, the secant method approximates the derivative by secant lines [152]. Though the secant method is likely to require more iterations than Newton's method, it does not need to calculate the derivative and has a faster converge process than the bisection method.

When using the secant method to determine T_{cfss}, the function F_1 of T_{cfss} is defined as the difference between the square of the given I_f and the square of the steady-state line current estimated from an assumed T_{cfss} and wc. A termination criterion of $|F_1(T_{cfss})| < 0.1A^2$ is found in the tests conducted here to be sufficient for the secant method to produce an accuracy of 1×10^{-4}°C. Two initial iterations are carried out at the air temperature and a maximum allowable conductor temperature T_{cmax} respectively.

The secant method is also employed to adjust the transient-state DLR I_{ts} until the calculated transient-state final conductor temperature T_{cfts} reaches T_{cmax} at the end of a specified future time period (i.e. 10, 20 and 30 minutes in this study). The function $F_2(I_{ts})$ in the secant method is defined as the deviation between T_{cmax}

and T_{cfts} that is estimated from an assumed I_{ts}, T_{ci} and weather forecasts using the enhanced analytical method. The iterative calculation is terminated when $|F_2(I_{ts})| < 0.001℃$.

6.2.4. Transient-state DLR forecasts and constraints

Changes in weather forecasts at each future time (up to three 10-minutes time steps ahead) are considered to predict transient-state DLRs. Given an assumed 30-minute transient-state DLR forecast $I_{ts,3}$, the 10-minute-ahead weather forecasts wf_1 are first used to estimate the growth in T_c from the initial temperature T_{ci} to T_{c10} at the end of the first future 10 minutes, which then increases to T_{c20} at the end of the second future 10 minutes under the 20-minute-ahead weather forecasts wf_2; the 30-minute-ahead weather forecasts wf_3 are finally used to determine the increase in T_c from T_{c20} to T_{c30}.

A higher level of transient-state DLR is generally obtained for a shorter time period. The relationships among transient-state DLRs for up to a half hour ahead, $I_{ts,1}$, $I_{ts,2}$ and $I_{ts,3}$, should be such that $I_{ts,1} \geq I_{ts,2} \geq I_{ts,3}$. Otherwise, T_{cmax} would be exceeded. In some extreme cases where, for example, wf_3 provides more significant cooling on the conductor than wf_2, the calculated $I_{ts,3}$ may be greater than $I_{ts,2}$, which leads to T_c exceeding T_{cmax} at the end of the 20 minute period and then reducing to T_{cmax} at the end of 30 minutes. Table 6-1 shows that the steady-state DLR at span CQ34-CQ35 calculated for 12:10 – 12:20 on 28/03/2013 was much higher than that for 12:00 – 12:10, meaning that weather conditions over 12:10 – 12:20 were much more conducive to cooling the conductor. In this extreme case, $I_{ts,3}$ estimated for the period of 11:50 – 12:20 was greater than $I_{ts,2}$ estimated for the period of 11:50 – 12:10. Fig. 6-1 shows that the conductor temperature of span CQ34-CQ35 operated at the unrestricted $I_{ts,3}$ would exceed T_{cmax} at 12:10 and then decrease to T_{cmax} at 12:20. Therefore, values of $I_{ts,2}$ and $I_{ts,3}$ must be

limited to the calculated $I_{ts,1}$ and the calculated or restricted $I_{ts,2}$ respectively so as to avoid the risk of T_{cmax} being exceeded in such extreme cases.

Table 6-1. The 10-minute, 20-minute and 30-minute transient-state DLRs (A) and the steady-state DLR (A) for each 10-minute period during 11:50 – 12:20 on 28/03/2013 for span CQ34-CQ35.

Time period	Steady-state DLR	Time horizon	Transient-state DLR
11:50 – 12:00	620.6A	10 minutes	695.1A
12:00 – 12:10	567.9A	20 minutes	598.0A
12:10 – 12:20	602.0A	30 minutes	600.9A
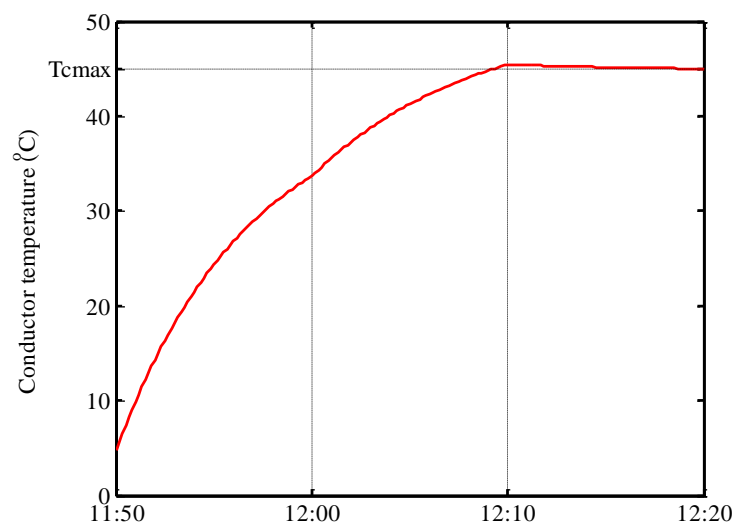
Fig. 6-1. Transient-state conductor temperatures of span CQ34-CQ35 operated at the unrestricted 30-minute transient-state DLR derived from weather observations during 11:50 – 12:20 on 28/03/2013

In Monte Carlo simulation, sampled values of 10-minute, 20-minute and 30-minute transient-state DLR forecasts for a particular span in proximity to a weather station are determined from random weather samples that are generated from the modelled predictive distributions for up to 3 steps (half hour) ahead in each of 10^4 generated scenarios. Two initial iterations in the secant method for determining $I_{ts,1}$ are carried out at the 10-minute-ahead steady-state DLR $I_{ss,1}$ and $1.5I_{ss,1}$. When determining $I_{ts,2}$ and $I_{ts,3}$, two initial iterations are carried out at the calculated 20-minute-ahead steady-state DLR $I_{ss,2}$ and $I_{ts,1}$, and the 30-minute-ahead steady-state DLR $I_{ss,3}$ and $I_{ts,2}$ respectively.

6.3. Results and Model Validation

The accuracies of conventional approaches and analytical methods in transient-state conductor temperature modelling are first assessed based on the experimental data for a 'Drake' conductor used in the transient-state calculation example given in [4] and also the measured weather data and line currents for two particular spans, i.e. CQ34-CQ35 and AC102-AC101B, comprising different conductors and in proximity to weather stations. The process of estimating probabilistic forecasts of 10-minute, 20-minute and 30-minute DLRs is then detailed, followed by an assessment in terms of the forecast accuracy and the calibration of probabilistic forecasts.

6.3.1. Assessment of conventional and analytical methods

The influence of time interval Δt on the two conventional approaches, i.e. evaluating the T_c dependent variables at the initial conductor temperature $T_{ci,\Delta t}$ or the average conductor temperature $T_{cav,\Delta t} = (T_{ci,\Delta t} + T_{cf,\Delta t})/2$ over each Δt, is assessed here based on the experimental data used in the calculation example given in [4], as tabulated in Table 6-2.

Table 6-2. Weather data and line currents in three subsequent 10-minute periods in the calculation example given in [4]

Time Periods $(hh:mm)$	Air Temperature (℃)	Wind Speed (m/s)	Attack Angle $(degree)$	Solar Radiation (W/m^2)	Current (A)
Prior to 00:00	24.0	1.9	55	0	802
00:00 – 00:10	23.7	1.7	62	0	819
00:10 – 00:20	23.5	0.8	37	0	856

The transient-state conductor temperatures estimated by different conventional approaches that use $T_{ci,\Delta t}$ or $T_{cav,\Delta t}$ with a 10-second or 1-minute Δt are compared in Fig. 6-2.
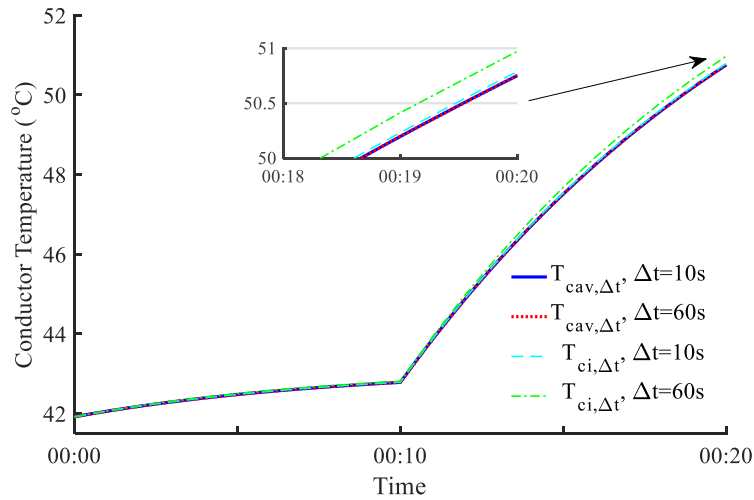
Fig. 6-2. Transient-state temperatures of the 'Drake' conductor modelled by different conventional approaches

The analysis results show that (a) given a relatively significant growth in current and/or reduction in wind cooling on the conductor, the $T_{ci,\Delta t}$-based conventional approach with a 1-minute Δt will overestimate T_c due to the cooling terms evaluated at $T_{ci,\Delta t}$ being underestimated over each Δt; and (b) the use of $T_{cav,\Delta t}$ results in the conventional approaches with different Δt being both reasonably accurate and conservative in this case.

Fig. 6-3 shows the transient-state temperatures of the 'Drake' conductor modelled by the CIGRE analytical method and the enhanced analytical method. Both analytical methods calculate the heating and cooling terms in equations (6-5) and (6-9) using the formulae provided in IEEE Std. 738 [3].
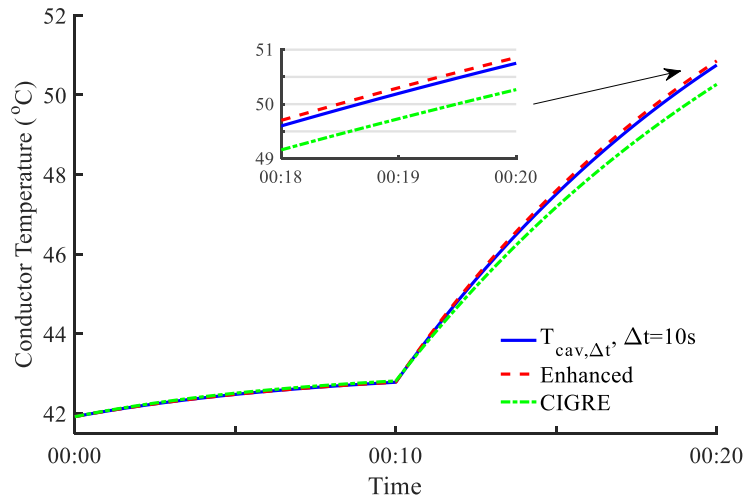
Fig. 6-3. Transient-state temperatures of the 'Drake' conductor modelled by analytical methods

The transient-state T_c at 00:20, $T_c(00:20)$, estimated by the CIGRE analytical method is found to be $0.7°C$ lower than that tracked by the conventional approach using $T_{ci,\Delta t}$ with a 1-minute Δt. The deviation is very close to the error obtained in the calculation example given in [4] which used the CIGRE formulae to evaluate heating and cooling terms. Compared with the benchmark adopted here, the enhanced analytical method shows a higher accuracy than the CIGRE analytical method. Furthermore, the enhanced analytical method overestimates $T_c(00:20)$ by around $0.1°C$ in this case where the cooling on the conductor is dominated by the forced convection heat loss rate which linearly changes with T_c. The enhanced analytical method's overestimation has been explained in Section 6.2.2.3 and also in **Appendix C**.

It is noted that the total heat capacity $m \cdot C_p$ of the conductor which should increase with T_c [4] is assumed to be a constant value evaluated at $(T_{ci} + T_{cfss})/2$ in the enhanced analytical method. This assumption may have little impact on the T_c modelling since an increment of $50°C$ in T_c increases $m \cdot C_p$ of the 'Drake' conductor slightly by around 1.62%, which is much smaller than the corresponding increase of 20.35% in the ac resistance.

6.3.2. Transient-state conductor temperature modelling

The transient-state conductor temperatures T_c of spans CQ34-CQ35 ('Lynx' ACSR $175mm^2$ conductors) and AC102-AC101B ('Poplar' AAAC $200mm^2$ conductors) in proximity to weather stations 4 and 6 are studied. Since the direct monitoring of T_c is not available, the transient-state T_c estimated from the measured line current and weather data by the $T_{cav,\Delta t}$-based conventional approach with a 10-second Δt is regarded as the actual T_c and used as a benchmark. The 30-minute average line current used in [10] is converted to 10-minute intervals, in common with that of the weather data, using a linear interpolation [153]. The variation in T_c over each 10-minute period is tracked by the $T_{ci,\Delta t}$-based conventional approach with a 10-second Δt and also by the enhanced analytical method based on the 'actual' T_c at the start of the period that is combined with the corresponding measured line current and weather data. Fig. 6-4 shows distributions of errors of the transient-state final conductor temperature T_{cfts} at the end of each 10-minute period modelled by the two methods during 28/01/2013 to 31/03/2013 for different spans. The average computation time used by the $T_{ci,\Delta t}$-based conventional approach with a 10-second Δt and the enhanced analytical method is around $4.5 \times 10^{-3}s$ and $5.4 \times 10^{-4}s$ respectively. (The computer being used for the transient calculation has a 64-bit operating system, 4GB of RAM, and an Intel Core i5-3470, 3.2GHz processor).
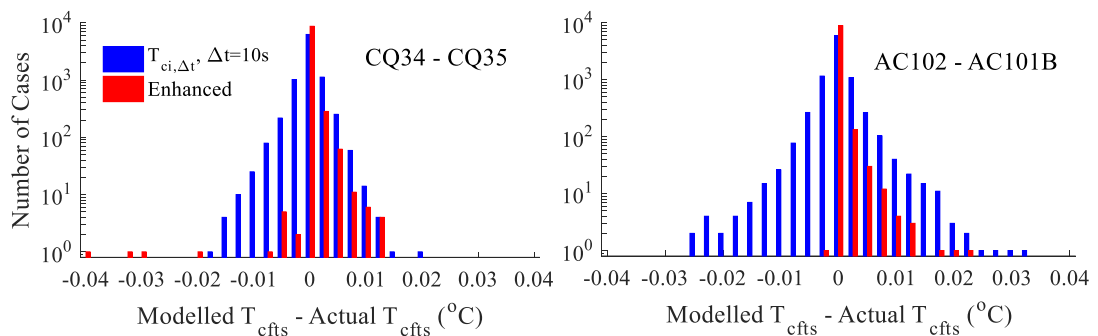
Fig. 6-4. Distributions of T_{cfts} errors modelled by the $T_{ci,\Delta t}$-based conventional approach with a 10-second Δt and the enhanced analytical method for spans CQ34-CQ35 and AC102-AC101B

The $T_{ci,\Delta t}$-based conventional approach is found to overestimate the growth or reduction in T_{cfts} to different extents, depending on the level of variations in line current and weather conditions. The enhanced analytical method is generally shown to produce more accurate estimates of T_{cfts}. Furthermore, T_{cfts} modelled by the enhanced analytical method is mostly greater than or equal to the actual value. As noted in Section 6.2.2.3, T_{cfts} would be overestimated by the enhanced analytical method under the assumption that the cooling terms linearly varied with T_c. Given a slight overestimation in the cooling terms after the linearization in most cases, T_{cfts} would then be overestimated.

In some particular cases, however, the enhanced analytical method underestimates T_{cfts} of CQ34-CQ35 by greater than 0.02°C. It is found that, in these particular cases, the convection heat loss rates Q_c evaluated at T_{ci} and T_{cfss} are determined by the forced convection heat loss rate $Q_{cf}(T_{ci})$ and the natural convection heat loss rate $Q_{cn}(T_{cfss})$ respectively. Fig. 6-5 compares the growths of Q_{cn}, Q_{cf} and the linearlized Q_c (denoted by $Q_{c,linearized}$) with $T_c \in [T_{ci}, T_{cfss}]$ and also shows the overestimation in Q_c in a particular case where T_{cfts} of CQ34-CQ35 over 18:20 – 18:30 on 16/03/2013 is underestimated by the enhanced analytical method.
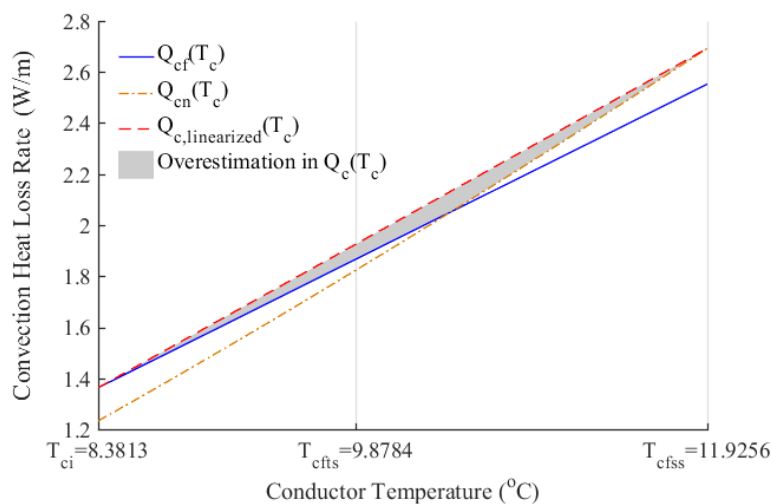
Fig. 6-5. The forced, natural and linearized convection heat loss rates and the overestimation after the linearization in a particular case where T_{cfts} of span CQ34-CQ35 over 18:20 – 18:30 on 16/03/2013 is underestimated by the enhanced analytical method

Fig. 6-6 compares the overestimations in $Q_c(T_c)$ and $Q_r(T_c)$ with the values of $\left(\Delta Gain(T_c) - \Delta Loss_{linearized}(T_c)\right)$ in this case. Before T_c reaches $T_{cfts} = 9.88°C$, $\left(\Delta Gain(T_c) - \Delta Loss_{linearized}(T_c)\right)$ is much greater than the overestimation in $Q_r(T_c)$, but significantly exceeded by the overestimation in $Q_c(T_c)$ when T_c is above a certain level. The total overestimation in $(Q_c + Q_r)$ after the linearization exceeding $(\Delta Gain - \Delta Loss_{linearized})$ over a given time period would lead to an underestimated T_{cfts} at the end of the time period.
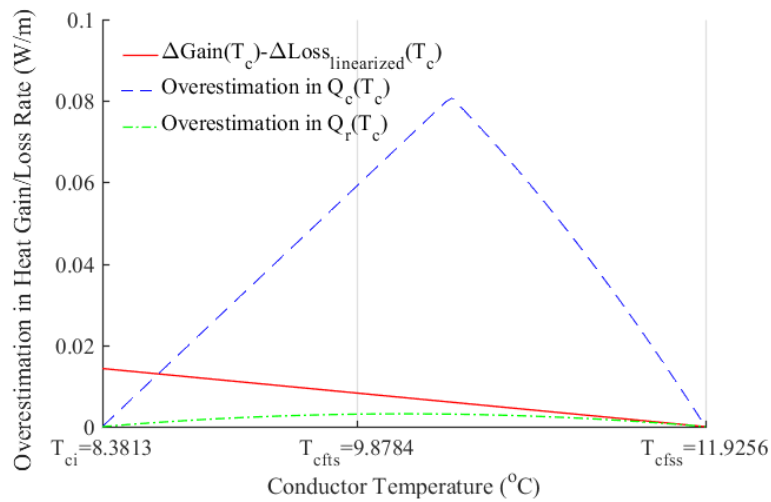
Fig. 6-6. Comparison of $(\Delta Gain - \Delta Loss_{linearized})$ against overestimations in Q_c and Q_r after the linearization in a particular case where the enhanced analytical method underestimates T_{cfts} of span CQ34-CQ35 over 18:20 – 18:30 on 16/03/2013.

6.3.3. Enhanced analytical method based transient-state DLR estimation

As noted above, the enhanced analytical method is likely to overestimate the growth in T_{cfts} after an increase in line current. Therefore, the short-term or transient-state DLR determined for a given short period based on the enhanced analytical method may be underestimated due to the actual T_{cfts} not increasing to the maximum allowable limit T_{cmax}. Fig. 6-7 shows the distributions of deviations between T_{cmax} and the 'actual' T_{cfts} at the end of the given time periods under the 10-minute, 20-minute and 30-minute DLRs that are estimated from weather observations using

190

the enhanced analytical method for the two spans. (The cases of 20-minute and 30-minute DLRs being restricted are omitted here simply for brevity).
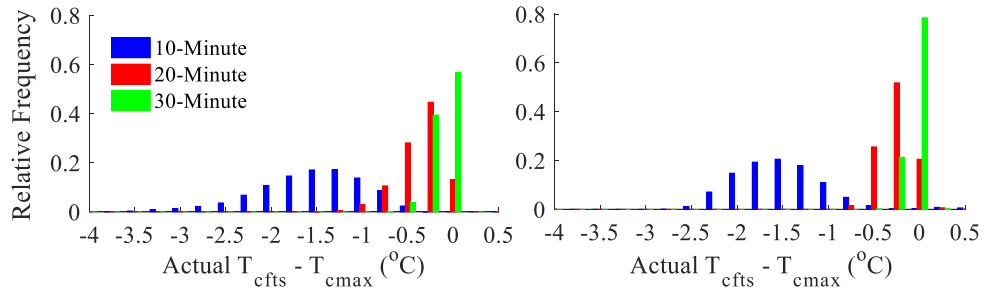
Fig. 6-7. Distributions of differences between T_{cmax} and the 'actual' T_{cfts} at the end of 10-minute, 20-minute and 30-minute periods under the corresponding enhanced analytical method based transient-state DLRs for two spans

The final temperature T_{cfts} of the conductor operated at the level of the enhanced analytical method based transient-state DLR, especially the 10-minute rating, does not reach T_{cmax} for most of the time. A smaller deviation from T_{cmax} is mostly observed at the end of the 30-minute period since the conductor has a long time to respond to the significant increase in line current. Therefore, transient-state DLRs estimated on the basis of the enhanced analytical method are usually conservative. It is noted that T_{cmax} is slightly exceeded in a few cases due to the overestimated cooling on the conductor after the linearization which has been discussed in Section 6.3.2. Fortunately, the created 5℃ safety buffer relative to the original maximum limit [10] is greater than these exceedances.

6.3.4. Assessment of probabilistic forecasting of transient-state DLR

In Monte Carlo simulation, random samples of air temperature and wind speed generated from the modelled predictive distributions for up to 30 minutes (3 steps) ahead over a particular future half-hour period are paired to have rank correlations similar to those among their observations within the most recent 15 days. Figs. 6-8 and 6-9 show that the paired random weather samples at the same and different future moments have rank correlations quite close to those computed from their recent observations at spans CQ34-CQ35 and AC102-AC101B. Furthermore, the

paired random samples of the same weather parameter at different future moments show a significant correlation.
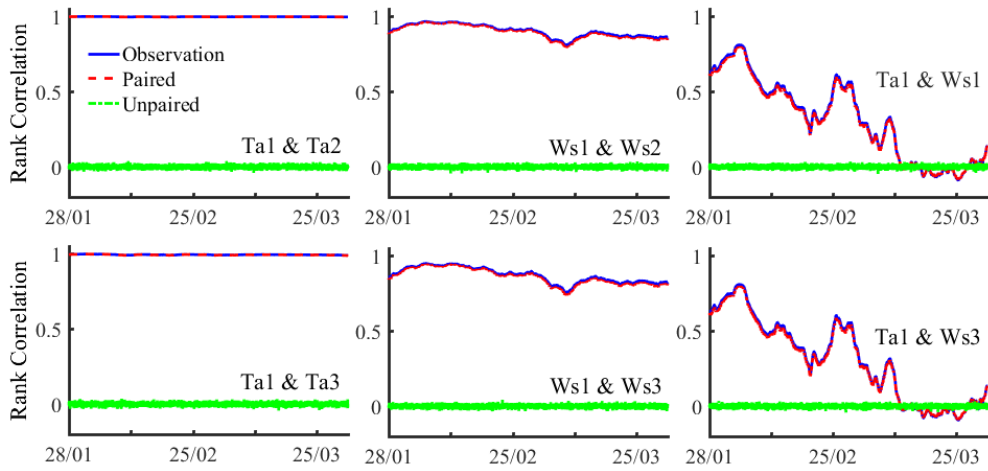
Fig. 6-8. Rank correlations between unpaired, paired random samples of air temperature and wind speed forecasts for up to 3 steps ahead (i.e. T_{ai} and $w_{s,i}$, $i = 1, 2, 3$) and their historic observations within the most recent 15 days at weather station 4 (span CQ34-CQ35)
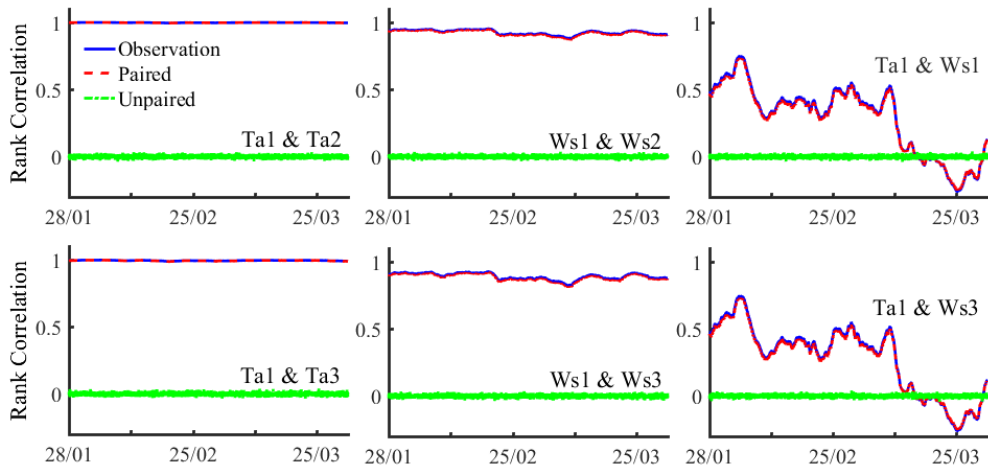
Fig. 6-9. Rank correlations between unpaired, paired random samples of air temperature and wind speed forecasts for up to 3 steps ahead (i.e. $T_{a,i}$ and $w_{s,i}$, $i = 1, 2, 3$) and their historic observations within the most recent 15 days at weather station 6 (span AC102-AC101B)

The sampled values of the 10-minute, 20-minute and 30-minute transient-state DLR forecasts are determined from the correlated and independent samples of air temperature and wind speed separately that are combined with independent wind direction samples and point forecasts of solar radiation for up to a half hour ahead over a particular future half-hour period in each of the 10^4 generated scenarios. The

192

calculations of 10-minute, 20-minute and 30-minute DLR forecasts for 2×10^4 scenarios are simultaneously processed through the matrix calculation realised in MATLAB, which require around 2 seconds. The cumulative distribution function (CDF) extracted from sampled values of the transient-state DLR forecast is then smoothed by kernel density estimation [148] to determine predictive percentiles for each time horizon. Figs. 6-10 and 6-11 show the ratios of the correlated weather samples based $5^{th} - 95^{th}$ percentiles, $25^{th} - 75^{th}$ percentiles, point forecasts of 10-minute and 30-minute DLRs and weather observation based transient-state DLRs to the static line ratings (SLRs) on 27/03/2013 for the two spans respectively.
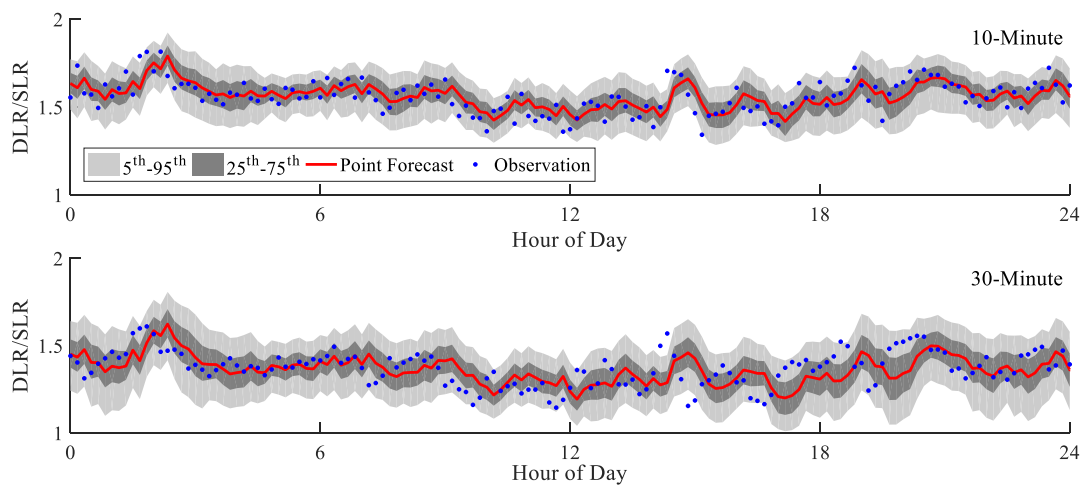
Fig. 6-10. Probabilistic forecasts of 10-minute and 30-minute transient-state DLRs on 27/03/2013 for span CQ34-CQ35
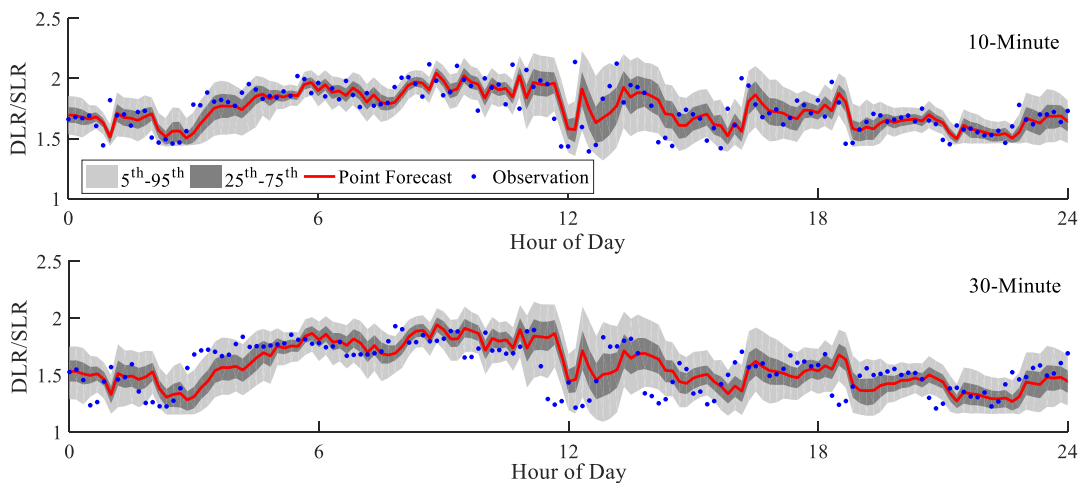
Fig. 6-11. Probabilistic forecasts of 10-minute and 30-minute transient-state DLRs on 27/03/2013 for span AC102-AC101B

The 10-minute DLR forecast is shown to offer a higher additional headroom in the conductor's ampacity, though lasting for a shorter period, than the 30-minute DLR forecast. In addition, the predictive distributions of the 30-minute DLR are less concentrated than that of the 10-minute DLR on average. This is because the forecast accuracy decreases with increasing look ahead and the uncertainties of weather forecasts for up to a half hour ahead are all included for estimation of the possible errors of a 30-minute DLR prediction.

The transient-state DLRs estimated from persistence forecasts of weather conditions are adopted as benchmarks to assess the accuracy of the point DLR forecasts generated by the conditionally heteroscedastic (CH) forecasting models based on correlated (CH-C) random weather samples. Since persistence forecasting supposes that weather forecasts in the future are equal to present values [102], weather predictions will be constant with the upcoming 30 minutes. The point forecasts of the CH-C model based 10-minute and 30-minute transient-state DLRs having root mean square errors (RMSEs) of around $35.8A$ and $46.8A$ respectively give 11% and 18.2% improvements over the persistence forecast based transient-state DLRs for span CQ34-CQ35. The corresponding RMSEs for span AC102-AC101B are $47.5A$ and $61.8A$ respectively which give 9% and 17.5% improvements over persistence. Although the transient-state DLRs predicted by the CH-C model are more accurate than the persistence forecast based DLRs on average, it is found that the CH-C forecasting models usually overestimates transient-state DLRs for both spans at the levels of their respective lower ratings (e.g. the smallest 5% of weather observation based transient-state DLRs) as shown in Fig. 6-12. Therefore, the lower percentiles of transient-state DLRs should be applied so as to avoid the risk of using the overestimated point forecasts of the CH-C model based transient-state DLRs.
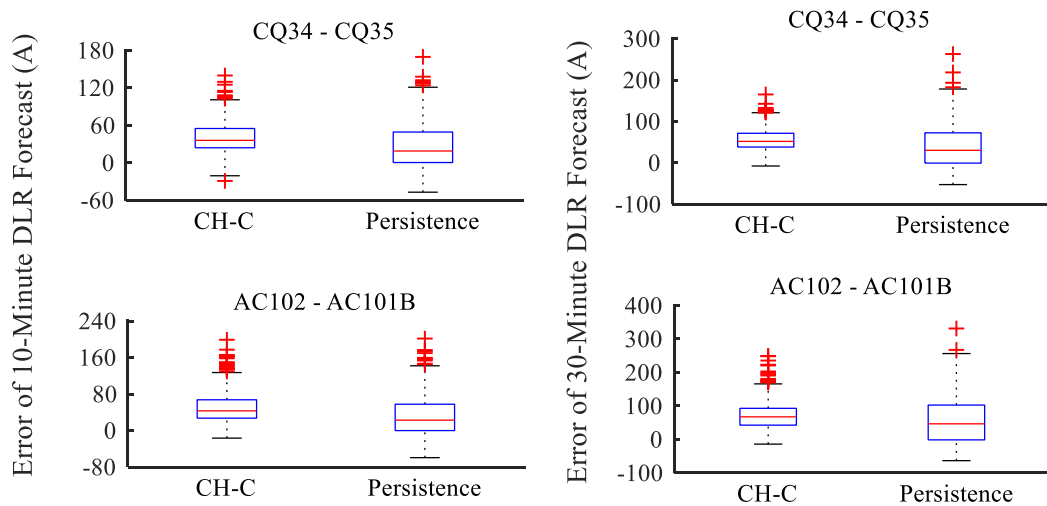
Fig. 6-12. Box plots of errors of 10-minute and 30-minute transient-state DLR forecasts estimated by the CH-C models and persistence forecasting for two spans at the low rating levels

In order to assess the calibration of probabilistic forecasts of transient-state DLR, histograms of probability integral transform (PIT) are plotted for DLR forecasts of two spans for different time horizons which are modelled from the independent (CH-I) and correlated (CH-C) random weather samples separately, as shown in Figs. 6-13 and 6-14. The relative frequency of 0.01 per percentile for a uniform PIT histogram which reveals probabilistic forecasts to be fully calibrated is denoted by a black solid line.
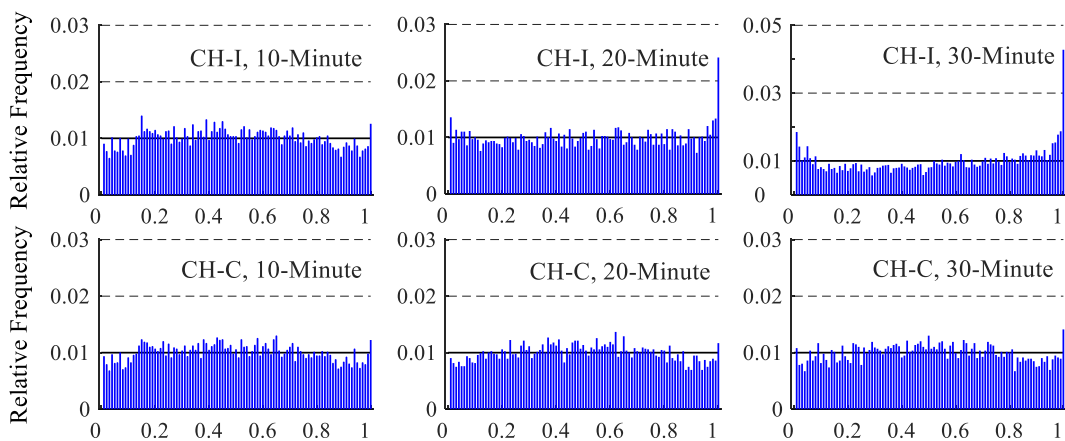
Fig. 6-13. PIT histograms of probabilistic forecasts of 10-minute, 20-minute and 30-minute transient state DLRs for span CQ34-CQ35
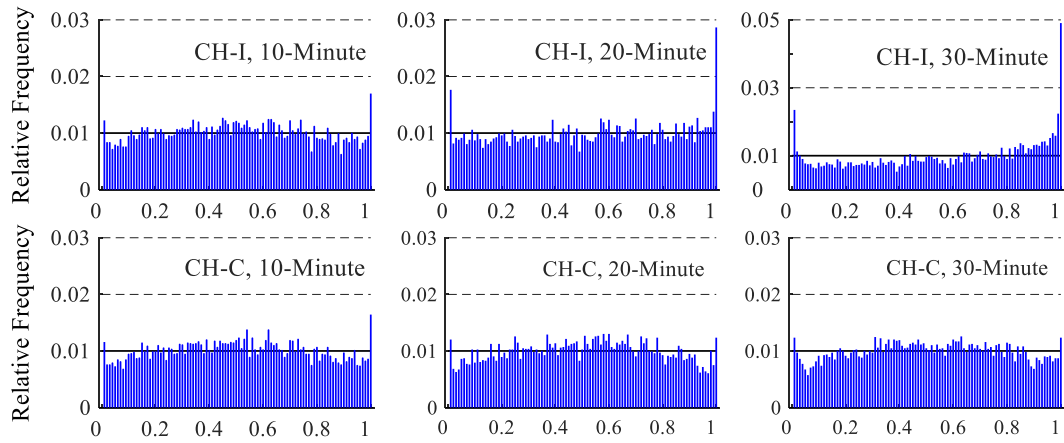
Fig. 6-14. PIT histograms of probabilistic forecasts of 10-minute, 20-minute and 30-minute transient state DLRs for span AC102-AC101B

The relative frequencies at both ends of PIT histograms of 10-minute DLR forecasts derived from the correlated weather samples are similar to those for the independent samples. Though the paired samples of one-step-ahead air temperature and wind speed forecasts showing long-term positive correlations have opposite cooling effects, their correlations may have a slight impact on the concentration of predictive distributions of 10-minute DLRs due to the relatively high accuracy of air temperature prediction. For 20-minute and 30-minute time horizons, the significant deviations from the ideal relative frequency of 0.01 at both ends of PIT histograms for the independent weather samples are successfully mitigated in the correlated samples based PIT histograms. The paired random samples of the same weather parameter at different future moments (up to 30 minutes ahead) that show significant positive correlations, in each of the 10^4 scenarios, will be at similar levels with respect to their respective ranges of the 10^4 random samples. The low wind speed forecasts or the high air temperature forecasts assigned to different future moments in a particular scenario would therefore lead to the calculated 20-minute and 30-minute DLR forecasts being at a certain low level, and vice versa. This means that the predictive distributions of 20-minute and 30-minute DLRs estimated from the paired weather samples are commonly more dispersive than those based on the unpaired

(independent) random samples. Therefore, predictive percentiles of transient-state DLRs modelled based on the correlated (paired) random weather samples generated from the CH forecasting models are preferred due to their improved calibration, especially at lower percentiles.

As noted in Section 5.2.3, a particular lower DLR percentile, e.g. the 5th percentile (P5 value) is likely to be selected from a probabilistic forecast and regarded as the thermal limit of the conductor to avoid any significant probability of the maximum allowable conductor temperature being exceeded. If the adopted P5 value works well, the actual transient-state DLR should exceed the thermal limit in no more that 5% of cases on average. To check the effectiveness of using the P5 forecast as the thermal limit, differences between the actual transient-state ratings and the 30-minute P5 forecasts that are limited to 25% above SLRs are examined. As shown in Fig. 6-15 where a negative value indicates the actual rating is greater than the P5 forecast, the P5 value limited to 125% of SLR exceeds the actual rating in only 2.95% and 1.62% of cases for spans CQ34-CQ35 and AC102-AC101B respectively.
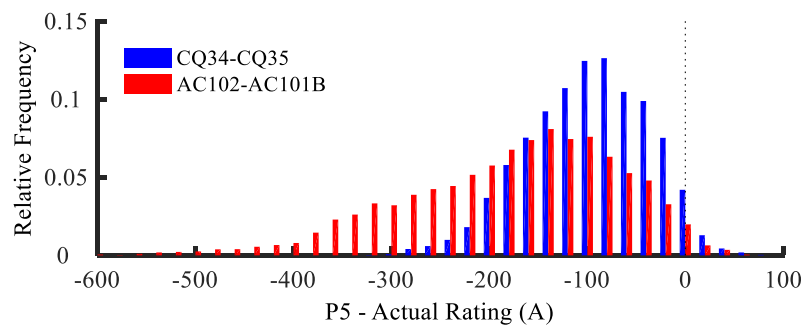
Fig. 6-15. Distributions of differences between the actual 30-minute ratings and the 30-minute P5 forecasts limited to 125% SLRs for different span.

6.3.5. Effects of uncertainty in coefficients of conductor's characteristics on transient-state calculations

Due to lack of direct measurements of conductor temperature, the transient-state T_c estimated from the measured line current and weather observations by the $T_{cav,\Delta t}$ based conventional approach with a 10-second Δt is regarded as the actual T_c. In a thermal model of the conductors that weather-based models rely on, the parameters describing the conductor's emissivity ε_e and solar absorptivity ε_s that respectively determine rates of radiation heat loss and solar heat gain are usually coarsely estimated. Although the transient-state DLR estimated by the enhanced analytical method is mostly conservative in the work conducted here, an overestimated ε_e or an underestimated ε_s may lead to the transient-state final conductor temperature T_{cfts} exceeding T_{cmax} at the end of the specified time period. Fig. 6-16 shows cumulative frequency distributions of deviations between T_{cmax} and T_{cfts} that are modelled by the conventional approach using $T_{cav,\Delta t}$ with a 10-second Δt under the weather observation based transient ratings for different time horizons for the two spans, assuming the actual values of ε_e or ε_s to be 0.1 or 0.2 smaller or greater than that used in this study as listed in Table 3-6. Since ε_e of energized conductors is highly correlated with ε_s and generally considered to be slightly higher than ε_s [74], the combinations of ε_e and ε_s tested here (i.e. $\varepsilon_e/\varepsilon_s$ equaling 0.5/0.7 or 0.4/0.6 for CQ34-CQ35 and 0.8/0.9 or 0.7/0.9 for AC102-AC101B) are expected to give the worst cases of T_{cmax} being exceeded. Therefore, a reasonable safety margin relative to the original maximum temperature limit is necessary for the transient-state DLR calculation in this research.

In practical application, some form of conductor temperature monitoring technique (e.g. Power Donut [37] that measures T_c at the fixed point) should be available to validate the 'actual' T_c calculated by the $T_{cav,\Delta t}$-based conventional approach and calibrate the conductor characteristic coefficients (e.g. ε_e and ε_s) used in the

thermal model of the conductors. For example, the value of ε_e was determined to minimize the average difference between the measured and simulated T_c for night-time periods in [154]. CIGRE Technical Brochure 299 [74] recommended that the value of ε_s could be set to be 0.1 higher than the estimated value of ε_e.
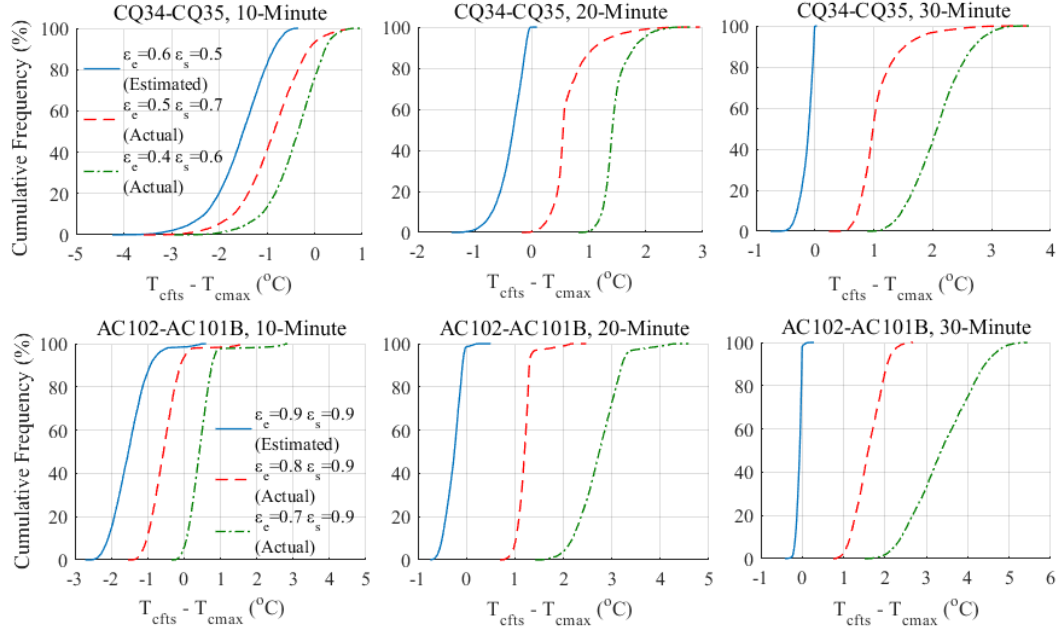
Fig. 6-16: Cumulative frequency distributions of deviations between T_{cmax} and T_{cfts} tracked by the $T_{cav,\Delta t}$-based conventional approach with a 10-second Δt under the enhanced analytical method based transient rating for different time horizons considering estimation errors in the conductors' emissivity ε_e or absorptivity ε_s for the two spans.

6.4. Conclusions

This chapter has proposed a weather-based approach to probabilistic forecasting of short-term or transient-state dynamic line rating (DLR) for a particular span based on an enhanced analytical method for transient-state conductor temperature calculation. The enhanced analytical method considers changes of weather conditions and fulfils the assumption of the conductor's thermal equilibrium at the start of a specified time period required by the IEEE analytical method. Using the conventional approach that evaluates heating and cooling terms at the average conductor temperature over each 10-second time interval as a benchmark, the enhanced analytical method is shown to

give more accurate estimates of transient-state conductor temperatures on average than the CIGRE analytical method and the conventional approach that estimates the associated terms at the initial conductor temperature over each time interval.

To reduce computation time, a fast root-finding algorithm, i.e. the secant method, is employed to determine the steady-state final conductor temperature corresponding to the final line current and weather conditions after step changes, and to adjust the transient-state DLR until the conductor temperature reaches the maximum allowable limit at the end of a specified time period. The weather-based approach developed here has been tested on two spans comprising different types of conductors. The enhanced analytical method based transient-state DLR is usually conservative since the conductor temperature is overestimated by the enhanced analytical method for most of the time. Although the point forecasts of transient-state DLRs show a higher accuracy than those that are calculated from persistence forecasts of weather parameters, they are generally overestimated at low rating levels. This problem can be overcome by adopting a certain low percentile from a probabilistic forecast of transient-state DLR. The percentiles of transient-state DLR forecasts for a particular span derived from the correlated random weather samples that are generated from the conditionally heteroscedastic auto-regressive forecasting models are preferred in this research due to their improved calibration at the lower percentiles for time horizons of 20 and 30 minutes. This is because the significant positive correlations among random samples of the same weather parameters (i.e. wind speed and air temperature) at different future moments expand the predictive distributions of 20-minute and 30-minute DLRs.

The weather-based approach to probabilistic forecasting of transient-state DLR requires around two seconds to calculate the 10-minute, 20-minute and 30-minute DLR forecasts for 2×10^4 scenarios. The short time required for the transient-state DLR calculation increases the practicability of applying the lower percentiles of transient-state DLR forecasts.

Forecast horizons of 30 minutes (three 10-minutes time steps) have been examined in the work conducted here. Given time for SCADA measurements to be received, a system state estimation to be updated and some consideration of the implications of the system's state relative to prevailing and anticipated ratings, this is sufficient time for a system operator to take action based on the forecast result. However, actions that might be taken to reduce loading if the forecast DLR would otherwise be exceeded are, in effect, limited to generation re-dispatch, most obviously curtailment of output at or near the sending end of the critical line, or some demand reduction in the vicinity of the receiving end, e.g. where possible, by switching demand to another substation through distribution network reconfiguration. (Where this is not possible, to avoid interruptions to demand that have not been contracted in advance, it might only be possible to effect modest reductions through changes to voltage targets within the distribution network.)

7. WIND POWER INTEGRATION WITH PROBABILISTIC FORECASTING OF DYNAMIC LINE RATING

7.1. Introduction

This chapter will illustrate the potential application of DLR forecasting to increase the utilisation of wind generation on the 132kV transmission network in North Wales as shown in Fig. 7-1.
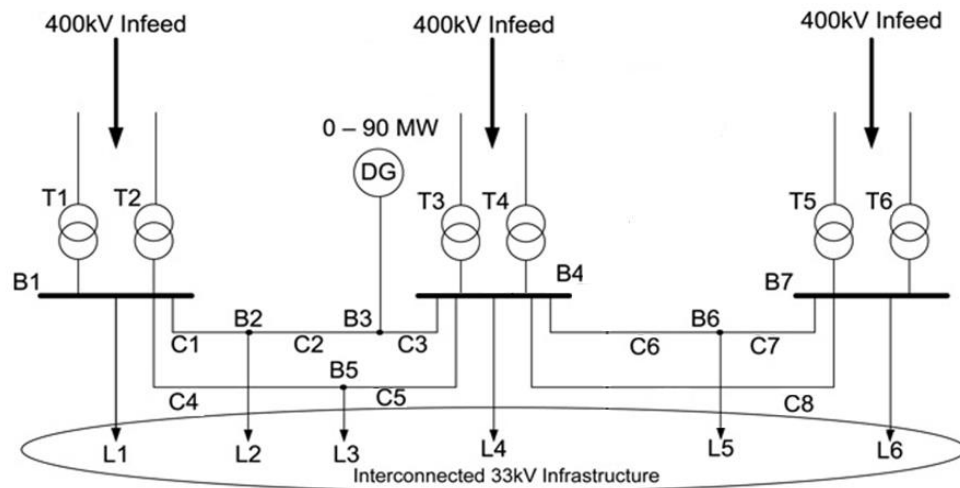
Fig. 7-1. The 132kV network in North Wales

The lower percentiles of steady-state DLR forecasts for up to 3 steps (half hour) ahead and real-time ratings have been estimated for eight 132kV overhead circuits (C1 – C8) that connect seven 132kV buses (B1 – B7); this analysis uses data from the period from 28/01/2013 to 31/03/2013. The 132kV network is supplied from the 400kV National Grid transmission system through 400kV/132kV super grid transformers at three 132kV substations B1, B4 and B7. The power at each 132kV substation is then fed into the 33kV distribution networks which are interconnected. For example, the 33kV substation L2 supplied from the 132kV substation B2 is connected with the 33kV substation L3 that is supplied from the 132kV substation

B5. The configuration and technical parameters of the 132kV network and 33kV interconnected distribution networks and the maximum load at each 33kV substation for the period 2012/2013 are available from '*Distribution Long Term Development Statement for the years 2013/14 to 2017/18*' [155].

The ampacity of an overhead line (OHL) provided in real time can only tell a system operator or a wind farm operator the concurrent maximum allowable rating. However, using only the real-time ratings may lead to a risk related to limited generation ramp rates in some particular cases. For example, there can be an issue if a significant reduction in the real-time rating over 10 minutes exceeds the maximum volume that a generator can ramp down in that period or, if it is available and needed, replacement generation in another location can ramp up. Therefore, providing the system operator with forecasts of ratings can effectively avoid this risk by providing sufficient time for a re-dispatch action to be started and completed. This chapter will estimate the degree to which wind generation curtailment can be alleviated through use of the lower percentiles of steady-state DLR forecasts in place of the static line ratings (SLRs) for each 132kV OHL over the evaluated period, based on which the impact from probabilistic DLR forecasting on wind power integration is assessed.

7.2. Modelling of Available Wind Power

Four wind farms were located around the 132kV and 33kV distribution networks over the evaluated period from 28/01/2013 to 31/01/2013. The 90MW Rhyl Flat offshore wind farm was connected to the 132kV bus B3 and the other three wind farms (a 60MW offshore wind farm and two onshore wind farms with installed capacities of 15.6MW and 21.25MW) were connected to the local 33kV substations [155]. The available wind power of each wind farm is modelled based on the wind speed $w_{s,hub}$ at the hub height combined with a generic power curve model which defines the available wind power output $WP^{av}(w_{s,hub})$ as a function of the rated power WP_{rated} and $w_{s,hub}$ [156, 157]:

$$WP^{av}\left(w_{s,hub}\right) =$$

$$\begin{cases} 0 & for \quad w_{s,hub} \le w_{s,in} \; or \; w_{s,hub} > w_{s,out} \quad (7\text{-}1) \\ WP_{rated}\left(a_{wp} + b_{wp} \cdot w_{s,hub} + c_{wp} \cdot w_{s,hub}^2\right) & for \quad w_{s,in} < w_{s,hub} \le w_{s,rated} \\ WP_{rated} & for \quad w_{s,rated} < w_{s,hub} \le w_{s,out} \end{cases}$$

where $w_{s,in}$, $w_{s,out}$ and $w_{s,rated}$ represent the cut-in, cut-out and rated wind speeds respectively for a wind turbine, and constants a_{wp}, b_{wp} and c_{wp} are only dependent on $w_{s,in}$ and $w_{s,rated}$ [156]:

$$a_{wp} = -\frac{w_{s,in} \cdot \left(w_{s,in} + w_{s,rated}\right) \cdot \left(w_{s,in}^2 + 2w_{s,in}w_{s,rated} - w_{s,rated}^2\right)}{2\left(w_{s,in} - w_{s,rated}\right)^2 \cdot w_{s,rated}^2} \qquad (7\text{-}2)$$

$$b_{wp} = \frac{w_{s,in}^4 + 4w_{s,in}^3 w_{s,rated} + 6w_{s,in}^2 w_{s,rated}^2 - 2w_{s,in}w_{s,rated}^3 - w_{s,rated}^4}{2\left(w_{s,in} - w_{s,rated}\right)^2 \cdot w_{s,rated}^3} \qquad (7\text{-}3)$$

$$c_{wp} = -\frac{w_{s,in}^3 + 3w_{s,in}^2 w_{s,rated} + 3w_{s,in}w_{s,rated}^2 - 3w_{s,rated}^3}{2\left(w_{s,in} - w_{s,rated}\right)^2 \cdot w_{s,rated}^3} \qquad (7\text{-}4)$$

Fig. 7-2 shows an example of a generic power curve estimated for a wind turbine that has technical parameters of $w_{s,in} = 4m/s$, $w_{s,out} = 25m/s$, $w_{s,rated} = 13.5m/s$ and $WP_{rated} = 3.6MW$ based on equation (7-1).
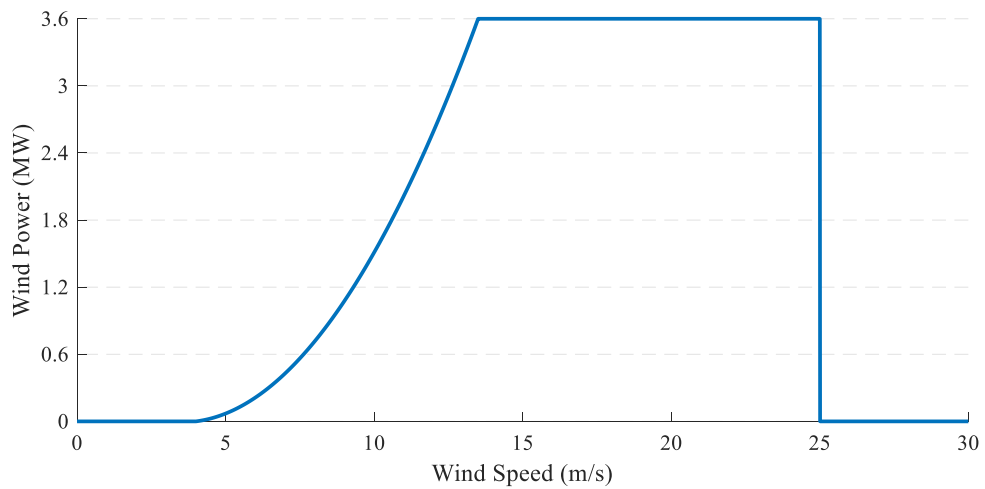
Fig. 7-2: A generic power curve for a 3.6MW wind turbine with cur-in, cut-out and rated wind speeds of $4m/s$, $25m/s$ and $13.5m/s$ respectively.

The hub height wind speed $w_{s,hub}$ at the centre of the wind farm is estimated from wind speeds measured at weather stations using the spatial interpolation models developed in Chapter 4. The trend surfaces of wind speeds at a reference level (300m above sea level) in terms of distance to ocean (DTO) at offshore wind farms are calculated for $DTO = 0$. The technical parameters of wind turbines and the useful information for each wind farm are provided in [158 – 165].

7.3. Permitted Outputs of Renewable Generation Plants

To investigate the impact of DLR forecasting on alleviating wind generation curtailment, the reductions in curtailment of wind power from Rhyl Flats wind farm through the replacement of the SLRs by the lower percentiles of steady-state DLR forecasts for eight 132kV OHLs are determined. This is because Rhyl Flats is the wind farm connected to the 132kV bus B3 and the produced electricity can be dispatched to 132kV substations B2 and B4 through two 132kV OHLs C2 and C3 for which probabilistic DLR forecasts for up to a half hour (3 steps) ahead have been estimated. It is assumed that the connection of Rhyl Flats to B3 is sufficient for the transfer of power available from Rhyl Flats. In addition to thermal limits of OHLs, the planned wind output is limited by the maximum allowable ramp rate and the expected available wind power. Table 7-1 and Fig. 7-3 show the procedure used to calculate the maximum output of a renewable generation plant such as a wind farm that is permitted to inject into the connected grid, taking into account the maximum allowable ramp rates of wind generation and the forecasts of available wind powers and lines' ratings for up to three 10-minutes time steps ahead:

Table 7-1. Procedure used to calculate the planned power output of a wind farm

Computation sequence		(3)	(2)	(1)
Time period	$t = 0$	$t = 1$	$t = 2$	$t = 3$
Expected available wind power		WP_1^{av}	WP_2^{av}	WP_3^{av}
Line rating forecast		DLR_1	DLR_2	DLR_3
Minimum wind farm output		$max\left\{\begin{matrix}WP_0 - \Delta WP^- \\ 0\end{matrix}\right\}$	$max\left\{\begin{matrix}WP_0 - 2 \cdot \Delta WP^- \\ 0\end{matrix}\right\}$	$max\left\{\begin{matrix}WP_0 - 3 \cdot \Delta WP^- \\ 0\end{matrix}\right\}*$
Maximum wind farm output		$min\left\{\begin{matrix}WP_0 + \Delta WP^+ \\ WP_1^{av} \\ WP_2 + \Delta WP^-\end{matrix}\right\}$	$min\left\{\begin{matrix}WP_0 + 2 \cdot \Delta WP^+ \\ WP_2^{av} \\ WP_3 + \Delta WP^-\end{matrix}\right\}$	$min\left\{\begin{matrix}WP_0 + 3 \cdot \Delta WP^+ \\ WP_3^{av}\end{matrix}\right\}*$
Planned wind farm output	WP_0	WP_1	WP_2	WP_3

* ΔWP^+ or ΔWP^-: the maximum volume that a wind farm is allowed to ramp up or ramp down in a 10-minute period given its maximum allowable ramp rate.
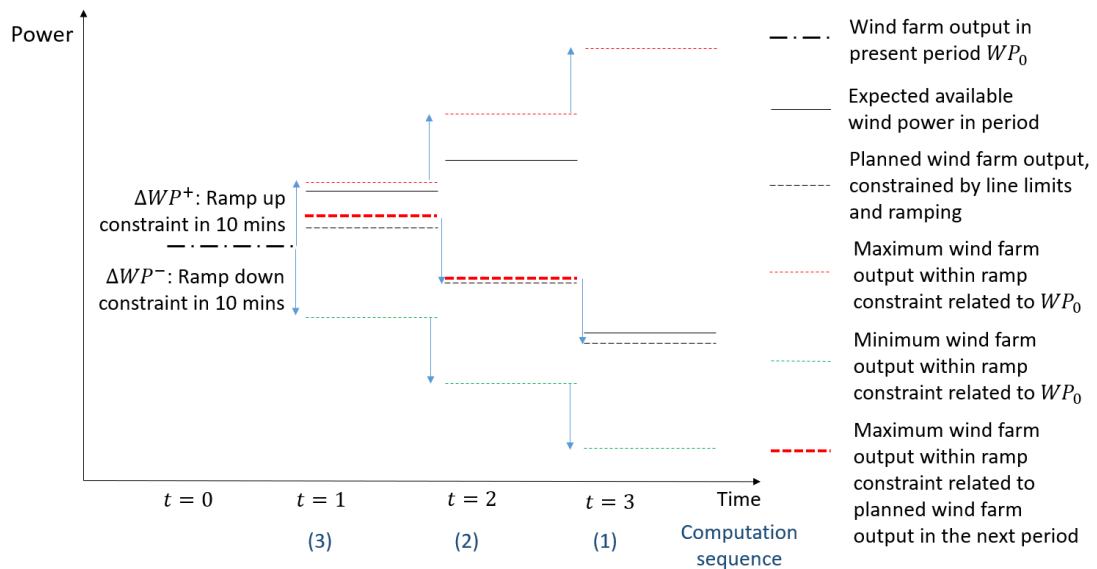
Fig. 7-3. A diagram showing the procedure of calculating the planned power output of a wind farm.

(1) The planned wind farm output after 30 minutes WP_3 (at $t = 3$) is calculated under the constraints of the steady-state rating forecasts DLR_3 with a maximum limit that is the lower value of the expected available wind power WP_3^{av} for half hour (3 steps) ahead or the sum of the present wind farm

output WP_0 (at $t = 0$) and the maximum volume that the wind farm can ramp up in three subsequent 10-minute periods $(3 \cdot \Delta WP^+)$ given its maximum allowable ramp rate. A minimum limit for WP_3 is determined as the larger value of zero or the difference between WP_0 and the maximum volume that the wind farm is allowed to ramp down in three subsequent 10-minute periods $(3 \cdot \Delta WP^-)$. The planned power output WP_3 of each generating plant and the powers at the three 132kV substations (B1, B4 and B7) fed by the 400kV National Grid transmission system at $t = 3$ are calculated by Optimal Power Flow (OPF) [166] with the objective of maximising the utilisation of renewable generation;

(2) The planned wind output after 20 minutes WP_2 (at $t = 2$) is limited by the 2-step-ahead rating forecasts DLR_2 with a maximum limit that is the lowest value among the expected available wind power WP_2^{av} (at $t = 2$), the sum of WP_0 and the maximum allowable ramp-up volume for the wind farm in two 10-minute periods $(2 \cdot \Delta WP^+)$, and the sum of WP_3 and the maximum allowable ramp-down volume in 10 minutes (ΔWP^-) given its maximum allowable ramp rate. This would ensure that the planned wind farm output WP_2 at $t = 2$ can ramp down to the planned power output WP_3 at $t = 3$ in 10 minutes. A minimum limit for WP_2 is determined as the difference between WP_0 and the maximum allowable ramp-down volume in two 10-minute periods $(2 \cdot \Delta WP^-)$. If WP_0 is smaller than $(2 \cdot \Delta WP^-)$, the minimum limit for WP_2 is set to be zero;

(3) The minimum limit for the planned wind output after 10 minutes WP_1 (at $t = 1$) equals the difference between WP_0 (at $t = 0$) and ΔWP^- so that a 10-minute period is sufficient for wind generation to ramp down from WP_0 to WP_1. A minimum limit of zero is applied if $(WP_0 - \Delta WP^-)$ is negative. The maximum limit for WP_1 is determined as the lowest value among the expected available wind power WP_1^{av} (at $t = 1$), the sum of WP_2 and

ΔWP^-, and the sum of WP_0 and the maximum allowable ramp-up volume in 10 minutes (ΔWP^+). This would ensure that the wind generation can ramp down from WP_1 to WP_2 and ramp up from WP_0 to WP_1 in 10 minutes given its maximum allowable ramp rate; and that the increased wind farm output would not exceed the expected available value. The 1-step-ahead steady-state rating forecasts DLR_1 are additionally used as thermal limits of 132kV OHLs for the estimation of WP_1;

(4) When the time $t = 1$ comes, the estimated value of WP_1 is used as the present wind power output WP_0 and the previous three steps are repeated.

7.4. Reduction in Wind Generation Curtailment by Applying DLR Forecasts

The 132kV and 33kV interconnected distribution networks in North Wales are represented in MATPOWER [167], including 182 buses and 222 branches. The layout and technical parameters of distribution lines such as impedances and SLR values can be found in [155]. The loads at 33kV buses are assumed to vary according to the normalised data which is extracted from historic time series of total electricity demand in England and Wales [168] for the year 2012/13.

Other types of renewable generation plants connecting to the 33kV interconnected distribution networks such as hydro and landfill are all included in the whole system model. It is assumed here that the hydroelectric plant is run-of-river with a limited amount of water storage and the landfill is combined heat and power plant that has a particular heat demand. These assumptions mean that, in effect, the run-of-river hydroelectricity and landfill generation cannot be re-dispatched like wind farms. Since power outputs from these generating plants are not provided, they are assumed to be constant at their ratings which are provided in [155]. The total capacity of these renewable generation plants excluding wind generators is 53.8MW, supplying around

12.3% of the total system demand (i.e. 435.8MW). Furthermore, it is assumed that all the renewable generation plants have 'perfect' forecasts of the expected available powers, i.e. the forecasts being equal to the actual values.

The maximum allowable ramp rates at which generating plants are required to be able to limit the changes of power outputs depend on region as listed in Table 7-2 [169]. Though the research area is in North Wales, the standards used in Scotland are adopted in this study for academic purposes as the maximum allowable ramp rates used in England & Wales rarely limit the outputs of Rhyl Flats. As a result, all the connected generating plants with an installed capacity over 15MW would be required to operate under the maximum allowable ramp rate limits. In addition to the ramp rate limits for renewable generation, the variations in steady voltages from the declared 33kV and 132kV should not exceed 6 per cent and 10 per cent respectively [155] and a $\pm 3\%$ voltage step change limit [170] is also used to constrain the step change in voltage from the present steady-state value in 10 minutes.

Table 7-2. The maximum ramp rates that generating plants are required to limit changes of power outputs at in different areas [169]

Ireland	England & Wales	Scotland
· 1 to 30MW/minute (1 minute average)	· No limit for a change of up to 300MW	· For Power Park Modules <15MW No limit
· 1 to 30MW/minute (10 minute average)	· 50MW/minute for a change between 300MW and 1000MW	· For Power Park Modules from 15MW to 150MW 20% of rated output/minute (1 minute average) 7% of rated output/minute (10 minute average)
(values specified by the TSO to each wind farm)	· 40MW/minute for a change over 1000MW	· For Power Park Modules above 150MW 30MW/minute (1 minute average) 10MW/minute (10 minute average)

Based on the procedure described in Table 7-1 and Fig. 7-3, the planned wind farm outputs after 10 minutes and the volumes of wind generation curtailment at Rhyl Flats over the period from 28/01/2013 to 31/03/2013 are calculated when the power transfer limits of eight 132kV OHLs are determined by the SLRs, the 1st, 3rd and 5th percentiles of steady-state DLR forecasts (denoted by P1, P3 and P5) and the 'perfect'

rating forecasts which are equal to the actual 'real-time' ratings (RTRs) respectively. It is found that Rhyl Flats would not be curtailed even when the 132kV OHLs are limited by SLRs. This is because the installed capacity of Rhyl Flats, i.e. 90MW, is smaller than the SLRs of either the circuit C2 or C3. Therefore, in order to test the probabilistic rating method, the installed capacity of Rhyl Flats is scaled up to 180MW, 270MW and 360MW to estimate how much curtailment could be avoided by using DLR forecasts. The volumes (GWh) of wind generation curtailments at Rhyl Flats for different installed capacities under different thermal limits of 132kV OHLs over the evaluated period are shown in Fig. 7-4.
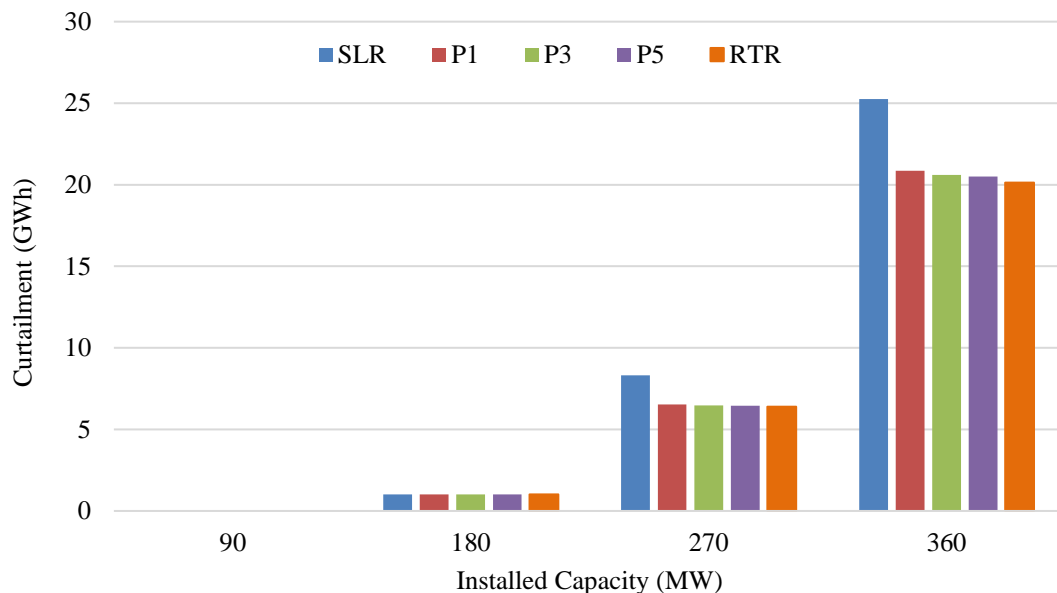
Fig. 7-4. Volumes (GWh) of wind generation curtailment at Rhyl Flats for different installed capacities subject to different thermal limits of 132kV OHLs over the evaluated period.

It is found that the levels of curtailment of Rhyl Flats under different thermal limits of 132kV OHLs are the same when Rhyl Flats has an installed capacity of 180MW. This suggests that Rhyl Flats may be curtailed due to other reasons (e.g. the ramp rate limit) rather than the ampacities of circuits C2 and C3. The electricity produced by Rhyl Flats can be dispatched to 132kV substations B2 and B4 through C2 and C3 (as shown in Fig. 7-1) which have the SLRs of 111MVA and 139MVA in winter

(January and February) and 100MVA and 133MVA in spring (March) respectively. Regardless of the limits of ramp rates, the maximum permitted power output of Rhyl Flats could reach 250MVA in winter or 233MVA in spring which is still higher than the 180MW installed capacity of Rhyl Flats. Therefore, there would be no curtailment with 180MW of wind capacity at Rhyl Flats caused by the thermal limits of C2 and C3.

To quantify the wind generation curtailment caused by line ampacity constraints only, the amounts of curtailment at Rhyl Flats due to other reasons are estimated through increasing power transfer capacities of the eight 132kV OHLs to infinity and then subtracted from the total volumes of wind generation curtailment. Fig. 7-5 shows the volumes (GWh) of wind curtailment at Rhyl Flats for different installed capacities caused by power transfer limits of 132kV OHLs *only* that are determined by the SLRs, lower percentiles of DLR forecasts and real-time ratings (RTRs) respectively.
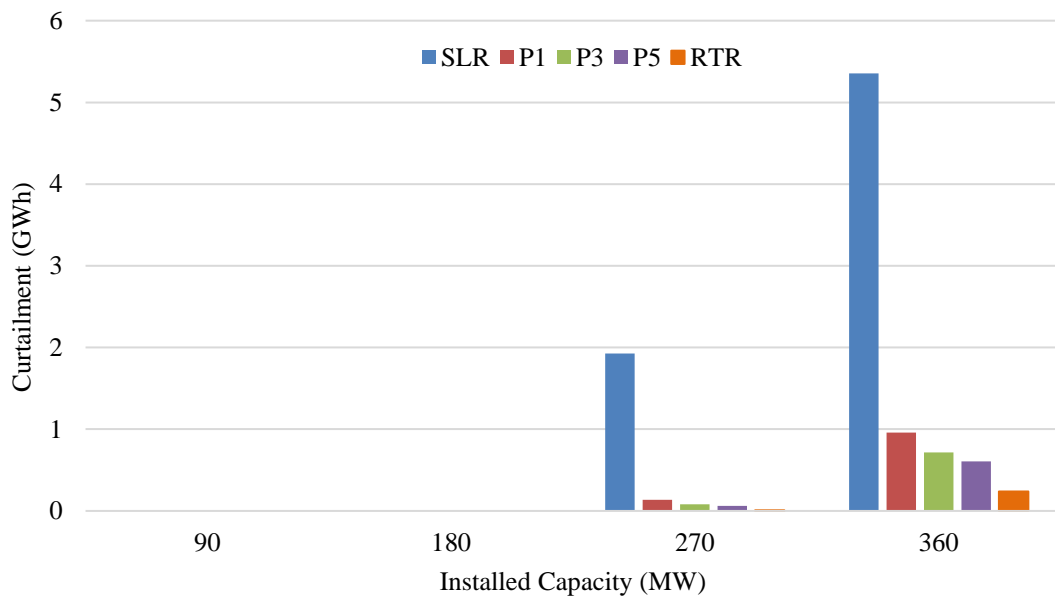
Fig. 7-5. Volumes (GWh) of wind generation curtailment at Rhyl Flats for different installed capacities caused by thermal limits of 132kV OHLs *only* that are determined by SLRs, P1, P3, P5 values and real-time ratings (RTRs) over the evaluated period

The simulation results demonstrate that (a) the power transfer capacities of 132kV OHLs would not limit the outputs of Rhyl Flats with installed capacities of 90MW and 180MW; (b) when Rhyl Flats is scaled up to 270MW, the 1.92GWh curtailment caused by the SLRs of 132kV OHLs is reduced by 1.79GWh (92.9%), 1.84GWh (95.7%) and 1.86GWh (96.8%) through the use of the P1, P3 and P5 values of DLR forecasts as the power transfer limits of 132kV OHLs; (c) when the installed capacity is increased to 360MW, the 5.35GWh wind curtailment due to the current-carrying capacities of 132kV OHLs limited by the SLRs is reduced by 4.4GWh (82.1%), 4.64GWh (86.7%) and 4.75GWh (88.7%) for the P1, P3, P5 forecasts respectively; and (d) when the current-carrying capacities of 132kV OHLs are determined by the 'perfect' DLR forecasts (i.e. 'real-time' ratings), a higher volume of reduced wind generation curtailment could be achieved, i.e. 99.7% for a 270MW installed capacity and 95.6% for a 360MW installed capacity.

As noted in Chapter 5, the upgrading of ratings relative to SLRs is usually limited to 25% due to various practical issues. When DLR forecasts are limited to 125% of SLRs, the 5.35GWh wind curtailment at 360MW Rhyl Flats caused by the SLRs of 132kV OHLs is reduced by 4GWh (74.8%), 4.15GWh (77.5%), 4.22GWh (78.7%) and 4.43GWh (82.8%) for the P1, P3, P5 and 'perfect' DLR forecasts respectively.

7.5. Risks of Using Dynamic Line Rating Percentiles

The lower percentiles of steady-state DLR forecasts estimated for 132kV OHLs have been found to be conservative since the percentages of time that the actual ratings exceed the lower DLR percentiles are generally less than the theoretical values as listed in Table 5-6. For example, the actual ratings are smaller than the 3-step-ahead P5 forecasts in only 2.2% of cases for circuit C2 and in 3.6% of cases for circuit C3. In practice, the probability of the line load scheduled by the P5 forecasts exceeding the actual rating will be smaller than the probability that the actual rating is below the P5 forecast since the line current cannot always reach the level of the P5 forecast.

To examine the risk of the line current exceeding the actual rating under the schedules derived from the P5 forecasts, the power flows passing through each 132kV OHL are compared with their actual ratings over the period from 28/01/2013 to 31/03/2013. The differences between the line currents and the actual ratings for circuits C2 and C3 are shown in Fig. 7-6 where Rhyl Flats is scaled up to 270MW and 360MW respectively. The line loads on circuit C2 are found to be always smaller than the actual ratings. When Rhyl Flats has 270MW and 360MW installed capacities, the line loads on circuit C3 exceed the actual ratings in 3 cases (0.03%) and 15 cases (0.17%) respectively.
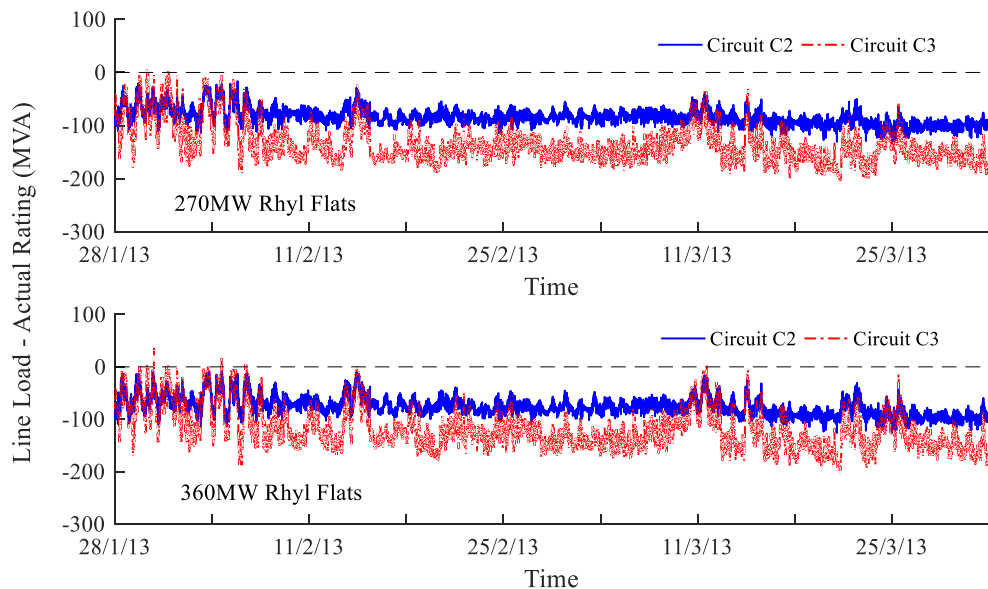
Fig. 7-6. Differences (MVA) between line loads and actual ratings on circuits C2 and C3 under the schedules derived from the P5 forecasts for different scales of Rhyl Flats wind farm

Though the actual ratings are shown to be smaller than the P5 forecasts in around 2% and 3% of cases for C2 and C3 respectively, the loads carried by C2 and C3 rarely exceed the actual ratings. When the power transfer limits of 132kV lines are removed (i.e. infinite power transfer capacities) during the OPF calculation, C3 is found to be overloaded in 85 cases (0.94%) where Rhyl flats is assumed to have an installed capacity of 360MW. The low probability of overloading on the two OHLs may be in

part due to relatively significant positive correlations between the available wind powers from Rhyl Flats and real-time ratings of C2 and C3 (i.e. 0.76 and 0.48 respectively). This is because they are all derived from the wind speed measurements at weather stations. The high current-carrying capacities of the connected circuits that coincide with the high available wind power are mostly sufficient to transfer the power outputs from Rhyl Flats with assumed installed capacities of 270MW and 360MW. Furthermore, the growth in the assumed installed capacity at Rhyl Flats is shown to increase the risk of overloading on the connected circuits.

The static rating itself is not without risk since the SLRs are found to be greater than the actual ratings in 1835 cases (20.23%) for C2 and in 3 cases (0.03%) for C3. However, the use of the SLRs as the thermal limits of 132kV OHLs does not result in C2 or C3 being overloaded. Due to the relatively significant positive correlations between the modelled available wind powers and the calculated line ratings, the high wind outputs at Rhyl Flats in the overloading cases are found to be accompanied by the actual real-time ratings of C3 that are higher than the SLRs. Therefore, when the SLRs are adopted as the thermal limits, the line overloading in these cases is avoided, but at a cost of losing a certain headroom for Rhyl Flats to generate over the complete evaluated period. This can be inspected in Fig. 7-5.

7.6. Conclusions

This chapter has evaluated the use of the lower percentiles of steady-state dynamic line rating (DLR) forecasts with respect to alleviating wind generation curtailment of differing wind farm capacities at Rhyl Flats wind farm (90MW and also a series of upscaled wind farms) that has a connection to the 132kV network in North Wales. The reductions in wind generation curtailment at Rhyl Flats achieved by using the lower percentiles of DLR forecasts of eight 132kV overhead lines (OHLs) in place of the static line ratings (SLRs) are estimated based on the assumptions of the available wind power forecasts being equal to their actual values and the connection of Rhyl Flats to the 132kV bus being sufficient for the transfer of power available from the wind farm.

The 132kV network and 33kV interconnected distribution networks in North Wales are represented in MATPOWER. Using Optimal Power Flow, the planned power outputs from wind farms are maximised under the constraints of the maximum allowable wind generation ramp rates, the expected available wind powers and forecasts of power transfer capacities of OHLs. The DLR forecasts for up to three 10-minutes time steps ahead are all considered to avoid the risk of the reduction in wind farm output required to meet the line ampacity constraint exceeding the maximum volume that the wind farm is allowed to ramp down in 10 minutes given its maximum allowable ramp rate. When Rhyl Flats is scaled up to 270MW and 360MW, the use of the lower percentiles (i.e. the 1st, 3rd and 5th percentiles) of steady-state DLR forecasts shows the potential to reduce the wind generation curtailment due to the thermal limits of 132kV OHLs determined by SLRs by greater than 90% (i.e. 92.9%, 95.7% and 96.8% for the three DLR percentiles) and 80% (i.e. 82.1%, 86.7% and 88.7% for the three DLR percentiles) respectively over the period from 28/01/2013 to 31/03/2013. When current-carrying capacities of 132kV OHLs are determined by the 'perfect' rating forecasts, i.e. real-time ratings, the wind

generation curtailment at Rhyl Flats with 270MW and 360MW installed capacities caused by the SLR based thermal limits is reduced by 99.7% and 95.6% respectively over the evaluated period.

In the modelling, the expected available wind power is approximately estimated based on inference of wind speed at hub height at the centre of the wind farm from wind speeds observed at weather stations combined with a generic power curve for a single turbine. This may lead to the correlations between the calculated available wind powers and the ratings of the connected lines derived from wind speed measurements being higher than in actuality. When the correlations are higher than actual values, conservatively set limits to transfer on the connected lines will often be high at the same time as there are high exports from Rhyl Flats. Thus, the reduction in wind generation curtailment achieved by using the lower DLR percentiles as the thermal limits of 132kV OHLs may be overestimated in the work conducted here. In addition, their significant positive correlations reduce the risk of overloading on the connected lines since the actual ratings of the connected OHLs are mostly sufficient to transfer the power outputs from Rhyl Flats even if they are smaller than the adopted DLR percentiles. Although the SLRs exceed the actual ratings in some cases, using the SLRs as line ampacity constraints would not result in the connected circuits being overloaded in this work, at a cost of losing a certain headroom for Rhyl Flats to deliver additional electricity to the network over the evaluated period.

8. CONCLUSIONS AND FUTURE WORK

The thesis has presented weather-based approaches to probabilistic forecasting of dynamic line rating (DLR) for overhead lines (OHLs). Conditionally heteroscedastic auto-regressive models have been developed to determine predictive distributions of the measured weather variables for a number of 10-minutes time steps ahead from historic weather observations recorded at weather stations along the route of OHLs. For a particular overhead span in proximity to a weather station, the distribution of continuous or steady-state DLR forecasts at a particular future moment is calculated from the predictive distributions identified for the measured weather variables using Monte Carlo simulation combined with a thermal model of overhead conductors. When estimating probabilistic forecasts of steady-state DLRs for an entire OHL, possible weather conditions at each span within the line are inferred from random samples of the measured weather variables at weather stations using suitable spatial interpolation models. The minimum value of steady-state DLR forecasts among all spans is identified as the DLR forecast for the entire OHL in each of the generated scenarios, from which predictive DLR percentiles of the OHL are estimated. The approach to probabilistic forecasting of transient-state or short-term DLRs for a particular span considers changes of weather forecasts at each future time step and the thermal inertia of the conductors. Using an enhanced analytical approach to the transient-state conductor temperature modelling, the transient-state DLR forecast is calculated as that which yields the maximum allowable conductor temperature at the end of a specified time period under weather predictions at different future moments in each generated scenario. The proposed weather-based DLR forecasting approaches have been tested on 132kV OHLs composed of different types of overhead conductors along which nine weather stations have been installed in North Wales. This chapter will conclude by summarising findings from the work undertaken on probabilistic weather forecasting, spatial interpolation of weather variables, probabilistic forecasting of both steady-state and transient-state DLRs and potential

application of probabilistic DLR forecasts for wind power integration. Future research that can further enhance the weather-based DLR forecasting model developed here is also discussed.

8.1. Probabilistic Steady-State DLR Forecasting for a Span

8.1.1. Probabilistic weather forecasting

Different time series forecasting models have been compared for the purpose of providing a probabilistic weather forecast, i.e. one that does not simply give a single point estimate but instead quantifies the range of future values and their likelihood. Univariate auto-regressive (AR) models and vector auto-regressive (VAR) models with different model orders and lengths of sliding training window are separately developed to determine point forecasts of the measured weather variables as a sum of a linear combination of historic de-trended data and temporal trends extracted from the training window by Fourier series. The suitable auto-regressive model along with model order and training window length is determined for each weather variable as that which gives the best improvement in root mean square error (RMSE) over persistence forecasting for each forecast time horizon. VAR forecasting models have been selected for air temperature and solar radiation since they give a more significant improvement in RMSE over persistence than AR models. For wind speed and wind direction, a higher-order AR model is preferred since it performs similarly to or even better than a VAR model of a lower order and has fewer model parameters which saves computation time in the process of minimising continuous ranked probability score (CRPS) value. Furthermore, to address the circular properties of wind direction, wind directions are decomposed into the northerly and easterly components before de-trending and the application of the AR model; then wind directions are predicted based on forecasts of the two separate components.

The predictive distributions of air temperature, wind speed and wind direction are assumed to be normal, truncated normal with a cut-off at zero and von Mises respectively. The adopted AR and VAR forecasting models are developed further to determine distributions of weather forecasts through modelling the predictive spread or concentration parameter as time variable, reflecting conditional heteroscedasticity. This spread is modelled as a linear function of the root mean square of recent changes in de-trended data within one hour for air temperature and wind speed or the concentration of historic observations within the most recent two hours for wind direction. The model parameters are determined to minimise the average value of CRPS (a summary indicator to assess probabilistic forecasts with respect to calibration and sharpness) in the training window. Probabilistic forecasts of weather variables produced by the conditionally heteroscedastic (CH) models show a smaller average CPRS value, a better calibration and a more concentrated distribution over half of the time than simply modelling the predictive spread or concentration parameter as a constant (as with homoscedasticity). Furthermore, point forecasts or expected values of probabilistic forecasts estimated by the VAR-CH or AR-CH models show higher accuracies than persistence forecasts for each weather variable. Moreover, a more significant improvement in RMSE over persistence is achieved with increasing look ahead. Therefore, suitable AR or VAR forecasting models combined with conditional heteroscedasticity are employed to produce predictive distributions of the measured weather variables.

8.1.2. Probabilistic steady-state DLR forecasts for a span

For a particular span in proximity to a weather station, predictive distributions of the measured weather variables can be directly used to calculate probabilistic forecasts of steady-state DLRs for the span by a combination of the Monte Carlo method, where random weather samples are independently generated from the modelled predictive distributions at a particular future time, and a thermal model of overhead conductors. Point forecasts of solar radiation are used in this research instead of

probabilistic forecasts since conductor temperature is insensitive to the change in solar radiation when wind speeds are above a modest level or conductor temperatures are relatively high. A rank correlation based pairing method is adopted to pair the independent weather samples so as to have correlations similar to those calculated from weather observations within the most recent 15 days. The rank correlations of the paired random weather samples are close to those among their recent observations, especially for linear variables, i.e. air temperature and wind speed.

The probabilistic forecasts of steady-state DLRs for a particular span estimated from independent random weather samples show a better calibration than those that are derived from correlated weather samples, especially at lower and higher percentiles. The overconcentrated distributions of DLR forecasts calculated from the paired weather samples are mainly due to the correlations added into random samples of wind speed and wind direction. Although positive correlations between samples of air temperature and wind speed can also narrow predictive distributions of DLRs, their impact on the concentration of probabilistic DLR forecasts is limited by the relatively high accuracy of air temperature prediction.

8.2. Probabilistic Steady-State DLR Forecasts for an OHL

8.2.1. Spatial interpolation models

To estimate probabilistic forecasts of steady-state DLRs for a complete OHL, suitable spatial interpolation models are required to infer possible weather forecasts experienced at each span within the OHL from random weather samples generated from the predictive distributions that are modelled for the measured weather variables at weather stations. An appropriate spatial interpolation model has been determined for each weather parameter from different combinations of an inverse distance weighting (IDW) model or a kriging interpolation model and the modelling of spatial trends in terms of the associated geographic variables.

In order to eliminate the influence of elevation, measurements of air temperatures and wind speeds at original levels are converted to those at their respective reference levels (i.e. the sea level for air temperature and 300 meters above sea level for wind speed) by using the lapse rate and the log-law wind profile respectively. After the spatial and temporal de-trending, the residuals of weather variables at the reference levels are used to model the semi-variograms which clearly present spatial variability between weather variables compared to those extracted from original data and are applied to determine parameters of the kriging models. The spatial trends estimated for target locations, e.g. all spans, are then added back into the interpolations at the end of the IDW or kriging process. The interpolation results for each span at the reference levels are converted back to the elevation of the span.

The use of lapse rate for air temperature and the modelling of spatial trends of wind speeds at 300m above sea level in terms of distance to ocean significantly improve the interpolation accuracy in RMSE over the spatial interpolation models used in previous work undertaken by Durham University which did not consider the change of air temperature with elevation and used 200m above ground level as the reference level for wind speed. The de-trended data of air temperature at sea level show similar spatial correlations (or semi-variances) at short distance lags, which weaken the kriging weight assigned to the nearest sampled location and lead to a higher accuracy of air temperature interpolation than IDW. For wind speed and solar radiation, the kriging models perform slightly better than the IDW methods at most target locations. This may be because (a) the limited number of weather stations increases the difficulty in accurately modelling spatial relationships among weather variables, especially at short distance lags and (b) their fairly even distribution constrains kriging's advantage of compensation for cluster effects, i.e. weakening the weights assigned to what are effectively duplicate measurements in similar locations. In addition, the nugget effect in the kriging model will weaken the weight assigned to the nearest sampled location. This may reduce the interpolation accuracy for wind

speeds that are very close to a sampled location since wind speeds generally have strong correlations at short distance lags. Therefore, the IDW models that show similar accuracies and require less computation time than kriging are used for interpolation of wind speed and solar radiation in this work. The IDW model has also been applied to the northerly and easterly components of wind directions separately due to the circular properties of wind direction. This achieves a higher accuracy than the direct application of IDW to original wind directions.

8.2.2. DLR forecasts and predictions of critical span for an OHL

The random samples of air temperature and wind speed generated from the modelled predictive distributions at different weather stations are first paired to have rank correlations quite close to those among their historic observations within the most recent 15 days before the application of spatial interpolation models. Then probabilistic forecasts of steady-state DLRs for each OHL are produced from the possible weather forecasts at all spans within the OHL that are inferred from the independent or correlated random samples of the measured weather variables by suitable spatial interpolation models. The significant positive correlations added into random samples of the same weather parameters (i.e. air temperature and wind speed) at different stations expand the distribution of DLR forecasts for an OHL at a particular future time. This alleviates the problem of overconcentration of predictive distributions of DLRs that are derived from the independent weather samples.

Furthermore, the critical span for each OHL at a particular future time has been predicted based on the frequency of each span having the minimum DLR forecast among all spans within the OHL in the generated scenarios. The location of the critical span is accurately predicted for the five most frequent critical spans in greater than 70% of cases for most lines. The OHL covering a short distance and comprising a small number of spans of similar orientation generally has more accurate forecasts of the critical span in this work.

8.3. Probabilistic Transient-State DLR Forecasting for a Span

8.3.1. Enhanced analytical method for conductor temperature modelling

The transient-state conductor temperatures within a specified time period after step changes in line current and weather variables are separately modelled by (a) conventional approaches that use the non-steady-state heat balance equation to track the variation in conductor temperature over each sufficiently small time interval (typically 10 seconds) and (b) analytical methods that estimate the conductor temperature as an exponential function of time by assuming the cooling terms in the non-steady-state heat balance equation to be linear with conductor temperature. The analytical method developed in IEEE Standard 738 is enhanced here to additionally consider changes in weather variables and fulfil the requirement of the conductor being in thermal equilibrium prior to the point when the step occurs through inference of an equivalent steady-state initial line current from the initial conductor temperature and weather conditions over a given time period. To reduce computation time, the secant method (a fast root-finding algorithm) is used to find the steady-state final conductor temperature corresponding to the line current and weather variables after step changes.

The conventional approach that evaluates heating and cooling terms at the average conductor temperature over each 10-seconds time interval is considered here to provide accurate estimates of transient-state conductor temperatures since field measurements of conductor temperatures are not available. Based on the experimental data used in a calculation example given in CIGRE Technical Brochure 601, the conventional approach that evaluates heating and cooling terms at the initial conductor temperature over each 1-minute time interval is found to overestimate the increase in conductor temperature given a relatively significant growth in line current. This means that the conventional approach using the initial conductor temperature to evaluate associated variables over each time interval requires a very small time

interval to ensure the accuracy in iterative calculations. When tracking transient-state conductor temperatures for two particular spans over each 10-minute period, the enhanced analytical method requires less computation time and generates more accurate estimates of conductor temperatures on average than the conventional approach that uses the initial conductor temperature with a 10-seconds time interval. Furthermore, the conductor temperatures are mostly overestimated by the enhanced analytical method that evaluates the ac resistance at the average of the initial and steady-state final conductor temperatures. However, in some particular cases, the enhanced analytical method may underestimate the conductor temperature at the end of a specified time period due to the linearized convection heat loss rates being much greater than the actual values.

8.3.2. Probabilistic transient-state DLR forecasts for a single span

The secant method is used here to adjust the transient-state DLR until the conductor temperature modelled by the enhanced analytical method reaches the maximum allowable limit at the end of a 10-minute, 20-minute or 30-minute period. The 20-minute DLR and 30-minute DLR are limited to the calculated 10-minute DLR and the calculated or restricted 20-minute DLR respectively so as to avoid the risk of the conductor temperature exceeding the maximum allowable limit over a specified time period and reducing back to the limit by the end of the time period. Under the transient-state DLR calculated from weather observations through the enhanced analytical method, the final conductor temperature estimated by the conventional approach using the average conductor temperature with a 10-seconds time interval does not reach the maximum allowable limit for most of the time due to the enhanced analytical method's overestimation in the growth of conductor temperature. Furthermore, the deviation from the maximum allowable conductor temperature decreases with an increased length of the specified time period. Therefore, the

transient-state DLRs estimated on the basis of the enhanced analytical method are usually conservative.

Random samples of air temperatures and wind speeds generated from the modelled predictive distributions at the same and different future moments over a particular future half-hour period are all paired to have rank correlations quite close to those that are computed from their recent weather observations. The changes of weather forecasts at each 10-minutes time step are all considered for the predictions of 10-minute, 20-minute and 30-minute transient-state DLRs in each generated scenario. The significant positive correlations among random weather samples of the same parameters at different future moments expand the distributions of 20-minute and 30-minute DLR forecasts which have better calibration at the lower and higher percentiles than those derived from the independent weather samples.

8.4. Accuracy and Effectiveness of Probabilistic DLR Forecasts

The point forecasts of steady-state and transient-state DLRs for a particular span or an entire OHL calculated from random weather samples that are generated by the conditionally heteroscedastic auto-regressive (AR-CH) forecasting models mostly show greater than 10% improvements in RMSE over those computed from persistence forecasts of weather variables. However, the AR forecasting models' overestimation at lower levels of wind speeds leads to unsatisfactory performance of the AR-CH models at the lower rating levels, e.g. the levels below the static line ratings (SLRs) for a particular span and below 90% SLRs for an OHL for steady-state DLRs, where the DLR forecasts are significantly overestimated by the AR-CH models. The adoption of a certain lower percentile from a probabilistic DLR forecast can mitigate the risk of using the overestimated point forecasts of the AR-CH models based DLRs.

The effectiveness of adopting a particular lower DLR percentile, e.g. the 5th percentile (P5 value), as the thermal limit for a particular span or an OHL has been assessed through an examination of the differences between the actual ratings and the P5 forecasts. The experimental results show that the P5 forecasts exceed the actual ratings in no more than 5% of cases on average.

8.5. Application of Probabilistic DLR Forecasting

The potential application of DLR forecasting to increase the use of wind generation on the 132kV network in North Wales has been investigated through an estimation of the degree to which wind generation curtailment can be alleviated by using certain lower percentiles of steady-state DLR forecasts in place of the SLRs for each 132kV OHL. The wind generation curtailment at Rhyl Flat wind farm that has a connection to the 132kV network in North Wales has been studied. The planned power outputs of various assumed wind farm capacities at Rhyl Flat (90MW and also a series of upscaled wind farms) are maximised using Optimal Power Flow under the constraints of the maximum allowable wind generation ramp rates, the expected available powers of Rhyl Flats and steady-state DLR forecasts of OHLs for up to three 10-minutes time steps ahead.

The replacement of the SLRs by the lower percentiles (i.e. the 1st, 3rd and 5th percentiles) of DLR forecasts and the 'perfect' rating forecasts (i.e. real-time ratings) for eight 132kV OHLs shows the potential to reduce the wind generation curtailment due to power transfer capacities of 132kV OHLs by 92.9%, 95.7%, 96.8% and 99.7% respectively for a 270MW Rhyl Flats wind farm and 82.1%, 86.7%, 88.7% and 95.6% respectively for a 360MW Rhyl Flats wind farm over an evaluated period of around two months from 28/01/2013 to 31/03/2013. Since the expected available wind powers and DLR forecasts of the connected 132kV OHLs are all inferred from wind speed measurements at weather stations, their positive correlations may be higher than in actuality. This may lead to that conservatively set limits to transfer on the

connected lines are usually high at the same time as there are high exports from Rhyl Flats. Therefore, the significant reduction in wind generation curtailment achieved by using DLR forecasts in place of SLRs may be overestimated in the work conducted here. Furthermore, the actual ratings of the connected OHLs are found to be mostly sufficient to deliver the outputs from Rhyl Flats due to their relatively significant positive correlations. This reduces the risk of overloading on the connected OHLs when the adopted lower DLR percentiles are greater than the actual ratings. The use of the relatively conservative SLRs is found to avoid the overloading on the connected OHLs, but at a cost of losing a certain headroom for Rhyl Flats to put additional electricity onto the network.

8.6. Future Work

8.6.1. Improving weather forecasting models

Building on the present work, future research can develop other probabilistic forecasting models for weather variables and assess their performance with respect to the calibration and sharpness of probabilistic forecasts so as to determine the most suitable models to produce distributions of weather forecasts. When developing the weather-based DLR forecasting approaches for different cases, the types of weather forecasting models should be carefully determined, including the model order, length of sliding training window, how often the model's parameters being updated, etc. Computation time is another issue to be considered. For example, a VAR forecasting model is found here to require longer time than an AR model to determine model's parameters during the process of CRPS minimisation (i.e. about 22.5 and 3.7 seconds on average for VAR(2) and AR(4) models respectively for wind speed forecasting). A univariate AR model of a higher order that has fewer auto-regressive parameters than a lower-order VAR model is then used for wind speed and wind direction forecasting due to the reduction in computation time and the similar forecasting performance.

Point forecasts of solar radiation have been used instead of probabilistic forecasts to estimate the distributions of DLR forecasts in this work. Future research can develop a probabilistic forecasting model for solar radiation and examine the histograms of probability integral transform for DLR forecasts that are derived from predictive distributions of solar radiation so as to estimate the degree to which the calibration of probabilistic DLR forecasts can be improved over use of point forecasts of solar radiation.

8.6.2. Modelling uncertainties of spatial interpolation

The uncertainties of weather forecasts have been successfully included in predictive distributions of DLRs in the present work. For a particular span in close proximity to a weather station, the uncertainty of DLR forecasts is mainly influenced by the size of errors of weather predictions. For an entire OHL, the spatial interpolation models used in the weather-based DLR forecasting model proposed here cannot model the uncertainties of spatial interpolations of weather variables for each span within the line though they have been improved to give more accurate point estimates than the methods employed in previous work undertaken by Durham University. Since spatial interpolation errors of weather variables are found to cause more significant errors of steady-state DLR estimates than weather forecast errors on average in this research, it is recommended that modelling the uncertainties of spatial interpolation between weather variables and reflecting their effects on DLR forecasts for a complete line should be addressed in future research.

8.6.3. Validation of DLR calculations

Probabilistic forecasts of steady-state and transient-state DLRs estimated from the AR-CH forecasting models have been assessed based on the ratings estimated via the weather observations when the time comes. A practical consideration is validation of both steady-state and transient-state DLR calculations. Since the weather-based DLR

forecasting model mainly relies on the thermal model of overhead conductors, the parameters (e.g. representing conductor material properties) in the steady-state and non-steady-state heat balance equations should be calibrated based on the accurate real-time measurements provided by some form of DLR monitoring techniques in future research. For example, conductor temperatures calculated from the measured weather data and line currents by the conventional approach that uses the average conductor temperature with a time interval of 10 seconds can be compared with what the monitoring (e.g. Overhead Transmission Line Monitoring [34] or Power Donut [37]) suggests they actually are.

8.6.4. Further enhancement in transient-state calculations

The analytical method enhanced here for the transient-state conductor temperature modelling has shown its adequate accuracy and fast-computational ability. However, the enhanced analytical method is likely to overestimate the growth in conductor temperature when there is a significant transient increase in line current. This will result in an underestimation in the enhanced analytical method based transient-state DLR, especially for the time horizon of 10 minutes. Future research can further refine the analytical method enhanced here to improve the accuracy of conductor temperature estimation. Furthermore, the approach to probabilistic forecasting of transient-state DLRs for a particular span should be extended for a complete OHL, using spatial interpolation models to infer possible weather predictions experienced at all spans. Moreover, future research can test the approaches' performance over longer forecast time horizons. However, given a longer time for a conductor to respond to the change in line current and an increase in the forecast error with an increased time horizon, a long time horizon forecast of transient rating is unlikely to give much enhancement over the steady-state DLR. In addition, the extra thermal headroom which can be exploited by the lower percentiles of steady-state DLR forecasts for a longer forecast horizon will decrease due to the increased forecast

error. For the steady-state DLR forecasting beyond around 6 hours, it would most likely depend on use of numerical weather prediction by specialist meteorologists rather than statistical models, though statistics can help in the evaluation of ensemble forecasts.

8.6.5. Challenges regarding the DLR application

When evaluating the potential application of probabilistic DLR forecasting for wind power integration, it is more reasonable to use an average power curve for multiple turbines within a wind farm to calculate the available wind powers rather than using a generic power curve for a single turbine which may have led to an overestimation in the available wind power in this work. If actual records of available power outputs from wind farms are provided, the relatively significant positive correlations between the expected available wind powers and power transfer capacities of the connected OHLs which are estimated from the wind speed measurements at weather stations in the work conducted here can be avoided. Furthermore, uncertainties in forecasts of system demands and available wind powers should be addressed and included in the scheduling in future research. It is also of value to compare the line current scheduled by the adopted percentiles of steady-state DLR forecasts with the transient-state DLR of each span to examine whether the maximum allowable conductor temperature will be exceeded over a specified time period.

For transmission systems operated to be N-1 or N-2 secure, the loading on most of their OHLs may be much lower than the SLR. This will lead to the extra thermal headroom exploited by the DLR techniques not being frequently used and constrain the benefits that can be brought by the DLR. For a heavily loaded network, system operators will tend to be risk averse and incur the penalty of, for example, higher congestion costs rather than exposed to any significant probability of a conductor's temperature exceeding its limit. The comfort zone of system operators is based on their hands-on knowledge of how the network responds to changes in a dynamic

event and which actions have greater reliability for this type of event and ambient conditions. Therefore, operations' risk averse is a constraint that has to be overcome before the wide application of DLR techniques. If the DLR forecasting methodology is such that the forecast percentiles can be regarded with confidence, they then give a probability of the actual rating being lower than the value being assumed by a system operator. The choice of percentile should be informed by the impact of exceedance, the corrective actions likely to be required and their costs [88]. This would allow the system operator to feel suitably confident about the risk associated with the selected DLR percentile. Future research should explore the nature of risk in relation to use of different percentiles of DLR forecasts and assess the costs of corrective actions when power transfers exceed the real-time ratings.

Another issue with the DLR application concerns the operator display integration. The display of information relevant to DLR required by different system operators vary widely based on the type of application and operating practice, etc. [17]. A basic requirement is to inform the rise of the real-time rating above the actual loading on an OHL. In the case of the line load exceeding the real-time steady-state rating, the time available for the system operator to sort out the overloading before violating a minimum required clearance (or the time when conductor temperature would reach a maximum permissible limit) should be displayed [17]. Furthermore, system operators can be informed with the transient rating that would last for 30 minutes or a longer period [171] based on the present state of the conductors (e.g. conductor temperature) and weather forecasts. To enable the application of the DLR forecasting methodology developed here, future research should develop effective displays that help system operators know the possible consequences of adopting each lower percentile of DLR forecasts and the corrective actions required if the real-time ratings are exceeded.

One other challenge regarding the DLR application is the accuracy of DLR estimates provided to system operators which may be degraded due to measuring errors of the monitoring devices. For the weather-based model developed here, a correction factor

can be applied to weather measurements based on the equipment specification sheets to ensure a conservative rating estimation [10]. As was discussed in Section 8.6.2, the weather-based model is likely to suffer from spatial interpolation errors of weather variables, especially for OHLs located in complex terrains. Therefore, it is necessary to place additional conductor temperature or sag/tension monitoring devices to cover microclimate regions or to monitor a circuit if it is highly critical or its loss of service would have a large impact. These monitoring technologies generally estimate ratings based on an effective perpendicular wind speed (EPWS) which is derived from the measured or inferred conductor temperature combined with the measured line current, air temperature and solar radiation. However, as noted in Section 2.6, the accuracy of the EPWS-based DLR would be reduced to varying extents due to measuring errors of different variables being monitored. A reasonable safety margin relative to the EPWS-based DLR estimate should be quantified for each specific case depending on the levels of the monitored variables and their measuring errors.

REFERENCES

[1] A. Michiorri, P.C. Taylor, S.C.E. Jupe, and C.J. Berry, "Investigation into the influence of environmental conditions on power system ratings," *Proc. Institution of Mechanical Engineers, Part A: Journal of Power and Energy*, vol. 223, no. 7, pp. 743-757, Nov. 2009.

[2] T. Ringelband, P. Schafer, and A. Moser, "Probabilistic ampacity forecasting for overhead lines using weather forecast ensembles," *Electrical Engineering*, vol. 95, no. 2, pp. 99-107, Jun. 2013.

[3] *IEEE Standard for Calculating the Current-Temperature of Bare Overhead Conductors*, IEEE Standard 738, 2007.

[4] CIGRE Working Group B2.43, "Guide for thermal rating calculations of overhead lines," CIGRE, Paris, Technical Brochure 601, Dec. 2014.

[5] C.F. Price and R.R. Gibbon, "Statistical approach to thermal rating of overhead lines for power transmission and distribution," *IEE Proc. C – Generation, Transmission and Distribution*, vol. 130, no. 5, pp. 245-256, Sep. 1983.

[6] C. Sinclair, W. Peat, and K. Smith, "Flexible electrical networks for a low carbon future: Network and built environment opportunities for enabling smarter networks," BRE Scotland and Scottish Power Energy Networks, Information paper, pp. 1-20, Apr. 2017.

[7] J. Fu, S. Abbott, B. Fox, D.J. Morrow, and S. Abdelkader, "Wind cooling effect on dynamic overhead line ratings," *45th Int. Universities Power Engineering Conference*, pp. 1-6, Aug. 2010.

[8] *Dynamic Line Rating,* Oncor Electric Delivery Company, Texas, Regional Demonstration Technical Performance Report, Aug. 2013. Available:
https://www.smartgrid.gov/files/FTR_Final_Oncor_DE-OE0000320.pdf

[9] *Oncor's Pioneering Transmission Dynamic Line Rating (DLR) Demonstration Lays Foundation for Follow-On Deployments*, U.S. Department of Energy, Apr. 2014. Available:
https://www.smartgrid.gov/files/Oncor_DLR_Case_Study_05-20-14_FINAL.pdf

[10] *Implementation of Real-Time Thermal Ratings*, Scottish Power Energy Networks, Glasgow, Final Close Down Report, LCNF SPT1001, Oct. 2013. Available:
https://www.ofgem.gov.uk/ofgem-publications/84214/finalclosedownreport09-10-2013.pdf

[11] S. Talpur, C.J. Wallnerstrom, P. Hilber, and C. Flood, "Implementation of dynamic line rating in a sub-transmission system for wind power integration," *Smart Grid and Renewable Energy*, vol. 6, pp. 233-249, Aug. 2015.

[12] J. Heckenbergerova and J. Hosek, "Dynamic thermal rating of power transmission lines related to wind energy integration," *11th Int. Conf. Environment and Electrical Engineering*, pp. 798-801, May 2012.

[13] E. Fernandez, I. Albizu, M.T. Bedialauneta, A.J. Mazon, and P.T. Leite, "Review of dynamic line rating systems for wind power integration," *Renewable and Sustainable Energy Reviews*, vol. 53, pp. 80-92, Jan. 2016.

[14] C.J. Wallnerström, Y. Huang, and L. Soder, "Impact from dynamic line rating on wind power integration," *IEEE Trans Smart Grid*, vol. 6, no. 1, pp. 343-350, Jan. 2015.

[15] S.C.E. Jupe, M. Bartlett, and K. Jackson, "Dynamic thermal ratings: The state of the art," *21st Int. Conf. Electricity Distribution, CIRED*, no. 918, pp. 1-4, Jun. 2011.

[16] *Dynamic Transmission Line Rating – Technology Review*, Hydro Tasmania Consulting, Tasmania, Australia, no. 208478-CR-001, Jul. 2009. Available: https://www.ea.govt.nz/dmsdocument/1872

[17] CIGRE Working Group B2.36, "Guide for application of direct real-time monitoring systems," CIGRE, Paris, France, Technical Brochure 498, Jun. 2012.

[18] Working Group on Monitoring & Rating of Subcommittee 15.11 on Overhead Lines, "Real-time overhead transmission-line monitoring for dynamic rating," *IEEE Trans. Power Delivery*, vol. 31, no.3, pp. 921-927, Jun. 2016.

[19] CIGRE Task Force B2.12.3, "Sag-tension calculation methods for overhead lines," CIGRE, Paris, Technical Brochure 324, 2007.

[20] A. Michiorri, P.C. Taylor, and S.C.E. Jupe, "Overhead line real-time rating estimation algorithm: description and validation," *Proc. Institution of Mechanical Engineers, Part A: Journal of Power and Energy*, vol. 224, pp. 293-304, May 2010.

[21] V.T. Morgan, *Thermal Behaviour of Electrical Conductors: Steady, Dynamic & Fault-Current Ratings*. Somerset, U.K.: Research Studies Press, 1991.

[22] J. Liu, H. Yang, S. Yu, S. Wang, Y. Shang, and F. Yang, "Real-time transient thermal rating and the calculation of risk level of transmission lines," *Energies*, vol. 11, no. 5, May 2018.

[23] J. Hosek, "Dynamic thermal rating of power transmission lines and renewable resources," *ES1002 Workshop on Weather Intelligence for Renewable Energies*, pp. 1-3, Mar. 2011.

[24] P. Patowary and N.J. Goyal, "Dynamic thermal rating and allowable operating time under transient conditions," *18th National Power Systems Conference*, pp. 1-6, Dec. 2014.

[25] E. Lindberg, "The overhead line sag dependence on weather parameters and line current," Master thesis, Uppsala University, Dec. 2011.

[26] T.S. Hlalele and S.Z. Du, "Real time monitoring of high voltage transmission line conductor sag: the state-of-the-art," *Int. Journal of Engineering and Advanced Technology (IJEAT)*, vol. 3, no. 1, pp. 297-302, Oct. 2013.

[27] *How It Works – Real Time Ampacity*, Ampacimon Overhead Line Monitoring, Mar. 2011. Available: http://www.ampacimon.com/wp-content/uploads/2015/09/How-Ampacity-works.pdf

[28] *Connecticut Siting Council Application – Appendix 3B – Illustrations of Transmission Line Structure Types*, The Connecticut Light and Power Company, Connecticut, U.S., Dec. 2011. Available:http://www.transmission-nu.com/residential/projects/IRP/csc/v1/V1_Section%203%20App%203B.pdf

[29] A. Arroyo, P. Castro, R. Martinez, M. Manana, A. Madrazo, R. Lecuna, and A. Gonzalez, "Comparison between IEEE and CIGRE thermal behaviour standards and measured temperature on a 132-kV overhead power line," *Energies*, vol. 8, pp. 13660-13671, 2015.

[30] W.H. McAdams, *Heat Transmission*, 3rd Ed. New York: McGraw-Hill, 1954.

[31] M. Gabrovsek and V. Lovrencic, "Temperature monitoring of overhead lines (OHLs) is Smart Grid solution for power grid," *Conf. Smart Grid 2010*, pp. 1-8, Sep. 2010.

[32] V. Lovrencic, M. Gabrovsek, M. Kovac, N. Gubeljak, Z. Sojat, and Z. Klobas, "The contribution of conductor temperature and sag monitoring to increased ampacities of overhead lines (OHLs)," *Periodica Polytechnica Electrical Engineering and Computer Science*, vol. 59, pp. 70-77, 2015.

[33] N. Gubeljak, V. Lovrencic, B. Banic, M. Pinteric, A. Ivec, and M. Jarc, "Application of an ice alarm in the OTLM system," *1st South East European Regional CIGRE Conf.*, pp. 1-12, 2016.

[34] Overhead Transmission Line Monitoring, "OTLM Device," 2016. Available: http://www.otlm.eu/about-otlm-system/otlm-device.

[35] L. Fish, "Power Donut^{tm} systems for overhead electric power line monitoring," 2012. Available:http://www.usi-power.com/Products%20&%20Services/Donut/Power_Donut2_Qualifications.pdf

[36] A. Bergstrom, U. Axelsson, and V. Neimane, "Vattenfall goes real time," *Transmission and Distribution World Magazine*, pp. 1-9, Jun. 2015. Available: http://www.usi-power.com/Products%20&%20Services/Donut/Vattenfall%20Goes%20Real%20Time.pdf

[37] *Power Donut2^{TM} The Instrumentation Platform for High Voltage Power Systems*, Underground Systems, Inc. (USi), New York, 2007. Available: http://www.amperespa.it/wp-content/uploads/2014/03/power_donut2.pdf

[38] M. Weibel, W. Sattinger, P. Rothermann, U. Steinegger, M. Zima, and G. Biedenbach, "Overhead line temperature monitoring pilot project," *CIGRE 2006 Session*, no. SC B2-311, pp. 1-8, 2006.

[39] *ThermaCAM P65 Infrared Camera*, FLIR Systems, Inc. Available: http://hurleyir.com/wp-content/uploads/2016/01/P65-Datasheet.pdf

[40] S. Beryozkina, A. Sauhats, and E. Vanzovichs, "Climate conditions impact on the permissible load current of the transmission line," *2011 IEEE PowerTech Conf.*, pp. 1-6, Jun. 2011.

[41] A. Ukil, H. Braendle, and P. Krippner, "Distributed temperature sensing: review of technology and applications," *IEEE Sensors Journal*, vol. 12, no. 5, pp. 885-892, May 2012.

[42] S.K. Allan and J.D. Alvarez, "A new experience of optical phase conductor (OPPC) in Red Electrica de Espana," *CIGRE Session*, no. *D2-109*, 2014.

[43] OZ Optics, "Fiber Optic Distributed Temperature Sensors (B-DTS)," Ottawa, Canada, Jan. 2018. Available: https://www.ozoptics.com/ALLNEW_PDF/DTS0127.pdf

[44] C. Bernauer, H. Bohme, V. Hinrichsen, S. Grobmann, S. Kornhuber, S. Markalous, M. Muhr, T. Strehl, and R. Teminova, "New method of temperature measurement of overhead transmission lines (OHTLs) utilizing surface acoustic wave (SAW) sensors," *XVth Int. Symp. High Voltage Engineering*, no. T7-554, pp. 1-6, Aug. 2007.

[45] H. Bohme, Z. Gao, S. Kornhuber, S. Markalous, W. Pfandl, and T. Strehl, "Overhead line temperature monitoring by using SAW sensor technology," *Proc. 16th Int. Symp. High Voltage Engineering*, no. E-45, pp. 1-6, 2009.

[46] C. Bernauer, H. Bohme, S. Grossmann, V. Hinrichsen, S. Kornhuber, S. Markalous, M. Muhr, T. Strehl, and R. Teminova, "Temperature measurement on overhead transmission lines (OHTL) utilizing surface acoustic wave (SAW) sensors," *19th Int. Conf. Electricity Distribution, CIRED*, no. 788, pp. 1-4, May 2007.

[47] H. Bohme, S. Kornhuber, S. Markalous, M. Muhr, and T. Strehl, "Operation ideas for overhead transmission lines (OHTLs) by using information of online temperature monitoring systems," *15th Int. Symp. High Voltage Engineering*, pp. 404-405, Aug. 2007.

[48] E. Golinelli, S. Musazzi, U. Perini, and G. Pirovano, "Laser based scanning system for high voltage power lines conductors monitoring," *20th Int. Conf. Electricity Distribution, CIRED*, no. 784, pp. 1-3, Jun. 2009.

[49] E. Golinelli, S. Musazzi, U. Perini, and F. Barberis, "Conductors sag monitoring by means of a laser based scanning measuring system: experimental results," *IEEE Sensors Application Symp.*, pp. 1-4, Feb. 2012.

[50] *Northern Ireland Snowstorms Report*, Utility Regulator, Belfast, May 2001. Available: http://www.uregni.gov.uk/news/northern_ireland_snowstorms_report

[51] G.F. Miceli and M. Parisi, "Methods and systems for analysing overhead line geometries," *United States Patent*, no. US 6853327 B2, Feb. 2005.

[52] G. Light, "More power to you: video sagometer helps utility companies tap unused capacity from power lines," *Technology Today*, pp. 10-11, 2003.

[53] *Increased Power Flow through Transmission Circuits: Overhead Line Case Studies and Quasi-dynamic Rating*, Electric Power Research Institute (EPRI), California, Technical Update Report 1012533, Dec. 2006.

[54] *Video Sagometer Application Guide*, EPRI, California, Final Technical Report 1001921, 2001. http://www.epri.com/abstracts/Pages/ProductAbstract.aspx?ProductId=000000000001001921

[55] S.U. Joutsenvuo, R. Pasonen, and S. Rissanen, "Maximising power line transmission capacity by employing dynamic line ratings – technical survey and applicability in Finland," Research Report VTT-R-01604-13, Espoo, Finland, Feb. 2013.

[56] S. Kamboj and R. Dahiya, "Application of GPS for sag measurement of overhead power transmission line," *Int. Journal on Electrical Engineering and Informatics*, vol. 3, no. 3, 2011.

[57] S.M. Mahajan and U.M. Singareddy, "A real-time conductor sag measurement system using a differential GPS," *IEEE Trans Power Delivery*, vol. 27, no. 2, Apr. 2012.

[58] *CAT-1^{TM} Dynamic Line Rating System*, USi, New York, May 2016. http://www.usi-power.com/

[59] *CAT-1 Transmission Line Monitoring System – Optimize Your Network Capabilities*, The Valley Group, Connecticut, U.S. Available: http://www.nexans.us/US/2008/CAT-1_Brochure_1.pdf

[60] Z. He and Y. Liu, "The field application analysis of dynamic line rating system based on tension monitoring," *2011 IEEE Power Engineering and Automation Conf.*, vol. 2, pp. 284-288, 2011.

[61] *CAT-1 Transmission Line Monitor – System Data Sheet*, The Valley Group, Connecticut. Available: http://www.nexans.us/US/2009/CAT-1%20Series%203_4.1%20Data%20Sheet

[62] *How It Works – Real Time Sag*, Ampacimon, Belgium, Mar. 2011. Available: http://www.ampacimon.com/wp-content/uploads/2015/09/How-Sag-work.pdf

[63] J.L. Lilien, S. Guerard, B. Godard, J. Destine, and E. Cloet, "Microsystem array for live high voltage line monitoring," *CIGRE Session*, Paris, paper B2-302-2006, pp. 1-8, Aug. 2006.

[64] E. Cloet and J.L. Lilien, "Uprating transmission lines through the use of an innovative real-time monitoring system," *IEEE PES 12th Int. Conf. Transmission and Distribution Construction, Operation and Live-Line Maintenance (ESMO)*, pp. 1-6, May 2011.

[65] E. Cloet, J.L. Lilien, and P. Ferrieres, "Experiences of the Belgian and French TSOs using the Ampacimon real-time dynamic rating system," *CIGRE Session*, Paris, paper C2-106-2010, 2010.

[66] *Innovative Solution for Dynamic Line Rating*, Ampacimon, Belgium. Available: http://www.ampacimon.com/wp-content/uploads/2015/09/Ampacimon-Brochure.pdf

[67] *The ThermalRate^{TM} System*, PIKE Electric, North Carolina. Available: http://www.pike.com/Docs/ThermalRate_Brochure.pdf

[68] J.R. Daconti and D.C. Lawry, "The ThermalRate System: a solution for thermal uprating of overhead transmission lines," *Power Technology*, issue 95, pp. 1-4, Apr. 2004.

[69] A. Phillips, "Evaluation of instrumentation and dynamic thermal ratings for overhead lines," *Electric Power Research Institute*, California, Final Report, Oct. 2013. Available: https://www.smartgrid.gov/files/NYPA_Final_Technical_Report_10-11-2013

[70] E.M. Carlini, F. Massaro, and C. Quaciari, "Methodologies to uprate an overhead line. Italian TSO case study," *Journal of Electrical Systems*, vol. 9, no. 4, pp. 422-439, Dec. 2013.

[71] W. Wang and S. Pinter, "Dynamic line rating systems for transmission lines," *Tropical Report*, U.S. Department of Energy, Apr. 2014. Available: https://www.smartgrid.gov/files/SGDP_Transmission_DLR_Topical_Report_04-25-14_FINAL.pdf

[72] P. Schell, H.M. Nguyen, and J.L. Lilien, "Quantifying the limits of weather based dynamic line rating methods," *CIGRE Conf. Power System*, Canada, pp. 1-8, Sep. 2011.

[73] J. Hosek, P. Musilek, E. Lozowski, and P. Pytlak, "Effect of time resolution of meteorological inputs on dynamic thermal rating calculations," *IET Generation, Transmission and Distribution*, vol. 5, no. 9, pp. 941-947, 2011.

[74] CIGRE Working Group B2.12, "Guide for selection of weather parameters for bare overhead conductor ratings," CIGRE Technical Brochure 299, Aug. 2006.

[75] J. Zhang, J. Pu, J.D. McCalley, H. Stern, and W.A. Gallus, "A Bayesian approach for short-term transmission line thermal overload risk assessment," *IEEE Trans. Power Delivery*, vol. 17, no. 3, pp. 770-778, Jul. 2002.

[76] D. Kim and J. Kim, "Prediction of transmission-line rating based on thermal overload probability using weather models," *European Trans. Electrical Power*, vol. 20, no 4, pp. 534-544, 2010.

[77] E. Fernandez, I. Albizu, G. Buigues, V. Valverde, A. Etxegarai, and G. Olazarri, "Dynamic line rating forecasting based on numerical weather prediction," *2015 IEEE PowerTech*, pp. 1-6, 2015.

[78] B. Adam, "Weather-based and conductor state measurement methods applied for dynamic line rating forecasting," *2011 Int. Conf. Advanced Power System Automation and Protection (APAP)*, pp. 762-765, 2011.

[79] G.P. Nason, "Stationary and non-stationary time series," *Statistics in Volcanology*, Chapter 11, Bath: Geological Society, 2006.

[80] Z. Yang, "Fourier analysis-based air temperature movement analysis and forecast," *IET Signal Processing*, vol. 7, no. 1, pp. 14-24, Feb. 2013.

[81] D.C. Hill, D. McMillan, K.R.W. Bell, and D. Infield, "Application of auto-regressive models to U.K. wind speed data for power system impact studies," *IEEE Trans. Sustainable Energy*, vol. 3, no. 1, pp. 134-141, Jan. 2012.

[82] G. Box, G. Jenkins, and G. Reinsel, *Times Series Analysis: Forecasting and Control*, 4th Ed., New Jersey: John Wiley & Sons, Inc., 2008.

[83] C. Heij, P. Boer, P.H. Franses, T. Kloek, and H.K. Dijk, *Econometric Methods with Applications in Business and Economics*, New York: Oxford, pp. 118-122, 2004.

[84] D. Yang, Z. Dong, T. Reindl, P. Jirutitijaroen, and W.M. Walsh, "Solar irradiance forecasting using spatio-temporal empirical kriging and vector auto-regressive models with parameter shrinkage," *Solar Energy*, vol. 103, pp. 550-562, May 2014.

[85] H. Lütkepohl, *New Introduction to Multiple Time Series Analysis*, New York: Springer-Verlag, 2005.

[86] D. Hooper, "Wind vector notation conventions," *The NERC MST Radar Facility at Aberystwyth*, Sep. 2002. Available: http://mst.nerc.ac.uk/wind_vect_convs.html

[87] F. Fan, K. Bell, and D. Infield, "Probabilistic weather forecasting for dynamic line rating studies," *19th Power Systems Computation Conference*, pp. 1-7, Jun. 2016.

[88] F. Fan, K. Bell, and D. Infield, "Probabilistic real-time thermal rating forecasting for overhead lines by conditionally heteroscedastic autoregressive models," *IEEE Trans. Power Delivery*, vol. 32, no. 4, pp. 1881-1890, Aug. 2017.

[89] T. Gneiting and M. Katzfuss, "Probabilistic forecasting," *The Annual Review of Statistics and Its Application*, vol. 1, pp. 125-151, Jan. 2014.

[90] T. Gneiting, F. Balabdaoui, and A.E. Raftery, "Probabilistic forecasts, calibration and sharpness," *Journal of the Royal Statistical Society: Series B (Statistical Methodology)*, vol. 69, no. 2, pp. 243-268, Apr. 2007.

[91] F.X. Diebold, T.A. Gunther, and A.S. Tay, "Evaluating density forecasts with applications to financial risk management," *Symp. Forecasting and Empirical Methods in Macroeconomics and Finance, Int. Economic Review*, vol. 39, no. 4, pp. 863-883, Nov. 1998.

[92] C. Carrillo, J. Cidras, E. Diaz-Dorado, and A.F. Obando-Montano, "An approach to determine the Weibull parameters for wind energy analysis: the case of Galicia (Spain)," *Energies*, vol. 7, pp. 2676-2700, 2014.

[93] E.P. Grimit, T. Gneiting, V.J. Berrocal, and N.A. Johnson, "The continuous ranked probability score for circular variables and its application to mesoscale forecast ensemble verification," *Quarterly Journal of the Royal Meteorological Society*, vol. 132, pp. 2925-2942, 2006.

[94] E.W. Weisstein, "Normal distribution," From *MathWorld* – A Wolfram Web Resource. Available: http://mathworld.wolfram.com/NormalDistribution.html

[95] T. Gneiting, K. Larson, K. Westrick, M.G. Genton, and E. Aldrich, "Calibrated probabilistic forecasting at the Stateline wind energy centre: the regime-switching space-time method," *Journal of the American Statistical Association*, vol. 101, no. 475, pp. 968-979, Sep. 2006.

[96] P. Berens, "CircStat: a MATLAB toolbox for circular statistics," *Journal of Statistical Software*, vol. 31, no. 10, pp. 1-21, Sep. 2009.

[97] T. Gneiting, A.E. Raftery, A.H. Westveld, and T. Goldman, "Calibrated probabilistic forecasting using ensemble model output statistics and minimum CRPS estimation," *Monthly Weather Review*, vol. 133, no. 5, pp. 1098-1118, May 2005.

[98] H. Hersbach, "Decomposition of the continuous ranked probability score for ensemble prediction system," *Weather and Forecasting*, vol. 15, no. 5, pp. 559-570, Oct. 2000.

[99] T. Gneiting and A.E. Raftery, "Strictly proper scoring rules, prediction and estimation," *Journal of the American Statistical Association*, vol. 102, no. 477, pp. 359-378, Mar. 2007.

[100] W. Jarosz, "Efficient Monte Carlo methods for light transport in scattering media," Ph.D. dissertation, Dept. Computer Science, Uni. California, San Diego, pp. 149-166, 2008.

[101] W.S. Cleveland, "Robust locally weighted regression and smoothing scatterplots," *Journal of the American Statistical Association*, vol. 74, no. 368, pp. 829-836, 1979.

[102] J. Parkes and A. Tindal, "Forecasting short term wind farm production in complex terrain," *Proc. EWEC Conf.*, London, U.K., 2004.

[103] P. Eredics, "Short-term external air temperature prediction for an intelligent greenhouse by mining climatic time series," *6th IEEE Int. Symp. Intelligent Signal Processing*, pp. 317-322, Aug. 2009.

[104] L. Bodri and V. Cermak, "Prediction of surface air temperatures by neural network, example based on three-year temperature monitoring at Sporilov station," *Studia Geophysica Geodaetica*, vol. 47, no. 1, pp. 173-184, Jan. 2003.

[105] T. Chai and R.D. Draxler, "Root mean square error (RMSE) or mean absolute error (MAE) – Arguments against avoiding RMSE in the literature," *Geoscientific Model Development*, no. 7, pp. 1247-1250, Jun. 2014.

[106] F. Fan, K. Bell, D. Hill, and D. Infield, "Wind forecasting using kriging and vector auto-regressive models for dynamic line rating studies," *IEEE PowerTech Conf.*, pp. 1-6, 2015.

[107] E. Erdem and J. Shi, "ARMA based approaches for forecasting the tuple of wind speed and direction," *Applied Energy*, vol. 88, no. 4, pp. 1405-1414, Apr. 2011.

[108] T.H.M. El-Fouly, E.F. El-Saadany, and M.M.A. Salama, "One day ahead prediction of wind speed and direction," *IEEE Trans. Energy Conversion*, vol. 23, no. 1, pp. 191-201, Mar. 2008.

[109] A.S. Hering and M.G. Genton, "Powering up with space-time wind forecasting," *J. American Statistical Association*, vol. 105, no. 489, pp. 92-104, Mar. 2010.

[110] E. Erdem, J. Shi, and Y. Peng, "Short-term forecasting of wind speed and power – a clustering approach," *Proc. 2014 Industrial and Systems Engineering Research Conf.*, 2014.

[111] J. Dowell, S. Weiss, D. Hill, and D. Infield, "Short-term spatial-temporal prediction of wind speed and direction," *Wind Energy*, vol. 17, no. 12, pp. 1945-1955, Oct. 2013.

[112] H.M. Diagne, M. David, P. Lauret, and J. Boland, "Solar irradiation forecasting: state-of-the-art and proposition for future developments for small-scale insular grids," *2012 World Renewable Energy Forum*, pp. 4802-4809, May 2012.

[113] R. Huang, T. Huang, and R. Gadh, "Solar generation prediction using the ARMA model in a laboratory-level micro-grid," *IEEE 3rd Int. Conf. Smart Grid Communication*, pp. 528-533, 2012.

[114] D. Yang, P. Jirutitijaroen, and W.M. Walsh, "Hourly solar irradiance time series forecasting using cloud cover index," *Solar Energy*, vol. 86, no. 12, pp. 3531-3543, Dec. 2012.

[115] J. Huang, M. Korolkiewicz, M. Agrawal, and J. Boland, "Forecasting solar radiation on an hourly time scale using a coupled auto-regressive and dynamical system (CARDS) model," *Solar Energy*, vol. 87, pp. 136-149, Nov. 2012.

[116] Y. Sun and R. Kok, "A solar radiation model with a Fourier transform approach," *2007 Canadian Society for Bioengineering Technical Conf.*, vol. 49, pp. 717-724, 2007.

[117] Y. Liu, M.C. Roberts, and R. Sioshansi, "A vector auto-regressive weather model for electricity supply and demand modelling," Dept. Integrated Systems Engineering, The Ohio State Uni., Jun. 2014.

[118] J. Boland, "Time series modelling of solar radiation," *Modelling Solar Radiation at the Earth's Surface: Recent Advances*. Berlin, Germany: Springer-Verlag, 2008, 11, pp. 283-312.

[119] R.Y. Rubinstein, *Simulation and the Monte Carlo method*, Wiley-Interscience, New York, 2007.

[120] The MathWorks Inc., *normrnd, Normal random numbers*. Available: https://uk.mathwors.com/help/stats/normrnd.html

[121] B. Luong, "Truncated Gaussian," *MATLAB Central File Exchange*. Available: http://uk.mathworks.com/matlabcentral/fileexchange/23832-truncated-gaussian

[122] R.L. Iman and W.J. Conover, "A distribution-free approach to inducing rank correlation among input variables," *Communications in Statistics – Simulation and Computation*, vol. 11, no. 3, pp. 311-334, 1982.

[123] N.I. Fisher, *Statistical Analysis of Circular Data*, Cambridge University Press, U.K., 1993.

[124] T.A. Jones, "MATLAB functions to analyse directional (azimuthal) data – II: Correlation," *Computers & Geosciences*, vol. 36, no. 4, pp. 520-525, Apr. 2010.

[125] G. Bohling, "Kriging," Lecture Notes, Kansas Geological Survey, Oct. 2005. Available: http://people.ku.edu/~gbohling/cpe940/Kriging.pdf

[126] J. Li and A.D. Heap, "A review of spatial interpolation methods for environmental scientists," *Geoscience Australia*, Record 2008/23, 2008.

[127] G. Bohling, "Introduction to geostatistics and variogram analysis," Lecture Notes, Kansas Geological Survey, 2005. Available: http://people.ku.edu/~gbohling/cpe940/Variograms.pdf

[128] J. Li, R. Pan, and F. Fan, "Spatial interpolation of surface air temperature by kriging models," *Journal of Southwest China Normal University (Natural Science Edition)*, vol. 41, no. 5, pp. 21-27, May 2016. [Chinese]

[129] R. Sunila and K. Kollo, "A comparison of geostatistics and fuzzy application for digital elevation model," *The International Archives of the Photogrammetry, Remote Sensing and Spatial Information Sciences*, vol. 34, Part XXX, 2007.

[130] A. Gribov, K. Krivoruchko, J. Hoef, "Modelling the semi-variogram: new approach, methods comparison and case study," *Stochastic Modelling II*, 2001. Available: http://faculty.mu.edu.sa/public/uploads/1338413445.6852GIS28.pdf

[131] M. Refaat, *Data Preparation for Data Mining Using SAS*, 1st Edition, California: Maple Press Company, pp. 157-159, 2006.

[132] The MathWorks Inc., *Least-Squares Fitting*, 2017. Available: https://uk.mathworks.com/help/curvefit/least-squares-fitting.html?requestedDomain=www.mathworks.com

[133] *Kriging Example*. Available: http://www2.imm.dtu.dk/~alan/krexample.pdf

[134] C.J. Morgan, "Theoretical and practical aspects of variography: in particular, estimation and modelling of semi-variograms over areas of limited and clustered or widely spaced data in a two-dimensional South African gold mining context," PhD Thesis, Faculty of Engineering and the Built Environment, University of Witwatersrand, Johannesburg, pp. 39-41 2011.

[135] C.V. Deutsch, "Correcting for negative weights in ordinary kriging," *Computers & Geosciences*, vol. 22, no. 7, pp. 765-773, Aug. 1996.

[136] S.R. Vieira, J.R.P. Carvalho, M.B. Ceddia, and A.P. Gonzalez, "De-trending non stationary data for geostatistical applications," *Bragantia*, vol. 69, pp. 1-8, 2010.

[137] W. Cao, J.X. Hu, and X. Yu, "A study on temperature interpolation methods based on GIS," *IEEE 17th Int. Conf. Geoinformatics*, pp. 1-5, 2009.

[138] A. Stepek and I.L. Wijnant, "Interpolating wind speed normal from the sparse Dutch network to a high resolution grid using local roughness from land use maps," *Koninklijk Netherlands Meteorological Institute*, Technical Report 321, Jun. 2011.

[139] N. Nawri, H. Bjornsson, G.N. Petersen, and K. Jonasson, "Empirical terrain models for surface wind and air temperature over Iceland," Icelandic Meteorological Office, Technical Report VI2012-009, Sep. 2012.

[140] H. Xue, R. Zhu, and Z. Yang, "Study on land wind speed variation in coastal area," *ATCA Energiae Solaris Sinica*, vol. 23, no. 2, pp.207-210, Apr. 2002.

[141] E.H. Isaaks and R. Mohan Srivastava, *An Introduction to Applied Geostatistics*, Oxford University Press, New York, 1989.

[142] M.F. Yazar, E. Ozelkan, and B.B. Ustundag, "Multi-parameter spatial interpolation of solar radiation in heterogeneous structured agricultural areas," *Third Int. Conf. Agro-geoinformatics*, pp. 1-6, Aug. 2014.

[143] J.A. Ruiz-Arias, J. Tovar-Pescador, D. Pozo-Vazquez, and H. Alsamamra, "A comparative analysis of DEM-based models to estimate the solar radiation in mountainous terrain," *Int. Journal of Geographical Information Science*, vol. 23, no. 8, pp. 1049-1076, Aug. 2009.

[144] X. Pons and M. Ninyerola, "Mapping a topographic global solar radiation model implemented in a GIS and refined with ground data," *Int. Journal of Climatology*, vol. 28, no. 13, pp. 1821-1834, Nov. 2008.

[145] H. Alsamamra, J.A. Ruiz-Arias, D. Pozo-Vazquez, and J. Tovar-Pescador, "A comparative study of ordinary and residual kriging techniques for mapping global solar radiation over southern Spain," *Agricultural and Forest Meteorology*, vol. 149, no. 8, pp. 1343-1357, Aug. 2009.

[146] M. Bezzi and A. Vitti, "A comparison of some kriging interpolation methods for the production of solar radiation maps," *Geomatics Workbooks*, Milano, Italy: Laboratorio di Geomatica, 2005.

[147] H. Chai, W. Cheng, C. Zhou, X. Chen, X. Ma, and S. Zhao, "Analysis and comparison of spatial interpolation methods for temperature data in Xinjiang Uygur Autonomous Region, China," *Natural Science*, vol. 3, no. 12, pp. 999-1010, Dec. 2011.

[148] B.E. Hansen, *Lecture Notes Nonparametrics*, University of Wisconsin, Madison, Wisconsin, USA, 2009. Available:
https://pdfs.semanticscholar.org/2c36/60a1844f55935f798b10a48197a665d1a825.pdf

[149] J.C. McCall and T. Goodwin, "Dynamic line rating as a means to enhance transmission grid resilience," *2015 Gird of the Future Symposium*, CIGRE, 2015.

[150] S. Hoffmann, "The application of probabilistic thermal ratings to distribution overhead lines," Western Power Distribution, presented at *Overhead Lines Colloquium*, Mar. 2018.

[151] E.W. Weisstein, "Bisection" From *MathWorld* – A Wolfram Web Resource. Available:
http://mathworld.wolfram.com/Bisection.html

[152] J. Lambers, *Lecture Notes The Secant Method*, Univ. Southern Mississippi, Mississippi, USA, 2010. Available: http://www.math.usm.edu/lambers/mat772/fall10/lecture4.pdf

[153] The MathWorks Inc., *Interpolation Methods*, 2018. Available:
https://uk.mathworks.com/help/curvefit/interpolation-methods.html?searchHighlight=linear%20interpolation&s_tid=doc_srchtitle

[154] J.R. Alvarez, J.A. Anderson, and C.M. Franck, "Validation of a thermal model for overhead transmission lines at high conductor temperature," *IEEE PES General Meeting*, Jul. 2016.

[155] *Distribution Long Term Development Statement for the years 2013/14 to 2017/18*, SP Manweb plc, Prenton, Nov. 2013. Available:
https://www.spenergynetworks.co.uk/userfiles/file/ScottishPower_Manweb_Long_Term_Development_Statement_2013.pdf

[156] R. Ak, V. Vitelli, and E. Zio, "Uncertainty modelling in wind power generation prediction by neural networks and bootstrapping," *Proc. European Safety & Reliability Conf.*, pp. 1-6, 2013.

[157] C.G. Justus, W.R. Hargraves, and A. Yalcin, "Nationwide assessment of potential output from wind-powered generators," *Journal of Applied Meteorology*, vol. 15, no. 7, pp. 673-678, 1976.

[158] *North Hoyle Offshore Wind Farm*, 4C Offshore [Online]. Available: http://www.4coffshore.com/windfarms/windfarms.aspx?windfarmId=UK16

[159] *Vestas 2MW, V80-2.0MW, V90-1.8/2.0MW, V100-1.8MW*, Vestas [Online]. Available: https://www.ledsjovind.se/tolvmanstegen/Vestas%20V90-2MW.pdf

[160] *Rhyl Flats Offshore Wind Farm*, 4C Offshore [Online]. Available: http://www.4coffshore.com/windfarms/rhwww.gyl-flats-united-kingdom-uk19.html

[161] *Wind Turbine SWT-3.6-107: Technical Specifications*, Siemens [Online]. Available: https://www.siemens.com/content/dam/internet/siemens-com/global/market-specific-solutions/wind/data_sheets/data-sheet-wind-turbine-swt-3-6-107.pdf

[162] *Tir Mostyn & Foel Goch (United Kingdom)*, The Wind Power [Online]. Available: http://www.thewindpower.net/windfarm_en_1496_tir-mostyn-foel-goch.php

[163] *GAMESA G52-850KW*, Gamesa [Online]. Available: http://www.wind-power-program.com/Library/Turbine%20leaflets/Gamesa/Gamesa%20G52%20850kw.pdf

[164] *Moel Maelogen (United Kingdom)*, The Wind Power [Online]. Available: http://www.thewindpower.net/windfarm_en_1510_moel-maelogen.php

[165] *SWT-1.3-62 (Siemens)*, The Wind Power [Online]. Available: http://www.thewindpower.net/scripts/fpdf181/turbine.php?id=24

[166] H.M. Dommel and W.F. Tinney, "Optimal power flow solutions," *IEEE Trans. Power Apparatus and Systems*, vol. PAS-87, pp. 1866-1876, 1968.

[167] R.D. Zimmerman, C.E. Murill-Sanchez, and R.J. Thomas, "MATPOWER: Steady-state operations, planning, and analysis tools for power systems research and education," *IEEE Trans. Power System*, vol. 26, pp. 12-19, 2011.

[168] *Historical Demand Data, Data Explorer*, National Grid [Online]. Available: http://www2.nationalgrid.com/UK/Industry-information/Electricity-transmission-operational-data/Data-Explorer/

[169] Sinclair Knight Merz, "New generation technologies and GB grid codes – Report on change proposals to the grid codes in England & Wales and in Scotland," 2004. Available: https://www.ofgem.gov.uk/ofgem-publications/62336/9346-gridcodechanges.pdf

[170] C.J. Dent, L.F. Ochoa, and G.P. Harrison, "Network distributed generation capacity analysis using OPF with voltage step constraints," *IEEE Trans. Power System*, vol. 25, no. 1, pp. 296-304, Feb. 2010.

[171] R. Stephen, "Description of state of the art methods to determine thermal rating of lines in real-time and their application in optimising power flow," *CIGRE Paris Session 2000*, no. 22-304, 2000.

[172] *Calculation for sag and tension of a single overhead span*, East China Jiaotong University, 2012 [Chinese]. Available: http://www.docin.com/p-539192528.html

[173] *Analytical solutions for first-order LTI systems*, Thayer School of Engineering, Dartmouth. Available: http://www.dartmouth.edu/~sullivan/22files/1storder.pdf

APPENDIX

Appendix A. Formula Derivation for a Level Span [172]

For a static level span as shown in Fig. A-1, the net force is zero so that the net forces along the horizontal and vertical directions are both zero. That is, horizontal tensions at two attachments H_A and H_B are equal to a common value H; the sum of their vertical tensions V_A and V_B equals the total weight of the line that is the product of the line length L_c and the weight per unit length w:

$$H_A = H_B = H \tag{A-1}$$

$$V_A = V_B = wL_c/2 \tag{A-2}$$
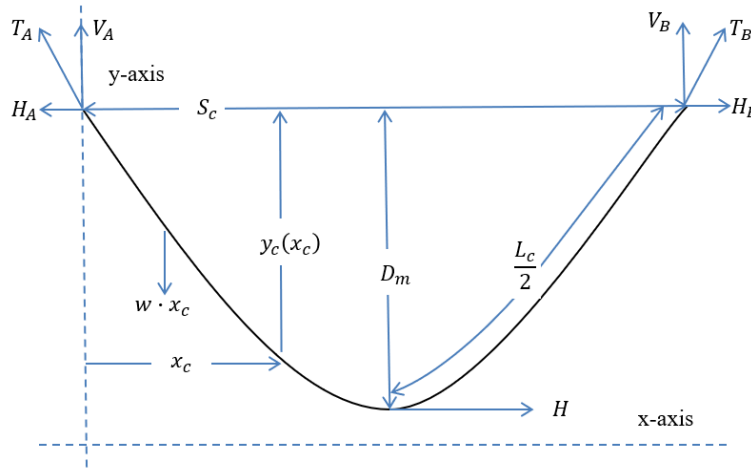
Fig. A-1. A level span [25]

The net torque $\sum M_o$ at any point along the static line, e.g. that has a horizontal distance x_c and a vertical distance $y_c(x_c)$ from the left attachment is also zero:

$$\sum M_o = H_A \cdot y_c(x_c) + w \cdot x_c \cdot \frac{x_c}{2} - V_A \cdot x_c = 0 \tag{A-3}$$

Taking equations (A-1) and (A-2) into equation (A-3), it can be obtained that:

$$H \cdot y_c(x_c) = x_c \cdot \frac{w}{2} \cdot (L_c - x_c) \tag{A-4}$$

The length of a line is assumed nearly equal to its span length in the parabolic approximation, i.e. $L_c \cong S_c$, which leads to:

$$H \cdot y_c(x_c) \cong x_c \cdot \frac{w}{2} \cdot (S_c - x_c) \tag{A-5}$$

The vertical distance $y_c(x_c = S_c/2)$ from the lowest point $x_c = S_c/2$ to the level of attachment points is the sag D_m for a level span:

$$D_m \cong \frac{wS_c^2}{8H} \tag{A-6}$$

Based on equations (A-5) and (A-6), a function of the horizontal distance from the left attachment point x_c representing the shape of the span can be defined as:

$$y_c(x_c) = \frac{4x_c \cdot (S_c - x_c) \cdot D_m}{S_c^2} \tag{A-7}$$

Appendix B. Formula Derivation for an Inclined Span [172]

An inclined span of two attachment points being at different levels, as shown in Fig. B-1 is considered to consist of half sections of two level spans with different sags D_L and D_R which are calculated as:

$$D_L = \frac{w(2X_L)^2}{8H} = \frac{wX_L^2}{2H} \tag{B-1}$$

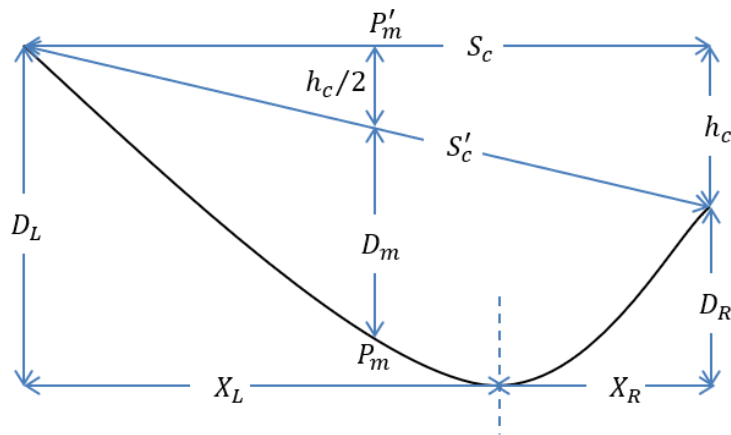$$D_R = \frac{w(2X_R)^2}{8H} = \frac{wX_R^2}{2H} \tag{B.2}$$

Fig. B-1. An inclined span [25]

where the sum of X_L and X_R representing the horizontal distances from the lowest point to left and right attachment points is equal to the horizontal distance between two attachment points S_c. Then the vertical distance between two attachment points is defined as:

$$h_c = D_L - D_R = \frac{w}{2H}(X_L - X_R)(X_L + X_R) = \frac{wS_c}{2H}(X_L - X_R) \tag{B-3}$$

Based on $S_c = X_L + X_R$ and equation (B-3), X_L and X_R are solved to be:

$$X_L = \frac{S_c}{2} + \frac{Hh_c}{wS_c} = \frac{S_c}{2}\left(1 + \frac{8Hh_c}{4wS_c^2}\right) = \frac{S_c}{2}\left(1 + \frac{h_c}{4D_m}\right) \tag{B-4}$$

$$X_R = \frac{S_c}{2} - \frac{Hh_c}{wS_c} = \frac{S_c}{2}\left(1 - \frac{8Hh_c}{4wS_c^2}\right) = \frac{S_c}{2}\left(1 - \frac{h_c}{4D_m}\right) \tag{B-5}$$

where $D_m = wS_c^2/8H$ can be considered to be the sag of a level span that has a span length equal to S_c, or the midpoint sag of an inclined span that has a horizontal span length equal to S_c.

The following derivations are to prove the midpoint sag of an inclined span equalling the sag of a level span with the same horizontal span length S_c. As shown in Fig. B-1, the midpoint sag D_m of an inclined span is the difference between P_mP_m', i.e. the vertical distance from the horizontal midpoint of the span to the level of left attachment point, and $h_c/2$, i.e. half of the vertical distance of two attachment points which has been defined in equation (B-3). The value of P_mP_m' can be estimated based on equation (A-7):

$$P_mP_m' = \frac{4 \cdot \frac{S_c}{2} \cdot \left(2X_L - \frac{S_c}{2}\right)}{(2X_L)^2} \cdot \frac{w(2X_L)^2}{8H} = \frac{wS_c \cdot \left(2X_L - \frac{S_c}{2}\right)}{4H} \tag{B-6}$$

Based on equations (B-3) and (B-6), the midpoint sag D_m for an inclined span is:

$$\begin{aligned} D_m &= P_mP_m' - \frac{h_c}{2} \\ &= \frac{wS_c}{4H}\left(2X_L - \frac{X_L + X_R}{2} - X_L + X_R\right) = \frac{wS_c}{4H} \cdot \left(\frac{X_L + X_R}{2}\right) = \frac{wS_c^2}{8H} \end{aligned} \tag{B-7}$$

which equals the sag of a level span with a span length S_c.

Appendix C. Enhanced Analytical Method

In a non-steady-state heat balance equation for overhead conductors [3], the radiation heat loss rate per unit length Q_r is non-linear with conductor temperature T_c, and the convection heat loss rate per unit length Q_c will be non-linear with T_c if (a) Q_c is determined by the natural convection heat loss rate Q_{cn} throughout a specified time period or (b) Q_c evaluated at the initial conductor temperature T_{ci} and the steady-state final temperature T_{cfss} are determined by the forced convection heat loss rate Q_{cf} and Q_{cn} respectively. Assuming the cooling terms to be linear with $T_c \in [T_{ci}, T_{cfss}]$, the non-steady-state heat balance equation can be written as:

$$\frac{\Delta(T_c(t) - T_a)}{\Delta t} = -\frac{K_c \cdot (T_c(t) - T_a)}{m \cdot C_p} + \frac{I^2 \cdot R(T_c(t)) + Q_s}{m \cdot C_p} \tag{C-1}$$

where $\Delta(T_c(t) - T_a)/\Delta t$ is the change rate of the rise of T_c above air temperature T_a at time t; terms $I^2 \cdot R$, Q_s and $m \cdot C_p$ represent the Joule heat gain rate, solar heat gain rate and total heat capacity of the conductor per unit length. The sum of Q_c and Q_r is assumed to linearly increase with $(T_c - T_a)$ at a rate K_c over the given time period. As discussed in Section 6.2.2.3, the conductor's thermal equilibrium at the start of a given time period is created by inference of an equivalent steady-state initial line current $I_{i,eq}$ from T_{ci} and weather conditions wc over the time period using a steady-state heat balance equation [3]. Under the assumption that $(Q_c + Q_r)$ linearly varied with $(T_c - T_a)$ at a rate K_c, the steady-state heat balance equation at the start of the time period is written as:

$$I_{i,eq}^2 \cdot R(T_{ci}) + Q_s(wc) = Q_c(T_{ci}, wc) + Q_r(T_{ci}, wc) = K_c \cdot (T_{ci} - T_a) \tag{C-2}$$

When T_c reaches the steady-state final conductor temperature T_{cfss} corresponding to the final line current I_f and wc after the step changes, the steady-state heat balance equation is written as:

$$I_f^2 \cdot R(T_{cfss}) + Q_s(wc) = Q_c(T_{cfss}, wc) + Q_r(T_{cfss}, wc) = K_c \cdot (T_{cfss} - T_a) \quad \text{(C-3)}$$

The value of K_c can then be estimated from equations (C-2) and (C-3):

$$K_c = \frac{I_f^2 \cdot R(T_{cfss}) - I_{i,eq}^2 \cdot R(T_{ci})}{T_{cfss} - T_{ci}} \quad \text{(C-4)}$$

The equation (C-1) can be considered as a first-order linear time invariant (LTI) system which has a time constant τ and has the solution [173]:

$$T_c(t) - T_a = (T_{cfss} - T_a) + \left((T_{ci} - T_a) - (T_{cfss} - T_a)\right) \cdot e^{-t/\tau} \quad \text{(C-5)}$$

which can also be written as:

$$T_c(t) = T_{ci} + (T_{cfss} - T_{ci}) \cdot (1 - e^{-t/\tau}) \quad \text{(C-6)}$$

provided that the increase in Joule heat gain rate after the step occurs is a step input. This requires the value of the ac resistance to be assumed as a constant over the time period. According to [3], the constant ac resistance is evaluated at the average T_{avg} of T_{ci} and T_{cfss}, denoted by $R(T_{avg})$. Thus, the steady-state heat balance equations in (C-2) and (C-3) are re-defined as:

$$I_{i,eq}^2 \cdot R(T_{avg}) + Q_s(wc) = K_c' \cdot (T_{ci} - T_a) \quad \text{(C-7)}$$

and,

$$I_f^2 \cdot R(T_{avg}) + Q_s(wc) = K_c' \cdot (T_{cfss} - T_a) \quad \text{(C-8)}$$

Therefore, the enhanced analytical method assumes that the sum of the cooling terms linearly changes with $(T_c - T_a)$ at a rate K_c':

$$K_c' = \frac{I_f^2 \cdot R(T_{avg}) - I_{i,eq}^2 \cdot R(T_{avg})}{T_{cfss} - T_{ci}} \quad \text{(C-9)}$$

According to [173], the time constant τ of the first-order LTI system is then calculated as:

$$\tau = \frac{m \cdot C_p}{K'_c} = \frac{m \cdot C_p \cdot \left(T_{cfss} - T_{ci}\right)}{\left(I_f^2 - I_{i,eq}^2\right) \cdot R\left(T_{avg}\right)} \qquad \text{(C-10)}$$

The Joule heat gain rate $I_f^2 \cdot R(T_c)$ over the given time period, in actuality, changes with $R(T_c)$ which is approximately estimated by linear interpolation between the given resistance values specified at two particular conductor temperatures [3]. Fig. C-1 compares (a) the actual and assumed variations in $I_f^2 \cdot R(T_c)$ with T_c that increases from T_{ci} to T_{cfss} and also (b) the changes of the linearized $(Q_c + Q_r)$ with T_c from $K_c \cdot (T_{ci} - T_a)$ to $K_c \cdot \left(T_{cfss} - T_a\right)$ and from $K'_c \cdot (T_{ci} - T_a)$ to $K'_c \cdot \left(T_{cfss} - T_a\right)$. Since Q_s is a constant value over the given time period, it is not considered in the following analysis for simplicity. Then the values of cooling terms $K_c \cdot (T_{ci} - T_a)$, $K_c \cdot \left(T_{cfss} - T_a\right)$, $K'_c \cdot (T_{ci} - T_a)$ and $K'_c \cdot \left(T_{cfss} - T_a\right)$ equal $I_{i,eq}^2 \cdot R(T_{ci})$, $I_f^2 \cdot R(T_{cfss})$, $I_{i,eq}^2 \cdot R\left(T_{avg}\right)$ and $I_f^2 \cdot R\left(T_{avg}\right)$ respectively.
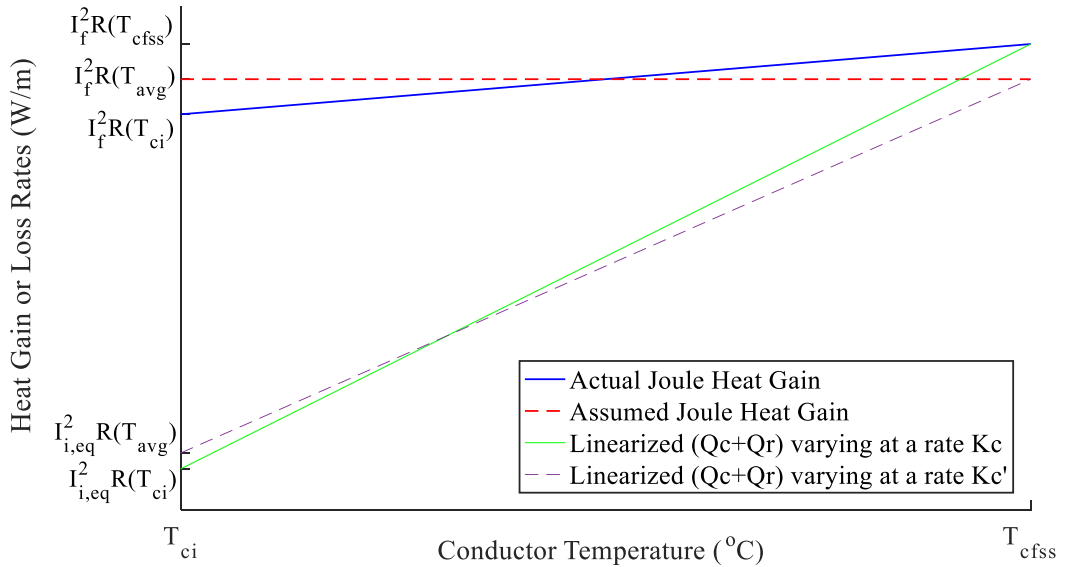

Fig. C-1. The actual and assumed Joule heat gain rates evaluated at T_c and the variations in the linearized cooling terms with T_c at different rates.

The difference between the assumed Joule heat gain rate per unit length (the first term on the right-hand side of equation (C-11)) and the actual value (the second term) evaluated at T_c is calculated as:

$$\Delta Gain(T_c) = I_f^2 \cdot R(T_{avg}) - \left[I_f^2 \cdot R(T_{ci}) + \frac{I_f^2 \cdot R(T_{cfss}) - I_f^2 \cdot R(T_{ci})}{T_{cfss} - T_{ci}} \cdot (T_c - T_{ci}) \right] \quad \text{(C-11)}$$

A positive $\Delta Gain(T_c)$ means an overestimated heat gain rate, and vice versa. (The overestimation in Joule heat gain rate means the overestimation in the total heat gain rate due to the constant Q_s over the specified time period). The difference between the linearized cooling terms $(Q_c + Q_r)$ evaluated at T_c which vary with $(T_c - T_a)$ at K_c' (the first term on the right-hand side of equation (C-12)) and K_c (the second term) is calculated as:

$$\Delta Loss_{linearized}(T_c)$$
$$= \left[I_{i,eq}^2 \cdot R(T_{avg}) + \frac{I_f^2 \cdot R(T_{avg}) - I_{i,eq}^2 \cdot R(T_{avg})}{T_{cfss} - T_{ci}} \cdot (T_c - T_{ci}) \right]$$
$$- \left[I_{i,eq}^2 \cdot R(T_{ci}) + \frac{I_f^2 \cdot R(T_{cfss}) - I_{i,eq}^2 \cdot R(T_{ci})}{T_{cfss} - T_{ci}} \cdot (T_c - T_{ci}) \right] \quad \text{(C-12)}$$

A positive $\Delta Loss_{linearized}(T_c)$ means an overestimation in the linearized heat loss rate, and vice versa. The difference between $\Delta Gain(T_c)$ and $\Delta Loss_{linearized}(T_c)$ at T_c is then calculated from equations (C-11) and (C-12):

$$\Delta Gain(T_c) - \Delta Loss_{linearized}$$
$$= (I_f^2 - I_{i,eq}^2) \cdot [R(T_{avg}) - R(T_{ci})] \cdot \left(1 - \frac{T_c - T_{ci}}{T_{cfss} - T_{ci}}\right) \quad \text{(C-13)}$$
$$= (I_f^2 - I_{i,eq}^2) \cdot \frac{R(T_{cfss}) - R(T_{ci})}{2} \cdot \left(1 - \frac{T_c - T_{ci}}{T_{cfss} - T_{ci}}\right) \quad \forall T_c \in [T_{ci}, T_{cfss}]$$

Equation (C-13) is also applied to the case where T_c decreases from T_{ci} after a reduction in line current from $I_{i,eq}$ to I_f. The right-hand side of equation (C-13) is found to be always greater than or equal to zero. This means that, under the assumption of a linear variation in $(Q_c + Q_r)$ from $K_c \cdot (T_{ci} - T_a)$ to $K_c \cdot$

$\left(T_{cfss} - T_a\right)$, the overestimation in heat gain rate is greater than that in the linearized heat loss rate (or the underestimation in heat gain rate is smaller than that in the linearized heat loss rate). In other words, the enhanced analytical method that evaluates the ac resistance R at $T_{avg} = \left(T_{ci} + T_{cfss}\right)/2$ would overestimate conductor temperature at the end of the given time period if the $(Q_c + Q_r)$ did linearly vary with $(T_c - T_a)$ over the time period.

However, as noted above, the actual change rate of $(Q_c + Q_r)$ is not constant but increases with T_c. This means that the linearized heat loss rate $K_c \cdot (T_c - T_a)$ is always greater than or equal to the actual $(Q_c + Q_r)$ evaluated at $T_c \in \left[T_{ci}, T_{cfss}\right]$. The total overestimation in $(Q_c + Q_r)$ after the linearization exceeding $(\Delta Gain - \Delta Loss_{linearized})$ over a specified time period will lead to an underestimated final conductor temperature at the end of the time period. The analysis results in Sections 6.3.2 and 6.3.3 have shown that the transient-state final conductor temperature is overestimated by the enhanced analytical method for most of the time and slightly underestimated in a few cases.